



**SELÇUK  
ÜNİVERSİTESİ**

**SELÇUK ÜNİVERSİTESİ  
MÜHENDİSLİK - BİLİM VE  
TEKNOLOJİ DERGİSİ**

**SELÇUK UNIVERSITY  
JOURNAL OF ENGINEERING SCIENCE AND  
TECHNOLOGY  
(SUJEST)**

**EISSN 2147-9364**

**HAKEMLİ DERGİDİR**

OWNER/SAHİBİ

Owner on Behalf of Engineering Faculty of Selcuk University **Prof. Dr. Ferruh YILDIZ**  
Selçuk Üniversitesi Mühendislik Fakültesi Adına Dekan **Prof. Dr. Ferruh YILDIZ**

Chief Editor/Şef Editör

**Prof. Dr. Muzaffer KAHVECİ**

Editors/Editörler

**Prof. Dr. Mustafa TABAKCI**  
**Assist. Prof. Dr. Ömer Kaan BAYKAN**

Advisory Board/Danışma Kurulu

Prof. Dr. Cengiz ALYILMAZ, Ataturk University	Prof. Dr. Dervis KARABOGA, Erciyes University
Prof. Dr. Ercan AKSOY, Bitlis Eren University	Prof. Dr. Ibaraki SOICHI, Kyoto University
Prof. Dr. Lena HALOUNOVA, Czech Technical University	Prof. Dr. Matchavariani LIA, Tbilisi State University
Prof. Dr. Petros PATIAS, The Aristotle University	Prof. Dr. Seref SAGIROGLU, Gazi University
Prof. Dr. Sitki KULUR, Istanbul Technical University	Prof. Dr. Vijay P. SINGH, Texas A and M University

Language Editing/Yabancı Dil Editörü

**Prof. Dr. Ali BERKTAY**

Composition and Printing/Baskı ve Dizgi

**Dr. Lutfiye Karasaka**  
**Res. Assist. Ismail KOC**

Correspondance Address/Yazışma Adresi

Selçuk Üniversitesi Muhendislik Fakültesi Dekanlığı  
42075-Kampüs, Selçuklu, Konya-TURKEY

Tel : 0 332 241 0 634  
Fax : 0 332 241 0 635  
E-mail : [sujest@selcuk.edu.tr](mailto:sujest@selcuk.edu.tr)  
Web : <http://sujest.selcuk.edu.tr>

## **Editorial Board (Yayın Kurulu)**

- Ahmet Afsin Kulaksiz, Selcuk University, TURKEY
- Alla Anohina-Naumeca, Riga Technical University, LATVIA
- Ashok K. Mishra, Clemson University, USA
- Baris Binici, Middle East Technical University, TURKEY
- Coskun Bayrak, University of Arkansas, USA
- Demetrio Fuentes Ferrera, University of Castilla-La Mancha, SPAIN
- Fahrettin Ozturk, The Petroleum Institute, UAE
- Haci Murat Yilmaz, Aksaray University, TURKEY
- Heinz Ruther University of Cape Town, SOUTH AFRICA
- Homayoun Moghimi, Payame Noor University, IRAN
- Ihsan Ozkan, Selcuk University, TURKEY
- John Trinder, The University of New South Wales, AUSTRALIA
- Kerim Kocak, Selcuk University, TURKEY
- Loredana Judele, Technical University of Iasi, ROMANIA
- Mohamed Bouabaz, Université 20 août 1955-Skikda, ALGERIA
- Mohd Arif Wani, California State University, USA
- Mortaza Yari, University of Tabriz, IRAN
- Ömer Aydan, University of the Ryukyus, JAPAN
- Sanchoy K. Das, New Jersey Institute of Technology, USA
- Selim Dogan, Selcuk University, TURKEY
- Spase Shumka, Agricultural University of Tirana, ALBANIA
- Tahira Geroeva, Baku State University, AZERBAIJAN
- Vladimir Androkhonov, Novosibirsk Soil Research Institute, RUSSIA
- Ali Kocak, Yildiz Technical University, TURKEY
- Alpaslan Yazar, Selcuk University, TURKEY
- Ataur Rahman, University of Western Sydney, AUSTRALIA
- Cihan Varol Sam Houston State University, USA
- Dan Stumbea, Alexandru Ioan Cuza University of Iasi, ROMANIA
- Eva Burgetova, Czech Technical University, CZECH REPUBLIC
- Georgieva Lilia, Heriot-Watt University, UNITED KINGDOM
- Halil Kursad Ersoy, Selcuk University, TURKEY
- Hi-Ryong Byun, Pukyong National University, SOUTH KOREA
- Huseyin Devenci, Selcuk University, TURKEY
- Iraida Samofalova, Perm University, RUSSIA
- Juan Maria Menendez Aguado, University of de Oviedo, SPAIN
- Laramie Vance Potts, New Jersey Institute of Technology, USA
- Mila Koeva, University of Twente, NETHERLANDS
- Mohamed Metwaly Abu Anbar, Tanta University, EGYPT
- Moonis Ali Khan, King Saud University, KSA
- Murat Karakus, University of Adelaide, AUSTRALIA
- Saadettin Erhan Kesen, Selcuk University, TURKEY
- Selcuk Kursat Isleyen, Gazi University, TURKEY
- Shukri Maxhuni, Prizen University, KOSOVA REPUBLIC
- Syed Tufail Hussain Sherazi, University of Sindh, PAKISTAN
- Thomas Niedoba, AGH University of Science and Technology, POLAND
- Zoran Sapuric, University American College Skopje, MACEDONIA

**SELÇUK ÜNİVERSİTESİ MÜHENDİSLİK, BİLİM VE TEKNOLOJİ DERGİSİ**  
**Selcuk University Journal of Engineering, Science and Technology**  
**(SUJEST)**

ISSN 2147 – 9364 (Elektronik)

Cilt	6	Mart	2018	Sayı	1
Volume	6	March	2018	Number	1

**İÇİNDEKİLER (CONTENTS)**

**Araştırma Makalesi (Research Article)**

**ANALYSES OF ROCK SURFACE COLOUR CHANGES DUE TO WEATHERING**

Analyses of Rock Surface Colour Changes Due To Weathering

.....**Mehmet Kemal GOKAY (English) 1-13**

**DÜŞEY MADEN KUYULARINDA BETON TAHKİMAT KALINLIKLARININ BELİRLENMESİNE YÖNELİK BİR TASARIM YAKLAŞIMI**

A Design Approach for Determination of Concrete Support Thickness in Vertical Mine Shafts

.....**Said Shahzada HUSSAINI, İhsan ÖZKAN 14-27**

**INFLUENCE OF FLAKE SIZE ON THE MORPHOLOGY OF WET SPUN GRAPHENE OXIDE FIBERS**

Influence of Flake Size on the Morphology of Wet Spun Graphene Oxide Fibers

.....**Volkan ESKİZEYBEK (English) 28-37**

**YENİ BİR YÜKSEK HIZLI KALP DESTEK POMPASININ SAYISAL VE DENEYSEL ANALİZİ**

Numerical and Experimental Analysis of A New High-Speed Heart Assist Pump

.....**Hasan ÇINAR, Rafet YAPICI 38-54**

**INFLUENCE OF VACUUM APPLICATION ON THE TRIBOLOGICAL PROPERTIES OF PORCELAIN WASTE REINFORCED EPOXY COMPOSITES**

Influence of Vacuum Application on the Tribological Properties of Porcelain Waste Reinforced Epoxy Composites

.....**Nurcan Calis ACIKBAS, Bilge YAMAN, Gokhan ACIKBAS (English) 55-69**

**A FUZZY LOGIC APPROACH FOR THE ESTIMATION OF PERFORMANCE HYDROXY DRY CELL WITH DIFFERENT PLATE COMBINATION**

A Fuzzy Logic Approach for the Estimation of Performance Hydroxy Dry Cell with Different Plate Combination

Yusuf YILMAZ, Sadık ATA, Gürol ÖNAL, Abdullah IŞIKTAŞ, Kevser DINCER (English) 70-87

**DESIGN AND IMPLEMENTATION OF AN OPEN ACCESS GEOPORTAL**

Design and Implementation of an Open Access Geoport

.....Fatih SARI (English) 88-99

**A FAST BISECTION BASED ANALYZER DESIGN FOR THE DETERMINATION OF MODES IN CIRCULAR WAVEGUIDES**

A Fast Bisection Based Analyzer Design for the Determination of Modes in Circular Waveguides

.....Coşkun DENİZ (English) 100-113

**A K-MEANS CLUSTERING BASED SHAPE RETRIEVAL TECHNIQUE FOR 3D MESH MODELS**

A K-Means Clustering Based Shape Retrieval Technique for 3D Mesh Models

.....Mohammadhassan REZAEI, Erkan GUNPINAR (English) 114-128

**A STUDY FROM JUNK MARKET TO THE PRODUCTION OF 5.25% EFFICIENT DYE-SENSITIZED SOLAR CELLS**

A Study from Junk Market to the Production of 5.25% Efficient Dye-Sensitized Solar Cells

.....Sunay TURKDOGAN (English) 129-139

**KİTOSAN KAPLI KAOLİN BONCUKLARIN SULU ÇÖZELTİLERDEN KROM(VI) UZAKLAŞTIRILMASINDA ADSORBAN OLARAK KULLANIMI**

Removal of Chromium (VI) from Aqueous Solutions Using Chitosan Coated Kaoline Beads as Adsorbent

.....Şerife PARLAYICI, Türkan ALTUN 140-151

**INVESTIGATION OF SURFACE ROUGHNESS AND MICROHARDNESS IN BALL BURNISHING PROCESS OF AZ31B MAGNESIUM ALLOY**

Investigation of Surface Roughness and Microhardness in Ball Burnishing Process of AZ31B Magnesium Alloy

.....Berat Baris BULDUM (English) 152-161

**BAĞLAYICI OLARAK PİROLİTİK SIVI KULLANILAN MgO-C REFRAKTER TUĞLALARIN  
MEKANİK ÖZELLİKLERİNİN İNCELENMESİ**

Investigation of the Mechanical Properties of MgO-C Refractory Bricks by Incorporation of Pyrolytic  
Liquid as Binder

...Tuba BAHTLI, Veysel Murat BOSTANCI, Derya Yeşim HOPA, Şerife Yalçın YASTI 162-174

## ANALYSES OF ROCK SURFACE COLOUR CHANGES DUE TO WEATHERING

<sup>1</sup>Mehmet Kemal GOKAY

<sup>1</sup>Selcuk University, Mining Engineering Department, Campus, Selcuklu, Konya, TURKEY

<sup>1</sup>mgokay@selcuk.edu.tr

(Geliş/Received: 16.03.2017; Kabul/Accepted in Revised Form: 21.07.2017)

**ABSTRACT:** Description parameters of rock masses and minerals include their colours as well. Colours appear in daylight for surfaced rock masses are changing slightly due to weathering layers which have been covering its surface gradually. Healthy human eyes can manage to differentiate visible light spectrum to identify colours of substances including rock masses. Then visible blackish colours of magnetite minerals, reddish colours of Terra- Rosa soils, greenish colours of weathered copper ore, pure white of salt minerals and many others are differentiable by naked eyes. Different colours and homogeneity of colour distribution for natural rocks are also main grading parameters of natural rock surfaces. In addition, colour can also be parameter to identify weathered rock surfaces. Outcrop rock mass surfaces or rock discontinuity surfaces which could be influenced by weathering factors, have their altered surface colours in general that, those colours can be different from the original rock colours. In this study, colour changes were determined in digital manner by obtaining rock surfaces' Red, Green, Blue digital colour (RGB) values. Digital colour differences have been then analyzed more specifically to evaluate rock weathering and colour changes.

**Key Words:** Color analyses, Colour change, Decolourisation, Rock weathering,

### Kaya Yüzey Renklerinde Bozuşma Sonucu Oluşan Değişimin İncelenmesi

**ÖZ:** Kayaçları ve onları oluşturan mineralleri tanımlama işleminde, gözlenen kayaç ve mineral yüzey renklerinin farklılığı, onları tanımlama işleminde önemli bir yer tutmaktadır. Kaya kütleleri buldukları lokasyonlarda, derinliklerde veya yeryüzünde, farklı etkilerden dolayı zaman içinde alterasyona uğrayarak bozurlar. Bu kayaç kütlelerinin sediman haline gelirken geçirdikleri kaçınılmaz kayaç döngüsünün önemli bir parçasıdır. Kayaçlardaki bozuşma çoğu durumda kayaç renginde önemli değişikliklere neden olur. Bu değişim sağlıklı insan gözleri tarafından algılanabilecek seviyede veya daha düşük seviyelerde gerçekleşebilir. İnsanlar çevrelerindeki kayaçları ve mineralleri onların renginden tanımlayabilirler. Manyetit mineralinin siyahlığı, terra-rosa toprağının kırmızı rengi, bozuşmuş bakır cevherinin yeşilliği, tuz mineralinin beyazlığı ve daha birçok mineral ve kayaç rengi bunları tanımlamak için kullanılmaktadır. Kayaç yüzeylerindeki renkler, bunların dağılımı ve renklerin homojenliği, kayaçlarda gerçekleşen bozuşmanın derecelendirilmesinde kullanılan parametrelerdendir. Kayaç yüzey renkleri, bu yüzeylerde bozuşma olup olmadığını anlamada karar verici özellik taşırlar. Kayaçların gün yüzüne çıkmış yüzeyleri ve kayaç içindeki süreksizlik yüzeyleri, bu yüzeyleri etkisi altına alan bozuşma, başkalaşım, faktörleri nedeniyle renk değiştirmeye açıktır. Bu araştırma kapsamında, kayaç yüzeylerindeki bozuşmaya bağlı renk değişimleri sayısallaştırılarak analiz edilmiştir. İncelemeye alınan lokasyonlarda, yeni kırılmış-bozuşmamış kayaç yüzeyleri ve bozuşmaya uğramış kayaç yüzey renkleri Kırmızı (R), Yeşil (G), Mavi (B) renk kodlamasına sahip, RGB renk sistemine göre sayısallaştırılarak ayrı ayrı incelenmiştir. Farklı kayaçlardan elde edilen kayaç yüzey renkleri, RGB kodlamaları, bu çalışma kapsamında kendi aralarında değerlendirmeye alınarak, renklerdeki değişimler incelenmiştir.

**Anahtar Kelimeler:** Renk analizi, Renk değişimi, Renksizleşme, Kayaç bozuşması,

## INTRODUCTION

Rock masses were early solid materials in the earth. After their first solidification, earth crust has been repeated its rock mass regeneration from mantle together with its demolishing process. Crustal movements, climate, sun radiation, chemical reactions, magmatic inner crust and volcanic activities have been main factors influencing these progressions. It is obvious that each volcanic discharge from magma has its own mineral mixture which turns out different coloured rock masses according to solidification processes. Magmatic, metamorphic and sedimentary rocks with various chemical compositions can be explored around us together with their original rock colours and weathered surface parts' colours. When rock mass related engineering activities have more been concentrated on rock weathering, engineers have studied more closely on rock surface colours. Because rock surface colours are first distinguishing factors to visualize rock weathering influences on the selected rock surfaces. While weathering has been slowly advanced in/on the rock masses, related rock surfaces have gradually altered their colours. Weathering of rocks covers progressive complex reactions which have been taken place under particular environments (deep or shallow locations in the earth crust; sometimes at the earth surface) influenced by gravity, pressure, bioactivity, radioactivity, heat, chemical reactions, climate etc. In rock mechanics concerns, most of the weathering activities have generally influenced rock mass mechanical properties. It is negative effect in general. Therefore any excavation works in or on rock masses which includes stability analyses, should cover detail rock mechanic tests for original and weathered parts of projected rock masses.

In nature, it is difficult to find massive rock masses, Rock masses in general have discontinuities and defect zones. Most of the discontinuities in rock masses are also passage ways of groundwater which has slurry type composition. Groundwater circulating in rock masses includes chemically dissolve materials and it may show basic or acidic activities in different strength. When the rock masses have contacted with groundwater slurry at their discontinuities, colours of contacted rock mass surfaces have gradually differentiated. Therefore, rock mass outcrops and rock discontinuity surfaces are main weathering locations in the rock masses. Clayton et al. (1982) mentioned that chemical rock weathering processes fully depend on the presence of water in or around the rock masses and this type of weathering result in the alteration or dissolution of the component minerals grains. They said that "the chemical decomposition of the rock material starts at discontinuity walls and works inwards towards the centre of the intact blocks". Rock weathering can be recognized by rock surface discolouration. Original rock surface colours may start to change gradually as weathering activities progressed. Therefore each engineering project located in/on rock masses should cover also rock mass discontinuity analyses. Aperture, spacing, orientation, fillings, undulation, roughness, moisture, groundwater seepage level, unconfined compressive strength of discontinuity surfaces, colours and textures observed on original and weathered rock surfaces are the other parameters which project engineers have to be informed. Colours of rocks and colours of discontinuity surfaces have long been used in quick, practical and descriptive identification of rock masses and rock surface weathering.

Rock colours and rock forming mineral colours have possibly been coded by using Munsell colour charts (Munsell, 1905; Cleland, 1921; Munsell Colours, 2017). Usage of this charts have brought widespread applications during identification and naming of rocks and minerals. This is one of earliest method to describe the same rock colours with the same digital codes which eliminates complexity in colour identification. Rock outcrops around us have their own surface appearances and colours, which might be a little different than the original colours of that particular rock mass. Rock surface colours have been affected by several natural influences like; climate effects, micro-organism attacks, chemical weathering, radioactive decaying etc. When the rock masses are forced to be broken down from their corners, its original colours can be seen in deep parts of the rock fragments where there is no weathering effect at all. This is one of the means how engineers can recognize the colour differences of weathered and original rock surfaces. If there are colour changes on these surfaces and if these can be recognized by naked eyes, these differences can also be codified by using Munsell charts or similar colour systems. In

order to eliminate irregularities occurred in colour tones identification due to human eyes capacities, colour digitizing method have recently been employed for engineering applications. This method produces standard colour reading outputs by using high definition colour photographs. There are several systems describing colours like; CAM, CIE, RGB, YUV and others (CMYK, Colouroid, HSV, HSI, HCl etc.). Rock surface colours obtained from weathered or original rock surface in this study were analyzed in RGB colour system. Rock surfaces were photographed in daylight and filed in computers according to their locations and rock mass types. Digitizing these images and obtaining RGB colour codes were the second steps in this work. During this study, high quality photographic images taken from six different locations including open pit mines, quarries, hydraulic dam construction sites, village road cuts were used to analyze colour differences between original and weathered rock surfaces. The aim was selected here to present these colour differentiation for the selected rock masses.

### COLOUR ANALYSES APPLIED FOR ROCK MATERIALS

Colour changes of rock surfaces happened during natural weathering progress have not searched in detail. On the other hand weathering of rock masses have been recognized as one of the main strength decreasing factors for rock masses. When underground openings, open pit slopes, civil purposed tunnels are planned in/on the weathered rock masses, engineers test these rock masses by using test samples taken from fresh and weathered parts of them. Similarly, dimensional building stones used for houses, pavements, parks, etc have also been tested for their strength. Building stones should not be cut from weak weathered rock masses. Moreover, these kinds of rock usages should be tested for their weathering strength according to their position of usage in construction industry. Hence identification of weathered parts of rock masses has always been an important. Clayton, et al. (1982) stated that weathering of rock may be detected by controlling their weathered parts' strength and colours. They wrote that "In many cases the most noticeable effect of weathering at the rock material scale will be discolouration and/or weakening adjacent to discontinuities". This statement stresses on the importance of original rock masses colours and their discolouration due to weathering. Clayton et al. (1982) especially mentioned the rock colour chart produced by Geological Society of America (1963). They wrote that, since the original colours of rock masses fully depend on associated mineral composition of the constituent particles or the cementing material (in the case of sedimentary rocks), these colours should be identified accurately without causing any further misleading. According to them researchers had earlier been worked on rock weathering to provide classification scheme. One of them for example concentrated on chemical weathering of granitic rocks (Anon, 1970). In later years, Geological Society of London (1977) organized a "Working Party of Engineering Group" to define effects of rock weathering. They described weathering for rock material (micro) and rock mass (macro) scales. As the engineering projects had been commissioned to construct in/on rock masses in modern world, intact and weathered rock differences and their identification have become important. As Clayton et al. (1982) reported that British Standard (BS 5930:1981) in this respect, offered to use following terms for weathered rock materials; *decomposed*, *disintegrated*, *fresh and discoloured* to order engineering usage of weathering terms. Importantly, "no guidance for determining and describing the degree of weathering" was also reported for this BS standard by these researchers. However, it demonstrated that rock decolourisation in nature is important stage in rock weathering activities.

Eggleton et al. (1987) were also studied rock weathering by concentrating on basalts. They stated that main weathering action they had been revealed was dissolution process. According to them plagioclases are weathered initially along fractures and cleavage planes. This weathering activities cause decolourisation (yellowing) of the related rock surfaces. They reported that "the colour change is largely caused by a change in the colour of the palagonite from yellow to orange-red and by the complete replacement of olivine and pyroxene by a dark-red, isotropic alteration product, predominantly goethite". Some other rock types have also been analysed for their weathering characteristics. Andesite located near Ankara (Turkey) for example evaluated by Karpuz and Pasamehmetoglu (1997) for their

weathering properties as well. They suggested idealized weathering profile and the scale of rock mass weathering grades. They described andesite rock masses in special terms, each shows andesite weathering levels; These terms are; colour, grain size, structure-texture, block size-shape, discontinuity spacing, weathering stage (hydrothermal alteration etc.), minor lithological characterization (layering, fracture, strength) and other additional characteristics (such as; discontinuity conditions, fillings, dominant joint sets, existence of hydrothermal alteration, etc.). Time effect on rock weathering is important. How long the fresh rock surfaces have been stayed under the weathering actions is other consideration parameters. Figure 1 shows here two graphical results given by Yokoyama and Nakashima (2005). These two researchers analysed colours of four rhyolites which have different volcanic eruption times (1100, 1800, 26000 and 52000 years ago) in Kozushima Island in Japan. They determined that these eruptions have similar chemical compositions at the time of eruption. This means common colours around the volcano was whitish lava colours just after each eruption. As it was stated in Yokoyama and Nakashima paper, the surface colours of these rhyolites were different in 2005 due to weathering effects in time. Since these rhyolites had been formed in different volcanic eruptions, oldest rhyolites have more yellow-brownish weathered rock surface colours. According to the researchers, colour changes which have gradually been arisen at rhyolite rock masses indicate the formation of iron (hydr) oxides on their surfaces.

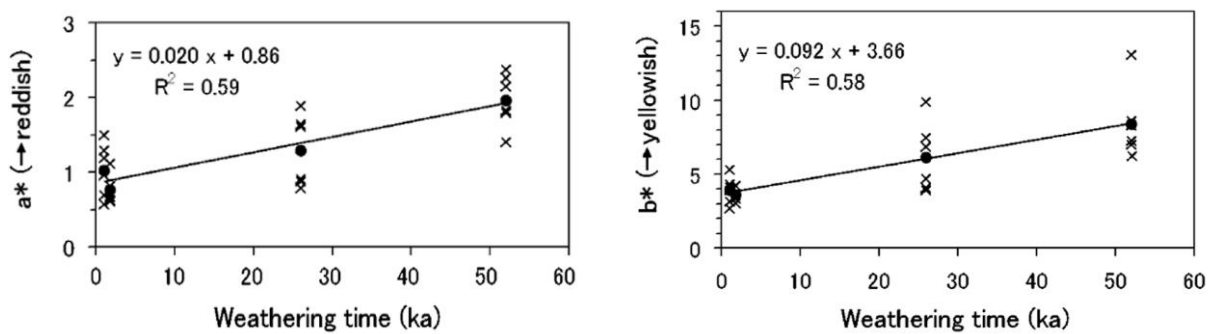


**Figure 1.** Rock powder colours ( $a^*$  and  $b^*$  colour values of L.a.b. colour system) determined from rhyolites samples were plotted here against total weathering time (ka= (x1000) years), (Yokoyama and Nakashima, 2005).

Chemical composition changes on the surfaces of rock masses where the weathering actions are more predominant differentiate rock surface colours. However there are other factors forcing the rock surface colour changes. For example Annerel and Taerwe (2011) examined colour changes of concrete structures exposed to fire. They applied HSI and CIE Lab colour space to obtain these changes in digital manner. They reported an elliptically shaped colour path changes. In some cases, weathering of rock materials have been analysed by using “ageing tests” like Heidari et al. (2017). They compared different ageing effects by using fuzzy inference system to estimate weathering degrees on monument stones of three historical sites in Iran. Ageing tests they performed on fresh rock materials were a) freeze-thaw, b) thermal shock, c) salt crystallization, d) dissolution and e) wetting-drying. These are the climatic influences on building stones which may cause severe weathering. Grossi et al. (2015) studied weathering degree of Itaquera Granite used for historical the Ramos de Azevedo monument in São Paulo, Brazil. They had monitored colour variation of granite on this monument to compare rock surface colours obtained from fresh granite surfaces which were mined from the same historical granite quarry. Colour values had been determined in this study for a while to understand effects of time and pathologies. Weathering effects (yellowing) on the monument’s granite surfaces were determined as; oxidation of iron-rich minerals, pollution influences, biological colonization, leaching of bronze statue over the granite base, and the dissolution-precipitation of monument mortars.

Weathering effects and colour changes on building stones are become common research activities after general acceptance of historical sites and their cultural values. Vazquez, et al. (2016) researched on six natural building stone types to understand weathering effects on them. They performed aging tests on these rock samples. Samples were exposed to four strong acidic atmospheres consist of the following acids: H<sub>2</sub>SO<sub>3</sub>, HNO<sub>3</sub>, and two mixed solution with different proportions of H<sub>2</sub>SO<sub>3</sub> and HNO<sub>3</sub>. They recorded; weight, colour, roughness and microscopic feature changes on the tested rock surfaces. They reported sample surface colour changes in L.a.b. colour system. In this colour analyses; “L” is lightness, “a” and “b” are colour channels where; “a” scales green-red colour values; “b” scales yellow-blue colour values (Hunter, 1948; Hunter-Labs, 1996). The graphs in Fig. 2 illustrate colour variation occurred during their ageing processes. This graphs show also that, even rock weathering factors are under control, the resultant colour changes happened on rock surfaces can be different. This shows also that rock types and properties are also main governing factors in weathering processes.

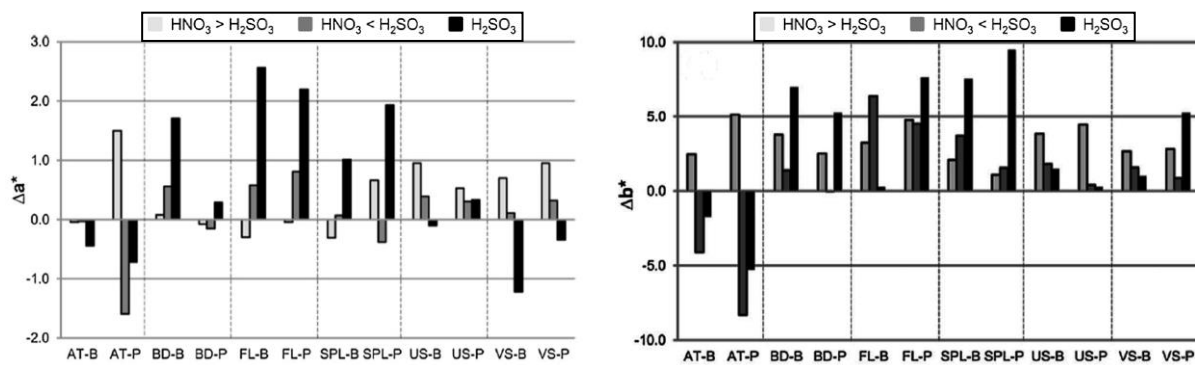


**Figure 2.** Variations in colour parameters “a” and “b” (in L.a.b. colour space) after each ageing test for the “bush hammered finish, (B)” and the “polished finish, (P)” natural stones. (Test samples were codified as; AT: Albox travertine, BD: Boñar dolostone, FL: Fraga limestone, SPL: Santa Pudia limestone, US: Uncastillo sandstone, VS: Villaviciosa sandstone), (Vazquez, et al., 2016).

Borrelli et al. (2007) analysed the relationship between rock mass weathering grades and slope instabilities. To reach this aim they prepared weathered rock maps for their project, study, areas. One of the factors they controlled in their field works was discolouration of the rock surfaces. They recorded discolouration of rock mass as; completely, partially, along discontinuity or none. After that, they combined all rock mass related data to decide on rock masses’ weathering grades. In computer colour analyses, colour systems have recently been used to digitize natural and industrial material’s colours. As Patel and Chatterjee (2016) stated that the study of computer vision-based rock-type classification is limited. Thus, they developed a computer vision-based rock-type classification algorithm to achieve consistent raw material classification for cement industry. In this work, Patel and Chatterjee utilized computer based RGB colour recognition systems and colour image histogram-based features to recognise rock types inputting to cement factory as a raw materials.

## DEGREE OF ROCK SURFACE WEATHERING

Differences in colours of rock masses illustrate certain property differences and this can be used by engineers in mining and civil engineering fields. Rock weathering and appeared colour intensity on rock mass surfaces have long been used to classify them in visual bases. Colour changes due to rock weathering on the other hand analysed digitally here in this study to evaluate if there is any colour related features. In order to realize any common attributes, fresh rock surfaces and weathered rock surfaces of the same rock types have been tested for their colour changes. Since limestone layers can easily be reached around Konya (Turkey), first colour analyses were performed for limestone

formations. Most of the outcropped limestone layers here have white, white to light gray, white to beige and gray in colours. These limestone layers are fractured and most of the open fractures near the surface had been filled by overburden materials. These materials are generally soils, decomposed rocks or their influents which are facilitated chemical weathering process in these discontinuities.

A research area in this study was decided then to explore digital RGB colour codes of fresh and weathered rock mass surfaces. The question here is; *“if there is any pattern or relation in rock decolourisation during weathering procedures”*. Weathered rock surfaces may get their colour in randomly progressed chemical reactions on those surfaces. In order to explicate colour change patterns at rock surfaces due to weathering, observations obtained from the rock masses outcropped around Konya regions were used. These tested rock masses were limestone, serpentine, andesite, travertine and tuff rocks.

In order to digitize weathered rock surface colours, first test site was selected at hard crystalline dolomitic limestone outcrop. It is Silurian-Devonian era rock mass (Eren, 1993) and it has dark gray in colour. This rock outcrop is located at 30 km away from Konya city centre. It was embodied at the North side of Konya-Yukselen village road. Since this limestone has high strength, hydraulic hammers were used to obtain enough space to construct village road. Due to these rock fragmentation techniques, road cut slopes at test location have fresh rock surfaces similar to the ones illustrated in Fig. 3a. Weathered rock surfaces in this location were generally discontinuity surfaces where some of them were day lighted due to road cut rock fragmentation. As it is seen at Fig. 3b, weathered dolomitic limestone surfaces here have light brown to light reddish or brownish in colours. Differences in weathered dolomitic limestone colours are mostly related with degree of decomposition and weathering levels.

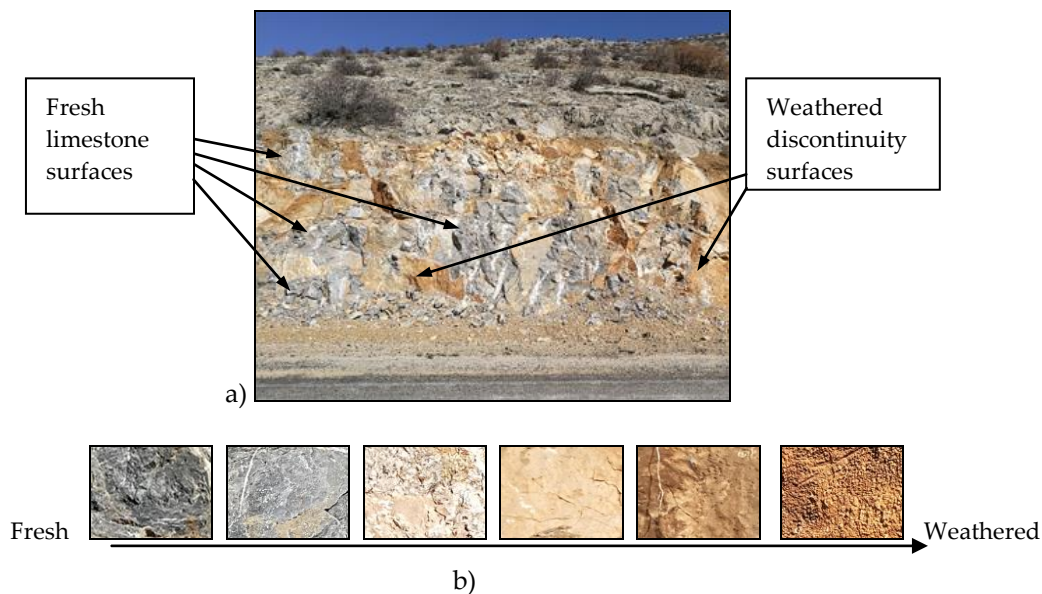


**Figure 3.** Fresh and weathered limestone surfaces at Konya-Yukselen road cut.

Colours at weathered rock surfaces in these images were determined and they were differentiating from light brown (light beige) to dark brown. Defining these colours and their tones differences in *“words”* bring always complexity in engineering communications. Referring common pre-defined charts like *Munsell colour charts* and tables in colour description have been one solution to this complexity. These types of colour identification methodologies can be called *“colour comparison-colour matching”* methods. They require obviously fine printed colour charts or booklets and healthy eyes. It should be mentioned here that the capacity of human eyes to differentiate colours and their tones are different among human beings. Because of these irregularities, colour analyses in industry have gradually been facilitated by finer equipments and machines. Colour sensors, cameras and computers are used today to define colours and their tones. In this research, images of rock surfaces were photographed by camera lens which have 20 megapixels in monochrome and 12 megapixels in RGB format capacity.

**Table 1.** Digitized RGB colours of dolomitic limestone rock mass located at Konya-Yukselen road cut, (Total data contains 93 lines of RGB readings but, this table presents only 5 lines of them as an example).

Fresh limestone surfaces			Weathered limestone surfaces		
Red (R)	Green (G)	Blue (B)	Red (R)	Green (G)	Blue (B)
134	129	122	59	33	17
166	155	144	127	82	48
119	110	98	141	93	54
128	127	127	99	67	38
180	176	170	126	93	67

After saving original pictures in JPEG file format into computers, selected parts of the images are analysed for their colour identifications (Table 1) by using MRA colour analyses program. This software was especially developed to define rock surface colours and their colour distribution homogeneities, (Gokay and Gundogdu, 2008). The RGB data, (obtained from 93 micro pixel-based areas), were then used to analyze colour changes by 2D and 3D graphics. These graphics were drawn by using Excel together with Xlstat-3D module (2017). Colour coding in RGB format defines totally ( $t=255 \times 255 \times 255$ ) 16,581,375 tones of colour values. This number of tones is seemed to be higher than the human eyes can handle in repetitive manner. In RGB codification, maximum and minimum limit values and their representing colours are as follows; RGB value of (0,0,0) represents total blackness, (255,255,255) value represents total whiteness in colour. Figure 4 shows that there are obvious graphical differences between fresh and weathered dolomitic limestone surfaces analysed here. Actually, original, fresh, colours of this rock mass at the selected slope of Konya-Yukselen road cut (Fig. 3a) are dark greyish in colour. Therefore colour data obtained from these fresh dolomitic limestone rock surfaces have graph points (square shaped data points) at graphics shown in Fig. 4 which can clearly detachable from the plot points representing weathered surfaces' colours (rectangular shaped data points). RGB data obtained from weathered dolomitic limestone surfaces produced scattered graph points as seen in Fig. 4. However when these graphs analysed in detail, (in other words when the weathered rock surface colours and observed weathering degrees were compared), it could be concluded that more weathered surfaces in this road cut location provide graphs' points closer to graphs' origin, (near to (0,0) values). Similarly when the plotted colour data points are observed closer to (255, 255) colour values in Fig. 4, the colours of dolomitic limestone weathered surfaces were observed for them as light-brownish (light-beige) which also means less degree of weathering.

At the earlier work performed at the same dolomitic limestone slopes, Gokay (2003) pointed out that fresh and weathered rock surfaces provided different chemical compositions. Samples obtained from fresh, (Fr), and weathered, (wth), surfaces were tested for their chemical compositions in that study and selected dominant chemical compounds were reported with the following composition values. These results (in percentage) are presented here for fresh rock (Fr) surfaces, weathered rock (wth) surfaces and discontinuity filling material (fill) as follows; CaO (Fr: 55.74 - wth: 49.78 - fill: 17.98), Al<sub>2</sub>O<sub>3</sub> (Fr: 0.17 - wth: 2.44 - fill: 8.44), Fe<sub>2</sub>O<sub>3</sub> (Fr: 0.24 - wth: 1.09 - fill: 6.07), MgO (Fr: 0.46 - wth: 5.23 - fill: 11.42) and SiO<sub>2</sub> (Fr: 0.89 - wth: 4.66 - fill: 33.45). That means; weathered rock surfaces shown in Fig. 4 have higher concentration of the following compounds (*multiplication values=wth/Fr*); Al<sub>2</sub>O<sub>3</sub> (14.35), Fe<sub>2</sub>O<sub>3</sub> (4.54), MgO (11.36) and SiO<sub>2</sub> (5.23). CaO concentration on the other hand was found lower for weathered rock surfaces, CaO (0.89). Combination effects of these chemical compound differences on dolomitic limestone rock surfaces should be the main reason of the colour changes due to weathering.

In order to understand the differences in weathered rock surface colours, originally whitish coloured (white, light gray, light beige) limestone outcrops in North-West side of the Konya city was also taken into evaluation. This limestone formation has Late Myosin-Early Pliocene aged (Eren, 1993) and it has gray-beige fresh surfaces. It contains very small amount of clay minerals in its composition as well. As it is seen in Fig. 5, rock weathering has been occurred here at the surface of discontinuities. Terra-rosa soiling activity and seepage of their influent into this limestone layers (Fig. 5) have been main

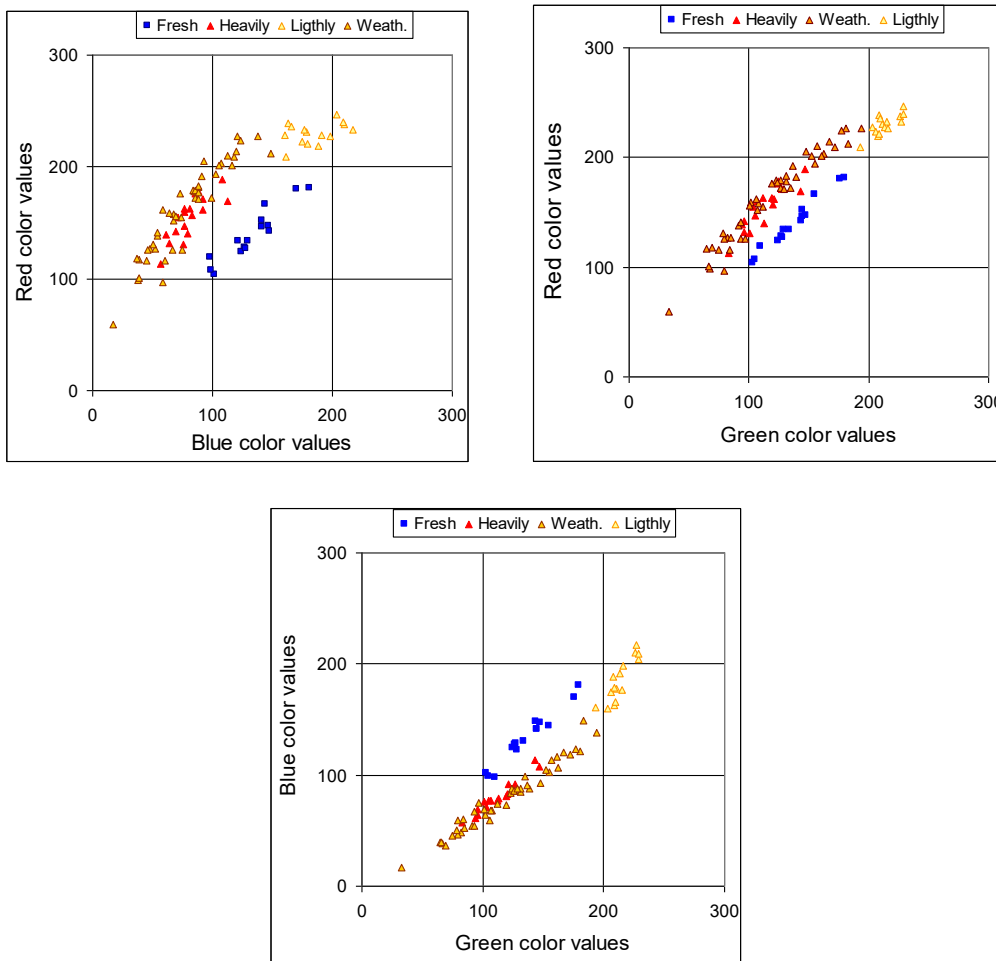


**Figure 4.** Selected colour-band graphics for digitized RGB data obtained from fresh and weathered dolomitic limestone surfaces (tested at Konya-Yukselen road cut).

weathering factors. Main differences between these two sets of data which were obtained from dolomitic limestone (1<sup>st</sup> case) and beige coloured limestone (2<sup>nd</sup> case) rock masses were their colours and compositions. Main chemical compound was CaO but there are many others which influence on their naming and weathering progress. In first case, the rock mass is dolomitic limestone therefore fresh rock surfaces are blackish, dark gray, with crystalline characters. In second case the rock mass is lake deposited limestone, its fresh rock surfaces are light gray, beige, and beige to gray in colour. Due to different sedimentation and tectonic conditions, (which they have been passed through in geological eras), their fresh rock colours gradually changed in some parts of them due to weathering actions. When the images given in Fig. 3a and Fig. 5a were analyzed, it can be seen that weathered parts of the rock masses have different colours with respect to fresh rock surfaces. Weathered rock colours are usually identified at these rocks' discontinuity surfaces and their day lighted surfaces. Total colour data obtained from lake deposited, beige coloured, limestone rock mass contain 87 points' RGB values. Each colour datum contains R, G, and B colour values separately. Selected colour band graphics supplied for beige coloured limestone, demonstrate weathering decolourisation (Fig.6) as well. That is as weathering effects were observed intensive, the colour codes obtained from weathered beige coloured limestone were plotted gradually towards the dark colour zones, (near to origin of graphs), of RGB colour graphics. However dolomitic limestone and beige coloured limestone have different graph point locations for their fresh surface colours (Fig. 4 and Fig. 6). Unlike the colour of beige limestone, (*Lst-2*, fresh surface colours were plotted near whiteness corners, 255,255,255), crystalline dark gray, dolomitic limestone, (*Lst-1*) produced fresh surface colours which have plot points near the blackness corner, (0,0,0).

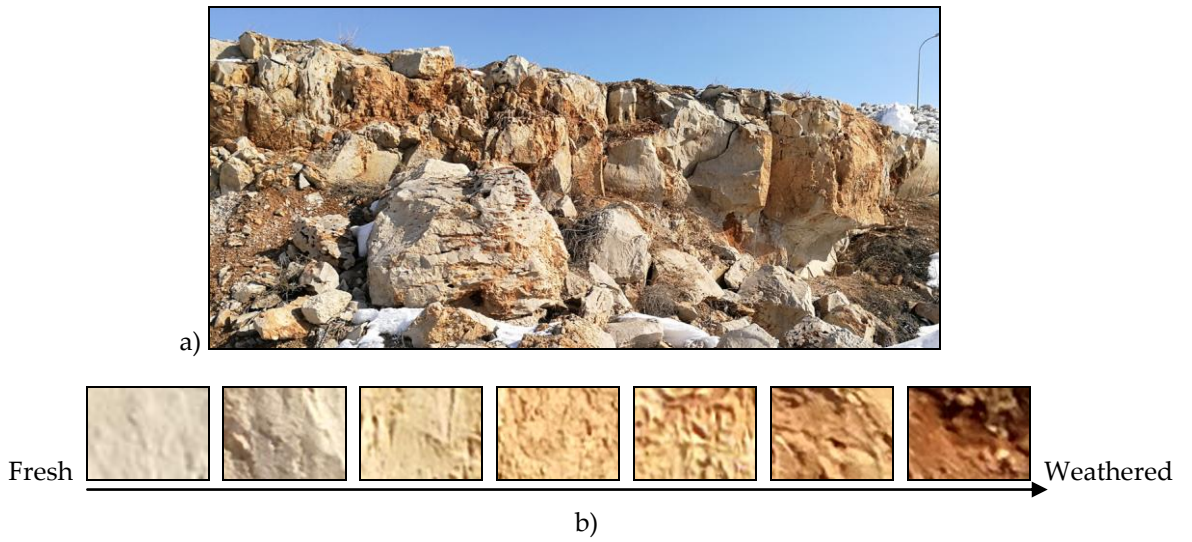


**Figure 5.** Fresh and weathered limestone surfaces and their colour differences at North-West side of Konya city centre.

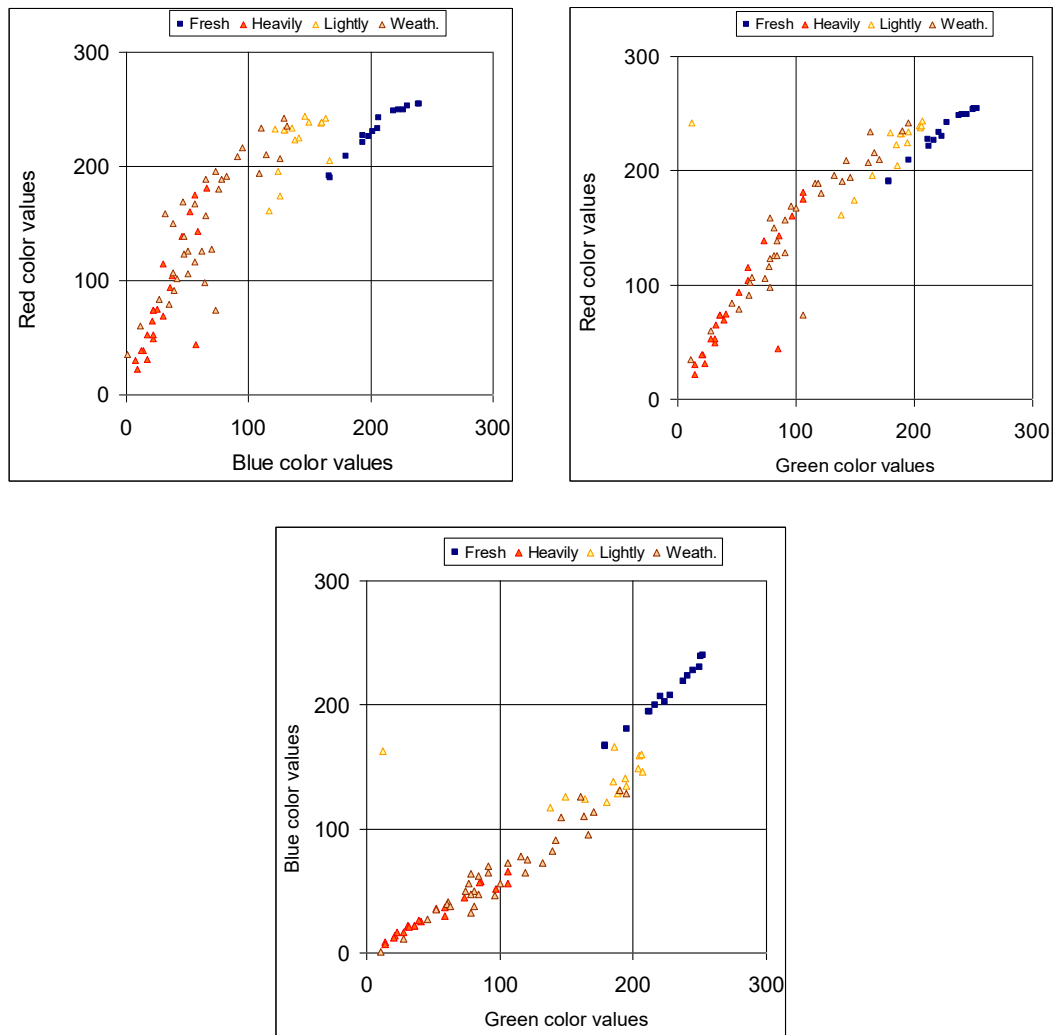


**Figure 6.** Selected colour-band graphics for digitized RGB data obtained from fresh and weathered beige limestone surfaces. This rock mass is located at North-West side of Konya.

Graphics presented in Fig. 4 and 6 exhibit colour value plots which seem to have distribution relations. These two figures show that fresh and weathered rock surface colours of certain rock masses can be identified as colour groups named as; fresh, lightly-weathered, weathered, and heavily-weathered.

### COLOUR CHANGES AT ROCK MASS SURFACES IN GENERAL

Colour determination research study was performed here for limestone rock masses include fresh and weathered rock surfaces' colours. This study was then decided to extend other rock mass types outcropped around Konya region. In order to analyse the colours of fresh and weathered surfaces of these rock masses, required high quality photographs were obtained from them and evaluated accordingly. Colour changes due to weathering actions were researched for the following rock masses as well; a) Limestone formations, *Lst-3*, (Konya cement factory-Limestone quarry, Konya), b) Limestone formations, *Lst-4*, (aggregate quarry North site of Konya), c) Limestone rock clift, *Lst-5*, (landslide area, Taskent, Konya), d) Limestone formations, *Lst-6*, (hydraulic dam construction site, Ermenek, Karaman), e) Andesite formations, *And-1*, (dimensional stone quarry, Sandikli, Afyon), f) Tuff formations, *Tuff*, (Evliyatepe, Konya), g) Travertine formations, *Trav-1*, (abandoned open mine, Ardicli-Konya), h) Travertine formation, *Trav-2*, (abandoned open cuts, Esentepe-Konya) i) Serpentine formation, *Serp*, (Dere village connection road cut, Meram-Konya).

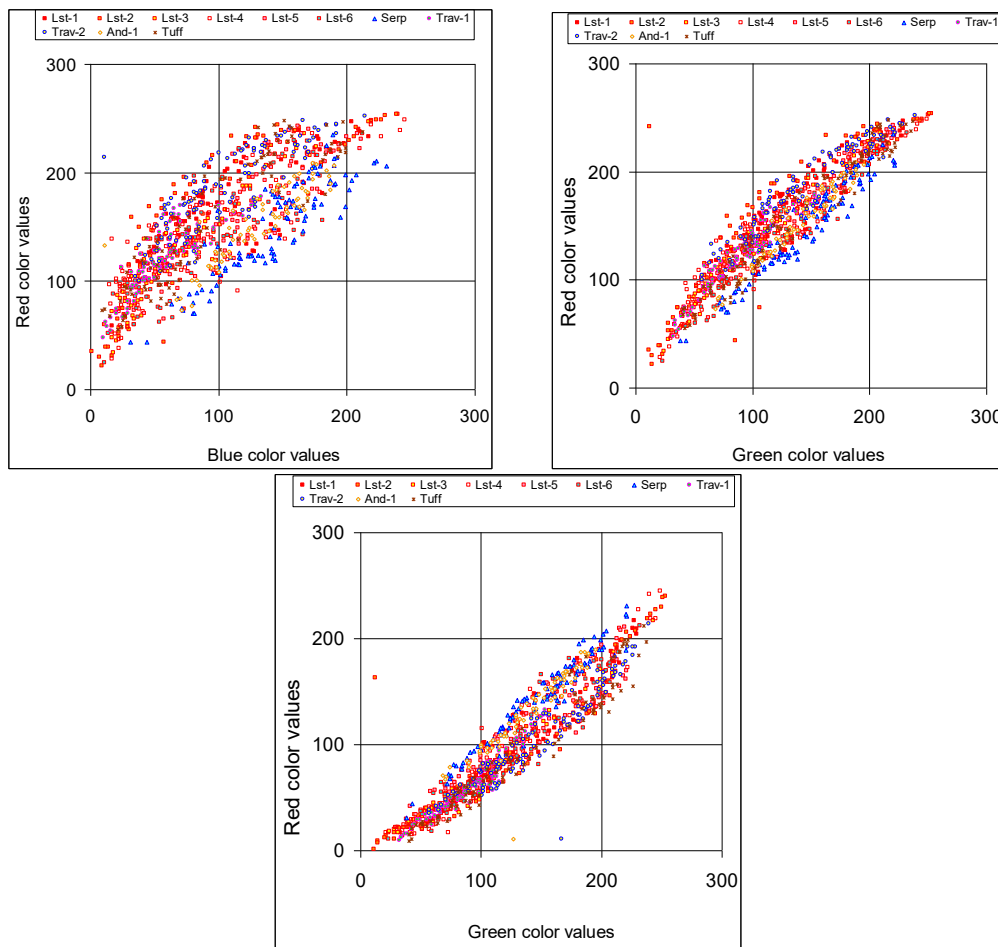


**Figure 7.** Selected 2D colour-band graphics for digitized RGB data obtained for fresh and weathered rock masses around Konya region; [*Limestone formations (Lst-1: Konya-Yukselen road cut, Lst-2: North-west side, Konya, Lst-3: Cement factory quarry, Konya, Lst-4: Limestone aggregate quarry, Konya, Lst-5: Landslide area, Taskent-Konya, Lst-6: Hydraulic dam construction area, Ermenek-Karaman, Serp: Serpentine rock mass outcrops, Dere village, Meram-Konya, Trav-1: Travertine mine, Ardicli-Konya, Trav-2: Abandoned travertine mine, Esentepe-Konya, And-1: Andesite dimensional stone quarry, Sandikli-Afyon, Tuff: Crystalline tuff mine, Evliyatepe, Konya)*].

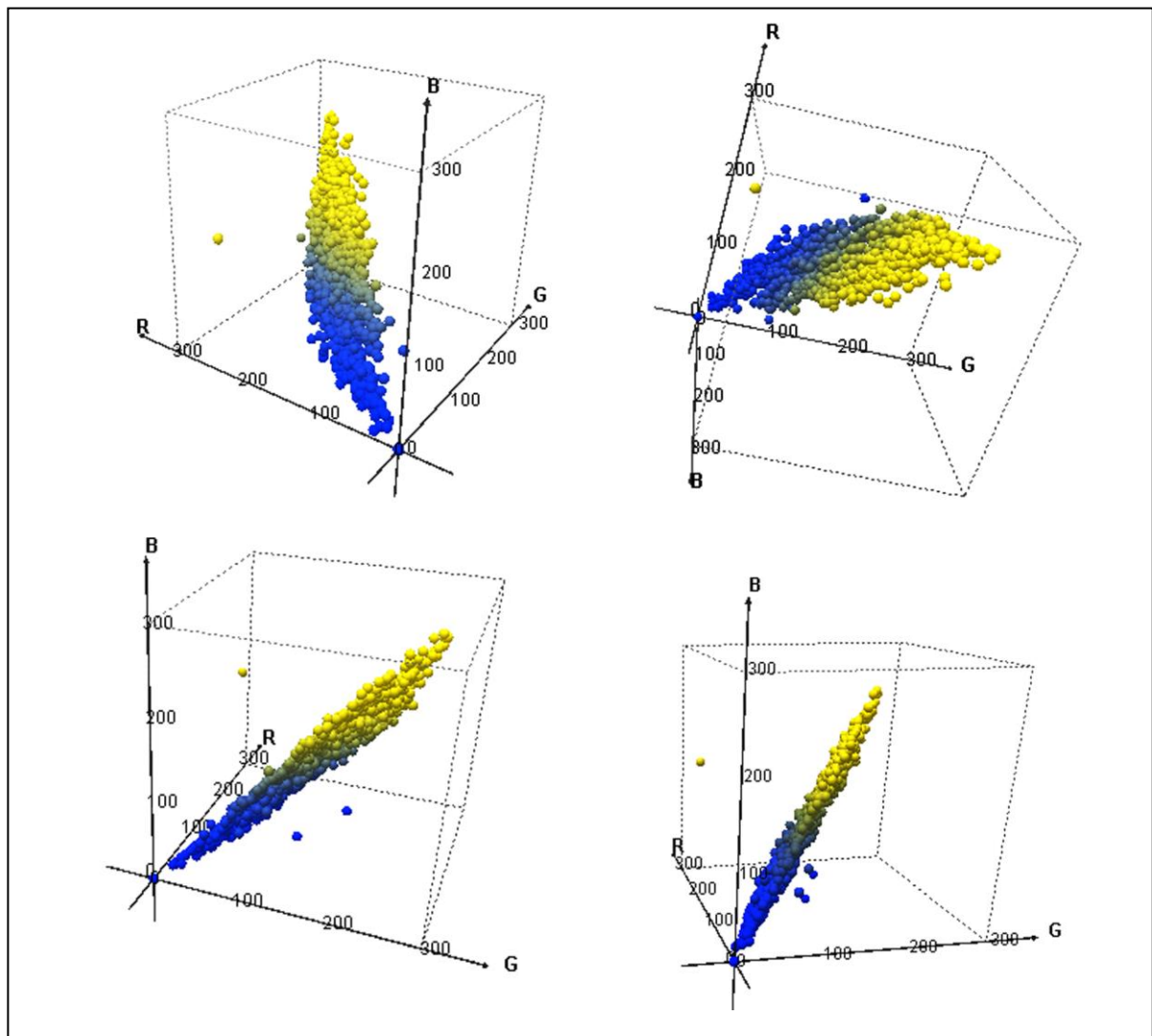


**Figure 8.** Colour data collected from the rock masses around Konya region were used to obtain these 3D graphs. Fresh and weathered rock masses' (limestone, serpentine, andesite, travertine and tuff formations) colours were all handled (totally 1009 colour data) here to obtain these plotting.

When the digital RGB colour determination of fresh and weathered rock surfaces were realised, their selected band colour graphics were plotted (Fig.7). In order to capture rock surface colours, certain surface area were selected from rock surface images in micro-pixel, scale. Average RGB colour codes were then calculated and recorded for those micro areas. Total number of micro-pixel areas was 1009 for the tested 11 different rock mass locations. Selected colour band graphics of whole test data for RGB colour codes were then plotted to verify general colour distribution in 2-dimension. These graphics have axis of Red-Blue, Red-Green and Blue-Green (Fig. 7). In order to understand 3-dimensional RGB colour changes due to rock mass weathering, whole colour data were used to achieve 3-D graphs as illustrated in Fig. 8. Graphics in Fig. 7 and Fig. 8 show clearly that, colour differentiation due to rock weathering in these 11 rock mass locations has elliptical volumetric shape. Colour distributions in Fig. 8 are not seemed to be randomly distributed. It is obvious that; absolute black colour value has coordinate RGB values as 0,0,0 and absolute white colour value has coordinate RGB values as 255,255, 255, these two minimum and maximum colour coordinate values should definitely be the pointed limits of formed volumetric shapes. That is, volumetric shape covers all the plotted points appeared on 3-D colour graphs for rock colours should obviously have these two pointed ends at minimum and maximum values. When Fig. 8 was evaluated with this concept, two flattened, half-parabolic cone shapes which are pointed opposite

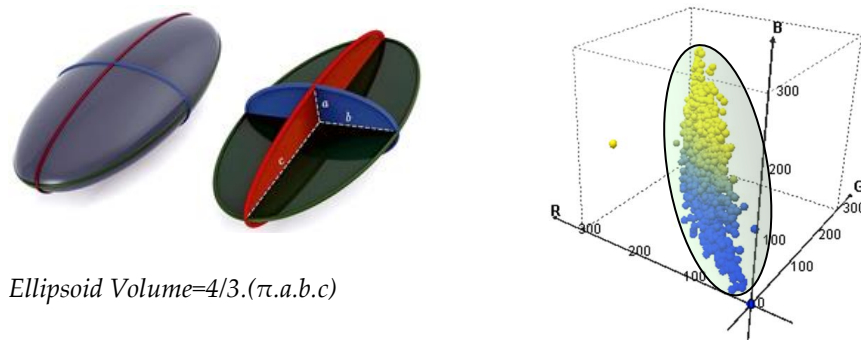


**Figure 9.** Triaxial-ellipsoid volume (Wikipedia, 2012), and its coverage in the selected RGB colour space.

coordinate end points (0,0,0 and 25,255,255). These 3D plotted colour points can also be encapsulated with a volumetric shape looks like triaxial-ellipsoid (Fig. 9) as well. This encapsulated volume shapes and their extension limits are further steps to be researched. Since, extension of colour data obtained from fresh and weathered rock surfaces might bring more accurate 3D volumetric explanations in this research.

## CONCLUSION

Mining and civil engineering applications cover engineering projects located in/on rock masses. Exploration works on these project sites include rock identifications, rock mechanical tests, discontinuity research etc. Engineers in these fields have their projects on; mining galleries, tunnels, metro stations, open pit slopes, road cut slopes, cliff stability, foundation stability of all engineered constructions, underground openings, big scale underground excavations, cave stability, highways and railways etc. Thus they have well experienced about fresh and weathered rock mass property differentiations. Weathered rock zone usually means weak stability and discoloured rock surface sectors in rock masses. In this study, fresh and weathered rock mass surface colours were analysed to define their colour differences. It is obvious that, fresh rock surface colours are discoloured while different types of weathering activity (in/on earth crust) have been progressed. Colour tests had been performed on eleven rock mass locations in this research. Fresh and weathered surfaces of rock masses located there were digitized for their colour analyses. It was evaluated that rock surface colours obtained during this study produced 3D graph points which can be encapsulated by means of triaxial-ellipsoid volume. That means, these colour data demonstrated certain distribution patterns (limitations) in RGB colour graphics. Actually, this statement needs further colour tests on other types of rock masses as well. However, major rock masses observed near Konya city provided the presented graphical results as illustrated in Fig. 7 and 8. Determination of triaxial-ellipsoid dimensions and influences of weathering types on these dimensions can be further studies realized.

## REFERENCES

- Annerel, E., Taerwe, L., 2011, "Methods to Quantify the Colour Development of Concrete Exposed to Fire", *Construction and Building Materials*, Vol. 25(10), pp. 3989-3997.
- Anon, 1970, "Using a Remotely Controlled Borehole Camera", *Ground Engineering*, Vol. 3(5), pp. 20-21.
- Borrelli, L., Greco, R., Gullà, G., 2007, "Weathering Grade of Rock Masses as A Predisposing Factor to Slope Instabilities: Reconnaissance and Control Procedures", *Geomorphology*, Vol. 87, pp.158–175.
- Clayton, C.R.I., Matthews, M.C., Simons, N.E., 1982, *Site Investigation*, Second Edition, Department of Civil Engineering, University of Surrey, Halsted Press, p466.
- Cleland, T.M., 1921, "A Practical Description of the Munsell Colour System, with Suggestions for Its Use", *Munsell Colour Company*, Boston, USA.

- Eggleton, R.A., Foudoulis, C., Varkevisser, D., 1987, "Weathering of Basalt: Changes in Rock Chemistry and Mineralogy", *Clays and Clay Minerals*, Vol. 35(3), pp. 161-169.
- Eren, Y., 1993, *Eldes-Derbent-Tepekoy-Sogutozu (Konya) Regions' Geolgy, PhD Thesis*, Selcuk University, Department of Geological Engineering, Konya, Turkey.
- Geological Society of America, 1963, "Rock Colour Chart", *Geological Society of America*, www.geosociety.org, Boulder, CO, USA.
- Geological Society of London, 1977, "The Description of Rock Masses for Engineering Purposes", *Engineering Group Working Party Report, Q. J. Eng. Geology*, Vol. 10(4), pp. 355-388.
- Gokay, M.K., 2003, "Effects of Natural Weathering of Rock Masses on Their Colour Appearances", *Madencilik Journal, Turkish Chambers of Mining Engineers, Mining Journal*, (technical note), Vol.42, 1, pp. 35-42, Ankara, Turkey. (in Turkish).
- Gokay, M.K., Gundogdu, I.B., 2008, "Colour Identification of Some Turkish Marbles", *Construction and Building Material*, Vol. 22(7), July 2008, pp. 1342-1349.
- Grossi, D., Del Lama, E.A., Garcia-Talegon, J., Inigo, A.C., Vicente-Tavera, S., 2015, "Evaluation of Colourimetric Changes in the Itequera Granite of Ramos De Azevedo Monument, Sao Paulo, Brazil", *International Journal of Conservation Science*, Vol. 6 (3), pp. 313-322, ISSN: 2067-533X
- Heidari, M., Chastre, C., Torabi-Kaveh, M., Ludovico-Marques, M., Mohseni, H., 2017, "Application of Fuzzy Inference System for Determining Weathering Degree of Some Monument Stones in Iran", *Journal of Cultural Heritage*, available online 25 January 2017.
- Hunter, R.S., 1948, "Photoelectric Colour-Difference Meter", *Proceedings of the Winter Meeting of the Optical Society of America, JOSA*, Vol. 38, 7, 661.
- Hunter, Labs., 1996, "Hunter Lab Colour Scale, Insight on Colour", (August 1-15, 1996), *Hunter Associates Laboratories*, Reston, VA, USA.
- Karpuz, C., Pasamehmetoglu, A.G., 1997, "Field Characterisation of Weathered Ankara Andesites", *Engineering Geology*, Vol. 46, pp. 1-17.
- Munsell, A.H., 1905, *A Colour Notation*, G.H. Ellis Company, Boston, USA.
- Munsell Colours, 2017, Official Site of Munsell Colour © ", *X-Rite incorporated web-page*, www.Munsell.com.
- Patel, A.K., Chatterjee, S., 2016, "Computer Vision-Based Limestone Rock-Type Classification Using Probabilistic Neural Network", *Geoscience Frontiers*, Vol. 7(1), Special Issue: Progress of Machine Learning in Geosciences, January 2016, pp. 53-60.
- Xlstat, 2017, *Data Analysis and Statistical Solution for MS-Excel*, Addinsoft, Paris, France.
- Vazquez, P., Carrizo, L., Thomachot-Schneider, C., Gibeaux, S., Alonso, F.J., 2016, "Influence of Surface Finish and Composition on The Deterioration of Building Stones Exposed to Acid Atmospheres", *Construction and Building Materials*, Vol. 106, pp. 392-403.
- Wikipedia, 2012, *Wikipedia web-page*, [https://commons.wikimedia.org/wiki/File:Triaxial\\_Ellipsoid.jpg](https://commons.wikimedia.org/wiki/File:Triaxial_Ellipsoid.jpg)
- Yokoyama, T., Nakashima, T.S., 2005, "Colour Development of Iron Oxides During Rhyolite Weathering Over 52,000 Years", *Chemical Geology*, Vol. 219, pp. 309-320.



## DÜŞEY MADEN KUYULARINDA BETON TAHKİMAT KALINLIKLARININ BELİRLENMESİNE YÖNELİK BİR TASARIM YAKLAŞIMI

<sup>1</sup>Said Shahzada HUSSAINI, <sup>2</sup>İhsan ÖZKAN

<sup>1,2</sup>Selçuk Üniversitesi, Mühendislik Fakültesi, Maden Mühendisliği Bölümü, Kampüs, Konya  
<sup>1</sup>seh.afg20@gmail.com, <sup>2</sup>ozkani@selcuk.edu.tr

(Geliş/Received: 03.07.2017; Kabul/Accepted in Revised Form: 17.07.2017)

**ÖZ:** Yeraltı maden ocaklarında kuyu duraylılığı çok önemlidir. Kuyu cidarında yapılacak olan tahkimat bunu sağlayabilmektedir. Bu çalışmada, 9m çaplı ve 900m derinliğe ulaşan düşey bir kuyunun beton tahkimat kalınlıkları, iki boyutlu sayısal analizler ile belirlenmiştir. Sayısal analizlerde farklı derinlik (Z), tek eksenli basma dayanımı ( $\sigma_c$ ), kaya kütle sınıflama sistemi (M-RMR), kuyu kazısında patlatmaya dayalı çevre kayacın örselenme durumu (D) parametreleri kullanılmıştır. 9 m çaplı kuyunun sırasıyla 100, 300, 500, 700 ve 900 metrelerinin her birinde M-RMR değerinin 10, 20, 30, 40, 50, 60, 70, 80, 90, 100 olduğu durumlarda ve tek eksenli basma dayanımının 50MPa koşulu altında ve ayrıca patlatmaya dayalı kuyu çevre kayalarında oluşan örselenme (D=0 ve D=0.5) durumuna bağlı sayısal analizler Phase2 yazılımı ile yapılmıştır. Sonuç olarak parametrik bu çalışmada, toplam 100 senaryo analiz edilmiştir. Her bir senaryo için C20 sınıfı beton ile optimum beton tahkimat kalınlıkları ( $t_c$ ) belirlenmiştir. Phase2 yazılımından sırasıyla, en büyük asal gerilme ( $\sigma_1$ ), toplam yerdeğiştirme (U), kuyu çevre kayacında oluşan yenilen element sayısı, dayanım faktörü (SF) ve yenilme bölgesi kalınlığı ( $h_t$ ) belirlenmiştir. Oluşturulan veri tabanı yardımıyla beton tahkimat tasarımı için bütüncü 10 abak hazırlanmıştır. Kaya kütle sınıflama değerinin (M-RMR) bilinmesi durumunda; geliştirilen ilgili abak kullanılarak kuyu çevre kayacında yenilme bölgesi kalınlığı ( $h_t$ ), beton tahkimat kalınlığı ( $t_c$ ) ve bu beton tahkimatın uygulanması sonucunda kuyu cidarında oluşacak yerdeğiştirme miktarı (U) belirlenebilmektedir.

**Anahtar Kelimeler:** Beton tahkimat, Maden kuyusu, Sayısal çözümler

### A Design Approach for Determination of Concrete Support Thickness in Vertical Mine Shafts

**ABSTRACT:** Stability in underground shafts is very important. Shaft lining can supply it. In this study, the concrete support thicknesses of a vertical shaft of 9 m diameter and reaching a depth of 900 m were determined by 2D numerical analysis. In numerical analysis different depths (Z), uniaxial compressive strength ( $\sigma_c$ ), rock mass classification system (M-RMR) and also the surrounding rocks situation based on blasting (D) parameters were used. In each of the nine-meter-diameter shafts has 100, 300, 500, 700 and 900 meters where the M-RMR value is 10, 20, 30, 40, 50, 60, 70, 80, 90, 100 and the uniaxial compressive strength 50MPa and also situation formed in shafts surrounding rocks based on blasting (D = 0 and D = 0.5) the numerical analysis were made by Phase2 software. As a result, in this parametric study, a total of 100 scenarios were analysis. The optimum thickness ( $t_c$ ) of concrete support with C20 class concrete have been identified for each scenario. The maximum principal stresses ( $\sigma_1$ ), total displacement (U), the number of yielded elements formed in the surrounding rocks, strength factor (SF) and thickness of yielded region ( $h_t$ ) respectively were determined. Using Phase2 software 10 integrated charts were prepared. By data base to determine of concrete support thickness If the rock mass classification value (M-RMR) is known the thickness of yielded surrounding rocks ( $h_t$ ), concrete support thickness ( $t_c$ ) the total of displacement (U) to be formed in the shaft can be determined.

**Key Words:** Concrete support, Mine shaft, Numerical analysis

## GİRİŞ (INTRODUCTION)

Yeraltı madencilik çalışmalarında düşey kuyuların ana görevleri; yeraltı çalışmaları için gerekli temiz havanın, tahkimat malzemelerinin, basınçlı havanın, haberleşme ve aydınlatma amaçlı iletim hatlarının yeraltına iletilmesinde ve ayrıca yeraltından üretilen cevherin yeryüzüne nakliyesinde bir yol görevi görmektir. Kuyu açma, büyük hazırlıkların önemli bir kısmını oluşturmaktadır. Kuyu, istenilen derinliğe ulaştıktan sonra kuyudan itibaren diğer hazırlıklara başlanır. Kuyunun açıldığı kaya sağlam ve az su gelirine sahipse normal kuyu açma yöntemleri uygulanır. Buna karşı kaya sağlam değil ve fazla su gelirine sahipse veya bu iki husus birlikte etki ediyorsa özel kuyu açma yöntemlerinin uygulanışı zorunlu hale gelmektedir (Saltoğlu, 1976). Kuyu kesitleri kare, dikdörtgen, daire ve elips olarak sıralanabilir. Kuyunun birinci işlevi olan nakliye ele alınırsa en uygun kesit kare ve dikdörtgen kesit olmaktadır. Ancak duraylılık açısından bakılırsa yeraltı arazi gerilmelerinin en uygun dağılım gösterdiği kesitin daire kesit olduğu bilinmektedir. Bu nedenle sığ derinliklerde kare ve dikdörtgen kesit tercih edilirken derinliğin arttığı madenlerde genelde daire kesit tercih edilmektedir. Maden kuyu kazısında tahkimat tasarım çalışmalarında kaya kütle özellikleri, derinliğe bağlı arazi gerilmeleri ve beton tahkimat özellikleri öncelikle önem kazanmaktadır.

## KAYA KÜTLE SINIFLAMA SİSTEMLERİ (ROCK MASS CLASSIFICATION SYSTEMS)

Kaya mühendislik yapılarının tahkimat tasarım çalışmalarında ihtiyaç duyulan girdi parametrelerinin belirlenmesinde kaya kütle sınıflama çalışmaları sıklıkla kullanılmaktadır. Tasarım çalışmalarında genel olarak RMR (Bieniawski, 1973; Bieniawski, 1989) ve Q (Barton ve diğ., 1974) sınıflama sistemleri yaygın olarak kullanılmaktadır. Günümüzde 30'a yakın geliştirilmiş olan sınıflama sistemi mevcuttur. Bunların büyük bir çoğunluğu RMR (Rock Mass Rating - Jeomekanik Sınıflama Sistemi) ve Q (Rock Mass Quality - Kaya Kalite İndeksi) sınıflama sistemlerinin özel kaya yapıları için yeniden düzenlenmesi ile ortaya çıkmıştır. Özellikle zayıf-tabakalı-kil içerikli anizotropik ve kırıklı kaya kütlelerinde, RMR ve Q sınıflama sistemlerine ait bazı kütle parametrelerinin belirlenmesinde yetersiz kaldığını belirleyen Unal ve Ozkan (1990), M-RMR (Modified Rock Mass Rating-Yeniden Düzenlenen Kaya Kütle indeksi) sınıflama sistemini geliştirmişlerdir.

Sınıflama sisteminin uygulanması için öncelikle, kaya kütlesi belirli özellikleri açısından benzerlik taşıyan yapısal bölgelere ayrılır. Pek çok durumda yapısal bölgelerin sınırları; fay ve dayk gibi ana süreksizliklerle çakışmaktadır. Yapısal bölgeler belirlendikten sonra, kazı aynaları boyunca veya sondaj karotları üzerinde sınıflandırmanın gerektirdiği parametreler tayin edilir. RMR ile ilgili parametreler kullanılarak "Temel, Düzeltilmiş ve Tasarım RMR indeks değerleri" belirlenebilmektedir. RMR sınıflama indeks değeri 0-100 arasında değişmektedir (Bieniawski, 1989).

Unal ve Ozkan (2012), 1989-2005 yılları arasında ülkemizde ETİBANK-Bigadiç-Simav kolemanit, TKİ-OAL-Çayırhan kömür, Çayeli Bakır İşletmesi-ÇBİ bakır ve ETİBANK-Bey pazarı-Trona maden ocaklarında karşılaşılan kaya kütlelerinin RMR (Bieniawski, 1973; Bieniawski, 1989) ve Q (Barton ve diğ., 1974) sınıflandırma indeks değerlerini belirlenmeye çalışmışlardır. Bu çalışmalarında araştırmacılar, özellikle zayıf, anizotropik, tabakalı, kil içerikli ve çatlaklı kaya bölgelerinde kütle parametrelerinin belirlenmesinde RMR ve Q sistemlerinin yetersiz kaldığını tespit etmişlerdir. Zayıf, anizotropik, tabakalı, kil içerikli, çatlaklı kaya yapıları için geliştirilen M-RMR sistemine (Unal ve Ozkan, 1990) ait değerlendirmeler araştırmacılar tarafından çeşitli yurt içi ve yurt dışı yayınlarda (Unal ve Ozkan, 1988; Ozkan, 1989; Unal ve Ozkan, 1990; Ulusay ve diğ., 1992; Unal ve diğ., 1992; Ozkan, 1995; Ozkan ve Unal, 1996; Unal, 1996; Ozkan ve Unal, 2012) ayrıntıları ile sunulmuştur. Bu çalışmada dikkate alınan M-RMR sınıflama sistemi için Unal ve Ozkan (1990) tarafından önerilen eşitlik aslında üç parçadan oluşmaktadır. Bunlar sırasıyla Temel M-RMR, Düzeltilmiş M-RMR ve Tasarım M-RMR olarak adlandırılabilir (Unal ve Ozkan, 1990). Bahsedilen eşitlikler aşağıda sunulmuştur.

$$\text{Temel M-RMR} = F_c \{ [I_{PLT}] + [I_{RQD}] + [I_{JC}] \} + [I_{JS}] + [I_{GW}] \quad (1)$$

$$\text{Düzeltilmiş M-RMR} = [\text{Temel M-RMR}] + [I_{OI}] \quad (2)$$

$$\text{Tasarım M-RMR} = [\text{Düzeltilmiş M-RMR}] * [A_w * A_b] \quad (3)$$

Eşitlik 1-3'de geçen parametreler sırasıyla;

$I_{\sigma_c}$  : Tek eksenli basınç dayanımına bağlı indeks değeri (0-15)

$I_{PLT}$  : Nokta yükleme dayanımına bağlı indeks değeri (0-15)

$I_{RQD}$  : RQD (Rock Quality Designation- Kaya Kalite Değeri) değerine bağlı indeks değeri (0-20)

$I_{JS}$  : Süreksizlikler arası mesafeye bağlı indeks değeri (0-20)

$I_{JC}$  : Süreksizlikler arası durum indeks değeri (0-30)

$I_{GW}$  : Yeraltı su durumuna bağlı indeks değeri (0-15)

$I_{OI}$  : Eklem takım konumuna bağlı indeks değeri (maden galeri ve tüneller için : 0-(-12))

$F_c$  : Suda dağılma dayanımına bağlı bir katsayı (0.7-1.15)

$A_w$  : Büyük süreksizlik düzlemi ve zayıflık düzlemlerine dayalı düzeltme katsayısı (0.70-1.0)

$A_b$  : Patlatmaya dayalı düzeltme katsayısı (0.80-1.0)

#### MADEN KUYULARI İÇİN BETON TAHKİMAT TASARIM YAKLAŞIMLARI (CONCRETE SUPPORT DESIGN APPROACHES FOR MINE SHAFTS)

Dairesel maden kuyularının tahkimat çalışmalarında tahkimat elemanı olarak beton tahkimat sıklıkla kullanılmaktadır. Elastik teoriye göre geliştirilen beton tahkimat yönelik eşitlikler aşağıda sunulmuştur (Carranza-Torres ve Fairhurst, 2000).

$$P_s^{\max} = \frac{\sigma_{cc}}{2} \left[ \frac{(r - t_c)^2}{r^2} \right] \quad (4)$$

$$t_c = r \left[ 1 - \sqrt{1 - \frac{2P_s^{\max}}{\sigma_{cc}}} \right] \quad (5)$$

$$K_s = \frac{E_c}{(1 - \nu_c)r} \frac{r^2 - (r - t_c)^2}{(1 - 2\nu_c)r^2 + (r - t_c)^2} \quad (6)$$

Burada:

$P_s^{\max}$  : Beton tahkimatın yenilmeden önce taşıyabileceği en yüksek basınç gerilmesi (MPa)

$\sigma_{cc}$  : Beton malzemesinin tek eksenli basma dayanımı (MPa)

$r$  : Düşey kuyu yarıçapı (m)

$t_c$  : Beton tahkimat kalınlığı (m)

$E_c$  : Beton malzemesinin Elastik Modülü (MPa)

$\nu_c$  : Poisson oranı

$K_s$  : Beton malzemesinin elastik katılığı (MPa/m)

#### SAYISAL ANALİZLER İÇİN GİRDİ PARAMETRELERİ (INPUT PARAMETERS FOR NUMERICAL ANALYSIS)

Bu çalışmada dairesel kesitli maden kuyusunun kumtaşı içerisinde açıldığı kabul edilmiştir. Kuyu çapı (2r) 9 m ve derinliği (Z) 900 m seçilmiştir. Bu çerçevede RocLab (Rocscience, 2002) programı kullanılarak kumtaşı kaya birimi için aşağıda sıralanan iki temel parametre tespit edilmiştir.

1. Genelleştirilmiş Hoek-Brown görgül yenilme ölçütünde (Hoek ve ark., 1995) kullanılan sağlam kaya sabiti ( $m_i$ ) değerinin kumtaşı kaya birimi için 10 olduğu tespit edilmiştir.
2. Kumtaşı kaya birimine ait modül oranı (MR) değerinin 200 olduğu tespit edilmiştir.

Sayısal çözümlenmelerde kullanılacak girdi parametrelerinin hazırlanmasında temel olarak derinlik (Z, m), kaya malzemesinin tek eksenli basma dayanımı ( $\sigma_{ci}$ , MPa), kaya kütle sınıflama sistemi (M-RMR) ve kuyu açılırken örselenme durumunu gösteren sabit (D) dikkate alınmıştır. Bu değerlere ait aralıklar aşağıda verilmiştir.

1. Derinlik (Z) parametresi 100m, 300m, 500m, 700m ve 900m olarak dikkate alınmıştır.
2. Kaya malzemesinin tek eksenli basma dayanımı ( $\sigma_{ci}$ , MPa) parametresi 50 MPa olarak her derinlik (Z) için ayrı ayrı dikkate alınmıştır.
3. Kaya kütle sınıflama sistemi (M-RMR) parametresi 10, 20, 30, 40, 50, 60, 70, 80, 90 ve 100 değerleri her derinlik (Z) için ayrı ayrı dikkate alınmıştır.
4. Kuyu açılırken örselenme durumunu gösteren sabit (D) için örselenmemiş koşuluna ait D=0 değeri dikkate alınırken örselenmiş durum için D=0.5 hesaplamalara dahil edilmiştir.

Yukarıda özetlenen ana parametrelere ait girdi verilerinin tespiti için RocLab (Rocscience, 2002) programı kullanılarak elde edilen sonuçlar sırasıyla aşağıda verilmiştir (Çizelge 1).

İki boyutlu düzlemde sayısal analiz yapabilen Phase2 (Rocscience, 2002) yazılımı için hazırlanan modelde kullanılmak amacıyla seçilen beton tahkimata ait mekanik özellikler topluca Çizelge 2'de sunulmuştur. Bu çalışmada C20 beton sınıfı ( $\sigma_{cc} = 20$  MPa) için başlangıçta rastgele seçilen beton kalınlığı her bir analiz koşulunda sistematik olarak değiştirilmiş ve optimum beton kalınlıkları ( $t_c$ ) tespit edilmiş ve böylelikle tahkimata etkiyen  $P_0$  (MPa) basınç değerleri Phase2 yardımıyla belirlenmiştir. Sayısal analizlerde kullanılan kaya kütle malzemesi ve beton tahkimat plastik ortam kabul edilmiş ve genelleştirilmiş Hoek-Brown yenilme ölçütü kullanılmıştır.

**Çizelge 1.** Patlatma ile kazı çalışmalarında örselenmemiş (D=0) ve örselenmiş (D=0.5) koşulu altında kuyu çevre kayacına ait girdi parametre aralığı

*Table 1. Input parameter ranges for undisturbed (D=0) and disturbed (D=0.5) shaft environment rock in excavation*

Girdi parametreler	$\sigma_{ci} = 50$ MPa	$\sigma_{ci} = 50$ MPa
	D = 0 (örselenmemiş durum)	D = 0.5 (örselenmiş durum)
M-RMR	10-100	10 -100
Derinlik (m)	100-900	100 -900
MR	200	200
$m_i$	10	10
$m_b$	0.402-10	0.138 -10
S	0.0000454-1	0.0000614 -1
A	0.5-0.585	0.5 - 0.585
c (MPa)	0.48 - 5.042	0.48 - 5
$\varphi$ (°)	17.98 - 42.95	11.1 - 42.95
$\sigma_t$ (MPa)	(-0.003) - (-2.5)	(-0.002) - (-5)
$\sigma_{cm}$ (MPa)*	0.072 - 25	0.045 - 50
$\sigma_{cm}$ (MPa)**	1.321 - 23.163	1.409 - 46.325
$E_m$ (MPa)	152.52 - 4971.64	240.05 - 7328.58
$E_i$ (MPa)	10000	10000
$\sigma_3$ max	12.5	12.5

\*Roclab çıktısında Genelleştirilmiş Hoek-Brown yenilme ölçütünde tek eksenli basma dayanımı \*\*Roclab çıktısında Mohr-Coulomb yenilme ölçütünden tek eksenli basma dayanımı

## SAYISAL ANALİZ SONUÇLARI (RESULTS OF NUMERICAL ANALYSIS)

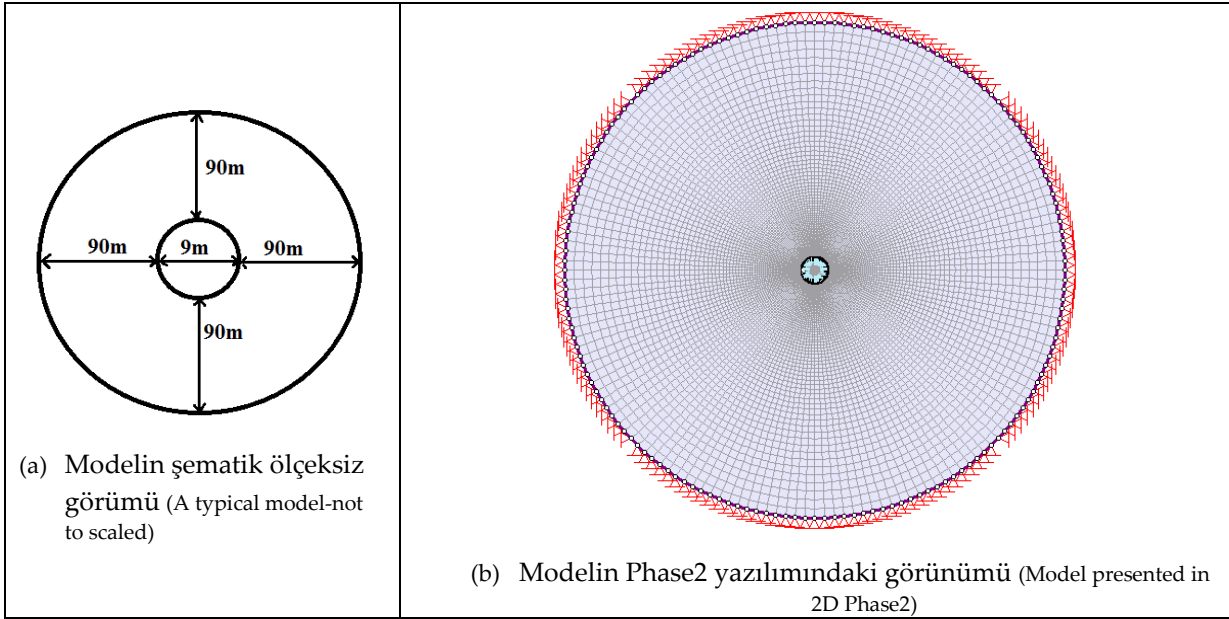
Bu bölümde sunulan düşey dairesel kesitli maden kuyularının beton tahkimat kalınlıklarının belirlenmesine yönelik parametrik sayısal çözümlenmelerde, Phase2 yazılımı kullanılmıştır. Phase2 programı sonlu elemanlar yöntemine dayalı zemin veya kaya ortamında yapılan yeraltı ve yerüstü yapıları için düzlem birim şekil değiştirme durumunda iki boyutlu ve eksenel simetri durumunda kısmen üç boyutlu gerilme çözümlenmeleri yapabilmektedir. Yeraltı açıklıkları için beton, püskürtme

beton, kaya saplaması, çelik tahkimat ve bunların kombinasyonlarından oluşan tahkimatlar için gerilme çözümlenmeleri yapılmaktadır. Bu yazılım için bir model hazırlanmıştır. Bu modelde dairesel kesitli kuyu çapının ( $2r$ ) 9 m olduğu kabul edilmiştir. Modeli çevreleyen dış sınır yatay ve düşey yönde yerdeğiştirmelere izin vermeyecek şekilde sabit mesnetlenmiştir. Kazı etki alanının modelin dış sınırından etkilenmemesi için modelin dış sınırının açıklığa olan uzaklığı kuyu çapının yaklaşık 10 katı olacak şekilde oluşturulmuştur. Bir başka ifade ile kuyu kesitinden etkilenecek bölgenin kuyu çevresinden itibaren 90 metrelik bölge olduğu ve bu bölgenin de Şekil 1'de görüldüğü üzere kuyu çevresine paralel olduğu var sayılmıştır.

**Çizelge 2.** Model için Phase2 yazılımında kullanılan beton özellikleri

*Table 2. Characteristics of concrete used for the model in Phase2 software*

<b>Elastik özellikler</b>	Young Modülü (MPa)	28000
	Poisson Oranı	0.2
<b>Dayanım parametreleri</b>	Basma Dayanımı - $\sigma_{cc}$ (En büyük) (MPa)	20
	Basma Dayanımı (Kalıcı) (MPa)	5
	Çekme Dayanımı (En büyük) (MPa)	1.6
	Çekme Dayanımı (Kalıcı) (MPa)	0
<b>Doğrusal tür</b>	Beam	Timoshanko
<b>Geometri</b>	Kalınlık	0.152



**Şekil 1.** İki boyutlu sayısal analizde kullanılan model

*Figure 1. Model used in 2D numerical analysis*

Hazırlanan modelde sonlu elemanlar ağı (mesh) tipi radial ve element tipi 4 noded quadrilaterals seçilmiştir. Birincil gerilmelerin tüm bileşenlerinin eşit olduğu ( $P_0=P_v=P_{h1}=P_{h2}$ ) yani hidrostatik birincil gerilme alanı varsayılmıştır. Bu çalışmada derinlik (Z) 100m, 300m, 500m, 700m ve 900 m alındığı için sabit arazi gerilmeleri sırasıyla 2.5 MPa, 7.5 MPa, 12.5 MPa, 17.5 MPa ve 22.5 MPa olduğu aşağıda verilen temel eşitlikten hesaplanmıştır.

$$P_0 = Z\gamma \quad (7)$$

Burada  $P_0$ , düşey birincil gerilme (MPa);  $Z$ , derinlik (m);  $\gamma$ , birim hacim ağırlığı ( $MN/m^3$ ) dır. Tahkimatlı ve tahkimatsız koşullarda yapılan sayısal analizlerde tahkimatsız durum için 2 aşama (stage), tahkimatlı durum için 3 aşama (stage) planlanmıştır. Tahkimatsız durumda birinci aşama kazı öncesi olurken ikinci aşama kazı sonrası ancak tahkimat yapılmamış durumu yansıtmaktadır. Tahkimatlı durumda birinci aşama kazı öncesi, ikinci aşama kazı sonrası (tahkimatsız) iken üçüncü aşamada tahkimatın yapıldığı var sayılmıştır. Bu duruma göre beklenen yerdeğiştirmenin ( $U$ ), kazı öncesinde %0 olacağı (Stage-1), kazı yapıldıktan sonra (tahkimat öncesinde) %70 olacağı (Stage-2), tahkimat sonrasında ise %30 (Stage-3) olacağı kabul edilmiştir (Geniş ve Acun, 2015; Geniş ve Derin, 2016).

Yukarıda belirtilen parametrelere göre sadece derinlik 100 m için tek eksenli basma dayanımına ( $\sigma_c$ ) ait 50MPa için toplam 20 adet sayısal analize konu olan senaryo oluşmaktadır. Analiz edilen diğer derinliklerde dikkate alınırsa ( $Z = 300m, 500m, 700m$  ve  $900 m$ ) ayrı ayrı analize tabi tutulan toplamda 100 adet senaryo ortaya çıkmaktadır. Ancak her bir senaryo için optimum beton tahkimat kalınlığını belirleyebilmek amacıyla yaklaşık 10 kez sayısal analiz yapılmıştır. Her bir analizde beton tahkimat kalınlığı Phase2 (Rocscience, 2002) yazılımına girilmiş bu tahkimatın yenilip yenilmediği kontrol edilmiştir. Eğer beton tahkimat yenilmiş ise bir sonraki analizde beton tahkimat kalınlığı artırılmıştır. Sonuç olarak 100 adet senaryo için optimum beton kalınlığını bulmak amacıyla toplamda yaklaşık 1000 adet sayısal analiz gerçekleştirilmiştir. Ayrıca bu 100 adet senaryo için tahkimatsız koşulu altında analizler de yapılmıştır.

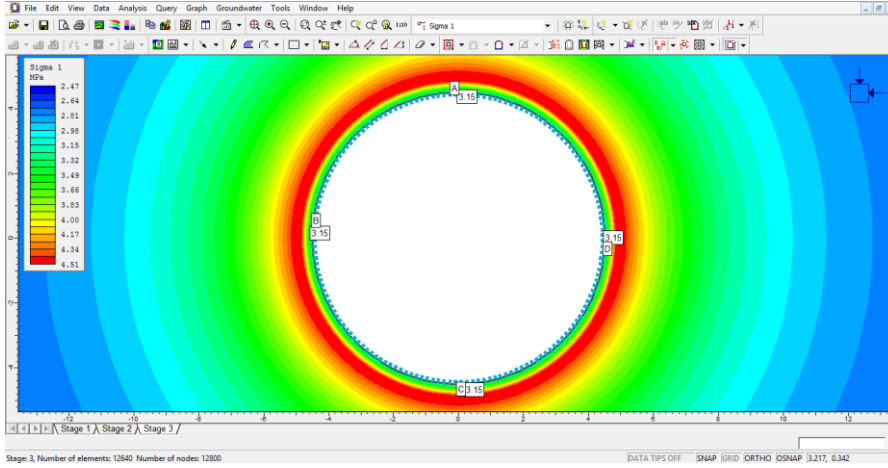
Takip eden bölümde tahkimatlı koşul altında belirlenen 100 adet senaryodan sadece bir tanesi aşağıda tipik bir örnek olarak hazırlanmıştır. Bu örnek çözümde kuyu cidarındaki örselenme durumu, sırasıyla ( $D$ ) 0 ve 0.5 olarak alınmıştır.

Bu makale de sunmak amacıyla hazırlanan iki örnek Şekil 2, 3, 4 ve 5'te sunulmuştur. İlk örnek kuyu kazısında patlatmadan kaynaklanan örselenme hasarının  $D=0$  olması durumunda yapılan analizlerde derinlik ( $Z$ ) 100m, tek eksenli basma dayanımı ( $\sigma_c$ ) 50 MPa, Yeniden Düzenlenen Kaya Kütle İndeksi (M-RMR) 40 alınmıştır. Bu koşul altında ilk önce beton tahkimat kalınlığı ( $t_c$ ) rastgele 0.01m alınmıştır. Bu durum için yapılan sayısal analiz sonuçları en büyük asal gerilme ( $\sigma_1$ ) ve toplam yerdeğiştirme ( $U$ ) için sırasıyla Şekil 2 ve 3'de sunulmuştur. Bu tasarım çıktılarına göre kuyu cidarında  $90^\circ$  ara ile tanımlanan A, B, C ve D noktalarında oluşan en büyük asal gerilme ( $\sigma_1$ ), toplam yerdeğiştirme ( $U$ ), yenilme bölgesi (%) ve dayanım faktörü (SF) Çizelge 3'de görülmektedir. Bu koşul altında beton tahkimatta yenilme görülmemiştir.

İkinci örnek kuyu kazısında patlatmadan kaynaklanan örselenme hasarının  $D=0.5$  olması durumunda yapılan analizlerde derinlik ( $Z$ ) 100m, tek eksenli basma dayanımı ( $\sigma_c$ ) 50 MPa, Yeniden Düzenlenen Kaya Kütle İndeksi (M-RMR) 40 koşulu altında beton tahkimat kalınlığı ( $t_c$ ) rastgele 0.074m alınmıştır. Bu durum için yapılan sayısal analiz sonuçları sırasıyla Şekil 4 ve 5'de sunulmuştur. Bu tasarım çıktılarına göre kuyu cidarında oluşan en büyük asal gerilme ( $\sigma_1$ ), toplam yerdeğiştirme ( $U$ ), yenilme bölgesi (%) ve dayanım faktörü (SF) Çizelge 4'de verilmiştir. Bu koşulu altında beton tahkimatta her hangi bir yenilmenin olmadığı tespit edilmiştir.

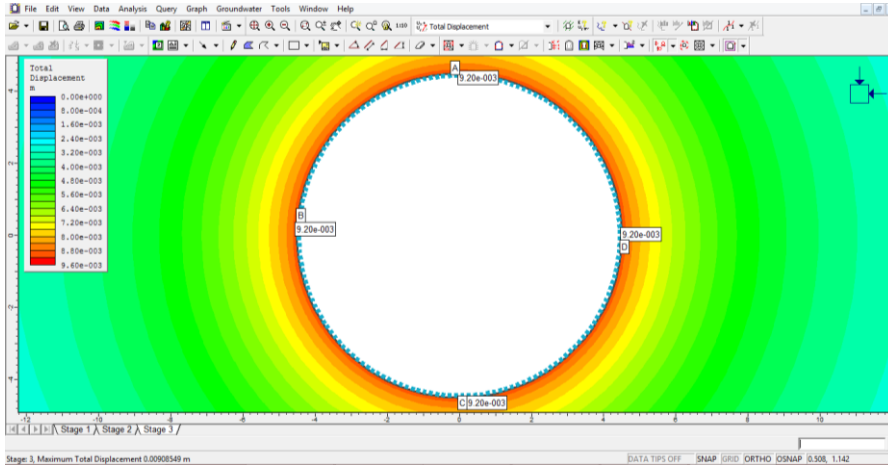
## **BETON TAHKİMAT KALINLIKLARININ BELİRLENMESİ İÇİN BİR YAKLAŞIMIN GELİŞTİRİLMESİ (DEVELOPMENT OF AN APPROACH FOR DETERMINING OF CONCRETE SUPPORT THICKNESS)**

Phase2 yazılımı yardımıyla yapılan analizlere bağlı ilk değerlendirme ışığında Şekil 6 ve 7 hazırlanmıştır. Phase2 programı kullanılarak yapılan sayısal analizlere göre M-RMR değeri arttıkça beton tahkimat kalınlıklarının azaldığı, ayrıca derinlik arttıkça beton tahkimat kalınlıklarının buna karşı arttığı gözlenmiştir (Şekil 6 ve 7).



Şekil 2.  $Z=100m$ ,  $\sigma_{ci}=50 MPa$ ,  $M-RMR = 40$  ve  $D = 0$  koşulunda  $t_c=0.01m$  için en büyük asal gerilme ( $\sigma_1, MPa$ )'ye göre Phase2 analiz çıktısı

Figure 2. According to  $\sigma_1(MPa)$ , to Phase 2 analysis output for  $t_c = 0.01m$  under condition  $Z=100m$ ,  $\sigma_{ci}=50MPa$ ,  $M-RMR = 40$  and  $D = 0$



Şekil 3.  $Z=100m$ ,  $\sigma_{ci}=50 MPa$ ,  $M-RMR = 40$  ve  $D = 0$  koşulunda  $t_c=0.01m$  için yerdeğiştirme ( $U, mm$ )'ye göre Phase2 analiz çıktısı

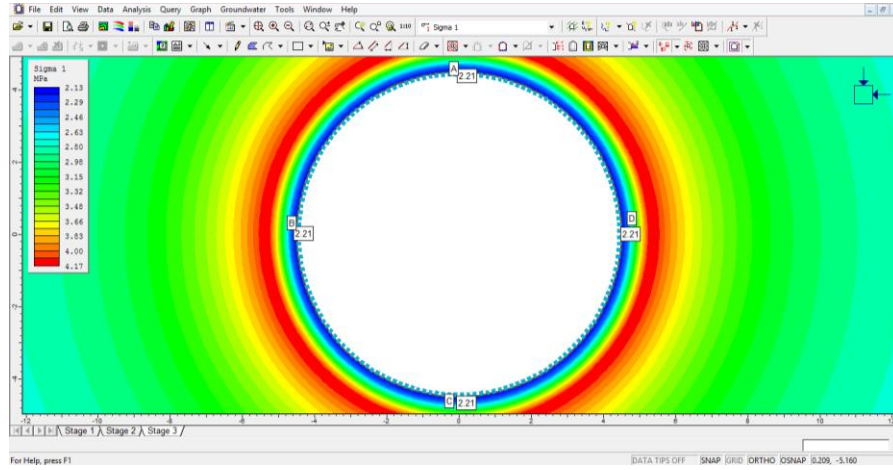
Figure 3. According to  $U (mm)$ , Phase2 analysis output for  $t_c = 0.01$  under condition  $Z=100m$ ,  $\sigma_{ci}=50MPa$ ,  $M-RMR = 40$  and  $D = 0$

Çizelge 3.  $Z=100m$ ,  $\sigma_{ci}=50 MPa$ ,  $M-RMR = 40$  ve  $D = 0$  koşulunda  $t_c = 0.01m$  için sayısal analiz sonuçları

Table 3. The numerical analysis results for  $t_c = 0.01m$  under condition  $Z=100m$ ,  $\sigma_{ci}=50MPa$ ,  $M-RMR = 40$  and  $D = 0$

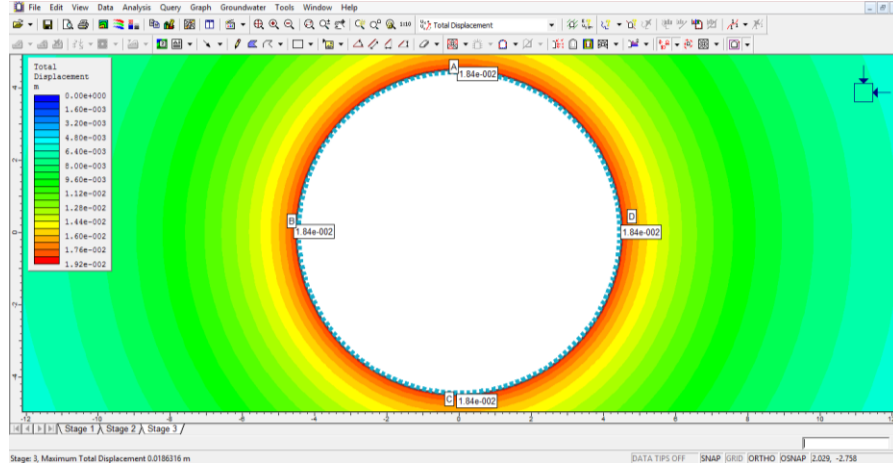
Aşama (Stage)	Kuyu Cidarındaki Analiz Noktası	$\sigma_1$ (MPa)	U (cm)	Dayanım Faktörü (SF)	Kaya Kütlelerinde Yenilme Bölgesi Kalınlığı (m)	Beton Tahkimatta Yenilme Bölgesi Kalınlığı (m)
Tahkimatsız Aşama-2	A	2.10	0.945	1.04	0.457 (YES=320)	-
	B	2.10	0.945	1.04		
	C	2.10	0.945	1.04		
	D	2.10	0.945	1.04		
Tahkimatlı Aşama-2	A	2.29	0.630	1.04	0.271 (YES=160)	-
	B	2.29	0.630	1.04		
	C	2.29	0.630	1.04		
	D	2.29	0.630	1.04		
Tahkimatlı Aşama-3	A	3.15	0.920	1.04	0.457 (YES=320)	0 (YES=0)
	B	3.15	0.920	1.04		
	C	3.15	0.920	1.04		
	D	3.15	0.920	1.04		

YES: Yenilen Element Sayısı



Şekil 4.  $Z=100\text{m}$ ,  $\sigma_{ci} = 50\text{ MPa}$ ,  $M\text{-RMR} = 40$  ve  $D = 0.5$  koşulunda  $t_c=0.074\text{m}$  için en büyük asal gerilme ( $\sigma_1, \text{MPa}$ )'ye göre Phase2 analiz çıktısı

Figure 4. According to  $\sigma_1$  (MPa), to Phase 2 analysis output for  $t_c = 0.074\text{m}$  under condition  $Z=100\text{m}$ ,  $\sigma_{ci} = 50\text{MPa}$ ,  $M\text{-RMR} = 40$  and  $D = 0.5$



Şekil 5.  $Z=100\text{m}$ ,  $\sigma_{ci} = 50\text{ MPa}$ ,  $M\text{-RMR} = 40$  ve  $D = 0.5$  koşulunda  $t_c=0.074\text{m}$  için yerdeğiştirme ( $U, \text{mm}$ )'ye göre Phase2 analiz çıktısı

Figure 5. According to  $U$  (mm), Phase2 analysis output for  $t_c = 0.074$  under condition  $Z=100\text{m}$ ,  $\sigma_{ci} = 50\text{MPa}$ ,  $M\text{-RMR} = 40$  and  $D = 0.5$

Çizelge 4.  $Z=100\text{m}$ ,  $\sigma_{ci} = 50\text{ MPa}$ ,  $M\text{-RMR} = 40$  ve  $D = 0.5$  koşulunda  $t_c = 0.074\text{m}$  için sayısal analiz sonuçları

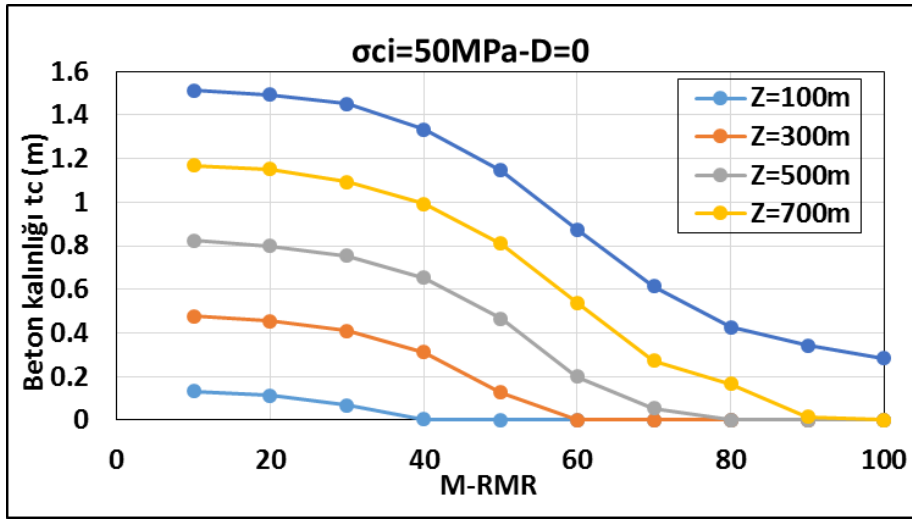
Table 4. The numerical analysis results for  $t_c = 0.074\text{m}$  under condition  $Z=100\text{m}$ ,  $\sigma_{ci} = 50\text{ MPa}$ ,  $M\text{-RMR} = 40$  and  $D = 0.5$

Aşama (Stage)	Kuyu Cidarındaki Analiz Noktası	$\sigma_1$ (MPa)	U (cm)	Dayanım Faktörü (SF)	Kaya Kütleğinde Yenilme Bölgesi Kalınlığı (m)	Beton Tahkimatta Yenilme Bölgesi Kalınlığı (m)
Tahkimatsız Aşama-2	A	1.05	2.40	1.04	1.286 (YES=960)	-
	B	1.05	2.40	1.04		
	C	1.05	2.40	1.04		
	D	1.05	2.40	1.04		
Tahkimatlı Aşama-2	A	1	1.56	1.04	0.858 (YES=640)	-
	B	1	1.56	1.04		
	C	1	1.56	1.04		
	D	1	1.56	1.04		
Tahkimatlı Aşama-3	A	2.21	1.84	1.30	0.854 (YES=620)	0 (YES=0)
	B	2.21	1.84	1.30		
	C	2.21	1.84	1.30		
	D	2.21	1.84	1.30		

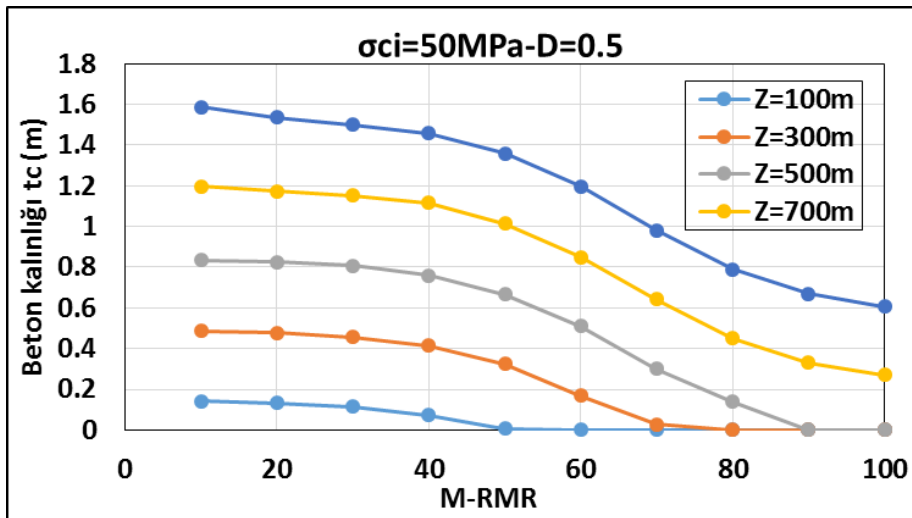
YES: Yenilen Element Sayısı

İki boyutlu sayısal çözümleme yapabilen Phase2 yazılımı ile kurgulanan modelde dairesel kuyu kesiti cidarında sırasıyla belirlenen yenilme bölgesi kalınlığı ( $h_t$ ) ve yerdeğiştirme (U) değerleri her bir koşul için (farklı M-RMR değerlerinde) kritik beton tahkimat kalınlığında belirlenmiştir. Hazırlanan veri tabanı kullanılarak bir seri grafikler hazırlanmıştır.

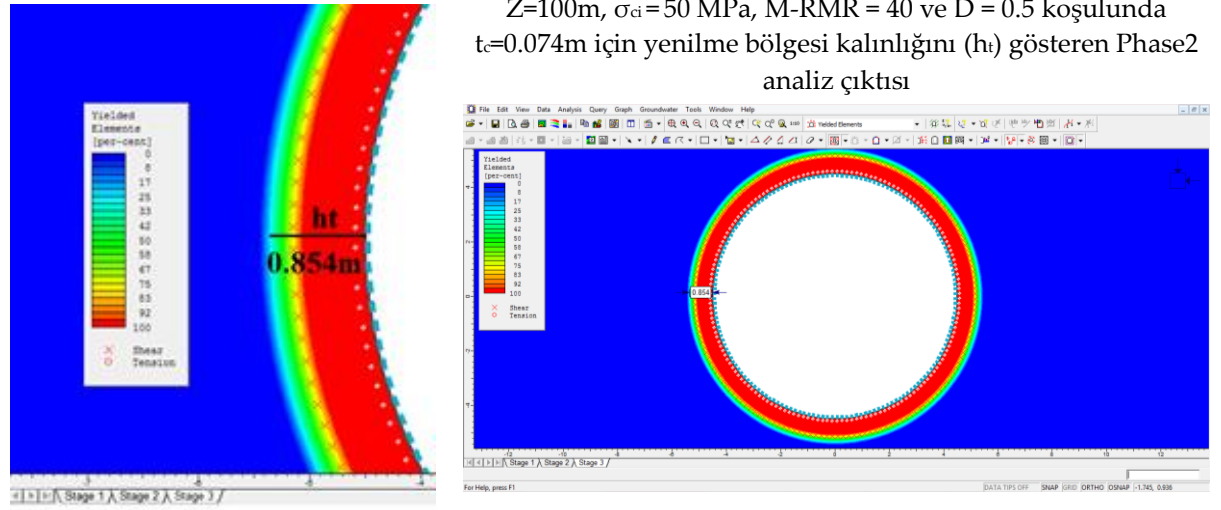
Makineler ile yapılan kazıya dayalı hasarsız ( $D=0$ ) ve patlatmaya dayalı hasarlı kazıya ( $D=0.5$ ) bağlı olarak düşey kuyu etrafında oluşan yenilme bölgesi, bu çalışmada  $h_t$  olarak tanımlanmıştır (Şekil 8). Kaya kütleline, derinliğe ve beton tahkimat kalınlığına bağlı olarak  $h_t$  kalınlığı (Şekil 8) azalmakta ya da artmaktadır. Bu çalışma için tipik örnek olarak hazırlanan  $Z=100\text{m}$  ve  $D=0$  koşulu altında belirlenen davranışlar Şekil 9'da sunulmuştur. Hazırlanan grafiklerden görüldüğü üzere (Şekil 9a) M-RMR değerleri küçüldükçe yenilme bölgesi kalınlığı ( $h_t$ ) artmaktadır. M-RMR'ye bağlı oluşan yenilme bölgesi kalınlıklarının ( $h_t$ ) artması durumunda (Şekil 9b) gerekli olan beton kalınlıkları artmaktadır. M-RMR değerleri arttıkça belirlenen optimum beton kalınlıklarında kuyu cidarında beklenen yerdeğiştirmenin azaldığı belirlenmiştir (Şekil 9c). Belirlenen bu beton kalınlıklarında ise azalan M-RMR değerlerine bağlı olarak tahkimatın müsaade ettiği yerdeğiştirme değerlerinin büyüdüğü anlaşılmaktadır (Şekil 9d).



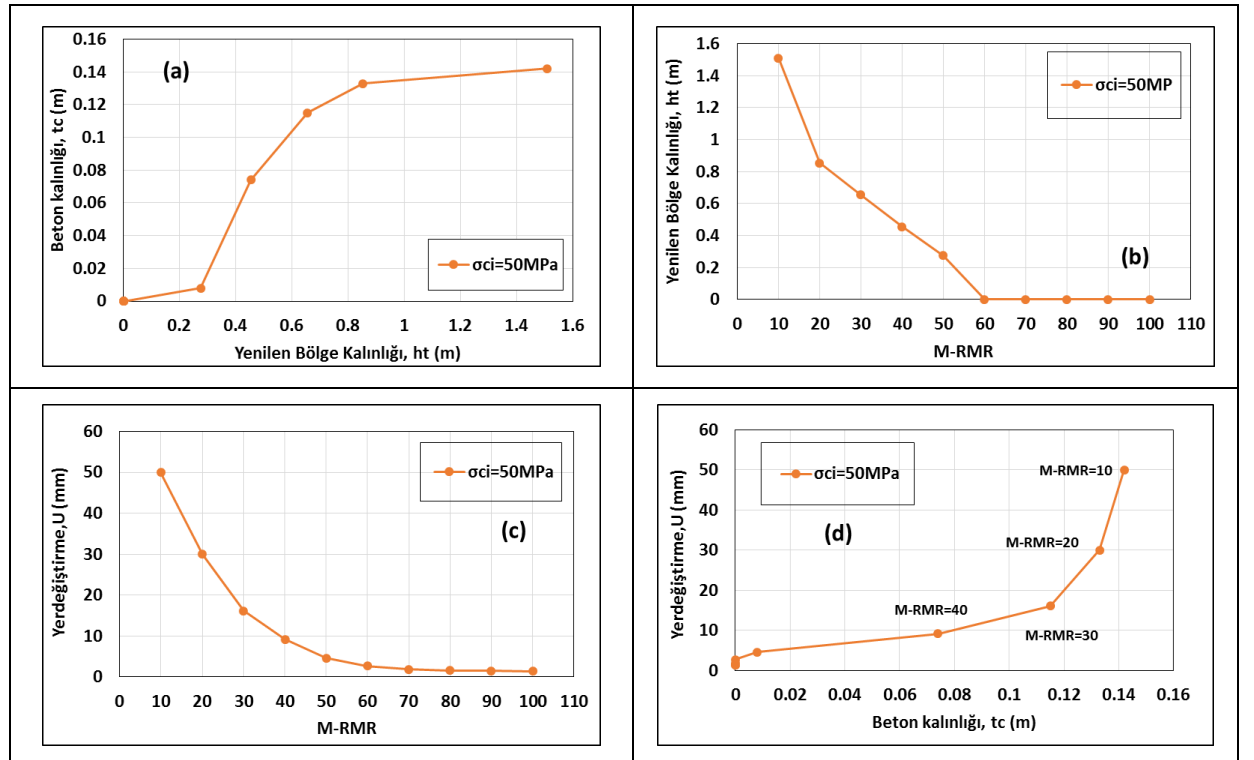
Şekil 6.  $D=0$  ve  $\sigma_{ci}=50\text{MPa}$  koşulu altında M-RMR'ye bağlı farklı derinlikte beton kalınlık değişimi  
Figure 6. The concrete thickness behavior based on M-RMR to different depths under condition  $D=0$   $\sigma_{ci} = 50$  MPa



Şekil 7.  $D=0.5$  ve  $\sigma_{ci}=50\text{MPa}$  koşulu altında M-RMR'ye bağlı farklı derinlikte beton kalınlık değişimi  
Figure 7. The concrete thickness behavior based on M-RMR to different depths under condition  $D=0.5$   $\sigma_{ci} = 50$  MPa



Şekil 8. Yenilme bölgesi kalınlığını ( $h_t$ ) gösteren tipik bir şekil  
Figure 8. A typical figure for thickness of yielded region



Şekil 9. Z=100m ve D=0 koşulunda kuyu etrafında oluşan  $h_t$ ,  $t_c$ , ve U davranışı  
Figure 9.  $h_t$ ,  $t_c$ , U behavior formed around the shaft under conditions Z=100 and D=0

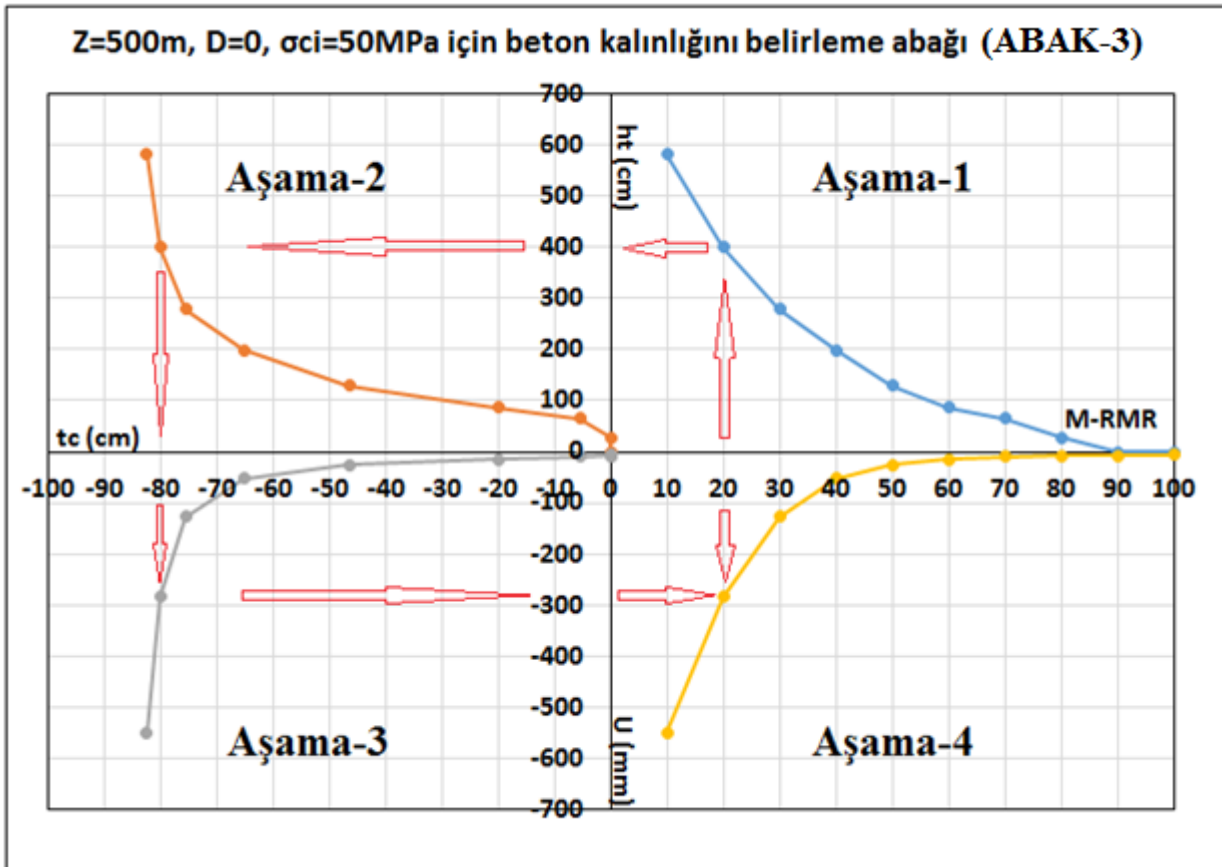
Yukarıda sunulan tipik grafikler (Şekil 9) incelenerek bütünleyici bir yaklaşım geliştirilmeye çalışılmıştır. Bu yaklaşımın 4 aşamadan oluşması planlanmıştır. Bu yaklaşımda bir mühendisin abak üzerinden kolayca tasarım sonuçlarına ulaşması hedeflenmiştir. Bu aşamalar aşağıda sırasıyla sunulmuştur.

- i. Aşama 1: M-RMR değerinin bilinmesi durumunda kuyu etrafında oluşan yenilme bölgesi kalınlığının ( $h_t$ ) belirlenmesi,
- ii. Aşama 2: Belirlenen yenilme bölge kalınlığına ( $h_t$ ) bağlı olarak gerekli olan beton tahkimat kalınlığının ( $t_c$ ) belirlenmesi,
- iii. Aşama 3: Tesbit edilen beton kalınlığına ( $t_c$ ) bağlı olarak müsaade edilmesi beklenen yerdeğiştirme ( $U$ ) miktarının belirlenmesi,
- iv. Aşama 4: M-RMR değerine bağlı olarak belirlenen yerdeğiştirme ( $U$ ) değerinin Aşama 3'den bulunan yerdeğiştirme değeriyle karşılaştırılması.

Yukarıda ifade edilen algoritmayı gösteren tipik bir abak,  $Z=500\text{m}$ ,  $D=0$  ve kaya dayanımı ( $\sigma_{ci}$ )  $50\text{MPa}$  koşulu için hazırlanan bütünleyici yaklaşım Şekil 10'da verilmiştir. Bu şekilde grafiği hazırlayabilmek için  $t_c$  ve  $U$  değerleri negatif (-) alınmıştır. Gerçekte bu değerler pozitif değer taşımaktadır.

Şekil 10'da sunulan abakta oklarla saatin ters yönünde hareket edilerek M-RMR değeri 20 iken tasarım mühendisi bu abaktan kolaylıkla kuyu etrafındaki yenilme bölgesi kalınlığının ( $h_t$ )  $400.6\text{cm}$ , bunu tahkim etmek için gerekli beton tahkimat kalınlığının ( $t_c$ )  $79.9\text{cm}$ , bu tahkimatın uygulaması neticesinde oluşacak yerdeğiştirme ( $U$ ) miktarının ise  $285\text{mm}$  olacağını belirleyebilecektir.

Şekil 10'da sunulan abaktan farklı M-RMR değerler için  $h_t$ ,  $t_c$  ve  $U$  değerleri belirlenerek aşağıdaki Çizelge 5 hazırlanmıştır. Farklı derinliklerde ( $Z=100\text{m}$ ,  $300\text{m}$ ,  $500\text{m}$ ,  $700\text{m}$ ,  $900\text{m}$ ) elde edilen sayısal çözümlere sonuçlarına bağlı olarak Şekil 10'daki gibi toplam 10 adet abak geliştirilmiştir. Makalede yer sorunu olduğu için ayrı ayrı 10 abak verilmesi yerine her bir abaktan bulunan sonuçlar Çizelge 5'deki gibi sırasıyla Çizelge 6, 7, 8 ve 9'da sunulmuştur.



Şekil 10.  $Z=500\text{m}$ ,  $D=0$  ve kaya dayanımı ( $\sigma_{ci}$ )  $50\text{MPa}$  koşulu altında bütünleyici yaklaşım

Figure 10. The integrated approach under condition  $Z=500\text{m}$ ,  $D=0$  and ( $\sigma_{ci}$ )  $50\text{MPa}$

**Çizelge 5.** Z=500m, D=0, D=0.5 ve kaya dayanımı ( $\sigma_{ci}$ ) 50MPa koşulu altında hazırlanan Şekil 10'dan elde edilen veriler (

*Table 5. The obtained data by Figure 10 under conditions Z=500m, D=0, D=0.5 and ( $\sigma_{ci}$ ) 50MPa*

M-RMR	D=0 (ABAK-3)			D=0.5 (ABAK-4)		
	$h_t$ (cm)	$t_c$ (cm)	U (mm)	$h_t$ (cm)	$t_c$ (cm)	U (mm)
10	582.1	82.4	550.0	2054.4	83.4	3300.0
20	400.6	79.9	285.0	1127.2	82.5	1200.0
30	279.6	75.4	127.0	664.3	80.6	440.0
40	199.4	65.2	52.5	401.0	7.6	165.0
50	129.1	46.5	25.5	251.7	6.67	63.0
60	86.1	19.9	14.4	151.8	5.11	28.5
70	64.9	5.4	9.9	85.2	3.01	15.4
80	26.9	0	8.05	26.8	1.4	11.5
90	0	0	7.35	0	0	9.9
100	0	0	6.9	0	0	9.6

$h_t$  : Yenilme bölgesi kalınlığı,  $t_c$  : Beton tahkimat kalınlığı, U : Beton tahkimatın müsaade edeceği yerdeğiştirme

**Çizelge 6.** Z=100m, D=0, D=0.5 ve kaya dayanımı ( $\sigma_{ci}$ ) 50MPa koşulu altında hazırlanan veriler

*Table 6. The obtained data under conditions Z=100m, D=0, D=0.5 and ( $\sigma_{ci}$ ) 50MPa*

M-RMR	D=0 (ABAK-1)			D=0.5 (ABAK-2)		
	$h_t$ (cm)	$t_c$ (cm)	U (mm)	$h_t$ (cm)	$t_c$ (cm)	U (mm)
10	151.0	13.2	50.0	337.8	14.2	99.0
20	85.4	11.3	30.0	225.7	13.3	63.0
30	65.6	6.8	16.1	151.6	11.5	34.5
40	45.5	0.2	9.2	85.4	7.4	18.4
50	27.6	0	4.6	46.2	0.8	9.9
60	0	0	2.7	27.2	0	5.25
70	0	0	1.84	0	0	3.15
80	0	0	1.54	0	0	2.4
90	0	0	1.43	0	0	2.04
100	0	0	1.38	0	0	1.92

$h_t$  : Yenilme bölgesi kalınlığı,  $t_c$  : Beton tahkimat kalınlığı, U : Beton tahkimatın müsaade edeceği yerdeğiştirme

**Çizelge 7.** Z=300m, D=0, D=0.5 ve kaya dayanımı ( $\sigma_{ci}$ ) 50MPa koşulu altında hazırlanan veriler

*Table 7. The obtained data under conditions Z=300m, D=0, D=0.5 and ( $\sigma_{ci}$ ) 50MPa*

M-RMR	D=0 (ABAK-5)			D=0.5 (ABAK-6)		
	$h_t$ (cm)	$t_c$ (cm)	U (mm)	$h_t$ (cm)	$t_c$ (cm)	U (mm)
10	368.4	47.6	230.0	1067.8	48.7	840.0
20	253.7	45.4	127.0	621.9	47.9	380.0
30	174.0	41.0	60.0	401.8	45.7	172.0
40	128.3	31.0	28.5	251.7	41.4	73.5
50	85.7	12.6	14.4	151.6	32.6	31.5
60	65.9	0	8.8	85.2	17.0	15.4
70	27.1	0	5.75	45.9	2.9	9.9
80	0	0	4.8	0	0	6.9
90	0	0	4.2	0	0	6.0
100	0	0	4.2	0	0	5.75

$h_t$  : Yenilme bölgesi kalınlığı,  $t_c$  : Beton tahkimat kalınlığı, U : Beton tahkimatın müsaade edeceği yerdeğiştirme

**Çizelge 8.** Z=700m, D=0, D=0.5 ve kaya dayanımı ( $\sigma_{ci}$ ) 50MPa koşulu altında hazırlanan veriler*Table 8. The obtained data under conditions Z=700m, D=0, D=0.5 and ( $\sigma_{ci}$ ) 50MPa*

M-RMR	D=0 (ABAK-7)			D=0.5 (ABAK-8)		
	ht (cm)	tc (cm)	U (mm)	ht (cm)	tc (cm)	U (mm)
10	850.4	116.9	1150.0	3091.9	119.8	7700.0
20	543.3	115.3	500.0	1695.5	117.4	2700.0
30	401.3	109.2	230.0	952.9	115.1	920.0
40	274.9	99.2	92.0	542.3	111.7	300.0
50	199.4	80.9	40.0	337.8	101.4	105.0
60	129.1	53.9	20.7	225.1	84.8	46.0
70	65.6	27.2	13.8	106.4	64.2	23.0
80	46.2	16.5	11.0	46.1	45.2	15.4
90	27.2	1.3	9.9	0	33.1	13.2
100	0	0	9.9	0	27.1	12.1

ht : Yenilme bölgesi kalınlığı, tc : Beton tahkimat kalınlığı, U : Beton tahkimatın müsaade edeceği yerdeğiştirme

**Çizelge 9.** Z=900m, D=0, D=0.5 ve kaya dayanımı ( $\sigma_{ci}$ ) 50MPa koşulu altında hazırlanan veriler*Table 9. The obtained data under conditions Z=900m, D=0, D=0.5 and ( $\sigma_{ci}$ ) 50MPa*

M-RMR	D=0 (ABAK-9)			D=0.5 (ABAK-10)		
	ht (cm)	tc (cm)	U (mm)	ht (cm)	tc (cm)	U (mm)
10	1126.1	151.3	2070.0	3853.8	158.8	12700.0
20	752.2	149.3	880.0	2265.0	153.5	5250.0
30	504.1	145.2	330.0	1257.2	150.1	1540.0
40	367.5	133.5	132.0	709.6	145.9	500.0
50	251.1	114.7	55.0	435.1	135.8	161.0
60	175.3	87.5	28.5	279.1	119.6	63.0
70	106.3	61.3	17.6	150.7	98.2	31.5
80	65.1	42.5	15.4	85.4	79.0	20.4
90	26.9	34.3	12.1	28.3	66.9	16.1
100	0	28.3	12.0	0	60.8	15.0

ht : Yenilme bölgesi kalınlığı, tc : Beton tahkimat kalınlığı, U : Beton tahkimatın müsaade edeceği yerdeğiştirme

## SONUÇLAR (CONCLUSIONS)

Yeraltı maden kuyuları yeraltı maden ocakları için vazgeçilmez bir unsurdur. Maden kuyularının ilk yatırımları ve işletme maliyetleri oldukça yüksektir. Bu maliyet içerisinde en büyük payı ise kuyu duraylılığını sağlayacak tahkimat almaktadır. Bu çalışmada, 9m çaplı ve 900m derinliğe ulaşan düşey bir kuyunun beton tahkimat kalınlıkları, iki boyutlu sayısal analizler ile belirlenmiştir. Parametrik olarak dikkate alınan veriler; farklı derinlik (Z: 100-900m), tek eksenli basma dayanımı ( $\sigma_{ci} = 50$  MPa), kaya kütle sınıflama sistemi (M-RMR: 10-100), kuyu kazısında patlatmaya dayalı çevre kayacın örselenme durumu (D: 0-0.5) dur. Parametrik bu çalışmada, toplam 100 senaryo model hazırlanmış ve analiz edilmiştir. Bütün senaryolar için C20 beton kalitesinde ( $\sigma_{cc} = 20$  MPa) optimum beton tahkimat kalınlıkları Phase2 yazılımı ile belirlenmiştir. Sayısal çözümlerle yardımcıyla sırasıyla, en büyük asal gerilme ( $\sigma_1$ ), toplam yerdeğiştirme (U), kuyu çevre kayacında oluşan yenilen element sayısı, dayanım faktörü (SF) ve yenilme bölge kalınlığı ( $h_t$ ) davranışları belirlenmiştir. Dikkate alınan veri tabanı ile M-RMR sınıflama sistemine bağlı beton tahkimat kalınlık değişimleri grafiksel formatta sunulmuştur. Ayrıca 9 m çaplı düşey kuyular için gerekli beton tahkimat tasarımında kullanılabilecek dört farklı grafikten oluşan bir bütünleyici abak tasarlanmıştır. Sonuç olarak bu çalışmada dikkate alınan 100 farklı senaryo için 10 abak hazırlanmıştır ancak bu makalede hepsi verilmemiştir. M-RMR kaya kütle sınıflama değerinin bilinmesi durumunda; geliştirilen ilgili abaktan kuyu çevre kayacında oluşan yenilme bölge kalınlığı ( $h_t$ ), beton tahkimat kalınlığı ( $t_c$ ) ve kuyu cidarında oluşacak yerdeğiştirme miktarı (U) belirlenebilmektedir. Bu çalışma ile önerilen beton tahkimat kalınlıkları ( $t_c$ ) optimum değerler olup uygulayan mühendisler, önerilen tahkimat beton kalınlıklarına eşit yada daha büyük

değerler seçmelidirler. Son olarak, bu çalışmadan elde edilen sonuçların tasarım girdi parametrelerinde ve çözümlenmelerde yapılan bazı idealleştirmelerin göz önünde bulundurulduğu koşullarda geçerli olacağı da göz ardı edilmemelidir.

#### TEŞEKKÜR (ACKNOWLEDGEMENT)

Yazarlar, bu makalenin değerlendirmesinde eleştirileri ile katkı koyan hakemlere teşekkürü bir borç bilir.

#### KAYNAKLAR (REFERENCES)

- Barton, N. R., Lien, R., Lunde, I., 1974, "Engineering Classification of Rock Masses for the Design of Tunnel Supports", *Rock Mechanics*, Vol.6(4), pp.189-239.
- Bieniawski, Z. T., 1989, *Engineering Rock Mass Classifications: A Complete Manual for Engineers and Geologists in Mining, Civil, and Petroleum Engineering*, John Wiley & Sons.
- Bieniawski, Z.T., 1973, "Engineering Classification of Jointed Rock Masses", *Civil Engineer in South Africa*, Vol. 15 (12), pp.335-343.
- Carranza-Torres, C., Fairhurst, C., 2000, "The Elasto-Plastic Response of Underground Excavations in Rock Masses that Satisfy the Hoek-Brown Failure Criterion", *International Journal of Rock Mechanics and Mining Sciences*, Vol. 36(6), pp. 777-809.
- Geniş, M., Acun, D., 2015, "Kuyu Duraylılığının Analitik ve Sayısal Yöntemler ile Karşılaştırmalı Bir İncelemesi", *Çukurova Ün. Müh. Mimar. Fak. Derg.*, Vol. 30 (2), pp. 201-215.
- Geniş, M., Derin, Z., 2016, "Zonguldak-Üzülmez Tünellerinin Çevre Kaya Özelliklerinin Belirlenmesi ve Duraylılığının Değerlendirilmesi", *Karadmas Fen ve Müh. Derg.*, Vol. 6 (1), pp. 144-151.
- Hoek, E., Kaiser, P. K., Barwden, W. F., 1995, *Support of Underground Excavations in Hard Rock*, Balkema, Netherlands, 215p.
- Ozkan I., 1989, *Determination of Classification Parameters for Weak and Stratified Rocks Based on RMR and Q-Systems*, MSc Thesis, 156p., METU, Ankara, Turkey.
- Ozkan, I., 1995, "Modified Rock Mass Rating (M-RMR) System and Roof Behavior Model", Pht Thesis, 370p., METU, Ankara, Turkey.
- Ozkan, I., Unal, E., 1996, "A Critical Review on Rock Mass Classification Systems", 3th Turkish Rock Mechanics Symposium, Ankara, Turkey, pp.181-193 (in Turkish).
- Ozkan. I., Unal, E., 2012, *Kaya Kütle Sınıflama Sistemleri ve M-RMR Sınıflama Sisteminin Yeri, Gelişme Raporu*, Selçuk Üniversitesi, Konya, 85s. (yayınlanmamış)
- Rocscience, 2002, Phase2, Toronto, Canada, <http://www.rocscience.com/>
- Rocscience, 2002, RocLab, Toronto, Canada, <http://www.rocscience.com/>
- Saltoğlu, S., 1976, *Madenlerde Hazırlık ve Kazı İşleri*. İstanbul Teknik Üniversite matbaası, Gümüşsuyu, İTÜ, İstanbul, Türkiye, 336p.
- Ulusay, R., Ozkan, I., Unal, E., 1992, Characterization of Weak, Stratified and Claybearing Rock Masses For Engineering Applications", *Proceedings of the Fractured and Jointed Rock Masses Conference*, Lake Tahoe, California, L.R. Mayer, N.G.W. Cook, R.E. Goodman and C.F. Trans (eds), 3-5 June 1992.
- Unal, E., 1996, *Modified Rock Mass Classification: M-RMR System, Milestone in Rock Engineering*, The Bieniawski Jubilee Collection, Balkema, Rotterdam.
- Unal, E., I. Ozkan, 1990, "Determination of Classification Parameters for Clay-bearing and Stratified Rock Mass", *Proceedings of the 9th International Conference on Ground Control in Mining*, Morgantown, USA, 4-6 June, 1990, pp. 250-259.
- Unal, E., Ozkan, I., 1988, Zayıf-Tabakalı-Anizotropik-Kil İçerikli Kaya Kütleleri İçin Kaya Kütle Karakteristiği, *Sivas I. Mühendislik Sempozyumu*, Sivas.
- Unal, E., Ozkan, I., Ulusay, R., 1992, "Characterization of Weak, Stratified and Claybearing Rock Masses", *ISRM Symposium: EUROCK'92 Rock Characterization*, Chester, UK, ed. J.A. Hudson, British Geotechnical Society, London, 14-17 September 1992, pp.330-335.

## INFLUENCE OF FLAKE SIZE ON THE MORPHOLOGY OF WET SPUN GRAPHENE OXIDE FIBERS

<sup>1</sup>Volkan ESKİZEYBEK

<sup>1</sup>Department of Materials Science and Engineering, Canakkale Onsekiz Mart University Turkey

<sup>1</sup>veskizeybek@comu.edu.tr

(Geliş/Received:13.06.2017; Kabul/Accepted in Revised Form:20.07.2017)

**ABSTRACT:** For using graphene in practical applications, it is crucial to transform the unique and individual properties of graphene flakes into ordered macroscopic materials. The physical and chemical properties of macroscale graphene structures are closely related to the size of graphene flakes as building blocks. However, the chemical methods adopted to synthesize graphene oxide (GO) flakes offer no tight control on the dimensionality of the ensuring flakes sizes. The goal of this study is to investigate morphological evaluation of graphene based fibers fabricated using building blocks with different average size.. A facile and effective centrifugation method was carried out for size sorting of graphene oxide flakes. Macroscopic graphene oxide fibers were continuously spun from graphene oxide/water suspensions followed by chemical and thermal reductions to obtain reduced graphene oxide fibers. All wet spinning parameters such as suspension concentration, injection rate and nozzle diameter were fixed to investigate the effect of average building block size on the structural morphology of the fibers. Microscopic investigations revealed that the flake size have an enormous impact on the morphology of graphene oxide fibers. The increased average flake size results in the fibers with rectangular-like cross-section and increased amount of voids within the graphene oxide fiber.

*Key Words:* Centrifugation, Colloid, Dimensional control, Graphene oxide, Image processing

### Grafen Oksit Kabukların Boyutlarına Göre Sınıflandırılması: Deneysel Çalışma

**ÖZ:** Pratik uygulamalarda grafen kullanmak için grafen kabukların eşsiz ve münferit özelliklerinin makroskopik, düzenli malzemelere dönüştürülmesi çok önemlidir. Makro boyuttaki grafen yapıların fiziksel ve kimyasal özellikleri, bu yapıları oluşturan yapıtaşları olan grafen kabukların boyutları ile yakından ilgilidir. Bununla birlikte, kimyasal yöntemler kullanılarak üretilen grafen oksit (GO) kabuklarının boyutları istenilen aralıklarda kontrol edilememektedir. Bu çalışmanın amacı, farklı ortalama boyutlara sahip grafen kabuklar kullanılarak üretilen grafen esaslı fiberlerin morfolojik değerlendirmesini araştırmaktır. Grafen oksit kabukların boyut sıralanması için basit ve efektif bir santrifüj yöntemi uygulanmıştır. Makroskopik grafen oksit fiberleri, grafen oksit/su süspansiyonlarının sürekli olarak eğrilmesi ile üretilmiş bunu takiben indirgenmiş grafen oksit elyafı elde etmek için kimyasal ve termal indirgeme işlemleri yapılmıştır. Süspansiyon konsantrasyonu, enjeksiyon hızı ve orifis çapı gibi tüm ıslak eğirme parametreleri sabit tutularak, yalnızca grafen kabuk boyutunun fiberlerin yapısal morfolojisine etkisi araştırılmıştır. Mikroskopik incelemeler kabuk boyutunun, grafen oksit fiberlerin morfolojisi üzerinde çok büyük bir etkisi olduğunu ortaya koymuştur. Artan ortalama kabuk boyutu, grafen oksit fiberlerin kesitinin dikdörtgen geometrisine benzemesine ve fiber içerisindeki boşlukların artmasına neden olmuştur.

*Anahtar Kelimeler:* Santrifüj, Kolloid, Boyut kontrolü, Grafen oksit, Görüntü işleme

## INTRODUCTION

Graphene is a planar monolayer of carbon atoms that arranged into a two-dimensional honeycomb lattice with  $sp^2$  hybridized bonds (Esmaeili and Entezari, 2014). The unique  $\pi$ -conjugation in graphene endows extraordinary mechanical, thermal and electrical properties which attract great scientific attention of many theoretical and experimental studies during recent years in various fields such as energy storage (Tong et al., 2011), electronic devices (Li et al., 2013) and nanocomposites (Zhuo et al., 2013). As a consequence, various graphene based structures in nano-, micro- and macro-scale have been synthesized and characterized, including 2D graphene papers (Chen et al., 2008) and 1D graphene fibers (Xu and Gao, 2011; Cheng et al., 2013).

The size of the building blocks fundamentally governs physical performances of the macro-scale graphene based structures since larger building blocks usually yields better mechanical and electrical properties up to three-fold increase (Chae and Kumar, 2008; Xiang et al., 2013). However, the difficulty of producing high quality graphene flakes with controlled size and chemical composition still remain as a challenge especially in scalable industrial processes. Chemical exfoliation of graphite with strong acid treatment, a method introduced by Hummers and Brodie, one of the most preferred production method to generate graphene oxide (GO) flakes (Allen et al., 2010). GO flakes exhibit good dispersion in water and other commonly used solvents to form liquid crystal phases due to existence of epoxy and hydroxyl groups formed in the basal plane and carbonyl and carboxylic acid groups in the edge sites (Aboutalebi et al., 2011). However, the oxidation and exfoliation processes of the graphite results diverse sizes of GO flakes. Therefore, the separation of the graphene based flakes with well-defined size is of importance for the accurate control of the macro-scale mechanical and electrical properties of the graphene based structures (Pan and Aksay, 2011).

Controlling the size of particles is a key parameter to tailor the physical and chemical properties. For example, the chemical and physical properties of nanoscale particles are significantly influenced by their size. Centrifugal separation process is a simple physical method used for size sorting of nano-scale materials distributed in liquid medium. The main outcome of the centrifugal separation is that no additional chemical is added into the solution for size sorting, and thus the physical and chemical properties of the particles in the solution are preserved. Although centrifugal dimensional sorting process is defined for spherical particles according to the Stoke law, it can also be utilized to particles with anisotropic morphology such as carbon nanotubes (CNTs), and DNA (Tirado et al., 1984; Arnold et al., 2008; Batista et al., 2014). Recently, centrifugation process has been utilized generally as a post-synthesis size sorting approach including GO flakes (Khan et al., 2012; Bonaccorso et al., 2013; Han et al., 2013). Since centrifugation time and rotational speed are the correlated parameters to control particle size during sedimentation, it must be addressed their relationship specifically to sort GO flakes with specific size ranges. Khan et al. (Khan et al., 2012) described a centrifugal separation method to separate an existing dispersion of small graphene flakes in N-methyl pyrrolidone solvent with mean flake length of  $\sim 1 \mu\text{m}$  into fractions and low concentrations. They fixed the centrifugation time as 45 min while altering the rotational speeds from 4000 to 500 rpm. However, it is need to be addressed quantitatively those of parameters for larger flake sizes distributed in aqueous medium. With this motivation, our group recently demonstrated the viability of centrifugation process for size selection of GO flakes of diameters up to  $40 \mu\text{m}$  using distilled aqueous medium without the need to use of chemical additives or other solutes (Özçakır et al., 2016; Özçakır and Eskizeybek, 2016).

The development of high-performance graphene based fibers (GBFs) could inspire more engineering applications of graphene. GBFs possess lots of advantages over traditional carbon fibers and newly developed carbon-nanotube (CNT) fibers, especially in terms of their simple processing conditions and cost effective production. GBFs can play an important role in the production of textiles, especially wearable energy storage, or other two- or three-dimensional macroscopic structures (Xu and Gao, 2011; Cong et al.,

2012; Dong et al., 2012). However, the nature and importance of the fiber building blocks have not been fully described, and the relationship between the building blocks and fiber properties also needs to be further clarified. The most effective and scalable process to produce graphene fiber from graphene oxide flakes is wet spinning. In this process, graphene oxide particles are dispersed in distilled water and this spinning dope is injected into a rotating coagulation bath. The most important parameters of wet spinning process are concentration of spinning dope, viscosity of coagulation bath, needle size, and injection rate (Xu and Gao, 2014).

In this study, the effect of building block size on the morphology of wet spun graphene based fibers was reported. For this purpose, a centrifugal sedimentation process was utilized to sort graphene oxide flakes with controllable average sizes. The centrifugation times for the specific size ranges were calculated based on Stokes' law to separate GO flakes from homogenously distributed aqueous medium. Then, the sorted graphene flakes were used as spinning dopes to prepare wet-spun graphene fibers. The morphologies of the macroscopic fibers were examined using scanning electron microscopy. A possible fiber formation mechanism was introduced depending on the different spinning dopes with different average flake sizes.

## MATERIAL AND METHOD

### Separation of GO Flakes with Centrifugation Process

Our initial experiments relied on simple sedimentation centrifugation. An empirical model developed by Walter et al. (Walter et al., 2015) was utilized to sort GO flakes in specific size ranges. The developed model is expressed in the following formula:

$$RCF = \frac{w^2 r}{g} = \frac{18\eta l \left(\frac{f_t}{f_0}\right)}{gt(\rho_{GO} - \rho_C)} \left(\frac{3h^3}{2q^2}\right)^{\frac{2}{3}} \quad (1)$$

In Eq (1) relative centrifugal force (RCF) is a function of the rotational speed and the sample position in the rotor normalized by the gravitational field of the earth which is typically utilized to compare centrifugal forces created by centrifuges with different geometry,  $w$  is angular velocity (rad/s),  $r$  is the radial position from the axes of rotation within the centrifuge (m),  $h$  is the single layer GO flake height (m),  $g$  is the gravitational acceleration,  $l$  is the length of the centrifuge tube;  $t$  is the experimental time,  $q$  is the aspect ratio which is the height  $h$  (1.5 nm for graphene oxide layer) divided by the hydrodynamic diameter  $d$  of GO flakes,  $\eta$  is the viscosity of solution (Pa.sn),  $\rho_{GO}$  is the density of GO flakes (kg/m<sup>3</sup>), and  $\rho_C$  is the density of solution (kg/m<sup>3</sup>). In addition,  $f_t/f_0$  is the translational friction coefficient of disk like particles which is calculated as follows;

$$\frac{f_t}{f_0} = 1.0408 + 0.0197k + 0.07255k^2 + 0.00303k^3 + 0.00123k^4 + 8.22E^{-5}k^5 + 6.44E^{-6}k^6 \quad (2)$$

In Eq. (2)  $k$  is defined as  $k = \ln(q)$ . Other terms used to calculate centrifugation times are given in Table 1.

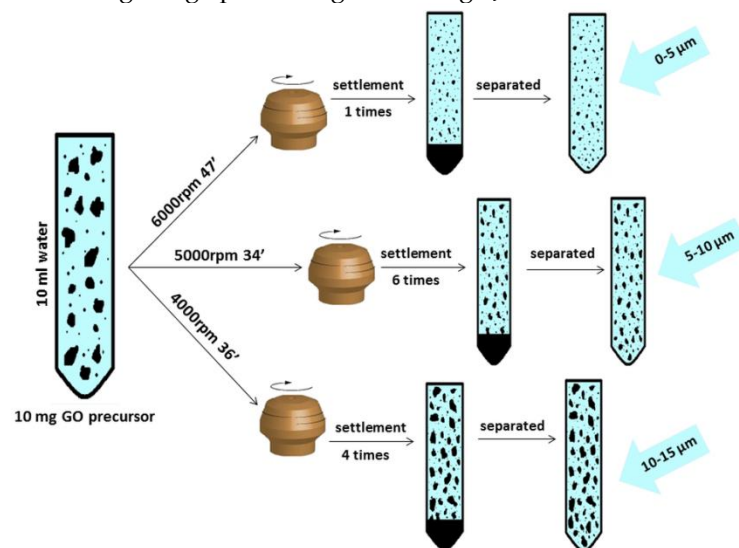
The centrifugation times according to Eq. (1) for fixed GO flake size ranges and rotational speeds were calculated and represented in Figure 1. The GO flakes were assumed as single layer with the height of 1.3 nm and the hydrodynamic diameters were selected between 5 to 15  $\mu$ m.

**Table 1.** Typical terms used to calculate centrifugation times for specific GO flake

Symbol	Definition	Value
$l$	Length of the centrifuge tube (m)	0.08
$\eta$	Viscosity of water (20 °C)( Pa.s)	$1.002 \times 10^{-3}$
$d$	Hydrodynamic diameter of GO flakes (m)	$5 \times 10^{-6}$ - $10 \times 10^{-6}$ - $15 \times 10^{-6}$ - $20 \times 10^{-6}$ - $25 \times 10^{-6}$ - $30 \times 10^{-6}$ - $35 \times 10^{-6}$
$\rho_{GO}$	Density of GO flakes ( $g/cm^3$ )	1.8 (20°C)
$\rho_c$	Density of water ( $g/cm^3$ )	1.0 (20°C)
$R$	Radius of rotation (m)	0.086
$w$	Angular velocity ( $rad.s^{-1}$ )	6000 RPM (628.319 $rad.s^{-1}$ ) 5000 RPM (523.599 $rad.s^{-1}$ ) 4000 RPM (418.879 $rad.s^{-1}$ ) 3000 RPM (314.159 $rad.s^{-1}$ ) 2000 RPM (209.440 $rad.s^{-1}$ )

GO flakes were purchased from Graphene Supermarket, USA (single layer flake content >97%) with flake sizes up to 40  $\mu m$ . The centrifugation process was described in our previous works in detail (Özçakır et al., 2016; Özçakır and Eskizeybek, 2016). Briefly, 1 mg mL<sup>-1</sup> of aqueous GO solution was prepared effectively by aid of sonication and magnetic stirring, respectively. Following, centrifugation process was utilized to separate GO flakes with specific sizes. Hettich EBA 20 centrifuge with a rotor radius 86 mm and a maximum rotational speed of 6000 rpm was used during centrifugation process. Note that, it takes approximately 30 s to accelerate centrifuge rotor and slow down and this time is not included into the calculated separation times. After separation, the supernatant solution was dried in a silicon mold at 60°C for 4 h under vacuum conditions for further use. The typical separation process of GO flakes with specific size ranges is schematically illustrated in Figure 1. The separation process was utilized successively to sort GO flakes with different average diameters by changing centrifugation speed and time. The resulting size sorted GO flakes were grouped into four groups including sediment as the remaining GO flakes after centrifugal sorting process.

The particle size distributions of the GO flakes were revealed by measuring the surface area of more than 3000 flakes by means of electron microscopy. Following, the measured surface area was transformed into hydrodynamic diameter using image processing with Image J®.

**Figure 1.** Schematic representation of the centrifugation process utilized to separate GO flakes with specific sizes

### Wet Spinning of Graphene Oxide Fibers

Size sorted GO flakes with different average flake sizes were well dispersed in DI water. The computer controlled wet spinning unit was utilized to spun graphene fibers. The GO colloids ( $12 \text{ mg mL}^{-1}$ ) were injected through a blunt-tipped needle with  $210 \mu\text{m}$  inner diameter at the rate of  $0.5 \text{ mL/min}$  into a rotating ( $15 \text{ rpm}$ ) aqueous chitosan ( $M_w=600.000-800.000$ , Acros Organics) coagulation bath ( $1 \text{ wt}\%$ ). The GO gel-state fiber formed immediately when met with the bath. The GO preparation steps were schematically illustrated in Figure 2. Note that no tension was applied during forming of the macroscopic fibers. After been soaked for  $20 \text{ min}$  in the coagulation bath, the GO fibers (GOFs) was extracted, rinsed with de-ionized water, and dried on a water absorbing paper overnight. The centrifugal separated GO flakes with different average sizes were used as spinning dopes to prepare GOFs, therefore three types of GOFs were fabricated.

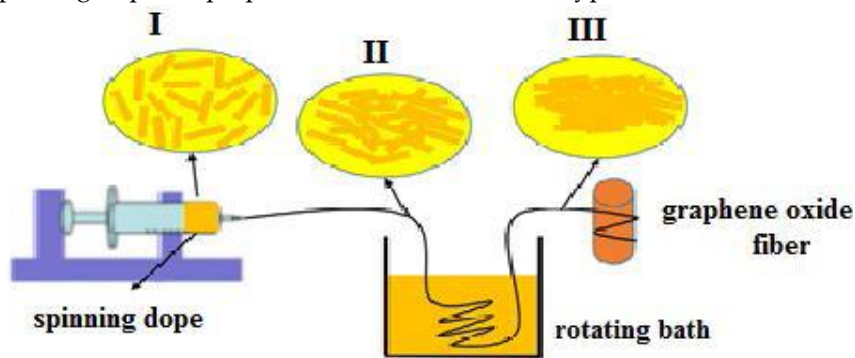


Figure 2. Schematic representation of wet-spinning process

### Characterization

The resulting graphene flakes and GOFs were monitored using scanning electron microscopy (JEOL SEM-7100-EDX). At least ten SEM images were recorded from different areas of the deposited graphene flake samples on Si wafer, and image processing was applied to measure their areas. Assuming GO flakes are disclike, the GO flake effective diameters were calculated from at least 3000 GO flakes.

### RESULTS AND DISCUSSIONS

The rational speed and the centrifugation time are crucial parameters for size sorting of GO flakes. In particular, by increasing the rational speed and reducing the centrifugation time, the amount of sediment increases: by centrifugation either at  $6000 \text{ rpm}$  for  $47 \text{ min}$ , at  $5000 \text{ rpm}$  for  $34 \text{ min}$ , and at  $4000 \text{ rpm}$  for  $36 \text{ min}$ , it is obtained  $6.15$ ,  $8.74$  and  $11.97 \mu\text{m}$  of the average GO flake sizes as shown in Figure 3a, respectively. Note that GO flakes smaller than  $5 \mu\text{m}$  were observed in all SEM images taken after second and third step of centrifugation process (Figure 3b-d). This is attributed to brake of large GO flakes during preparing GO sediments for next separation process. It is known that bath-sonication mixing of GO flakes results decreasing sizes and consequently decreases the average flake size of the sediment. Therefore, we applied bath-sonication to disperse GO sediment in water for  $5 \text{ min}$  to minimize damage and following mixed with vortex shaker for  $2 \text{ min}$ . The average size of GO flake sediment at the bottom of the tube is measured as  $17 \mu\text{m}$ . This proves the effectiveness of selective centrifugation for GO flake size sorting, while requiring low centrifugal fields, achievable with ordinary benchtop centrifuges. The size sorted GO flakes with different average effective diameters were used as spinning dopes to fabricate three types of GOFs. The fabricated GOFs were named as SGOFs, LGOFs

and HGOs based on the used spinning dopes 6.15, 11.97 and sediment with the efficient diameter 17  $\mu\text{m}$ , respectively.

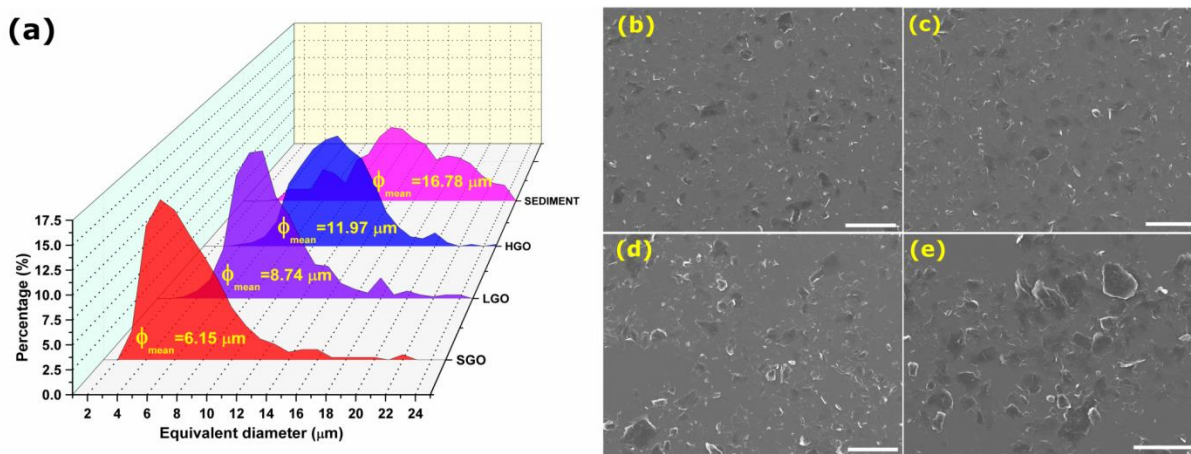


**Figure 3.** a) The average flake size distribution of separated GO supernatants and corresponding SEM images selected from image processing of the flakes (scale bars 10  $\mu\text{m}$ ), b) 6000 rpm 47 min, c) 5000 rpm 34 min, d) 4000 rpm 36 min, e) the sediment of graphene oxide flakes

The morphologies of GOFs could likely have an enormous impact on their physical features such as mechanical properties. The corrugated surface and cross sections of the fabricated GOFs were examined in detail by SEM analysis as shown in Figure 4. In general, all types of GOFs represent non-uniform axial morphology with wrinkles along the fiber axis. The surfaces of the fibers are rough and no droplets are observed in the fibers. In addition, the cross-sections of the fibers are not regular. The SGOFs were produced using the smallest GO flakes in average effective diameters. It is apparent that the SGOFs have lowest average diameters and the smallest cross-sectional areas with respect to LGOFs and HGOs. Further, diameters of the fibers were also measured along the axis from different areas; thereby average diameters of the fibers were calculated. Based on our measurements, the average diameters of SGOFs are measured as  $65 \pm 25 \mu\text{m}$  (Figure 4a). The cross sections of the SGOFs exhibit the closest morphology to the circular section while the section is composed of tightly packed GO layers, and rare voids are observed in the fiber (Figure 4d). LGOFs were prepared using GO flakes with an average effective diameter of  $\sim 12 \mu\text{m}$ . The surfaces of LGOFs represent increased roughness with respect to SGOFs and no droplet formation is observed in the fibers. The mean diameter of LGOFs is measured as  $84 \pm 30 \mu\text{m}$  and average cross-sectional areas of LGOFs are evaluated to be larger than the SGOFs (Figure 4b). The cross-sections of LGOFs have a star-like morphology with more indentations and protrusions than SGOFs. Further, it has been determined that the cross-section is composed of the tightly packed GO layers, and the amount of voids between the GO layers is increased with respect to SGOFs (Figure 4e). The HGOs were produced using GO flakes of sediment with an average effective diameter  $\sim 17 \mu\text{m}$ . The fibers have the highest surface roughness and without any droplet formation. The cross-sections of the HGOs have mostly rectangular-like morphologies, but with more indentations and protrusions. The mean diameters HGOs are measured as  $105 \pm 20 \mu\text{m}$  and their average cross-sectional areas are evaluated to be larger than the LGOFs (Figure 4c). However, it is observed that the amount of voids between the GO layers is at the highest level with respect to SGOFs and LGOFs (Figure 4f).

The enormous morphological differences are clearly originated from the contribution of average flake size as building blocks within the fiber and rapid liquid changes during gelation stage of the fiber since the GO colloid enters the coagulation bath. In the case of using larger GO flakes to prepare GO/water

dispersions, the amount of trapped water between the flakes increases. Thereby, larger GOFs with irregular cross-sections are formed. During the drying process namely densification or dehydration, the resulting fibers shrink more and try to fill the gaps due to the evaporation of the solvent trapped in between ordered GO flakes (Xu et al., 2013). As a result, the surface of fiber becomes wrinkled aligned with the fiber axis and the cross section also approaches a rectangle rather than a circular one with increasing GO flake sizes. Xiang et al. (Xiang et al., 2013) noted that the non-uniform morphology of fibers varies with the GO dimension and the fiber sections were obtained more circular when the dimensions of the GO flakes were lowered to 100 nm. This means that the small size GO flakes can easily fill the voids formed during dehydration and the cross section looks more uniformly circular.

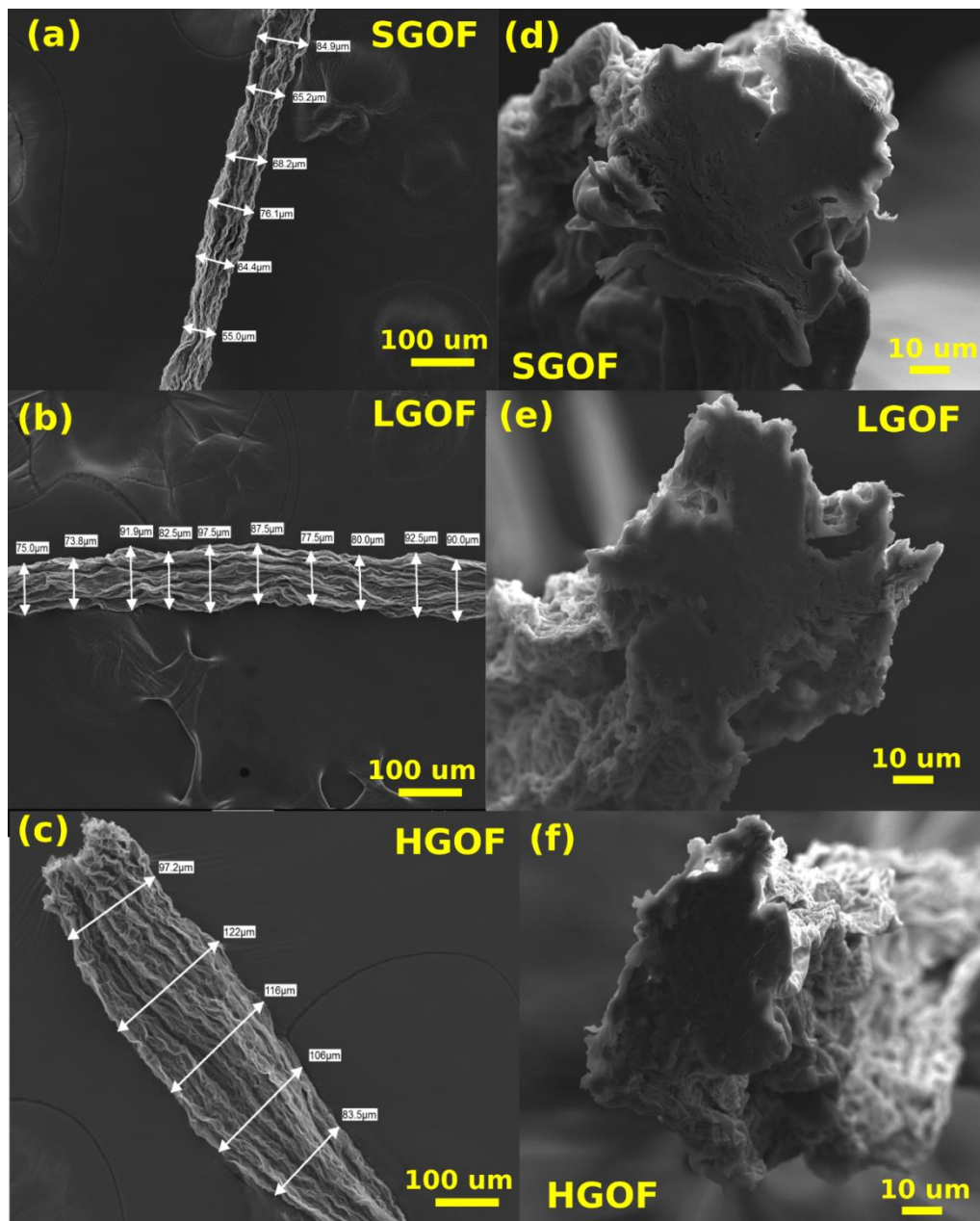


**Figure 4.** Typical SEM images of (a-c) the surface and (d-f) the cross-section of GOF produced by wet bending method. (a, d) SGOF (b, e) LGOFs (c, f) HGOFs

The relationship between the production of GOF in different surface and cross-sectional morphologies and the relationship of the GO sheet size is schematically illustrated in Figure 5. The voids in the fiber are due to the high mass transfer rate difference between the pure water in the colloid and the chitosan. However, these voids were reduced by washing with ethanol and drying processes due to the re-orientation of GO flakes and stacking closer to each other. It is confidentially believed that the small size GO flakes slip efficiently into these voids during fiber shrinkage in radial direction, therefore the average diameters of the SGOFs are smaller compared to LGOFs and HGOFs. Thus, the resulting SGOFs are produced with higher stacking density and flake orientation along the fiber axis. In the case of using GO flakes with larger average sizes, the slipping is limited within the fiber due to the friction between the flakes, so that the GO flakes are wrinkled and bent. Furthermore, since larger GO flakes cannot sufficiently slip into the voids, they cannot fill the voids which are clearly visible in the SEM images. The voids in GOFs can be thought of as nanoscale defects in the layers or microscopic voids. It is well known that these defects lead the fibers to break at lower tensile strengths and thus worsen their mechanical properties. On the other hand, the sheet boundaries decrease with the increasing average size of the GO flakes, and, as a result, the fibers withstand higher loads due to the improvement in the transfer of forces between the flakes. In addition, due to the increased contact between the bending of large-sized flakes, mechanical interlocking increase and larger forces are required to move the flakes over each other.

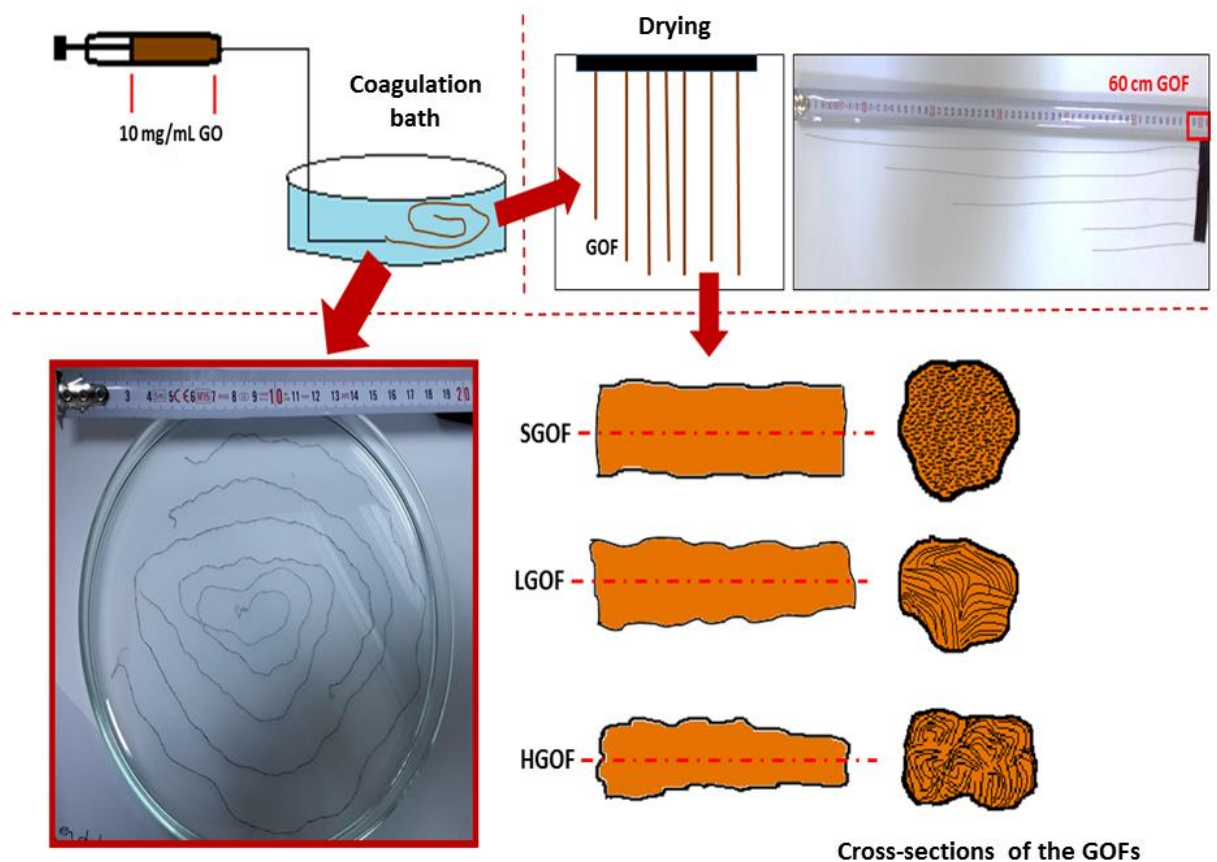


Figure 5. Schematic representation of the effect of GO flake size on fiber morphology in GOFs

## CONCLUSION

Graphene flakes with different average flake sizes were spun to fabricate macroscopic fibers with controllable physical properties. A facile and effective gradient centrifugation process was utilized for size sorting of graphene oxide flakes. Macroscopic graphene oxide fibers were continuously spun from graphene oxide/water suspensions. The surface morphology of the GO fibers was not smooth; moreover, the surface roughness increases with increasing flake sizes. The voids with the fiber were formed during drying process and the average flake size governs the amount of voids as larger flakes increase voids within the GOFs.

## ACKNOWLEDGEMENTS

This study was supported by The Scientific and Technological Research Council of Turkey (TUBITAK) under grant no. MAG-214M650.

## REFERENCES

- Aboutalebi, S.H., Gudarzi, M.M., Zheng, Q.B., Kim, J.K., 2011, "Spontaneous Formation of Liquid Crystals in Ultralarge Graphene Oxide Dispersions", *Advanced Functional Materials*, Vol. 21, pp. 2978-2988.
- Allen, M.J., Tung, V.C., Kaner, R.B., 2010, "Honeycomb Carbon: A Review of Graphene", *Chemical Reviews*, Vol. 110, pp. 132-145.
- Arnold, M.S., Suntivich, J., Stupp, S.I., Hersam, M.C., 2008, "Hydrodynamic Characterization of Surfactant Encapsulated Carbon Nanotubes Using an Analytical Ultracentrifuge", *Acs Nano*, Vol. 2, pp. 2291-2300.
- Batista, C.A.S., Zheng, M., Khripin, C.Y., Tu, X.M., Fagan, J.A., 2014, "Rod Hydrodynamics and Length Distributions of Single-Wall Carbon Nanotubes Using Analytical Ultracentrifugation", *Langmuir*, Vol. 30, pp. 4895-4904.
- Bonaccorso, F., Zerbetto, M., Ferrari, A.C., Amendola, V., 2013, "Sorting Nanoparticles by Centrifugal Fields in Clean Media", *Journal of Physical Chemistry C*, Vol. 117, pp. 13217-13229.
- Chae, H.G., Kumar, S., 2008, "Materials science - Making Strong Fibers", *Science*, Vol. 319, pp. 908-909.
- Chen, H., Muller, M.B., Gilmore, K.J., Wallace, G.G., Li, D., 2008, "Mechanically Strong, Electrically Conductive, and Biocompatible Graphene Paper", *Advanced Materials*, Vol. 20, pp. 3557-+.
- Cheng, H.H., Dong, Z.L., Hu, C.G., Zhao, Y., Hu, Y., Qu, L.T., Chena, N., Dai, L.M., 2013, "Textile Electrodes Woven by Carbon Nanotube-Graphene Hybrid Fibers for Flexible Electrochemical Capacitors", *Nanoscale*, Vol. 5, pp. 3428-3434.
- Cong, H.P., Ren, X.C., Wang, P., Yu, S.H., 2012, "Wet-Spinning Assembly of Continuous, Neat, and Macroscopic Graphene Fibers", *Scientific Reports*, Vol. 2, pp.
- Dong, Z.L., Jiang, C.C., Cheng, H.H., Zhao, Y., Shi, G.Q., Jiang, L., Qu, L.T., 2012, "Facile Fabrication of Light, Flexible and Multifunctional Graphene Fibers", *Advanced Materials*, Vol. 24, pp. 1856-1861.
- Esmaili, A., Entezari, M.H., 2014, "Facile and Fast Synthesis of Graphene Oxide Nanosheets via Bath Ultrasonic Irradiation", *Journal of Colloid and Interface Science*, Vol. 432, pp. 19-25.
- Han, J.T., Jang, J.I., Kim, S.H., Jeong, S.Y., Jeong, H.J., Lee, G.W., 2013, "Size Sorting of Chemically Modified Graphene Nanoplatelets", *Carbon Letters*, Vol. 14, pp. 89-93.
- Khan, U., O'Neill, A., Porwal, H., May, P., Nawaz, K., Coleman, J.N., 2012, "Size selection of dispersed, exfoliated graphene flakes by controlled centrifugation", *Carbon*, Vol. 50, pp. 470-475.

- Li, X.M., Zhao, T.S., Chen, Q., Li, P.X., Wang, K.L., Zhong, M.L., Wei, J.Q., Wu, D.H., Wei, B.Q., Zhu, H.W., 2013, "Flexible All Solid-State Supercapacitors Based on Chemical Vapor Deposition Derived Graphene Fibers", *Physical Chemistry Chemical Physics*, Vol. 15, pp. 17752-17757.
- Özçakır, E., Ballı, B., Eskizeybek, V., 2016, "Fabrication of Macroscale Graphene Fibers via Wet Spinning", *Proceedings of ISER International Conference*, Vol. Barcelona, Spain, 16 May 2016, pp.
- Özçakır, E., Eskizeybek, V., 2016, "A Facile and Effective Method for Size Sorting of Large Flake Graphene Oxide ", *Proceedings of the World Congress on Recent Advances in Nanotechnology (RAN'16)*, Vol. Prague, Czech Republic – April 1 – 2, 2016, pp.
- Pan, S.Y., Aksay, I.A., 2011, "Factors Controlling the Size of Graphene Oxide Sheets Produced via the Graphite Oxide Route", *Acs Nano*, Vol. 5, pp. 4073-4083.
- Tirado, M.M., Martinez, C.L., Delatorre, J.G., 1984, "Comparison of Theories for the Translational and Rotational Diffusion-Coefficients of Rod-Like Macromolecules - Application to Short DNA Fragments", *Journal of Chemical Physics*, Vol. 81, pp. 2047-2052.
- Tong, X., Wang, H., Wang, G., Wan, L.J., Ren, Z.Y., Bai, J.T., Bai, J.B., 2011, "Controllable Synthesis of Graphene Sheets with Different Numbers of Layers and Effect of the Number of Graphene Layers on the Specific Capacity of Anode Material in Lithium-ion Batteries", *Journal of Solid State Chemistry*, Vol. 184, pp. 982-989.
- Walter, J., Nacken, T.J., Damm, C., Thajudeen, T., Eigler, S., Peukert, W., 2015, "Determination of the Lateral Dimension of Graphene Oxide Nanosheets Using Analytical Ultracentrifugation", *Small*, Vol. 11, pp. 814-825.
- Xiang, C.S., Young, C.C., Wang, X., Yan, Z., Hwang, C.C., Ceriotti, G., Lin, J., Kono, J., Pasquali, M., Tour, J.M., 2013, "Large Flake Graphene Oxide Fibers with Unconventional 100% Knot Efficiency and Highly Aligned Small Flake Graphene Oxide Fibers", *Advanced Materials*, Vol. 25, pp. 4592-4597.
- Xu, Z., Gao, C., 2011, "Graphene Chiral Liquid Crystals and Macroscopic Assembled Fibres", *Nature Communications*, Vol. 2, pp.
- Xu, Z., Gao, C., 2014, "Graphene in Macroscopic Order: Liquid Crystals and Wet-Spun Fibers", *Accounts of Chemical Research*, Vol. 47, pp. 1267-1276.
- Xu, Z., Liu, Z., Sun, H.Y., Gao, C., 2013, "Highly Electrically Conductive Ag-Doped Graphene Fibers as Stretchable Conductors", *Advanced Materials*, Vol. 25, pp. 3249-3253.
- Zhuo, Q.Q., Ma, Y.Y., Gao, J., Zhang, P.P., Xia, Y.J., Tian, Y.M., Sun, X.X., Zhong, J., Sun, X.H., 2013, "Facile Synthesis of Graphene/Metal Nanoparticle Composites via Self-Catalysis Reduction at Room Temperature", *Inorganic Chemistry*, Vol. 52, pp. 3141-3147.



## YENİ BİR YÜKSEK HIZLI KALP DESTEK POMPASININ SAYISAL VE DENEYSEL ANALİZİ

<sup>1</sup>Hasan ÇINAR, <sup>2</sup>Rafet YAPICI

<sup>1</sup>İskenderun Teknik Üniversitesi, Enerji Sistemleri Müh. Bl. İskenderun/ Hatay TÜRKİYE  
<sup>2</sup>Selçuk Üniversitesi, Mühendislik Fakültesi, Makine Müh. Bl. Selçuklu/Konya TÜRKİYE  
[hasan.cinar@iste.edu.tr](mailto:hasan.cinar@iste.edu.tr), [rafet@selcuk.edu.tr](mailto:rafet@selcuk.edu.tr)

(Geliş/Received:08.05.2017; Kabul/Accepted in Revised Form:12.07.2017 )

**ÖZ:** Sol ventriküler destek cihazları kalp yetmezliğine sahip hastalarda kullanılmaktadır. Rotodinamik kan pompalarının santrifüj, aksel ve karışık akışlı olmak üzere üç tipi vardır. Aksel akışlı kan pompaları yüksek hızlı fakat küçük çaplı pompalardır.

Bu çalışmada, tasarlanan karışık akışlı (yarı aksel) bir kan pompasının Hesaplamalı Akışkanlar Dinamiği (HAD) yazılımıyla pompa karakteristiklerinin belirlenmesi ve bu karakteristiklerin deneysel olarak doğrulaması yapıldı. Pompanın tasarım noktası için 10000 dev/dak dönme hızı, 5 L/dak debi ve 100 mm-Hg basınç farkı değerleri seçildi. Pompa çarkı ve difüzörünün tasarımında pompa tasarım ve katı modelleme programları kullanıldı. Belirtilen tasarım verilerine göre katı modeli oluşturulan pompanın ANSYS Fluent programı ile simülasyonu yapıldı ve ilk tasarım değerlerinin sağlanması yapıldı. Debiye bağlı olarak basınç farkı, tork, cidar kayma gerilmesi ve hidrolik verim HAD yoluyla hesaplandı. Ayrıca bu çalışmada pompa çarkını tahrik eden milin, emme hattında ve basma hattında olduğu durumlar için ayrı ayrı HAD yazılımı ile pompa performansı belirlendi. HAD ile optimizasyon çalışmalarından sonra çarkın ve difüzörün nihai katı modelleri oluşturuldu. Bu iki elemanın prototipi, lazer sinterleme teknolojisi ile üretildi. Pompa gövdesi alüminyum malzemenen CNC dik işlem merkezinde imal edildi. Prototip pompanın deneysel performansı, tasarım ve tasarım basınç farkını sağlayan dönme hızında, su ve hacimce %40 gliserin- %60 su kullanılarak belirlendi. Su için HAD ve deney sonuçları kullanılarak debi-basınç farkı eğrileri oluşturuldu ve tasarım noktasında başlangıç tasarım değerinden 8 torr eksik basınç verdiği belirlendi. HAD sonuçlarına göre; pompa çarkını tahrik eden milin emme hattında veya basma hattında olmasının basınç farkına ve akış çizgilerine etkisi olmadığı görüldü.

**Anahtar Kelimeler:** HAD, Kalp pompası, Karışık akışlı pompa, Sol ventriküler destek cihazı

### Numerical and Experimental Analysis of A New High-Speed Heart Assist Pump

**ABSTRACT:** Left Ventricular assist devices are used in patients with heart failure. There are three types of rotodynamic blood pumps: centrifugal, axial and mixed flow. Axial flow blood pumps have high speed but they have small diameter pumps.

In this study, Pump characteristics were determined with the Computational Fluid Dynamics (CFD) software of a designed mixed-flow (semi-axial) blood pump and pump characteristics were experimentally verified. For the design point of the pump, 10000 rpm rotation speed, 5 L/min flow rate and 100 mm-Hg pressure difference values were selected. Pump design and solid modeling programs were used in the design of the pump impeller and diffuser. The pump having a solid model according to design data specified was analyzed with the ANSYS Fluent and verification of the initial design values was made. Depending on the flow rate, the pressure difference, torque, wall shear stress and yield were calculated by CFD. In addition, the pump performance was determined by CFD software separately for the case where the pump is driven by the shaft, the suction line and the discharge line. After optimization study with CFD, the final solid models of the impeller and the diffuser were generated. The

prototypes of these two elements were produced by laser sintering technology. The pump casing was made from aluminum material at the CNC vertical machining center. The experimental performance of the prototype pump was determined by water and volume of 40% glycerin-60% water at the rotational speed providing design and design pressure difference. Flow-pressure difference curves were constituted using CFD and experimental outputs for water. It has been determined that the initial design value of the design point is less than 8 torr. According to CFD outputs; the presence of the shaft that drives the pump impeller on the suction line or the discharge line has no effect on the pressure difference and the flow line.

**Key Words:** *CFD, Heart pump, Mixed flow pumps, Left ventricular assist device (LVAD)*

## GİRİŞ (INTRODUCTION)

Kalp rahatsızlıkları içinde kalp yetmezliği önemli bir yer tutar. Kalp yetmezliğinde, kalp birçok sebepten kaynaklanabilecek bozukluklardan dolayı pompalaması gereken miktarda kanı vücuda pompalayamaz ve hastalık genellikle ölümlü sonuçlanır. Kalp yetmezliğinde en etkili tedavi yöntemi kalp transplantasyonudur (TX). Ancak uygun vericinin bulunamaması, bekleme süresinin uzun olması gibi sebeplerden dolayı TX her zaman mümkün olamamaktadır. Böyle durumlarda mekanik destek cihazları hayatidir. Mekanik destek cihazlarının amacı hastayı TX'e kadar yaşatmak ya da TX'in mümkün olmadığı hastalarda kalıcı tedavi sağlamaktır (Eğrican ve diğ., 2010). Türkiye'de 2014 yılına kadar kalp nakli bekleyen hasta sayısı 498'dir ve 2014 yılına kadar kalp nakli yapılan hasta sayısı 259'dur (Taneri, 2014). Bu sebeplerden dolayı mekanik destek cihazları üzerine çalışmalar insan hayatı açısından oldukça önemlidir. Genel olarak yapay kalp pompaları iki ana özelliğine göre sınıflandırılabilir. Akış tipine göre; pulslu pompalar, dönel (rotodinamik) pompalar, hacimsel (volumetrik) pompalar olarak sınıflandırılabilir (Kim ve diğ., 2012). Pompanın amacına göre; tamamen yapay kalp (TAH) veya bir ventriküler sisteme yardımcı (VAS) olarak sınıflandırılabilir (Kim ve diğ., 2012). Dönel sürekli akışlı kan pompaları; eksenel, santrifüj ve karışık akışlı olmak üzere üçe ayrılır. Dönel pompalarda bulunan çark mekanik enerjiyi akışkana aktarır. Dönel pompaların sınıflandırılması debi, dönme hızı ve basınç kullanılarak hesaplanan özgül hıza göre yapılır. Genellikle, santrifüj kan pompalarının dönme hızı 2000-4000 dev/dak'dır. Eksenel kan pompalarının hızı 6000-12000 dev/dak'dır.

Günümüze kadar çeşitli dönel kan pompaları geliştirilmiş ve klinik olarak kullanılmıştır (Burke ve diğ., 2001; Wood ve diğ., 2005). Bu cihazlar tamamen kalbin yerini almaz, sol ya da sağ karıncık ile paralel olarak çalışır (Chua ve Su, 2011). Mekanik destek cihazları uzun süreli kullanım için kompakt boyut, biyo-uyumlu ve dayanıklı olmalıdır (Kim ve diğ., 2012). Bunun yanında hemoliz ya da trombis gibi kan hasarı oluşturmamalıdır. Kalp pompası tasarımında karşılaşılan en büyük sorunlardan biri yüksek kayma gerilmeleri sonucu kan hücrelerinin deformasyona uğraması ve bunun sonucunda hemoliz meydana gelmesidir (Reul ve Akdis, 2000). Hemoliz oluşumunu önlemek için kalp pompası tasarımında pompa içindeki oluşan kayma gerilmelerinin en düşük seviyede kalmasına dikkat edilmelidir. Kan hücrelerinin dayanabileceği maksimum kayma gerilmesi için genel olarak 400 Pa seviyesindeki gerilmeler sınır olarak kabul edilmektedir (Lu ve diğ., 2001). Kan hücrelerinin hasarı açısından kayma gerilmesinin şiddetinin yanında maruz kalma süreside çok önemlidir (Yen ve diğ., 2014). Dönel kan pompaları içinde eksenel pompalar küçük boyut ve boru tipinde olmasından dolayı büyük ilgi uyandırmıştır. Ancak eksenel kan pompalarının yüksek dönme hızından dolayı kırmızı kan hücrelerine hasar verme riski yüksektir. Santrifüj pompalar kan hücrelerine daha az hasar vericidir ve daha güvenlidir (Leme ve diğ., 2013).

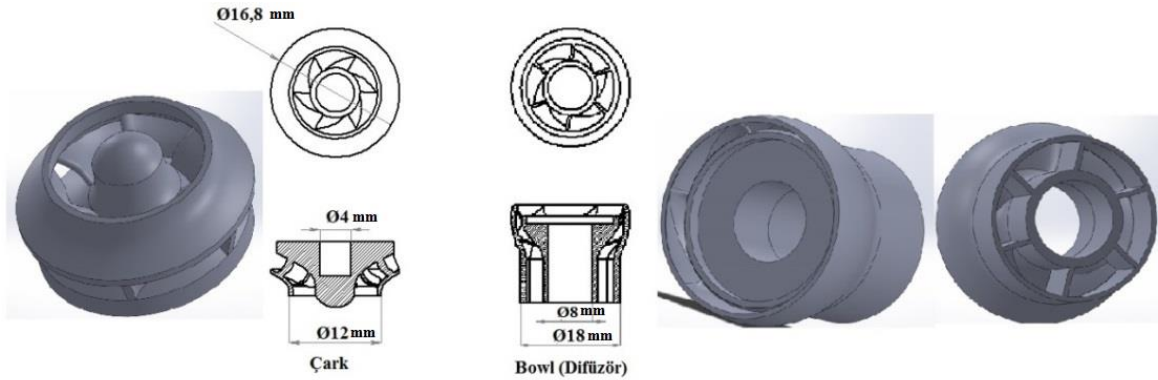
Bu çalışmada tasarlanan karışık akışlı kalp pompasının başlangıç tasarım değerleri 10000 dev/dak dönme hızı, 5 L/dak debi ve 100 mm-Hg basınç farkıdır. Yetişkin bir insan için istirahat halindeki nominal aortik basınç 100 mm-Hg pompa yükü ve nominal kan ihtiyacı 5 L/dak debidir (Behbahani ve diğ., 2009). Bu çalışmanın ana amacı, hazır pompa tasarım programları ile tasarlanan kalp destek pompası performansını sayısal ve deneysel olarak belirlemek ve sonuçları karşılaştırmaktır. Çalışmanın bir diğer amacı da milin çarkı emme tarafından ya da basma tarafından tahrik etme durumunun

pompanın basma yüksekliğine ve akış çizgilerine etkisinin olup olmadığının incelenmesidir. Kalp pompalarının tasarımları aşamasında hesaplamalı akışkanlar dinamiği metotları sayesinde karşılaşılabilecek olumsuzluklara karşı önlemler alınıp iyileştirmeler yapılabilmektedir. HAD, bize üretim öncesi pompanın hem hidrolik özelliklerini inceleme fırsatı hem de kan hasarı olup olmadığını inceleme fırsatı sunmaktadır. HAD çalışmaları ile pompanın akış çizgileri incelenmiş ve geri akış olup olmadığı gözlenmiştir. HAD verileri kullanılarak pompa hidrolik verimi hesaplanmış ve pompa performans eğrisi oluşturulmuştur.

## MATERYAL VE METOD (MATERIAL and METHOD)

### Geometrik Model (Geometric Model)

Bu çalışmada geometrik tasarım için ANSYS BladeGen, ANSYS Vista CPD ve Solidworks programları kullanıldı. Bir pompanın tasarımının yapılabilmesi için debi, devir ve manometrik basma yüksekliğinin bilinmesi yeterlidir. ANSYS programına başlangıç tasarım değerleri girilerek herhangi bir turbo makine tasarlanabilir. ANSYS programı kanat sayısı, kanat açısı, örtü tipi gibi çarkın tüm özelliklerinde değişiklik yapma olanağını bize sunar. ANSYS programı kalp pompaları gibi mini pompa elemanlarının oluşturulmasına olanak sağlamamaktadır bu sebeple bu çalışmada kullanılan çark ve difüzör olduğundan çok büyük olarak oluşturuldu ve daha sonra ölçeklendirme (benzerlik kuralları) ile uygun boyutlara indirildi. ANSYS programı ile oluşturulan çark ve difüzör Şekil 1’de görülmektedir. Çarkın geometrik düzenlemeleri, değişiklikleri ve montajı için Solidworks programı kullanıldı. Geometrik tasarım HAD çalışmaları ile eşzamanlı olarak yürütüldü ve toplam 15 denemeden sonra uygun çark ve difüzör tasarımı tamamlandı.



**Şekil 1.** Tamamlanan çark ve difüzör tasarımı

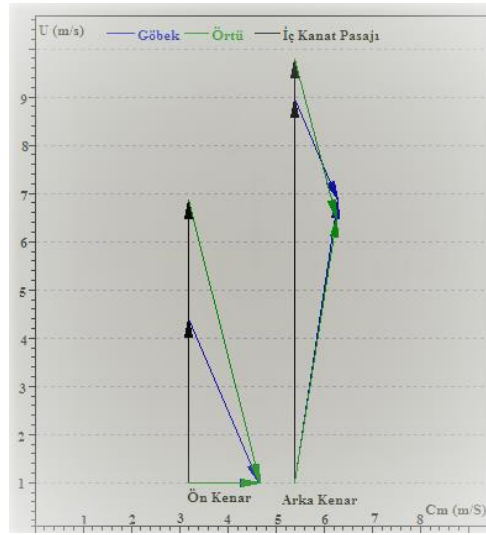
*Figure 1. Completed design of impeller and diffuser*

Pompa çarkı 11 mm emme (giriş) çapına ve 16 mm çark çapına sahiptir. Kanat sayısı 6 ve kanat profili 3 boyutludur. Çarkın örtü kalınlığı 0,6 mm’dir. Kanat kalınlığı 0,6 mm’dir. Kanat çıkış açısı 89 derecedir. Çarkın göbeğine akışın çarka düzgün bir şekilde (girdapsız) girmesi için Şekil 1’de görüldüğü gibi küçük bir kubbe verilmiştir. Pompa çarkına ait kanadın, göbek ve örtü arasındaki açılarının değişimi Şekil 2’de verilmiştir. Çark kanadına ait hız üçgenleri tasarım için kullanılan programdan alınarak, Şekil 3’de verilmiştir.

	$\beta_1^\circ$	$\beta_2^\circ$
1(Göbek)	53	85
2	46	86
3(Orta)	39	87
4	32	88
5(Örtü)	25	89

**Şekil 2.** Çark kanat açılarının örtü ile göbek arasındaki değişimi  
*Figure 2. The change of the impeller blade angle between the shroud and the hub*

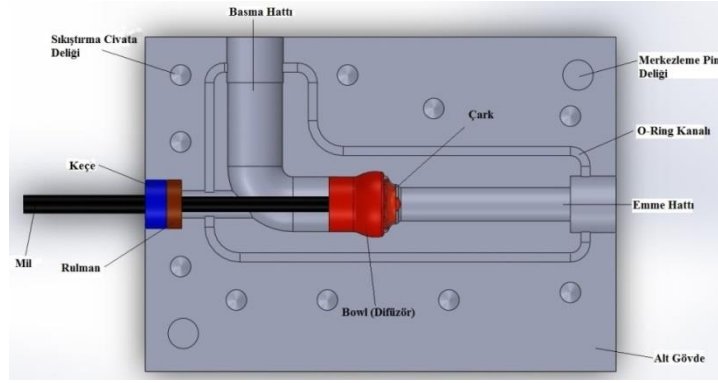
Çark tasarımı tamamlandıktan sonra bu çarka uygun difüzör tasarımı yapıldı. Difüzör tasarımı için yine ANSYS ve Solidworks programları kullanıldı. Pompa tasarımındaki ana amaçlardan birisi de pompa boyutlarının kompakt ve boru tipinde olması idi. Bu amacı karşılamak için Şekil 1’de görülen bowl (çanak tipi) difüzör tasarlandı. Bowl genellikle dikey türbin su pompalarında kullanılır.



**Şekil 3.** Çark kanadına ait hız üçgenleri  
*Figure 3. Speed triangles of the impeller blade*

Literatürde ki benzer radyal çarka sahip kan pompalarında, akışkan çarka eksenel yönde girip, radyal yönde (çarka göre) yâda radyal-eksenel karışımı olacak şekilde çıkmaktadır. Bu çalışmada tasarlanan pompada, akışkan çarka eksenel yönde girip bowl tipi difüzör sayesinde yine eksenel yönde çıkmaktadır. Bu özelliği ile tasarlanan pompa yeni bir tipte kan pompasıdır. Bowl’un amacı çarktan ayrılan akışkanın yönünü değiştirmek ve dönme eksenini boyunca akmasını sağlamaktır. Bowl, sürtünme kayıplarını arttırmamak için çok uzun olmamalıdır. Ancak akışın çevresel-eksenel yönünü sadece eksenel yöne dönüştürebilmesi için yeterli uzunlukta olmalıdır. Bowl tasarımı yapılırken bowl içindeki kayıplar en az seviyede tutularak Şekil 1’de görüldüğü gibi tasarım tamamlandı.

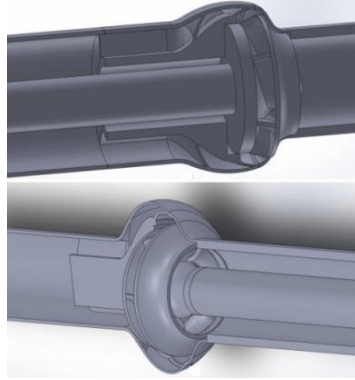
Çarkın ve difüzörün içinde çalışabileceği gövde Solidworks programında tasarlandı. Gövde ile birlikte diğer tüm elemanlar Şekil 4’de görülmektedir. Bu gövde kalıp şeklinde alt ve üst olmak üzere iki parçadan oluşturuldu. Gövdenin alt ve üst kısmı M8 civatalarla birbirine bağlandı. Deney sırasında sızdırmazlığı sağlamak için alt gövde üzerine O-ring kanalı açıldı. Mil boyunca sızdırmazlığı sağlamak için yaylı keçe kullanıldı.



**Şekil 4.** Çark, difüzör ve diğer elemanların montaj halı

*Figure 4. Assembly of impeller, diffuser and other elements*

Bu çalışmanın amaçlarından biri de pompa çarkını giriş kısmından ya da çıkış kısmından tahrik etmenin pompa performansına ve akış çizgisine etkisini incelemektir. Bu sebeple Şekil 5’de görüldüğü gibi iki farklı tasarım yapıldı ve HAD ile analiz edilerek hidrolik özelliklerin debiye göre değişimi gözlemlendi.

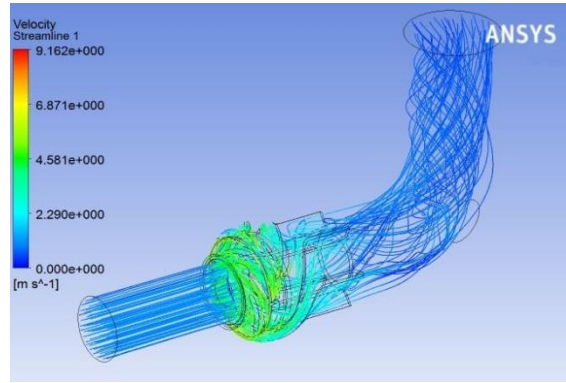


**Şekil 5.** Basma kısmından tahrikli tasarım ve emme kısmından tahrikli tasarım

*Figure 5. Two different designs according to drive location*

#### HAD Simülasyonu (CFD Simulation)

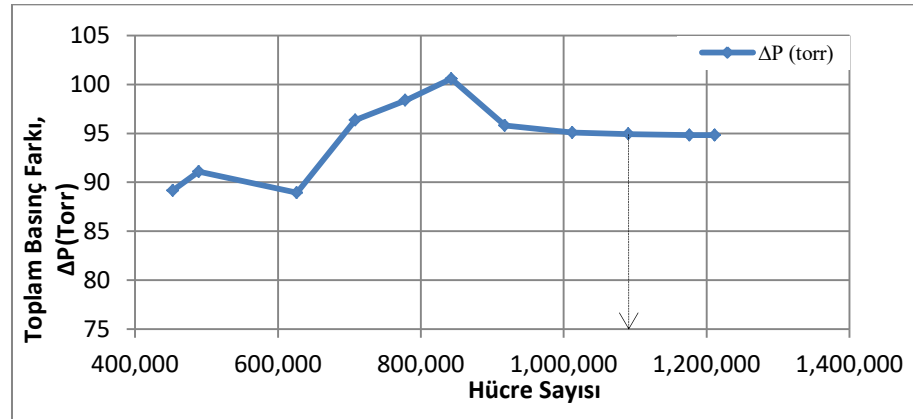
Bu çalışmada HAD analizi, pompanın hidrolik performansını iyileştirmek, akış yolu geometrisini iyileştirmek ve kayma gerilmesini azaltmak için etkili bir şekilde kullanıldı. HAD analizleri ticari paket programı ANSYS Fluent ile yürütüldü. HAD analizleri girişten tahrikli ve çıkıştan tahrikli iki sistem içinde aynı şartlar altında yapıldı. Her iki tasarım için tüm sonuçlar benzerlik gösterdi. Sonuçlar arasındaki farkın az olması ve tasarım kolaylığı açısından prototip üretimi için çıkıştan tahrikli tasarım seçildi. Seçilen tasarıma ait HAD ’den elde edilen akış çizgileri Şekil 6’da görülmektedir. HAD sonuçları incelendiğinde tasarımda geri akış görülmedi. HAD analizlerin de akışkan olarak su kullanıldı. Daha sonra Fluent programı içinde suyun özellikleri; yoğunluk  $1050 \text{ kg/m}^3$ , viskozite  $0,0035 \text{ Pa.s}$  olacak şekilde değiştirilerek HAD analizleri tekrarlandı. Suyun yoğunluğu ve viskozitesi bu şekilde değiştirilerek kana daha çok benzetildi (Untaroiu ve diğ., 2005; Gardiner ve diğ., 2007; Zhang ve diğ., 2007; Chua ve Su, 2011; Leme ve diğ., 2013). HAD çalışmaları sırasında Skewness ve Orthogonal Quality değerlerinin Fluent programının bulunduğu aralıkta kalmasına dikkat edildi.



Şekil 6. HAD 'den elde edilen akış çizgileri

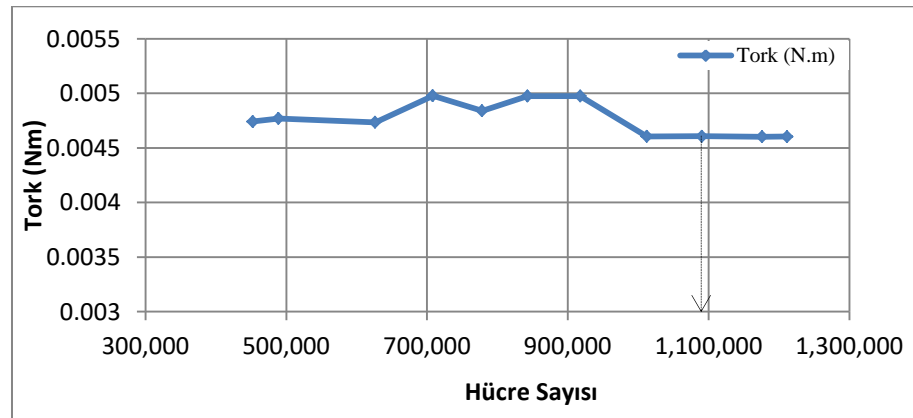
Figure 6. Flow lines obtained by CFD

HAD analizleri için pompa çarkı ve difüzörün içinde çalışacağı bir gövde modeli hazırlandı. Hazırlanan model için Fine 94 derecesinde çözüm ağı oluşturuldu. HAD çalışmalarındaki sonuçların çözüm ağı hücre sayısına bağlılığını tespit etmek için çözüm ağı bağımsızlık testi yapıldı. Bu testin sonuçları Şekil 7 ve Şekil 8'de verilmiştir. Bu testin sonucunda yaklaşık 1 milyon çözüm ağı hücre sayısından sonra basınç farkı ve tork değişiminin %1'in altına indiği görüldü ve diğer analizlerin 1090588 hücre sayısında yapılmasına karar verildi.



Şekil 7. Hücre sayısı ve basınç farkı arasındaki ilişki

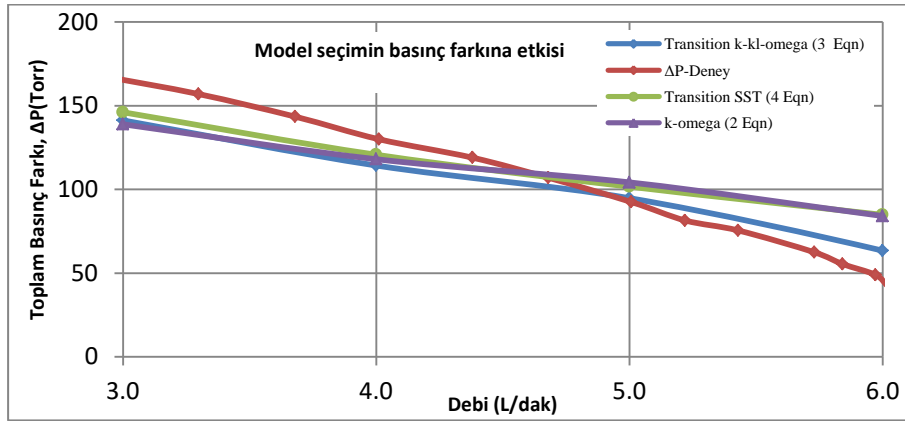
Figure 7. Relationship between cell number and pressure difference



Şekil 8. Hücre sayısı ve tork arasındaki ilişki

Figure 8. Relationship between cell number and torque

Akışın Reynolds sayısının tasarım noktasında 4000'den büyük olduğu ve tasarım noktasının altındaki debilerde 2300-4000 geçiş bölgesinde kaldığı gözlemlendi. ANSYS Fluent'te çözüm modeli olarak Transition k-kl-omega (3 eqn.) ve Transition SST (4 eqn.) modellerinin kullanılabilmesi öngörüldü (Fluent, 2009; Chua ve Su, 2011). Ancak yine de k-omega(2 Eqn), Transition k-kl-omega (3 Eqn) ve Transition SST(4 Eqn) olmak üzere üç model için çeşitli debilerde simülasyonlar yapıldı. Her üç model içinde sonuçlarda kararlılık olmadı ve yaklaşık aynı sonuçlar elde edildi. Transition k-kl-omega modeli ile yapılan çözümler daha hızlı sonuç verdi ve daha iyi yakınsadı. Ayrıca tasarım noktasının üstündeki debilerde, bu modelin sonuçlarının deneysel sonuçlara daha yakın olduğu görüldü. Bu sebeplerden dolayı diğer tüm analizlerde Transition k-kl-omega (3 eqn.) modeli kullanıldı. Türbülans model seçiminin sonuçlara etkisi Şekil 9'da verilmiştir.



Şekil 9. Türbülans model seçiminin toplam basınç farkı sonucuna etkisi

Figure 9. Effect of turbulence model selection on total pressure difference

Transition k-kl-omega modeli kullanılarak sabit 10000 dev/dak. dönme hızında 1-7 litre/dak. arasında 8 farklı noktada çözümler yapıldı. Çözücü tipi basınç temelli ve daimi olarak ayarlandı. Fluent çözücüsünde giriş şartları olarak 1-7 litre/dak. arasındaki debiler ve 10,5 mm hidrolik çap kullanıldı. Çıkış şartı olarak 100 torr basınç ve 10,5 mm hidrolik çap girildi. Yakınsama, 0,001 seviyelerine geldiğinde sonuçlarda kararlılık olduğu gözlemlendi. Çözüm yakınsama kriteri olarak daha güvenilir bir sonuç elde etmek amacıyla Fluent çözümlerinde; continuity, x-velocity, y-velocity, z-velocity, k, omega, intermit, retheta değerlerinin hepsi için 0,0001 derecesinde yakınsama kriteri kullanıldı. HAD sonuçlarını değerlendirmek için aşağıdaki denklemler kullanıldı.

Pompaya giriş ve çıkışta türbülans şiddetini tanımlamak için;

$$TI = 0,16 * Re^{-1/8} \quad (1)$$

bağıntısı kullanıldı.

Pompa performans eğrisi oluşturulmak için kullanılan parametrelerden:

Toplam basınç farkı;

$$\Delta P_t = P_{tç} - P_{tg} \quad (2)$$

Buradaki toplam basınç;

$$P_t = P + \rho * \frac{v^2}{2} \quad (3)$$

Pompa çarkının gücü;

$$N_{ç} = T * \omega \quad (4)$$

Akışkana aktarılan güç;

$$N_a = \Delta P_t * Q \quad (5)$$

Pompanın mil gücü;

$$N_m = N_{mot,yükte} - N_{mot,boşta} \quad (6)$$

Pompa hidrolik verimi;

$$\eta_h = \frac{\Delta P_t * Q}{N_c} = \frac{N_a}{N_c} \quad (7)$$

Pompa verimi;

$$\eta_p = \frac{N_a}{N_m} \quad (8)$$

Formülleriyle hesaplandı.

### Deneysel Yöntem (Experimental Method)

Deneyin ilk aşamasında akışkan olarak su kullanıldı. Sabit 10000 dev/dak dönme hızında 2-6,5 L/dak debi aralığında basınç vanası kısılarak 15 farklı noktada debi ölçümleri yapıldı. Deneyin ikinci aşamasında akışkan olarak kana daha çok benzetilmesi amacıyla hacimce %40 gliserin-%60 su çözeltisi (Untaroiu ve diğ., 2005) kullanıldı. Bu çözelti için de 2-5,5 L/dak debi aralığında 12 noktada ölçümler yapıldı.

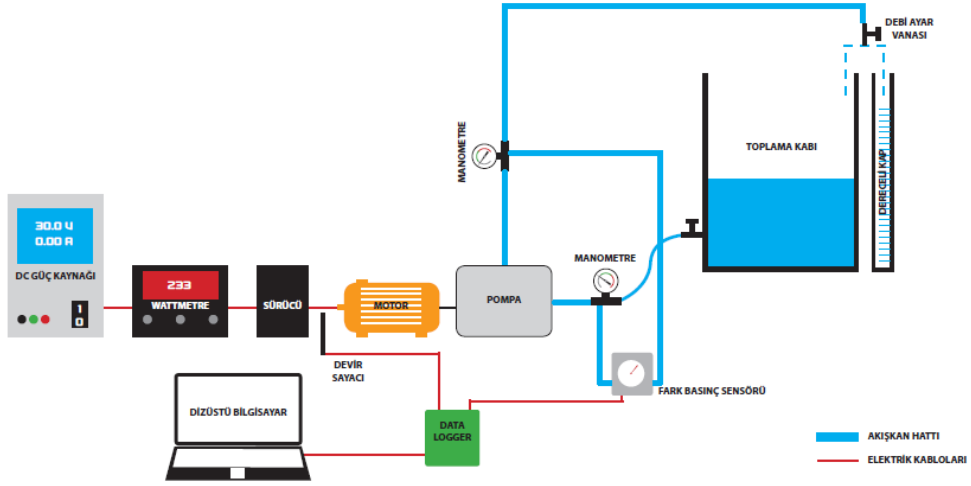
Pompa tasarım programı ile katı modeli oluşturulan pompa çarkı ve difüzör, lazer sinterleme teknolojisi ile Pa2200 (%100 naylon) malzemeden üretildi. Üretilen çark ve difüzörün fotoğrafı Şekil 10'da görülmektedir. Pompa çarkı ve difüzörün içinde çalışacağı pompa gövdesi alüminyum malzemeden CNC dik işlem merkeziyle üretildi. Pompa gövdesi kalıp mantığıyla iki farklı parça şeklinde imal edildi. Gövdenin iki kısmı arasındaki sızdırmazlığı sağlamak amacıyla gövdenin bir yarısına O-ring kanalı açıldı. Pompa mili paslanmaz çelik malzemeden CNC torna tezgâhında üretildi. Mil boyunda sızdırmazlığı sağlamak için 6X16X7 mm boyutunda yaylı döner mil keçesi kullanıldı. Milin yataklanması için kapaklı 625 rulmanı kullanıldı. Kurulan deney düzeneğinin şematik gösterimi Şekil 11'de verilmiştir.

Yaklaşık 12 litre hacme sahip ve atmosfere açık bir kap akışkan deposu olarak kullanıldı. Depodan pompa gövdesine girişi ve çıkışları için 10,5 mm çapında şeffaf ve esnek bir boru kullanıldı. Boşaltma hattının sonuna doğru debi ayarı yapmak için bir vana konuldu. Deneyde akışkanın debisini ölçmek için 20 ml hassasiyetli dereceli kap kullanıldı. Debi ölçümü sırasında akışkanın yönü değiştirilerek akışkan dereceli kaba yönlendirildi. Bir kronometre ile suyun alınma zamanı ve dereceli kapta biriken hacmi ölçülerek debi hesaplandı.

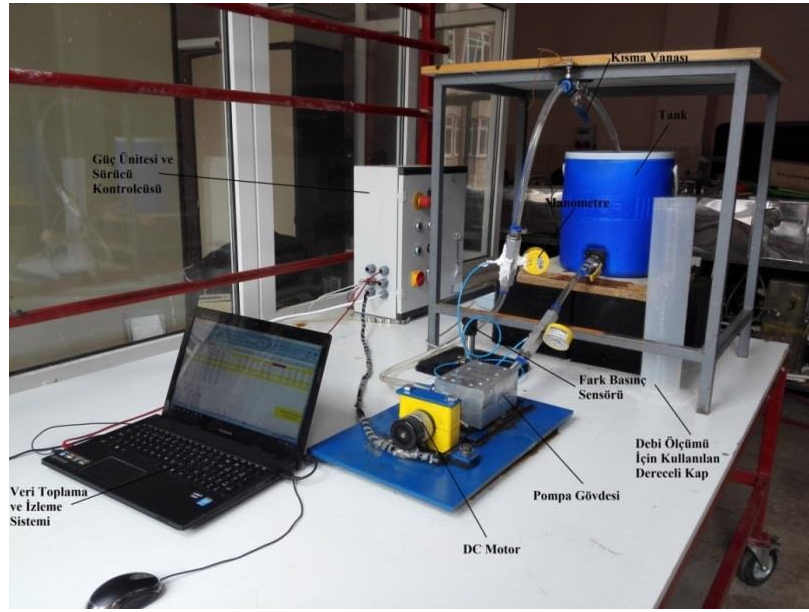
Motor dönme hızının ölçümü motor ile pompa milinin bağlantısı üzerine takılan endüktif proximity sensörüyle yapıldı. Motor devir sayacı olarak Sick IME1603 endüktif proximity sensör kullanıldı. Bu sensörün doğrulaması %0,05 ölçme hassasiyetine sahip Lutron DT2236 dijital foto takometre ile yapıldı. Deneyde güç ölçümü dijital göstergeli wattmetre ile yapıldı. Basınç ölçümlerini yapabilmek için emme ve basma hattına üzerlerinde 2 mm çapında delikler bulunan alüminyum bloklar imal edilip takıldı. Bu bloklara 2 mm çapında şeffaf ve esnek borular takılarak akışkan basınç sensörüne iletildi. Basınç ölçümü için %0,25 ölçüm hassasiyetine sahip Valcom 27D sensörü kullanıldı. Basınç ayarlanması emme ve basma hattına takılan iki adet manometre ile yapıldı. Deney setinin fotoğrafı Şekil 12'de görülmektedir.



Şekil 10. Lazer sinterleme teknolojisi ile üretilen çark ve difüzörün fotoğrafı  
 Figure 10. Photo of the impeller and diffuser produced by laser sintering technology



Şekil 11. Kurulan deney düzeneğinin şematik gösterimi  
 Figure 11. Schematic representation of the experimental setup

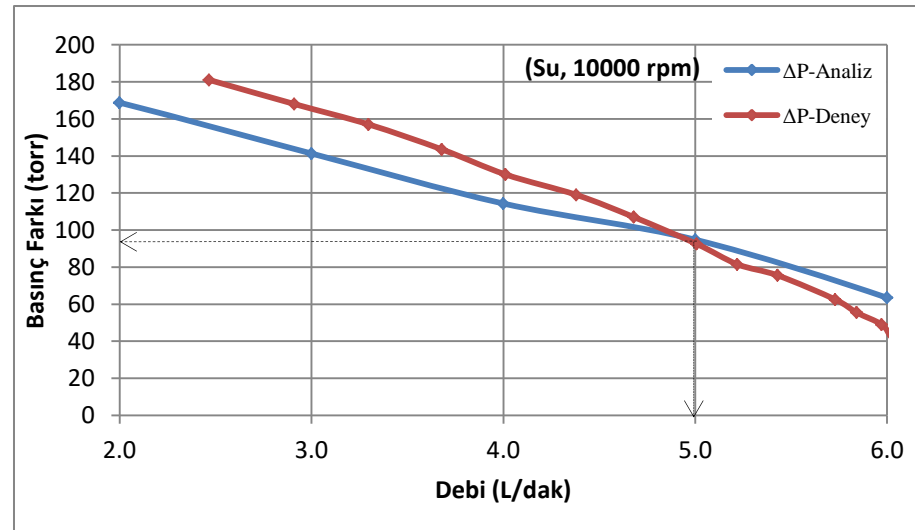


Şekil 12. Kurulan deney düzeneğinin fotoğrafı

Figure 12. Photo of the experimental setup

#### SAYISAL-DENEYSEL SONUÇLAR ve TARTIŞMA (NUMERICAL-EXPERIMENTAL RESULTS and DISCUSSION)

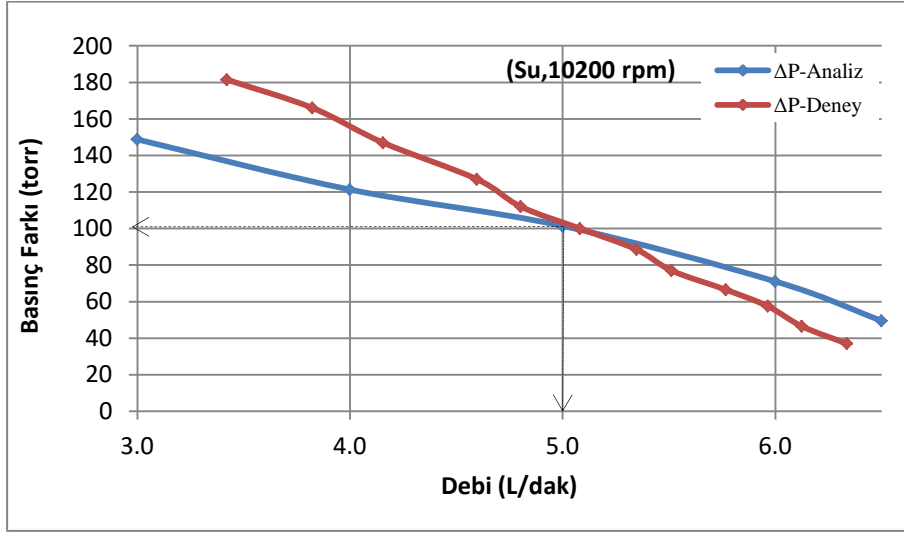
Akışkanın su olduğu durumdaki HAD ve deney basınç farklarının karşılaştırılması Şekil 13’de verilmiştir. Bu sonuçlardan görüldüğü üzere, tasarım debisi 5 L/dak ’da ve tasarım dönme hızı 10000 dev/dak ’da HAD simülasyonu ve deneyin ikisi için de 92 torr basınç farkı elde edilmiştir. HAD ve deney sonuçları arasında iyi bir uyum olduğu gözlenmiştir. Tasarım başlangıç değeri olan 100 torr basınç farkına hem HAD hem de deney için %8 sapma ile yani 92 torr basınç ile yaklaşılmıştır. Şekil 13’de görüldüğü üzere tasarım debisinden uzaklaştıkça HAD ve deney arasındaki fark artmaktadır.



Şekil 13. Su için 10000 dev/dak dönme hızında HAD ve deney basınç farkları karşılaştırılması

Figure 13. Comparison of CFD and test pressure differences for water at 10000 rpm rotation speed

Su için 10200 dev/dak dönme hızında 5 L/dak’lık tasarım debisinde 100 torr’luk tasarım basıncına ulaşılmıştır. 10200 devir/dakika dönme hızında HAD ve deney basınç farklarının karşılaştırılması Şekil 14’de görülmektedir.

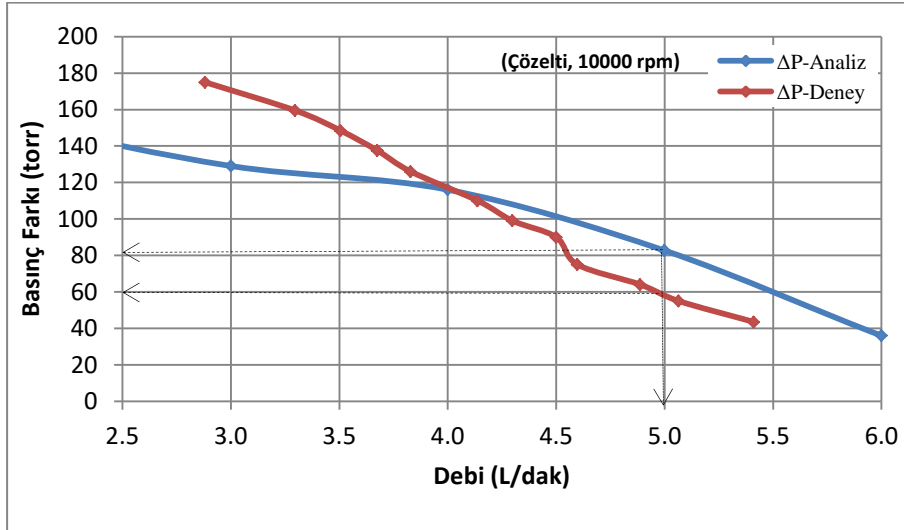


Şekil 14. Su için 10200 dev/dak dönme hızında HAD ve deney basınç farkları karşılaştırması

Figure 14. Comparing CFD and experimental pressure differences for water at a rotation speed of 10200rpm

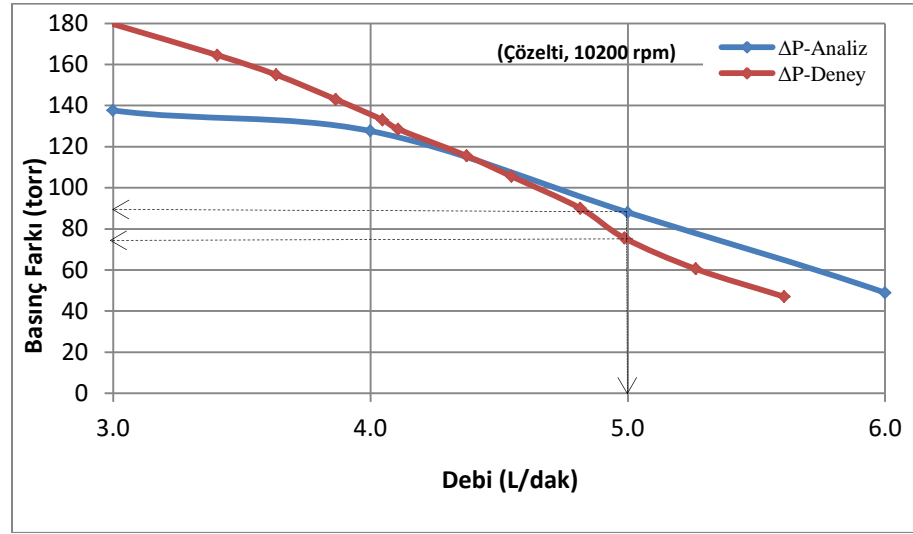
10200 dev/dak dönme hızında tasarım noktasından uzaklaştıkça HAD ve deney sonuçlarının birbirinden uzaklaştığı görülmektedir.

10000 dev/dak ve 10200 dev/dak dönme hızlarında su-gliserin çözeltisi için HAD ve deney basınç farkları karşılaştırmaları Şekil 15 ve Şekil 16'da verilmiştir. HAD 'de 10000 devir/dakika dönme hızında ve 5 L/dak debide çözelti için 80 torr basınç farkı elde edilmiştir. Deney 'de 10000 devir/dakika dönme hızında ve 5 L/dakika debide çözelti için 60 torr basınç farkı elde edilmiştir. HAD 'de 10200 devir/dakika dönme hızında ve 5 L/dakika debide çözelti için 89 torr basınç farkı elde edilmiştir. Deney 'de 10200 devir/dakika dönme hızında ve 5 L/dakika debide çözelti için 75 torr basınç farkı elde edilmiştir.



Şekil 15. Çözelti için 10000 dev/dak dönme hızında HAD ve deney basınç farkı karşılaştırması

Figure 15. Comparison of CFD and experimental pressure difference at 10000 rpm for solution



Şekil 16. Çözelti için 10200 dev/dak dönme hızında HAD ve deney basınç farkı karşılaştırması

Figure 16. Comparison of CFD and experimental pressure difference at 10200 rpm for solution

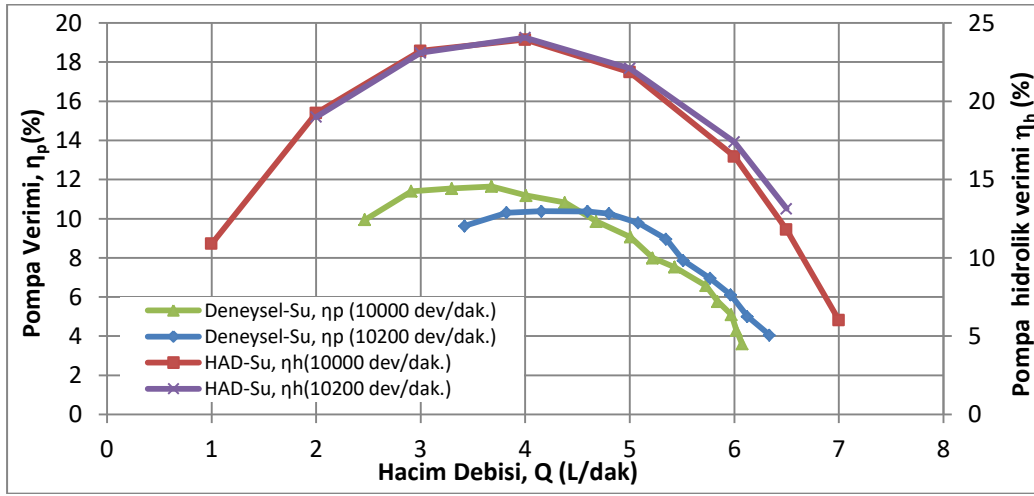
Su-gliserin çözeltisi deneyinde, 5 L/dak tasarım debisinde 100 torr'luk tasarım basıncına 10600 dev/dak dönme hızında ulaşılmıştır.

Bu çalışmada tasarım noktasının üstündeki debilerde deneysel sonuçlar HAD sonuçlarından yüksek çıkmıştır. HAD sonuçlarının deneysel sonuçlardan yüksek çıkması beklenebilir ancak bu her zaman böyle olmak zorunda değildir. Literatürde; Demir ve diğ. (2011), Hsu ve diğ. (2014), Chopski ve diğ. (2016) yapmış olduğu çalışmalarda da benzer durum ile karşılaşmıştır.

Tasarlanan pompanın tasarım noktasında su için HAD ve deney sonuçları birebir uyumuştur. Ancak tasarım noktasından uzaklaştıkça HAD ile deney sonuçları arasındaki fark artmıştır. Su için tasarım dönme hızında HAD ile deney sonuçları arasındaki maksimum sapma %13 olmuştur. Su-gliserin çözeltisi için tasarım dönme hızında ve tasarım debisinde HAD ile deney sonuçları arasında %25 sapma olmuştur ve maksimum sapma değeri %27 olmuştur. Sapma hesabı, sabit debide HAD ve deney sonuçları arasındaki farkın mutlak değeri alınıp, yüzde ye dönüştürülerek yapılmıştır. Akışkanın su-gliserin olduğu durumda sapma miktarının yüksek çıkmasının, pompanın tasarımının ve hesaplarının suya göre yapılmış olmasından kaynaklandığı düşünülmektedir. Bu çalışmada; deney sonuçları ile HAD sonuçları arasındaki fark su pompaları için yüksektir. Ancak literatürdeki kalp pompaları ile ilgili çalışmalar ile kıyaslandığı zaman makul değerler içinde kalmaktadır. Demir ve diğ. (2011) yapmış olduğu çalışmada, tasarım dönme hızında tasarım noktasında deney ve simülasyon arasında %9 sapma olmuştur ve maksimum sapma değeri %17 olmuştur (Akışkan olarak su kullanılmıştır). Aka ve diğ. (2014) yapmış olduğu çalışmada, tasarım noktasında ve tasarım dönme hızında HAD ile deney sonuçları arasında yaklaşık %14,5 sapma ve maksimum %18 sapma olduğu görülmüştür. Untaroiu ve diğ. (2005) yapmış olduğu kalp pompası tasarımında; 6000 dev/dak dönme hızında 5 L/dak debide deney ve simülasyon arasında yaklaşık %8,2 sapma olmuştur. Arvand ve diğ. (2004) yaptığı çalışmada; çark özelliklerine göre 3 farklı tasarım yapmışlardır (A, B ve C olmak üzere). Bu tasarımlardan A tasarımı için 5 L/dak ve 6000 dev/dak dönme hızında HAD ve deney arasındaki sapma % 15'dir. Aynı tasarım için 5 L/dak ve 7000 dev/dak dönme hızında deney ve HAD arasındaki sapma % 10,4'dür. B tasarımında 5 L/dak debi için 6000 dev/dak dönme hızında %9, 7000 dev/dak dönme hızında %6 ve 8000 dev/dak dönme hızında %3 sapma olmuştur. C tasarımında 5 L/dak debi için 7000 dev/dak dönme hızında %5 ve 6000 dev/dak dönme hızında %1 sapma olmuştur. Masuzawa ve diğ. (2009) yaptığı çalışmada 5 L/dak debi ve 1400 dev/dak dönme hızında HAD ve deney arasındaki sapma yaklaşık %14'dür.

10000 ve 10200 dev/dak 'da HAD simülasyonu ve deneysel olarak belirlenen verimler, su için Şekil 17 ve su-gliserin çözeltisi için Şekil 18'de hacim debisine bağlı olarak gösterilmiştir. Deneysel sonuçlara göre ifade edilen pompa verimi ( $\eta_p$ ); pompanın hidrolik, volumetrik ve mekanik verimlerini içermektedir. HAD simülasyonu sonuçlarına göre verilen ( $\eta_h$ ); pompanın sadece hidrolik verimini

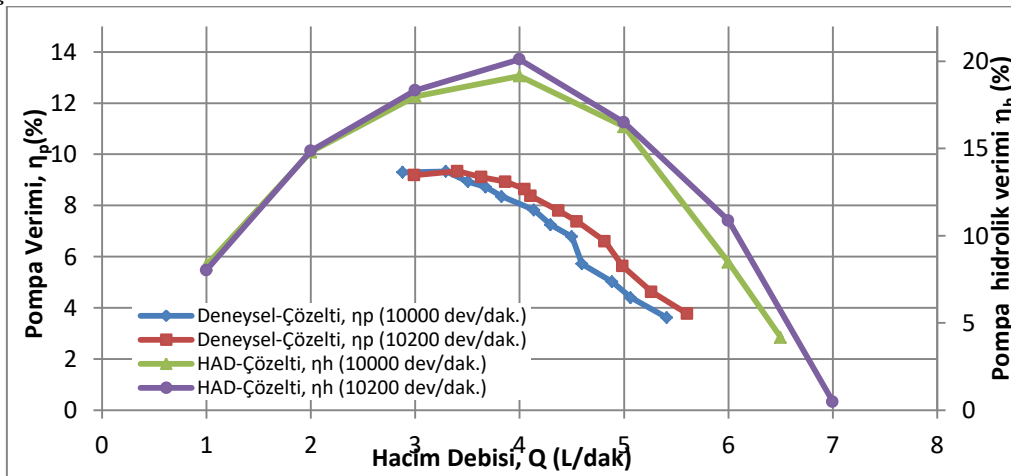
dikkate almaktadır. Bu yüzden verimler arasındaki fark çok büyüktür. HAD simülasyonu sonucuna göre her iki akışkan için de 4 L/dak debide hidrolik verim maksimum olmaktadır ve değeri % 19 ila 24 arasındadır. Bu verim büyük ölçekli pompalara göre çok küçüktür; ama bu tür mini pompalar için normal bir değerdir. Arvand ve diğ. (2004) tasarlamış oldukları 3 farklı A,B,C isimli çarklar için HAD yardımıyla sırasıyla %24, %31 ve %34 hidrolik verim elde etmişlerdir. Gardiner ve diğ. (2007) yapmış olduğu çalışmada HAD yoluyla hesaplanan pompa hidrolik verimleri çeşitli debiler için %10 ile %16 arasında değişmiştir. Gaddum ve diğ.(2012) farklı dönme hızlarına göre çeşitli tasarımlar yapmışlardır ve bu tasarımların deneysel verimleri %5 ile %40 arasında değişmiştir. Hsu ve diğ.(2014) yapmış olduğu çalışmada ise pompanın hem HAD yoluyla hesaplanan hidrolik verimi hem de deneysel yolla hesaplanan genel verimi % 1 ile %10 arasında değişmiştir. Literatürdeki kalp pompası ile ilgili çalışmaların hidrolik verimi genelde %15-%40 arasındadır. Bazı çalışmalarda bu değer %15'in altına indiği de görülmüştür.



Şekil 17. Su için HAD ve deney verimlerinin karşılaştırılması

Figure 17. Comparison of CFD and experimental efficiencies of water

Çok büyük ölçekli rotodinamik (çarklı) pompalarda verim % 85'in üzerinde olabilmektedir. Burada tasarım debisinde pompanın genel verimi su için %9-10 ve su-gliserin çözeltisi için yaklaşık %5 gibi çok küçük değerlere sahiptir. Bu verimler simülasyondaki verimlerle kıyaslandığında görülen büyük farklar, tasarlanan prototip yarı eksenel pompanın mekanik ve volumetrik verimlerinin iyileştirilmesi gerektiğine işaret etmektedir.



Şekil 18. Çözelti için HAD ve deney verimlerinin karşılaştırılması

Figure 18. Comparison of CFD and experimental efficiency for solution

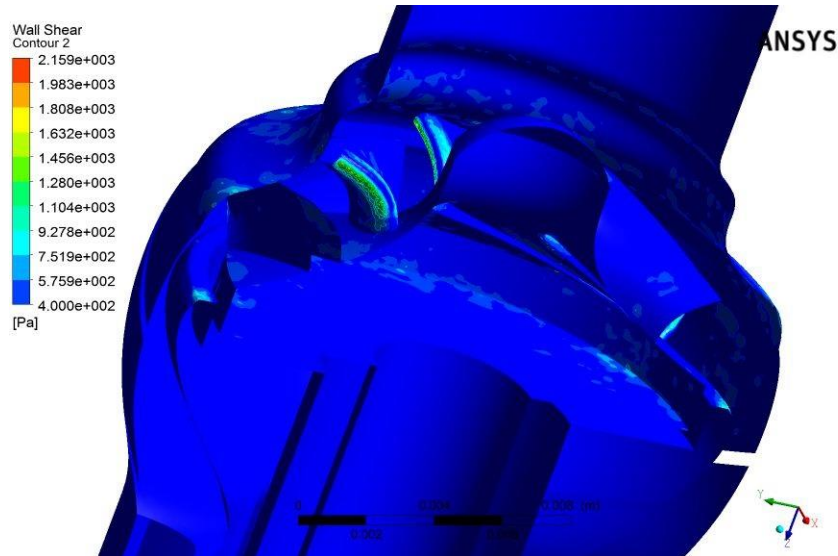
Akışkan olarak su kullanıldığı zaman pompa içinde meydana gelen kayma gerilmelerinin önemli olduğu bölgeler Şekil 19'da gösterilmiştir. Akışkan su olduğu zaman pompa içinde oluşacak en yüksek kayma gerilmesinin görüldüğü bölge olarak çark kanadının giriş kısmı ve difüzör kanadının giriş kısmı olarak belirlendi. Bu bölgelerde ki görülen en yüksek kayma gerilmesi değeri 1051 Pa'dır. Çark tabanı ile difüzör arasındaki boşluk 0,4 mm yapılarak bu bölgede oluşabilecek yüksek kayma gerilmesinin önüne geçildi. Bu boşluğun 0,3 mm'nin altında olduğu zaman kayma gerilmesinin 460 Pa'ın üzerinde olduğu görüldü.



Şekil 19. Su için HAD simülasyonu ile bulunan kayma gerilmeleri

Figure 19. Shear stresses found by CFD simulation for water

Su-gliserin çözeltisi için HAD simülasyonu ile belirlenen kayma gerilmeleri Şekil 20'de görülmektedir. Bu sonuçlara göre kayma gerilmesinin en büyük değeri 2159 Pa'dır. Bu değer görüldüğü bölge yine çark giriş ucu ve difüzör giriş kısmıdır. Pompa içinde oluşan kayma gerilmelerinin kan hücrelerine zarar verip vermeyeceğini söylemek için tek başına kayma gerilmesi değerinin şiddeti yeterli değildir aynı zamanda akışkanın kayma gerilmesine maruz kalma süresinin de hesap ve analiz edilmesi gereklidir (Yen ve diğ., 2014).



Şekil 20. Su-Gliserin çözeltisi için HAD simülasyonu ile bulunan kayma gerilmeleri

Figure 20. Shear stresses of water-glycerin solution found by CFD simulation

## ARAŞTIRMA SONUÇLARI (RESEARCH RESULTS)

Bu çalışmada özgün tasarıma sahip olan yeni bir tipte yarı eksenel kalp destek pompası tasarlanmış, HAD simülasyonu ile performansı belirlenmiş, görülen eksiklere göre katı modeli modifiye edilerek onun prototipi üretilmiştir. Üretilen bu mini pompanın, daha önce kurulan kalp destek pompası test ünitesinde deneysel performansı belirlenmiştir. Başlangıç tasarım değerlerine göre tasarımı yapılan ve prototipi üretilen pompadan ilk olarak beklenen özellik, HAD ve deney çalışmaları ile başlangıç tasarım değerlerinin doğrulamasının yapılabilmesiydi. Su için yapılan HAD ve deneysel çalışmaların ikisinde de tasarım noktasında 92 torr basınç farkı (tasarım basıncından 8 torr eksik) elde edildiği görülmüştür. Tasarım basıncı olan 100 torr'a 10200 dev/dak da ulaşılabilmektedir. Su için tasarım noktasında HAD ve deney sonuçları birebir uyumuştur ancak tasarım noktasından uzaklaştıkça HAD ve deney sonuçları arasındaki fark artmıştır. Su-gliserin çözeltisi için HAD ile deneysel sonuçlar arasındaki fark suya göre daha yüksektir. Bu farkın sebebinin pompa tasarımının suya göre yapılmış olmasından kaynaklandığı düşünülmektedir.

Pompa içindeki kayma gerilmelerinin dağılımına baktığımız zaman; çark kanadının giriş kısmı, difüzör kanadının giriş kısmı gibi bazı bölgelerde çok yüksek değerlere çıktığı, diğer bölgelerde ise bunlara göre çok daha düşük seviyelerde olduğu görülmektedir. Pompa içinde oluşan kayma gerilmelerinin kan hücrelerine zarar verip vermeyeceğini tek başına kayma gerilmelerinin büyüklüğüne bakılarak söylenemez. Pompa içindeki kanın hemolize uğrayıp uğramayacağı konusunda akışkanın kayma gerilmesine maruz kalma süresinde çok önemlidir. Akışkanın kayma gerilmesine maruz kalma süresinin hesabı ve analizi bu çalışmanın konusu değildir. Kayma gerilmelerini azaltma ve akışkanın maruz kalma süresiyle birlikte değerlendirilmesi başlı başına farklı bir konudur. Bu çalışmada, bir ön fikir oluşturması bakımından HAD den elde edilen kayma gerilme sonuçları verilmiştir. Bu konu üzerine iyileştirmeler gelecek çalışmaların konusu olarak planlanmaktadır.

Bu çalışmada tasarlanan pompanın HAD yoluyla hesaplanan hidrolik verimi literatürdeki pompalar ile kıyaslandığında makul değerler içindedir ancak hidrolik verim ile genel pompa verimi arasındaki fark büyüktür. Bu farkın deney setindeki mekanik sürtünmeler ve küçük sızıntı kaçaklarının ve prototiplerin yüzey pürüzlülüğünün sebep olduğu düşünülmektedir. Aynı tasarım üzerinden verim arttırmak için çalışmalar devam etmektedir. Normal su pompalarına göre kalp pompalarının verimi çok düşüktür. Kalp pompalarının verimden ziyade istenen basıncı ve debiyi sağlaması daha önceliklidir.

Bundan sonraki çalışmalarda aynı tasarım üzerinden çalışmalara devam ederek; monoblok tasarım, manyetik yataklama, kayma gerilmelerinin düşürülmesi ve akışkanın bu gerilmelere maruz kalma süresinin hesabı, pompa performans iyileştirmeleri gibi konular üzerine olacaktır.

## TEŞEKKÜRLER (ACKNOWLEDGEMENT)

Bu çalışma Selçuk Üniversitesi BAP Koordinatörlüğü tarafından 16201105 numaralı proje kapsamında desteklenmiştir.

## SEMBOLLER (NOTATION)

- $N_a$ : Güç (Akışkan)
- $N_m$ : Güç (Mil)
- $N_c$ : Güç (Çark)
- $N_{mot,y}$ : Yükteki motor gücü
- $N_{mot,b}$ : Boştaki motor gücü
- $n$ : Devir (dev/dak)
- $\eta$ : Verim
- $P$ : Basınç (Torr)
- $\Delta P$ : Toplam basınç farkı (Torr)
- $Re$ : Reynolds sayısı

T: Tork (Nm)  
 TI: Türbülans şiddeti  
 Q: Debi (L/dak)  
 $\omega$ : Açısal hız  
 U:Çevresel Hız (m/s)  
 C<sub>m</sub>:Meridyenel Hız (m/s)

## İNDİSLER (INDICES)

a: Akışkan  
 b: Boşta  
 ç: Çıkış  
 g: Giriş  
 h: Hidrolik  
 m: Mil  
 p: Pompa

## KAYNAKLAR (RESOURCES)

- Arvand, A., Hahn, N., Hormes, M., Akdis, M., Martin, M., Reul, H., 2004, "Comparison of Hydraulic and Hemolytic Properties of Different Impeller Designs of an Implantable Rotary Blood Pump by Computational Fluid Dynamics", *Artificial Organs*, Vol. 28 (10), pp. 892-898.
- Behbahani, M., Behr, M., Hormes, M., Steinseifer, U., Arora, D., Coronado, O., Pasquali, M., 2009, "A Review of Computational Fluid Dynamics Analysis of Blood Pumps", *European Journal of Applied Mathematics*, Vol. 20 (04), pp. 363-397.
- Burke, D. J., Burke, E., Parsaie, F., Poirier, V., Butler, K., Thomas, D., Taylor, L., Maher, T., 2001, "The HeartMate II: Design and Development of a Fully Sealed Axial Flow Left Ventricular Assist System", *Artificial Organs*, Vol. 25 (5), pp. 380-385.
- Chopski, S. G., Fox, C. S., Riddle, M. L., McKenna, K. L., Patel, J. P., Rozolis, J. T., Throckmorton, A. L., 2016, "Pressure-Flow Experimental Performance of New Intravascular Blood Pump Designs for Fontan Patients", *Artificial Organs*, Vol. 40 (3), pp. 233-242.
- Chua, L. P., Su, B., 2011, "Numerical Study on The Impeller of an Axial Flow Blood Pump", 2011 4th International Conference on Biomedical Engineering and Informatics (BMEI), 1153-1156.
- Demir, O., Biyikli, E., Lazoglu, I., Kucukaksu, S., 2011, "Design of a Centrifugal Blood Pump: Heart Turcica Centrifugal", *Artificial Organs*, Vol. 35 (7), pp. 720-725.
- Fluent, A., 2009, 12.0 Theory Guide, Ansys Inc, 5.
- Gaddum, N. R., Fraser, J. F., Timms, D. L., 2012, "Increasing the Transmitted Flow Pulse in a Rotary Left Ventricular Assist Device", *Artificial Organs*, Vol. 36 (10), pp. 859-867.
- Gardiner, J. M., Wu, J., Noh, M. D., Antaki, J. F., Snyder, T. A., Paden, D. B., Paden, B. E., 2007, "Thermal Analysis of the PediaFlow Pediatric Ventricular Assist Device", *ASAIO Journal*, Vol. 53 (1), pp. 65-73.
- Hsu, P.-L., Graefe, R., Boehning, F., Wu, C., Parker, J., Autschbach, R., Schmitz-Rode, T., Steinseifer, U., 2014, "Hydraulic and Hemodynamic Performance of a Minimally Invasive Intra-Arterial Right Ventricular Assist Device", *The International Journal of Artificial Organs*, Vol. 37 (9), pp. 697-705.
- Aka, İ.B., Dadgar, S., Sezer, M.E., Kadipaşaoğlu, A.K., "Bir Eksenel Akışlı Sol Ventrikül Destek Pompasının (SVDP) Fiziki Performans Testleri İçin Platform Tasarımı" , 14. Tıp Teknolojileri Ulusal Kongresi, Kapadokya, Nevşehir, 25-27 Eylül 2014.
- Kim, S. H., Hashi, S., Ishiyama, K., 2012, "Actuation of Novel Blood Pump by Direct Application of Rotating Magnetic Field", *IEEE Transactions on Magnetics*, Vol. 48 (5), pp. 1869-1874.

- Leme, J., da Silva, C., Fonseca, J., da Silva, B. U., Uebelhart, B., Biscegli, J. F., Andrade, A., 2013, "Centrifugal Blood Pump for Temporary Ventricular Assist Devices With Low Priming and Ceramic Bearings", *Artificial Organs*, Vol. 37 (11), pp. 942-945.
- Lu, P., Lai, H. ve Liu, J., 2001, A Reevaluation and Discussion on The Threshold Limit for Hemolysis in a Turbulent Shear Flow, *Journal of Biomechanics*, Vol. 34 (10), pp. 1361-1364.
- Masuzawa, T., Ohta, A., Tanaka, N., Qian, Y., Tsukiya, T., 2009, "Estimation of Changes in Dynamic Hydraulic Force in a Magnetically Suspended Centrifugal Blood Pump with Transient Computational Fluid Dynamics Analysis", *Journal of Artificial Organs*, Vol. 12 (3), pp. 150-159.
- Eğrican, N., Küçükaksu S., Akgün M., Lazoğlu İ., Ciblak N., An E., Sorgüven E., Şafark K., Okyar F., Uçak C., Şehirlioğlu M., 2010, *Minyatür Bir Yapay Kalp Pompa Sisteminin Tasarımı, Analizi ve Prototip Üretimi*, Tübitak Projesi, Proje No:106M309, İstanbul
- Reul, H. M., Akdis, M., 2000, "Blood Pumps for Circulatory Support, Perfusion", Vol. 15 (4), pp. 295-311.
- Taneri, D. B., 2014, "Acil Serviste Acil Tıp Hekimlerinin Organ Bağışı Sürecinde Yönetim, Duyarlılık ve Farkındalıkları", *Başkent Üniversitesi Tıp Fakültesi Acil Tıp Anabilim Dalı*, Ankara, 20-25.
- Untaroiu, A., Wood, H. G., Allaire, P. E., Throckmorton, A. L., Day, S., Patel, S. M., Ellman, P., Tribble, C., Olsen, D. B., 2005, "Computational Design and Experimental Testing of a Novel Axial Flow LVAD", *ASAIO Journal*, Vol. 51 (6), pp. 702-710.
- Wood, H. G., Throckmorton, A. L., Untaroiu, A., Song, X., 2005, "The Medical Physics of Ventricular Assist Devices, Reports on Progress in Physics", Vol. 68 (3), pp. 545-576.
- Yen, J. H., Chen, S. F., Chern, M. K., Lu, P. C., 2014, "The Effect of Turbulent Viscous Shear Stress on Red Blood Cell Hemolysis", *The Japanese Society for Artificial Organs*, Vol. 17 (2), pp.178-185.
- Zhang, Y., Xue, S., Gui, X.-m., Sun, H.-s., Zhang, H., Zhu, X.-d., Hu, S.-S., 2007, "A Novel Integrated Rotor of Axial Blood Flow Pump Designed With Computational Fluid Dynamics", *Artificial Organs*, Vol. 31 (7), pp. 580-585.

## INFLUENCE OF VACUUM APPLICATION ON THE TRIBOLOGICAL PROPERTIES OF PORCELAIN WASTE REINFORCED EPOXY COMPOSITES

<sup>1</sup>Nurcan Calis ACIKBAS, <sup>2</sup>Bilge YAMAN, <sup>3</sup>Gokhan ACIKBAS

<sup>1</sup>Bilecik Seyh Edebali University, Engineering Faculty, Dept. of Metallurgical and Materials Engineering,  
Gulube Campus, TR-11210 Bilecik, TURKEY

<sup>2</sup>Eskisehir Osmangazi University, Engineering Faculty, Dept. of Metallurgical and Materials Engineering,  
Meselik Campus, TR-26480, Eskisehir, TURKEY

<sup>3</sup>Bilecik Seyh Edebali University, Vocational School, Metallurgy Program, Gulube Campus, TR-11210 Bilecik,  
TURKEY

<sup>1</sup>nurcan.acikbas@bilecik.edu.tr, <sup>2</sup>byaman@ogu.edu.tr, <sup>3</sup>gokhan.acikbas@bilecik.edu.tr

(Geliş/Received: 29.06.2017; Kabul/Accepted in Revised Form: 28.07.2017)

**ABSTRACT:** This study evaluates the effect of employment of vacuum application on the mechanical and tribological properties of porcelain waste added epoxy matrix composites. Tribological characterization was determined by friction, wear rate and mechanisms using ball-on-disk test by tungsten carbide counter-part without lubrication at room temperature. It is investigated the role of vacuum application on the wear mechanisms, tribo-chemical layer formation on the wear surfaces, frictional property and tribological performance. The microstructure, mechanical and physical properties and wear behavior correlation were discussed comprehensively. Vacuum application provided fully embedded and well wetted particles, and strong bonding strength between matrix and filler. It is demonstrated that well bonded particle reinforced composites have higher wear resistance, by resulting lower friction coefficient, and more smoother tribochemical layer than compared with the unvacuumed composites.

**Key Words:** Epoxy matrix composite, Friction, Porcelain waste, Wear, Wear mechanisms

### Porselen Atık Takviyeli Epoksi Kompozitlerinin Tribolojik Özelliklerine Vakum Uygulamasının Etkisi

**ÖZ:** Bu çalışma, vakum uygulamasının atık porselen katkılı epoksi matrisli kompozit malzemelerin mekanik ve tribolojik özelliklerine etkisini değerlendirmektedir. Tribolojik karakterizasyon; tungsten karbür aşındırıcı bilye kullanılarak oda sıcaklığında yağlayıcı olmadan bilye-disk (ball-on-disk) konfigürasyonunda triboloji testleri gerçekleştirilerek sürtünme, aşınma oranları ve aşınma davranışları belirlenmiştir. Vakum uygulamasının; aşınma mekanizmaları, aşınma yüzeylerinde tribo-kimyasal tabaka oluşumu, sürtünme özellikleri ve tribolojik performans üzerindeki rolü araştırılmıştır. Mikroyapı, mekanik ve fiziksel özellikler ile aşınma davranışı ilişkisi ayrıntılı incelenmiştir. Vakum uygulaması partiküllerin daha iyi ıslatılmasına, matris ve partikül arasında daha kuvvetli bağ mukavemeti oluşmasına sebebiyet vermiştir. Vakum uygulamasıyla üretilmiş kompozitler, vakumsuz üretilmiş kompozitlere göre daha düşük sürtünme katsayısı ve daha düzgün tribokimyasal tabakanın oluşmasına sebebiyet vererek daha iyi aşınma dayanımı sergilemişlerdir.

**Anahtar Kelimeler:** Epoksi matrisli kompozit, Aşınma, Porselen atığı, Sürtünme, Aşınma mekanizmaları

## INTRODUCTION

Neat epoxies have excellent chemical resistance and adhesion, light weight, low shrinkage, low friction coefficient and self-lubrication capacity which properties demand in tribological applications (Kumar et al., 2015; Gill and Sidhu, 2016). On the other hand, they have generally low strength and stiffness and high wear loss in comparison with ceramics and metal counterparts. The most important limitation of their usage in demanding tribological applications is their tendency to degrade under different contact conditions, especially corresponding to sliding abrasion and impact erosion (Bobby and Samad, 2016). Various researchers have been studied improvement of tribological properties of the neat epoxies by adding one or more fillers (Srinivasa and Bhagyashekar, 2014; Baptista et. al, 2016; Qi et. al, 2016; Alajmi and Shalwan, 2015; Raju et. al, 2013; Basavarajappa et. al, 2009). Therefore in order to balance between good mechanical properties, low friction and low wear loses there is a need for using polymer matrix composites. For decade's different kinds of waste materials such as metallurgical slag, waste glass, waste rubber, ceramic wastes, gypsum-fiber like that has been successfully used as filler in polymer matrix composites (Acikbas et. al, 2017; Calis Acikbas and Acikbas, 2017; Acikbas et. al, 2014a; Acikbas et. al, 2014b; Katz and Mileski, 1987; Koleva et al., 2011; Alok and Amar, 2008; Pervaiz et. al, 2010; Acikbas and Göçmez, 2015; Acikbas and Göçmez, 2016a; Acikbas and Göçmez, 2016b; Acikbas and Göçmez, 2016c; Katz and Mileski, 1987). The usage of waste material both lessen production cost and eliminate environmental pollution and turn waste materials to value added product.

Tribology basically branch of science and technology investigating friction, wear and lubrication issues. These phenomena result in energy losses and machine break downs, and are of significant economic importance (Bhushan, 2000). It is estimated that approximately one third of the world's energy resources in present use are consumed in overcoming different kinds of friction and wear. Tribology is extrinsic material property which depends on many systems parameters. But some material properties such as microstructure, toughness, hardness, strength, thermal conductivity, chemical resistance, etc., effect the tribological behavior of materials (Myshkin et. al, 2005; Shi et al., 2004; Suresha et. al, 2006; Vasconcelos et. al, 2006; Yaman and Mandal, 2014; Mallik et. al, 2011; Kumar et. al, 2009; Kumar Mallik et. al, 2012).

Epoxy matrix composites have advantageous over metal counter parts in respect of lower density, less need for maintenance and also lower cost. Even though, higher mechanical strength can be obtained by addition of fillers in epoxy composite, there is also importance of cost reduction in manufacturing of these composites in terms of expensive ceramic and metal fillers. It is well-known that the recycling of industrial waste materials is in great interest for sustainable manufacture regarding economical and effective usage with the ecological environment. Recycling or reuse of waste materials provides preserving the natural resources, saving energy and reduction in material and production costs, etc. From this perspective, waste management strategies, selection of suitable waste filler amongst large amounts of alternative materials, and determination of the proper ratio of suitable filler addition become important issues in the fabrication of waste reinforced composites, recently (Cubeta, 2013).

The size of the world ceramic tableware and ornaments sector is approximately 15 billion \$ (Seramik Çalışma Raporu, 2015). During porcelain production the defective products sour to the range of 3 to 10 %. This waste quantity is quite high and it should be reevaluated. Usage of these kinds of waste materials in composite production provides enhanced tribological properties and allows recycling of wastes. The major advantageous of porcelain waste as a reinforcement phase are hardness and strength. Even though porcelain reinforced epoxy composites compared to metals and ceramics have many advantages such as cost-efficiency, easy preparation, self lubrication and so on, there is still insufficient knowledge on the tribology of porcelain added epoxy matrix composite materials.

In addition, porcelain added epoxy based materials becomes a promising alternative material for metallic and ceramics used in biomedicine. The bionic research related to tribology of polymer based composites used in biomedicine has been started and it will need a long time to realize considerable progress (E, 2015). The epoxy requirement for the biomedical applications varies markedly according to

the application being considered (Garcia et al., 2009). Epoxy composite materials can be applied in direct or indirect clinical restorations and used to fabricate dental core and post systems and dental brackets (Tai et al., 2015). It is well-known that wear and hardness are important factors in materials used in dentistry and the wear mechanism is affected by different filler loads and resin matrix (Sagsoz et al., 2014). Hence, it is important to develop good biocompatibility, low cost, low friction and wear, and low creep deformation epoxy based composites to adapt the increasing demand of biomedicine.

The objective of this study, production of high performance composites with addition of porcelain wastes as filler as well as reduces its cost; diminish environmental pollution and enhancing mechanical and tribological properties. Therefore in order to provide a good balance among mechanical properties and cost, 50 and 60 wt%. filler content were studied. And also process ability of resin-filler mixture as taken in consideration for selecting these filler ratios. The microstructure, mechanical, physical properties and tribological behavior relationship was discussed of developed epoxy matrix composites.

## MATERIAL AND METHOD

Polymer epoxy resin (EpoxAcast690) and hardener was provided from Smoth-on Limited, Canada. EpoxAcast® 690 is a UV resistant clear casting epoxy which can be used applications requiring a rigid, clear finished product. Castings cure with negligible shrinkage and are very hard and strong. Epoxy resin and hardener ratio was 73:27 by weight. Porcelain wastes are an industrial ceramic waste, taken from Porland Porcelain Company, Bilecik, Turkey. Porcelain wastes were ground and then was dry sieved to attain in a particle size between 90 to 150  $\mu\text{m}$ . The porcelain waste preparation procedure and characterization is similar with our previous study (Calis Acikbas and G. Acikbas, 2017). The theoretical density of waste was found as a 2,45  $\text{g}/\text{cm}^3$  (Micromeritics Accupyc II 1340 model He-gas pycnometer). The phase characterization was carried out by X-ray diffraction analyses (XRD-Panalytical, Empryan with Cu-K $\alpha$  radiation). XRD pattern of porcelain waste material was given in Figure 1. The graph revealed that quartz and the mullite are main phases of porcelain waste..

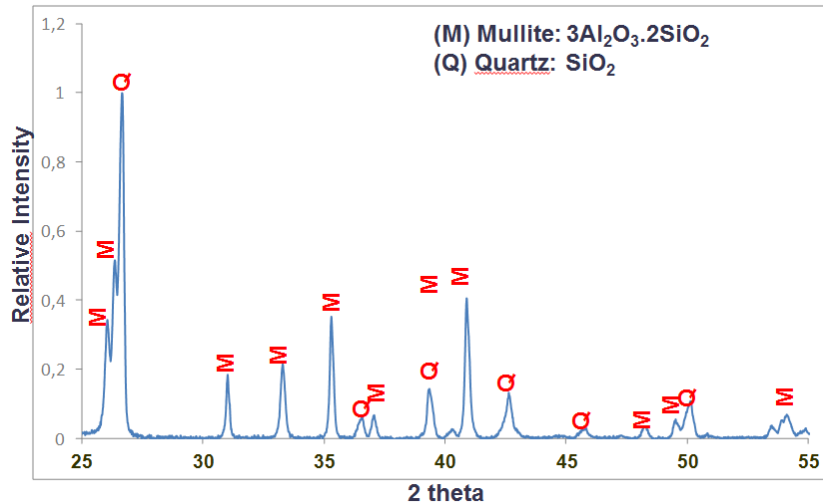
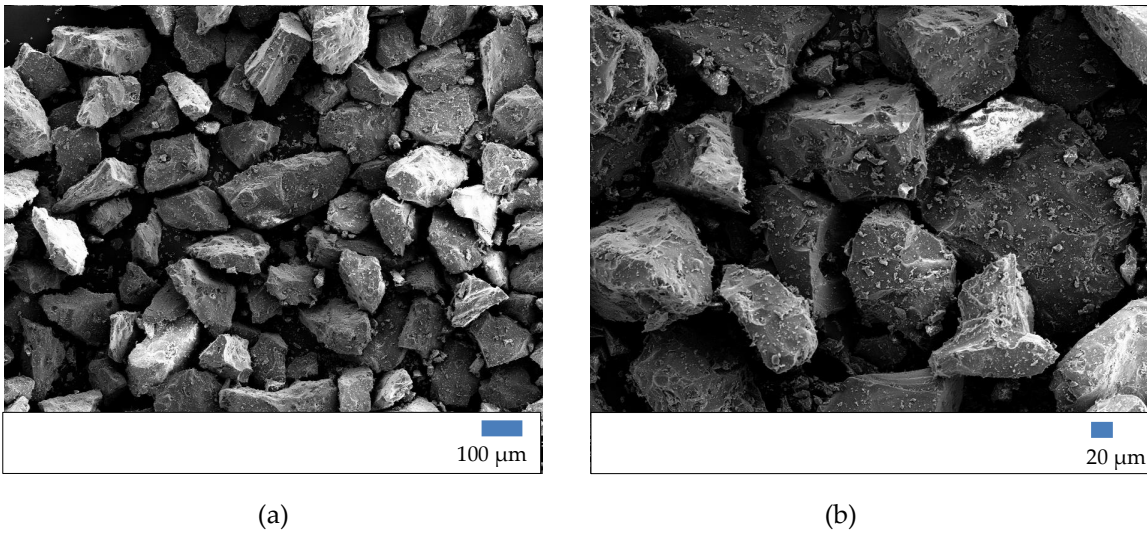


Figure 1. XRD spectra of porcelain wastes (M: mullite; Q: Quartz phases)

Figure 2 represents the secondary electron scanning electron microscopy (Zeiss Supra 40 VP FEG-SEM) images of ground porcelain waste particles. It was shown that waste particles are of irregular shape and sharp edge. Particle size is changing between 75 to 150 microns. The particle shape and size influences physico-mechanical properties and the process ability of composite.



**Figure 2.** Representative FEG-SEM images of porcelain waste particles (a) 200x, (b) 500x magnifications

The objectives of this study, production of composites with good mechanical properties by adding filler and reduces its cost. Therefore in maintaining a good balance among mechanical properties and cost, 50 and 60 wt% filler content were studied as taken reference in our former study (Table 1) (Acikbas et. al. 2014). And also process ability of resin-filler mixture as taken in consideration. Because addition of more than 60 wt.% filler would not be workable mix when it is prepared. On the other hand waste particle size kept as constant as between 90 to 150 microns. In order to observe the effect of vacuum, composites were produced with and without vacuum application. Vacuum was applied for 5 minutes, in order to remove bubbles in mixture. The coding is as follows: the first two figures represent the epoxy content. E5 means 50wt.% epoxy content. The two figures following 4 and 5, represent the waste content and the last figure represent the process condition. V means composites were produced under vacuum.

**Table 1.** Specifications of prepared composite materials

	E	E5P5	E5P5V	E4P6	E4P6V
<b>Epoxy (wt%)</b>	100	50	50	40	40
<b>Porcelain Waste (wt%)</b>	0	50	50	60	60
<b>Process</b>	Without	Without	With	Without	With
<b>Condition</b>	Vacuum	Vacuum	Vacuum	Vacuum	Vacuum

Polymer matrix composites were produced with the casting method. Detailed description of composites production stages were given in our previous study (Calis Acikbas and G. Acikbas, 2017). After production of composite materials some mechanical tests, analysis and characterization techniques were applied in order to determine properties. The theoretical densities of the waste and epoxy resin were used to calculate the theoretical density of the composites by using law of mixture as following equation (Harris, 1999).

$$\rho_c = \rho_m \cdot V_m + \rho_r \cdot V_r \tag{1}$$

where  $\rho_c$ , theoretical density of composite,  $\rho_m$ , theoretical density of matrix,  $\rho_r$ , theoretical density of reinforcement,  $V_m$ , volume fraction of matrix,  $V_r$ , volume fraction of reinforcement.

In order to measure the density and porosity of the samples the Archimedes principle was used. Bulk density, %theoretical density, and %total porosity were determined using the following equations.

$$\text{Bulk Density} = \frac{W_1}{W_3 - W_2} \times \rho_{\text{water}} \quad (2)$$

$$\%T.D. = \frac{B.D.}{T.D.} \times 100 \quad (3)$$

$$\% \text{ Total Porosity} = 100 - \%T.D. \quad (4)$$

where  $W_1$  is dry weight,  $W_2$  is wet weight suspended in water,  $W_3$  is wet weight, B.D. is Bulk Density, T.D. is Theoretical Density of samples.

Hardness values of composites were determined by Shore-D hardness measurement method. 3 point- flexural strength tests of samples was carried out according to TS 985 EN ISO 178 standard. At least five samples were used for mechanical tests. The flexural strength, elongation, flexural modulus were determined after 3 point- flexural strength test. The flexural modulus of composites was calculated using the following equation.

$$E = \frac{L^3}{4WD^3} \times m \quad (5)$$

where E is the flexural modulus, L is the distance between the span, m is slope, D is thickness and W is the width of the tested samples.

Wear characterization of the samples was determined with regards to friction, wear rates and mechanisms by carrying out ball-on-disk test. Tribometer designed according to DIN 50 324 and ASTM G 99-95a in a ball-on-disk configuration. Tungsten carbide ball is used as counter-part. 3N load was applied and tests were maintained to 400m. Wear track radius was selected as 5mm with the linear speed of 30cm/s. Surface profilometer (Mitutoyo SJ-401) was used in an attempt to calculate wear areas. Calculated surface areas integrated all over the circle of tracks and then the volumes were computed. Wear volume (V) divided by load (N) and wear distance (L) and the wear rates (W) were computed, as given in Eq. 6;

$$W = \frac{V}{F \cdot L} \quad (6)$$

The microstructural analysis of the worn surfaces of neat epoxy and composites was carried out scanning electron microscope (SEM-Zeiss Supra 40VP) after tribological tests.

## RESULT AND DISCUSSION

As it is seen from the graphics, coefficient of friction (CoF) of developed epoxy and epoxy matrix composites are changing between in 0.3 to 0.37 (Fig.3). Even the coefficient of friction is increased with the addition of hard ceramic fillers as expected, it can be considered that the friction behavior of epoxy is not affected majorly, according to these obtained close coefficient of friction values. The effect of production process on the friction behavior can be seen obviously in Fig 4, in comparison of porcelain added composite in same reinforcement content. It is achieved very close value of coefficient of friction in 50wt.% porcelain added composites (0.32) fabricated under vacuum compared to neat epoxy

coefficient of friction (0.30), whilst coefficient of friction of same composition fabricated without vacuum was obtained as high value as 0.36.

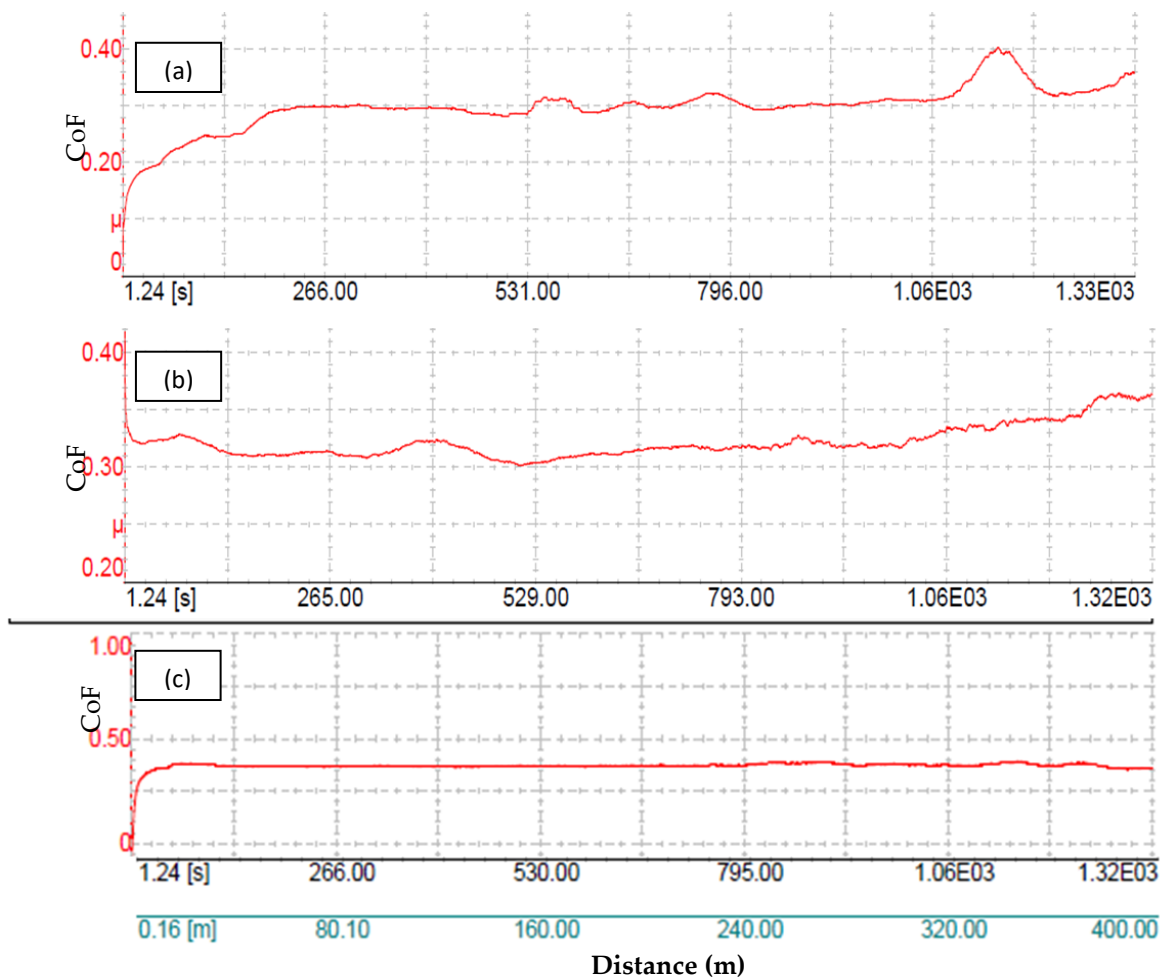


**Figure 3.** The friction coefficient graphs of (a) neat epoxy, (b) E5P5 and (c) E4P6 composites

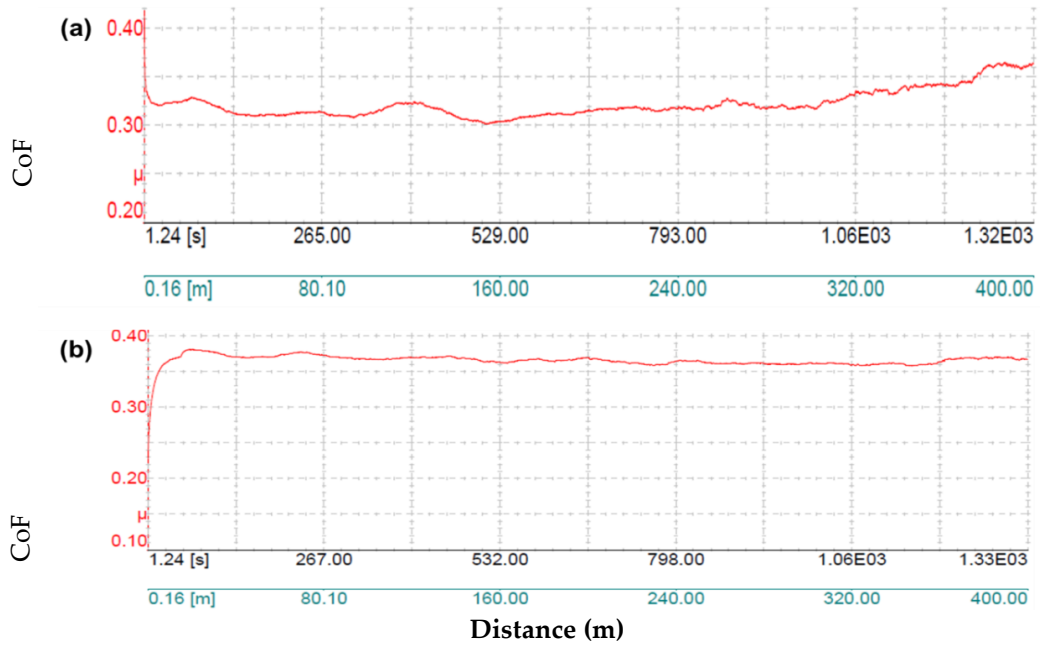


**Figure 4.** The effect of vacuum application on coefficient of friction (a) E5P5, (b) E5P5V composites

Table 2 shows some mechanical and physical properties of composites and its correlation with tribological behavior. The neat epoxy sample has the highest %T.D. value. The addition of fillers into epoxy provides more porous structure due to the formation of hard mixable mixture with increased viscosity. Vacuum application has positive effect on porosity elimination and hence higher %T.D. values were obtained. The flexural strength of neat epoxy is the highest one due to plastic behavior. With the addition of hard ceramic fillers into epoxy resin results in decreasing flexural strength values due to more brittleness structure. Since the vacuum application provides better interface bonding, flexural strength values showed a slight increase. Neat epoxy has the lowest flexural modulus and hardness as expected. The addition of hard particles enhances the flexural modulus as well as hardness. The addition of ceramic particles decreases the impact resistance. Vacuum applied and 60wt.% ceramic containing epoxy samples has the lowest wear rate and show high wear resistance. Hard ceramic particles has positive effect on wear rate since they carry load and provides in strengthening the surface which will result in improving the wear resistance of the polymer. As a result from the table, addition of filler and vacuum application enhances some mechanical properties. According to the literature, in order to develop or enhance the tribological properties of neat epoxies; the most common used reinforcements can be summarized as graphite; which helps in formation of lubricant film (Pan et.al., 2010), carbon nano tubes (CNT); that leads to improved tensile and flexural strength (Zhou et.al, 2008), graphene; which has high mechanical strength and fracture toughness (Khun et.al., 2015), titanium dioxide (TiO<sub>2</sub>); which helps to improve wear and impact resistance (Zhang et al., 2004), boron nitride (BN); which shows good mechanical properties (Gu et al., 2011), alumina (Al<sub>2</sub>O<sub>3</sub>); which improves the compressive strength, mechanical properties and also the wear resistance (Mohanty and Srivastava, 2012), nano clay (montmorillonit); that imparts a high wear resistance (Esteves et.al., 2013), polytetrafluoroethylene (PTFE) which acts as a lubricant (McCook et.al., 2006), etc. Zhang et al. (2004) studied wear properties of 15 vol% graphite, 5 vol% nano-TiO<sub>2</sub> and 15 vol% carbon fiber added epoxy composites against carbon steel ring (100Cr6) using a block-on-ring apparatus under dry conditions at the rotational speed of 1 m/s, under 1 MPa load. They reported a specific wear rate of composites of  $3,2 \times 10^{-7}$  mm<sup>3</sup>/Nm, which is about 100 times lower when compared to neat epoxy. Luo et al.(2010), used a chemical grafting method to modify nano-Si<sub>3</sub>N<sub>4</sub>, in order to improve the dispersion of nano-particles in the epoxy matrix and investigated the tribological behavior by pin-on-ring test configuration under the pressure of 3MPa. In comparison to the composites filled with untreated nano-Si<sub>3</sub>N<sub>4</sub> particles, the composites with the grafted

nano-Si<sub>3</sub>N<sub>4</sub> exhibit improved sliding wear resistance and reduced friction coefficient owing to the good chemical bonding at the filler/matrix interface. Khun et al.(2015), used graphene as a filler and tribology tests were carried out using a 100 Cr 6 steel ball on disk tribometer under a constant load of 1N over a sliding distance of 300 m. Increasing the graphene content resulted in reduced coefficient of friction and wear rate which explained by the formation of a tribochemical film owing to the presence of graphene sheets act as a solid lubricant in the interface. Consequently, it can be concluded that there are extensive studies in the literature related of tribological behavior of epoxy composites, on the other hand, the tribological behavior of porcelain added epoxy composites have not yet been explored comprehensively. In addition, it is well known that the variation of friction and wear rate depends on interfacial conditions such as normal load, geometry, relative surface motion, sliding speed, surface roughness of the rubbing surfaces, and type of material, system rigidity, temperature, stick slip, relative humidity, lubrication and vibration. Moreover; amongst them sliding speed and normal load are the two dominant factors in the variation of friction and wear rate (Chowdhury et al., 2011). Hence, in order to support these present experimental results, the findings were compared with the wear properties of neat epoxy in the literature. Vasconcelos et al. (2006), investigated the wear properties of epoxy resin based composites containing aluminum and milled carbon or glass fibers against steel (105Cr6) in dry conditions by reciprocating test at room temperature using 25N load and linear velocity of 0.13 m/s. Initially, at room temperature the neat epoxy exhibit a constant friction coefficient of 0.16 and after about 30m of sliding distance,  $\mu$  began to increase to 0.40 probably due to the thermal softening of the resin, as a result of the pressure and heat generated on the interface contact. Specific wear rate of neat epoxy obtained as  $1.82 \times 10^{-5}$  mm<sup>3</sup>/Nm. Sirinas and Bhagyashekar (2014), studied tribological behaviour of epoxy composites containing three different particulate fillers; Gr, SiC and Gr-SiC. Tribological tests conducted on a Pin on Disc type wear tester under dry sliding conditions under applied loads of 10-30N with the sliding velocity of 5.23m/s and obtained 0.76 of friction coefficient and wear rate of  $9.92 \times 10^{-5}$  mm<sup>3</sup>/Nm. The present study's test results are in good agreement with results in the literature. Although friction behavior is related to normal load, the differences in friction coefficient can be explained by there is no proportionality between these friction and load parameters and polymers behaves differently according to the various types of surface interactions and various test methods.

**Table 2.** Physical, mechanical and tribological properties of neat epoxy and composites

	$\mu$	%T.D.	Flexural Strength (MPa)	Flexural Modulus (GPa)	ShoreD Hardness	Impact Resistance (kJ/mm <sup>2</sup> )	Wear Rate (mm <sup>3</sup> /Nm)
E	0.298	98.9	106±1.3	3.2±0.3	81±0.4	12.9±1.1	6.7008E-05
E5P5	0.366	96.3	74.6±1.0	7.2±0.2	90±0.5	7.50±1.3	7.0762E-05
E5P5V	0.322	97.9	78.2±1.5	8.8±0.5	92±0.2	5.90±1.4	6.1551E-05
E4P6	0.373	95.4	72.1±1.2	8.3±0.2	91±0.6	7.10±1.0	8.5763E-05
E6P6V	0.370	97.2	75.3±1.1	9.6±0.2	93±0.3	5.60±1.4	6.0708E-05

Besides the determination of coefficient of friction and calculation of wear rates, microstructural characterization were carried out in order to explain wear mechanisms occurred at the interface. SEM-SE and EDX images of neat epoxy sample's worn surfaces were given in Fig.5. In the case of neat epoxy, wear debris and abrasive wear tracks and tribolayer formation are seen. Generally, it is known that tribological properties of polymer-based composites are improved according to the formation of transfer film and the enhancement of mechanical and thermal properties. Wear scars on the worn surface indicate the abrasion of the epoxy matrix by the asperities of the counter face. According to EDX analysis, C and O are main elements of tribolayer. The presence of little amount of W and Co elements, sign that abrasion wear since these elements come from ball.

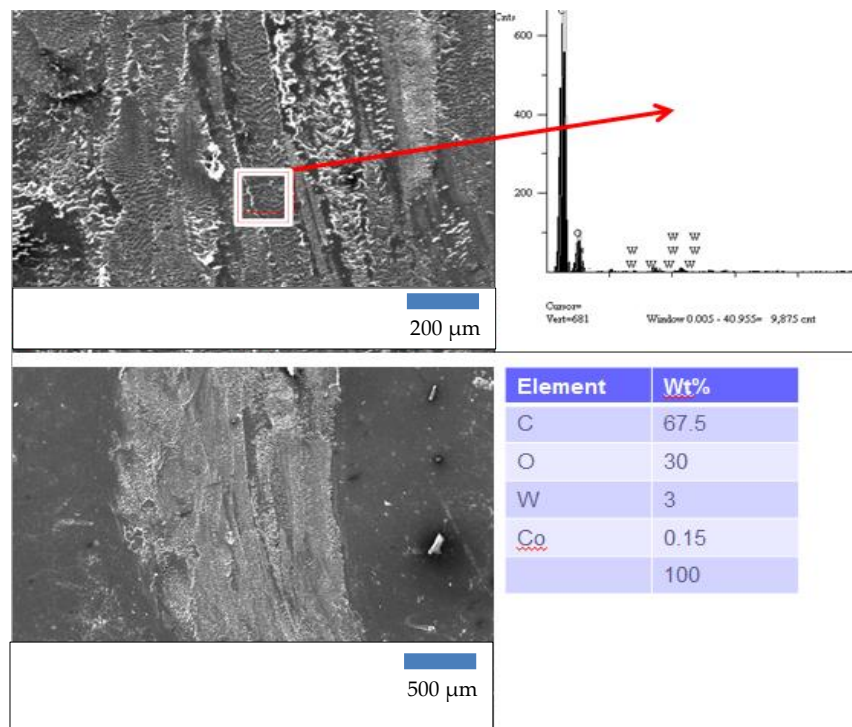


**Figure 5.** SEM-SE and SEM-EDX analysis of worn neat epoxy surfaces

From the EDX analysis of E5P5/E5P5V samples (Fig. 6 and 8), addition of filler provides thicker tribofilm formation compared to neat epoxy. The formation of thicker tribofilm than the neat epoxy can be explained by the difficulty of formation tribofilm since ceramic phases provides high degree of brittleness, high wear rate and coefficient of friction. The matrix-filler interface bonding is weak of E5P5 sample (see Fig.7). Increased interfacial strength between the matrix and fillers with application of vacuum results in less wear and changes were observed in tribolayer characteristics (Fig. 8 and 9). The enhancement of interface bonding strength between epoxy and porcelain particles lead to changes in tribolayer feature that shifts from fragile to more continuous. This affects the friction coefficient and wear rate. Due to weak interface bonding, more grain pullout was observed and hence rougher worn surface was obtained with E5P5 sample compared to E5P5V sample. Also EDX analysis results confirm this phenomenon (Fig. 6 and 8). With vacuum application Si, Al and O peaks intensity is getting lower values, which indicates less abrasive wear in load-carrier porcelain particles.

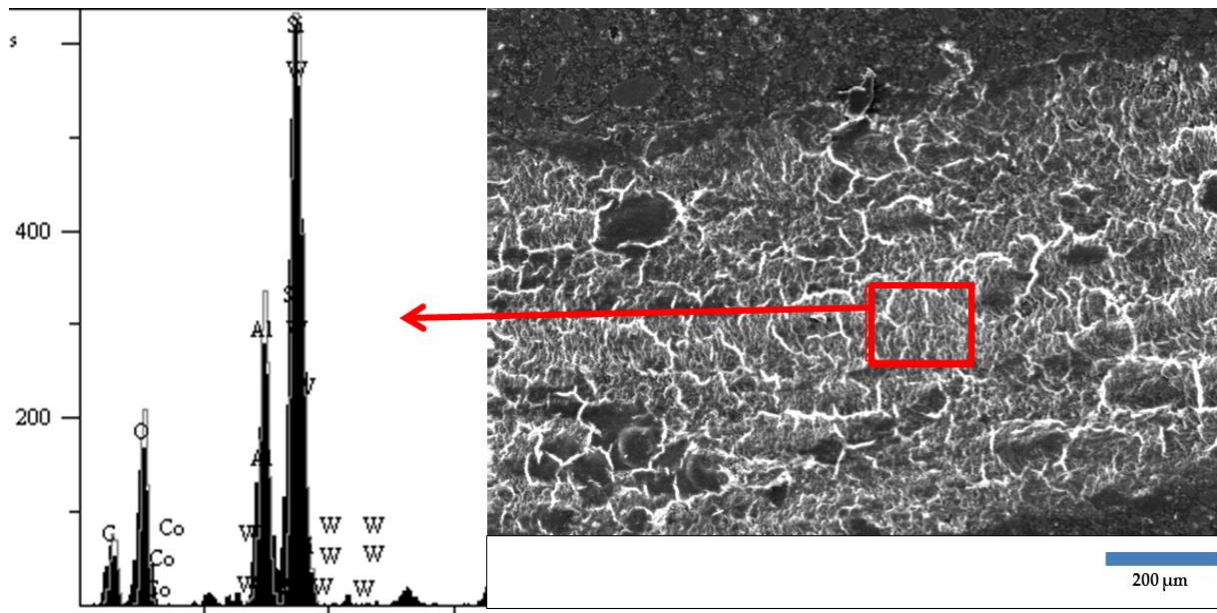


Figure 6. SEM-EDX analysis of worn E5P5 sample surface

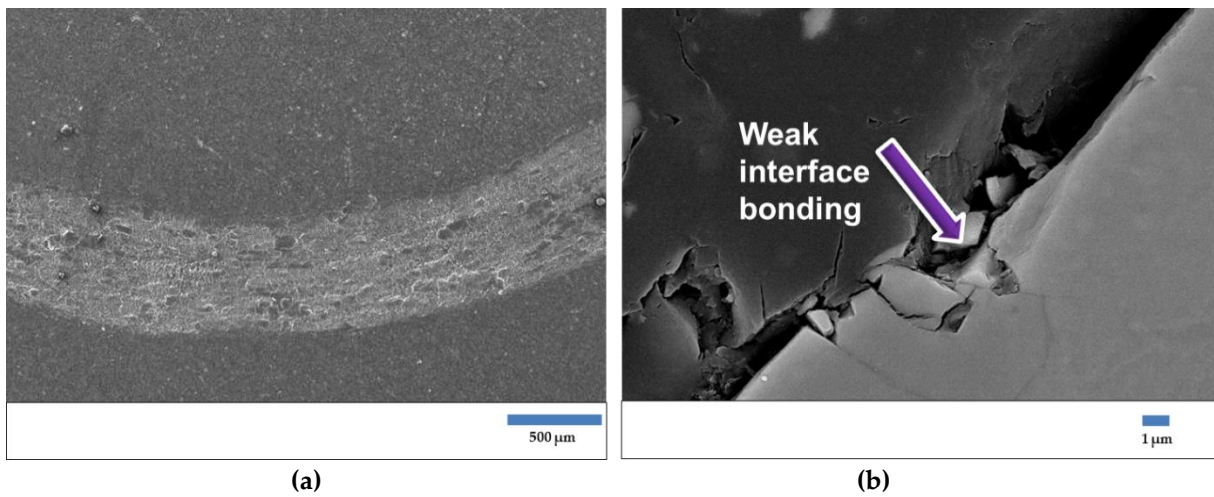


Figure 7. (a) Wear scar of E5P5 sample , (b) FEG-SEM image of matrix-filler interface of E5P5 sample

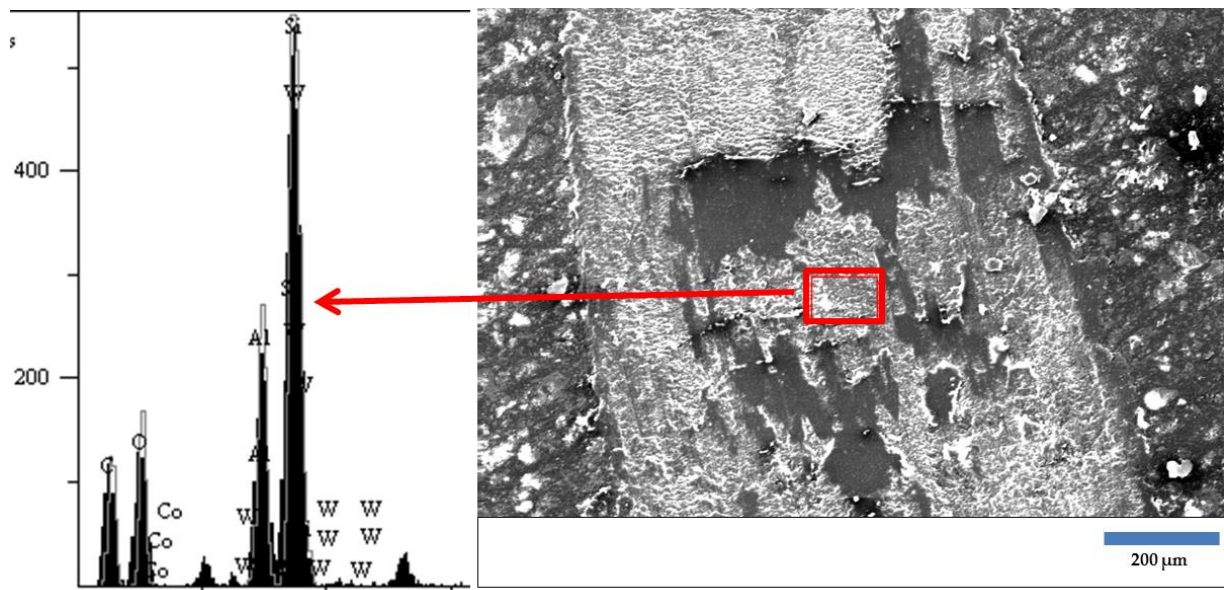
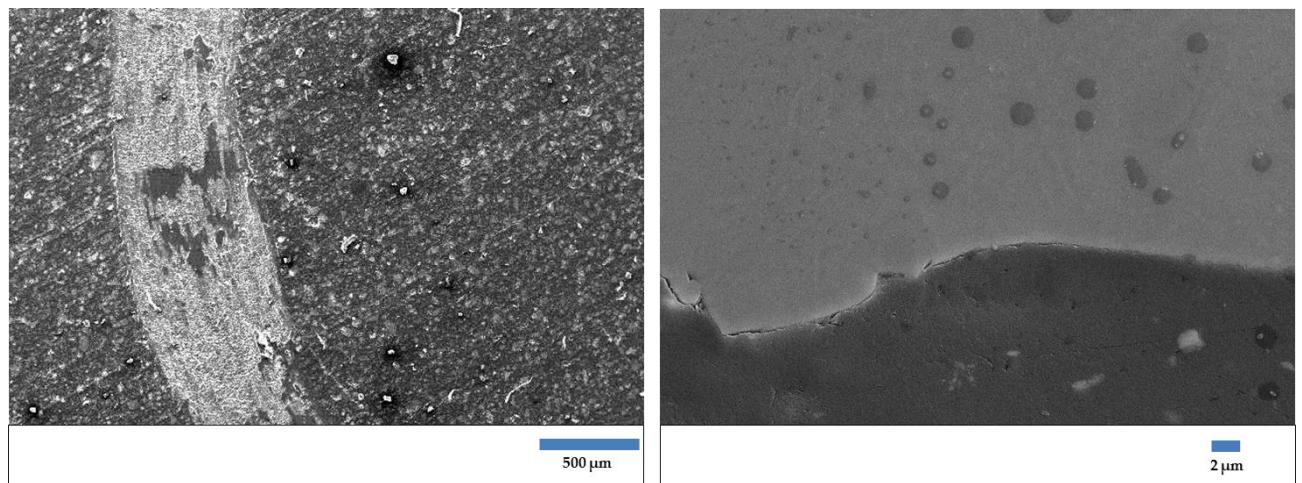


Figure 8. SEM-EDX analysis of worn E5P5V sample surface



(a)

(b)

Figure 9. (a) Wear scar of E5P5V sample, (b) FEG-SEM image of matrix-filler interface of E5P5V sample (better interface connectivity between matrix and filler with vacuum application)

From the EDX analysis of E4P6V samples worn surfaces, Si, Al, O and C peaks are obtained as main elements (Figure 10). This shows that tribofilm containing of porcelain particles and polymer. Because of the high elastic modulus and abrasion resistance of the porcelain particles, they carry most loads during the friction process and so decrease significantly the wear of the matrix. The addition of the fillers assists in strengthening the surface which will result in improving the wear resistance of the epoxy. With vacuum application, good interface bonding strength decrease the particle pull-out amount and cause less wear losses. The uniformity and thickness of this layer is increased with increasing filler content. The addition of more rigid particles into epoxy resin enhances the mechanical properties such as hardness and flexural modulus. This can lead to higher abrasion resistance of composites than the epoxy matrix.

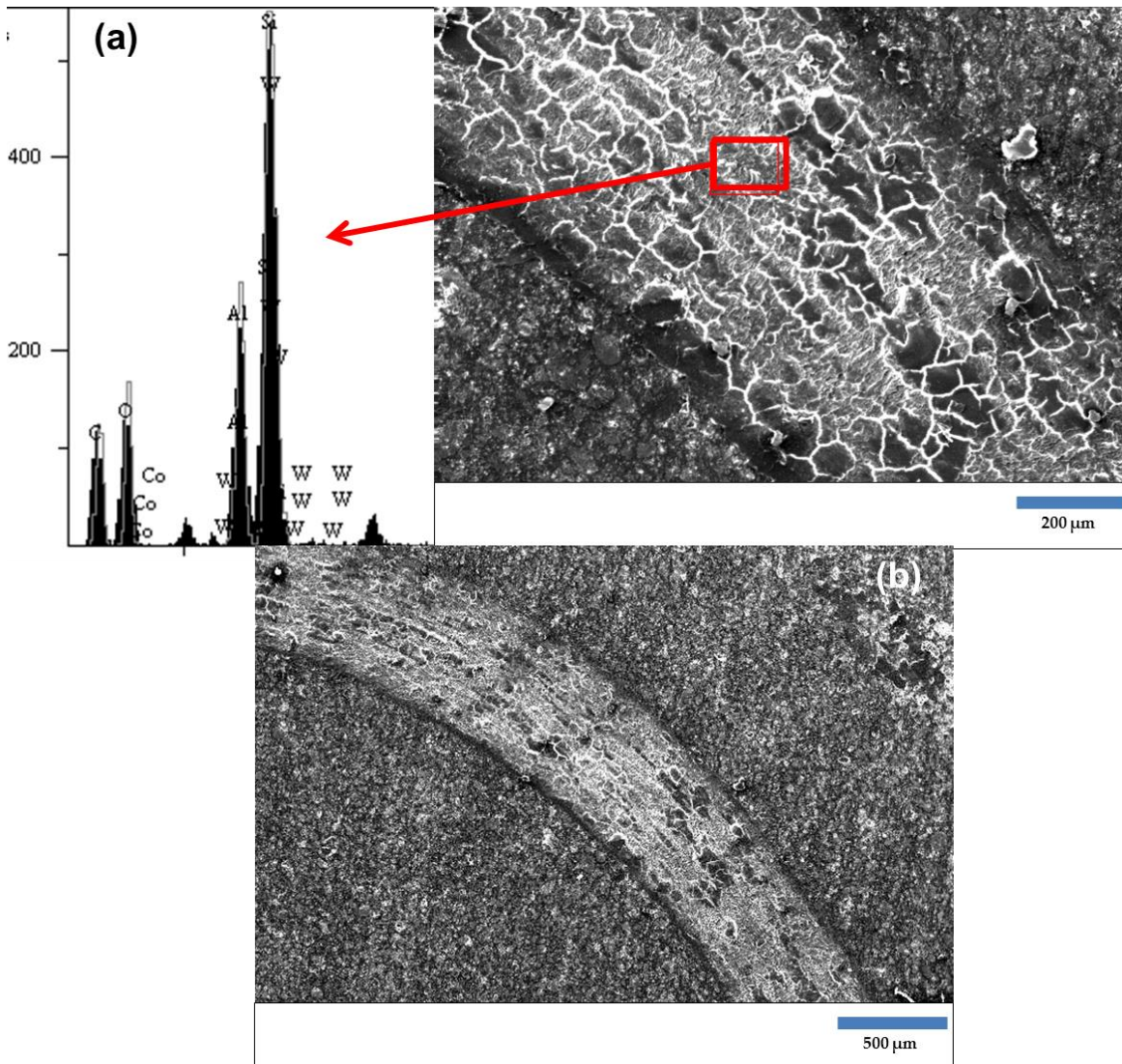


**Figure 10.** (a) SEM-EDX analysis of worn E4P6V surface and (b) FEG-SEM image of wear scar of E4P6V

## CONCLUSION

Based on experimental studies, the following results can be drawn. With the addition of filler; CoF, %T.D., flexural modulus, hardness increased, flexural strength, impact resistance and wear rate decreased. With increasing filler content; CoF, flexural modulus, hardness, wear rate enhanced, %T.D., flexural strength, and impact resistance reduced. Vacuum application leads to improvement in %T.D., flexural strength, flexural modulus, hardness and decrease in CoF, impact resistance and wear rate. Vacuum application provides fully embedded and well wetted particles, and strong bonding strength between matrix and filler and hence better tribological behavior was obtained. Wear mechanisms can be summarized as tribolayer formation, adhesive wear and abrasive wear.

## REFERENCES

Acikbas, G., Ozcan, S., Calis Acikbas, N., 2017, "Production and Characterization of a Hybrid Polymer Matrix Composite", *Polymer Composites*, DOI: 10.1002/pc.24471

- Acikbas, G., Calis Acikbas, N., Ikizek, E., Ozel, M., Eker, A. S., 2014a, "Characterization of Green Epoxy Matrix Composites Filled with Ceramic Wastes", Caglar, N., ISITES2014 2nd International Symposium on Innovative Technologies in Engineering and Science, Karabük, Turkey, 597-606, 18-20 June, 2014, pp. Academic Platform, available at: <http://www.isites.info/pastconferences/isites2014/isites2014/papers/A16-ISITES2014ID96.pdf>
- Acikbas, G., Calis Acikbas, N., Keskin, A., Ari, O. K., Ucer, D., 2014b, "Effect of Graphite Filler Loading Concentration on Physical and Mechanical Properties of Epoxy Matrix Composites", SERES'14 'III. International Ceramic, Glass, Porcelain Enamel, Glaze and Pigment Congress, Eskisehir, Turkey, 15-17 October 2014.
- Acikbas, G. and Göçmez, H., 2015, "Polyester Matrix Composites Containing Marble Waste", International Porous And Powder Materials Symposium And Exhibition, İzmir, Turkey, 15-18 September 2015, available at: <http://www.ppm2015.org/metin.aspx?ID=1420>
- Acikbas, G., Göçmez, H., 2016, "Effect of Glass Fiber Waste Content on Polyester Matrix Composites", paper presented at the 1st International Black Sea Congress on Environmental Sciences, Giresun-Turkey, 31 August- 3 September, 2016, available at: [http://muhendislik.giresun.edu.tr/fileadmin/user\\_upload/BOLUMLER/Cevre/IBCESS\\_Abstract\\_Book.pdf](http://muhendislik.giresun.edu.tr/fileadmin/user_upload/BOLUMLER/Cevre/IBCESS_Abstract_Book.pdf).
- Acikbas, G., Göçmez, H., 2016, "Effect of Vitreous China Sanitaryware Waste Amount on Polyester Matrix Composite Properties", 3.International Symposium on Environment and Morality, Alanya-Turkey, 4-6 November 2016, available at: <http://isem.info/PastConferences/ISEM2016/ISEM2016/papers/1-ISEM2016ID342.pdf>.
- Alajmi, M., Shalwan, A., 2015, "Correlation between Mechanical Properties with Specific Wear Rate and the Coefficient of Friction of Graphite/Epoxy Composites", *Materials*, Vol. 8, pp. 4162-4175; doi:10.3390/ma8074162.
- Alok, S., Amar, P., 2008, "Analysis of Dry Sliding Wear Behaviour of Red Mud Filled Polyethylene Composites Using Taguchi Method", *Journal of Reinforced Plastics and Composites*, Vol. 29, (24).
- Baptista, R., Mendão, A., Rodrigues, F., Figueiredo-Pina, C.G., Guedes, M., Marat-Mendes R., 2016, "Effect of High Graphite Filler Contents on the Mechanical And Tribological Failure Behavior of Epoxy Matrix Composites", *Theoretical and Applied Fracture Mechanics*, Vol. 85, pp. 113-124.
- Basavarajappa, S., Arun, K.V., Paulo Davim, J., 2009, "Effect of Filler Materials on Dry Sliding Wear Behavior of Polymer Matrix Composites – A Taguchi Approach", *Journal of Minerals & Materials Characterization & Engineering*, Vol. 8, No.5, pp 379-391.
- Bhushan, B., 2000, *Modern Tribology Handbook*, Two Volume Set, CRC Press, ISBN 9780849384035, December 28, Pages 1760 .
- Bobby S., Abdul Samad, M., 2016, "Enhancement of Tribological Performance of Epoxy Bulk Composites and Composite Coatings Using Micro/Nano Fillers: A Review", *Polymers for Advanced Technologies*, October 2016, DOI: 10.1002/pat.3961.
- Calis Acikbas N., Acikbas, G., 2017, "Epoxy Matrix Composites Containing Urea Formaldehyde Waste Particulate Filler", *Waste and Biomass Valorization*, Vol.8, pp. 669-678.
- Chowdhury, M. A., Khalil, M. K., Nuruzzaman, D. M., Rahaman, M. L. 2011, "The Effect of Sliding Speed and Normal Load on Friction and Wear Property of Aluminum", *Int. J. Mech. Mechatron. Eng*, Vol. 11 (01), pp. 53-57.
- Cubeta, Richard A., 2013, "Utilizing Recycled Fiberglass for Affordable", *Green Composite Technology*, COMPOSITES 2013, American Composite Manufacturers Association, January 29-31, 2013 Orlando, FL-USA.pp. 1-5.
- E, S.F., Shi, L., Guo, Z.G., Liu, W.M., 2015, "The Recent Progress of Tribological Biomaterials", *Biosurface and Biotribology*, Vol. 1,pp.81-97.

- Esteves, M., Ramalho, A., Ferreira, M. A. J., Nobre, P. J. 2013, "Tribological and Mechanical Behaviour of Epoxy/Nanoclay Composites", *Tribology Letters*, Vol. 52 (1), pp.1 –10.
- Garcia, F.G., Leyva, M. E., Alencar de Queiroz, A. A., Higa, O. Z., 2009, "Epoxy Networks for Medicine Applications: Mechanical Properties and In Vitro biological Properties", *Journal of Applied Polymer Science*, Vol. 112, pp.1215–1225.
- Gill C.S and Sidhu, J.S., 2016, "Dry Sliding Wear Behavior of Epoxy Based Composites Filled With WS<sub>2</sub> and B<sub>4</sub>C", *International Journal of Material Sciences and Technology*, Vol 6, No. 1, pp. 21-32.
- Gu, J., Zhang, Q., Dang, J., Xie, C., 2012, "Thermal Conductivity Epoxy Resin Composites Filled with Boron Nitride", *Polymers for Advanced Technologies*, Vol. 23(6), pp. 1025–1028.
- Harris, B., 1999, *Engineering Composite Materials*, The Institute of Materials, London
- Katz H.S., Mileski, J.V., 1987, *Handbook of Fillers For Plastics*, Springer Science&Business Media, Technology & Engineering .
- Khun, N. W., Zhang, H., Lim, L. H., Yang, J., 2015, "Mechanical and Tribological Properties of Graphene Modified Epoxy Composites", *International Journal of Applied Science and Technolog*, Vol. 8(2), pp. 101–109.
- Koleva, M., Zheglova, Fidancevska, A., Vassilev,, E. V., 2011, "Composites Containing Waste Materials", INTECH Open Access Publisher.
- Kumar, V., Sinha S. K. and Agarwal, A. K. , 2015, "Tribological Studies of Epoxy and Its Composite Coatings on Steel in Dry and Lubricated Sliding", *Tribology*, Vol 9, No 3, pp.144-153.
- Kumar, R., Calis Acikbas, N., Kara, F., Mandal, H., Basu, B., 2009, "Microstructure - Mechanical Properties - Wear Resistance Relationship of SiAlON Ceramics", *Metallurgical and Materials Transactions A*, pp.2319-2332.
- Kumar Mallik, A., Calis Acikbas N., Kara, F., Mandal, H., Basu, D., 2012, "A Comparative Study of SiAlON Ceramics", *Ceramics International*, pp.5757–5767.
- Kumar Mallik, A., Reddy, M., Calis Acikbas, N., Kara, F., Mandal, H., Basu, D., Basu, B., 2011, "Influence of SiC addition on tribological properties of SiAlON", *Ceramics International*, pp.2495–2504.
- Luo, Y., Yu, X. Y., Dong, X. M., Rong, M. Z., Zhang, M. Q. 2010, "Effect of nano-Si<sub>3</sub>N<sub>4</sub> Surface Treatment on the Tribological Performance of Epoxy Composite", *Express Polymer Letters*, Vol.4, No.3, pp. 131-140
- McCook, N. L., Boesl, B., Burris, D. L., Sawyer, W. G. 2006, "Epoxy, ZnO, and PTFE Nanocomposite: Friction and Wear Optimization", *Tribology Letters*, Vol. 22 (3), pp. 253–257.
- Mohanty, A., Srivastava, K. V., 2012, "Effect of Alumina Nanoparticles on the Enhancement of Impact and Flexural Properties of the Short Glass/Carbon Fiber Reinforced Epoxy Based Composites", *Int. J. Sci. Eng. Res.* Vol. 3(11), pp. 1–7.
- Myshkin, N.K., Petrokovets, M.I., Kovalev, A.V. , 2005, "Tribology of Polymers: Adhesion, Friction, Wear, and Mass-Transfer", *Tribology International*, Vol. 38, pp. 910–921.
- Qi, H., Zhang, G., Wetzal, B., Österle, W., Wang, T., Wang, Q., 2016, "Exploring the Influence of Counterpart Materials on Tribological Behaviors of Epoxy Composites", *Tribology International*, Vol.,103, pp. 566–573.
- Pan, G., Guo, Q., Ding, J., Zhang, W., Wang, X., 2010, "Tribological Behaviors of Graphite/Epoxy Two-Phase Composite Coatings", *Tribology International*, Vol.43, pp.1318–1325.
- Pervaiz, M.R., Mohanthy, S., Nayak, S.K., Mahanwar, P.A. , 2010, "Composites Reinforced with Fly Ash and Mica", *Journal of Minerals & Materials Characterization & Engineering*, Vol. 9, pp. 25-41.
- Raju, B. R., Suresha, B., Swamy, R. P., Kanthraju, B. S. G. , 2013, "Investigations on Mechanical and Tribological Behaviour of Particulate Filled Glass Fabric Reinforced Epoxy Composites", *Journal of Minerals and Materials Characterization and Engineering*, Vol.1, pp.160-167.
- Sagsoz, O., Ilday, N. O., Sagsoz, N. P., Bayindir, Y. Z., Alsaran, A., 2014, "Investigation of Hardness and Wear Behavior of Dental Composite Resins", *International Journal of Composite Materials*, Vol.4(4), pp. 179-184.

- Srinivas, K., Bhagyashekar, M.S., 2014, "Wear Behaviour of Epoxy Hybrid Particulate Composites", *Procedia Engineering*, Vol. 97, pp. 488 – 494.
- Shi G., Zhang M.Q., Rong M.Z., Wetzel B., Friedrich K., 2004, "Sliding Wear Behavior of Epoxy Containing nano-Al<sub>2</sub>O<sub>3</sub> Particles with Different Pretreatments", *Wear*, Vol. 256, pp. 1072–1081.
- Suresha B., Chandramohan G., Prakash J.N., Balusamy V., Sankaranarayananasamy K., 2006, "The Role of Fillers on Friction and Slide Wear Characteristics in Glass-Epoxy Composite Systems", *Journal of Minerals and Materials Characterization and Engineering*, Vol. 5, pp. 87-101.
- Tai, Y.-Y., Hsu, S.-H., Chen, R.-S., Su, W.-F., Chen, M.-H. , 2015, "Liquid Crystalline Epoxy Nanocomposite Material for Dental Application", *Journal of the Formosan Medical Association*, Vol.114, pp.46-51.
- Vasconcelos P.V., Lino F.J., Baptista A.M., Neto R.J.L., 2006, "Tribological Behavior of Epoxy Based Composites for Rapid Tooling", *Wear*, Vol. 260, pp. 30–39.
- Yaman, B., Mandal, H. , 2014, " Wear Performance of Spark Plasma Sintered Co/WC and cBN/Co/WC Composites", *International Journal of Refractory Metals and Hard Materials*, Vol.42, pp. 9–16.
- Seramik Kalkınma Raporu, available at:  
<http://www.kalkinma.gov.tr/Lists/zet%20htisas%20Komisyonu%20Raporlar/Attachments/266/Seramik%20%C3%87al%C4%B1%C5%9Fma%20Grubu%20Raporu.pdf>
- Zhang, Z., Breidt, C., Chang, L., Hauptert, F., Friedrich, K., 2004, "Enhancement of the Wear Resistance of Epoxy: Short Carbon Fibre, Graphite, PTFE and nano-TiO<sub>2</sub>", *Composites Part A: Applied Science and Manufacturing*, Vol. 35, pp. 1385–1392.
- Zhou, Y. X., Wu, P. X., Cheng, Z. Y., Ingram, J. , Jeelani, S. 2008, "Improvement in Electrical, Thermal and Mechanical Properties of Epoxy by Filling Carbon Nanotube", *Express Polymer Letters*, Vol. 2(1), pp. 40–48.



## A FUZZY LOGIC APPROACH FOR THE ESTIMATION OF PERFORMANCE HYDROXY DRY CELL WITH DIFFERENT PLATE COMBINATION

<sup>1</sup>Yusuf YILMAZ, <sup>2</sup>Sadık ATA, <sup>3</sup>Gürol ÖNAL, <sup>4</sup>Abdullah İŞIKTAŞ, <sup>5</sup>Kevser DINCER

<sup>1</sup>Selçuk Üniversitesi, Mühendislik Fakültesi, Makine Mühendisliği Bölümü, Konya

<sup>2</sup>KTO Karatay Üniversitesi, Mühendislik Fakültesi, Makine Mühendisliği Bölümü, Konya

<sup>3</sup>Selçuk Üniversitesi, Mühendislik Fakültesi, Makine Mühendisliği Bölümü, Konya

<sup>4</sup>Sinop Üniversitesi, Meslek Yüksekokulu, Makine ve Metal Teknolojileri Bölümü, Sinop

<sup>5</sup>Selçuk Üniversitesi, Mühendislik Fakültesi, Makine Mühendisliği Bölümü, Konya

<sup>1</sup>yyilmaz@selcuk.edu.tr, <sup>2</sup>sadik.ata@karatay.edu.tr, <sup>3</sup>gonal@selcuk.edu.tr,

<sup>4</sup>aisiktas@sinop.edu.tr, <sup>5</sup>kdincer@selcuk.edu.tr

(Geliş/Received: 10.10.2016; Kabul/Accepted in Revised Form: 20.06.2017 )

**ABSTRACT:** In this study, hydroxy (HHO) dry cell with different plate combination performances in terms of current, temperature and flow rate were experimentally investigated and modeled with Rule-Based Mamdani-Type Fuzzy (RBMFT) modeling technique. Input parameters plate number and time; output parameters current, temperature and flow rate were described by RBMFT if-the rules. The dimensions of the plates were 10x10 cm<sup>2</sup> and 11x11 cm<sup>2</sup>. Current and temperature were measured for the different plate combination. This paper presents a fuzzy logic based study for estimating the uncertainty of the HHO drycell parameters. The 80 values between 90th and 270th seconds, which are not obtained from experimental work for 10x10 cm<sup>2</sup> and 11x11 cm<sup>2</sup> current, temperature and flow rate are predicted by fuzzy logic method. One of the results is; the current value predicted by RBMFT for the 11-2 plate combination and t=90 s is less than the current value from the results of the experimental work for the 11-2 plate combination and t=60 s, but higher than the current value from the results of the experimental work for 11-2 plate combination and t=120s. The comparison between experimental data and RBMFT is done by using three different statistical method. These are, root mean square error (RMSE), mean absolute error (MAE) and the coefficient of multiple determination (R<sup>2</sup>). For 10x10 cm<sup>2</sup> dimension plate, RMSE, MAE and R<sup>2</sup> for the current is 0.13, 0.111 and 96.44% respectively. For 11x11 cm<sup>2</sup> dimension plate, RMSE, MAE and R<sup>2</sup> for the current is 0.07926, 0.06466 and 98.44% respectively. coefficient of multiple determinations (R<sup>2</sup>). As a result, RBMFT model has shown satisfying relation with experimental results, which suggests an alternative approach to estimation of performance HHO dry cell with different plate combination.

**Key Words:** Fuzzy logic, HHO dry cell, Plate combination

### Farklı Plaka Kombinasyonlarında HHO Hücresinin Performansının Tahmin Edilmesinde Bulanık Mantık Yaklaşımı

**ÖZ:** Bu çalışmada, hidroksi (HHO) hücresi farklı plaka kombinasyonlarında akım, sıcaklık ve debi yönünden deneysel olarak incelenmiş ve kural tabanlı Mamdani tipi bulanık mantık tekniği ile modellenmiştir. Bulanık mantık modelinde, giriş parametreleri plaka sayısı ve zaman; çıkış parametreleri akım, sıcaklık ve debi olarak tanımlanmıştır. Plaka boyutları 10x10 cm<sup>2</sup> ve 11x11 cm<sup>2</sup>'dir. Farklı plaka kombinasyonlarında akım, sıcaklık ve debi ölçülmüştür. Bu çalışmada, deneysel çalışmada yapılmayan değerlerin bulanık mantık ile tahmin edilmesi işlenmiştir. 10x10 cm<sup>2</sup> ile 11x11 cm<sup>2</sup> plaka boyutlarında deneysel olarak yapılmayan 90. ile 270. saniye arasında olan 80 değer, bulanık mantık ile tahmin ettirilmiştir. 11-2 plaka kombinasyonu ve t=90s için bulanık mantık modeli ile tahmin edilen

akım değeri, deneysel çalışmada 11-2 plaka kombinasyonu ve  $t=60s$  için belirlenen akım değerinden az; deneysel çalışmada 11-2 plaka kombinasyonu ve  $t=120s$  için belirlenen akım değerinden fazladır. Deneysel çalışma ve bulanık mantık ile elde edilen değerler üç farklı istatistik yöntemi kullanılarak karşılaştırılmıştır. Bu yöntemler; ortalama karesel hatanın karekökü (RMSE), ortalama mutlak hata (MAE) ve determinasyon katsayısı ( $R^2$ )'dır.  $10 \times 10 \text{ cm}^2$  plaka boyutu için, RMSE, MAE ve  $R^2$  değerleri sırasıyla 0.13, 0.111 ve %96.44 olarak belirlenmiştir.  $11 \times 11 \text{ cm}^2$  plaka boyutu için, RMSE, MAE ve  $R^2$  değerleri sırasıyla 0.07926, 0.06466 ve %98.44 olarak belirlenmiştir. Sonuç olarak, bulanık mantık ile elde edilen değerler, deneysel çalışmada tespit edilen değerler ile uyum göstermiştir. Bu çalışmada, farklı plaka boyutlarında HHO hücresinin performansının tahmin edilmesinde, bulanık mantık modelleme tekniğinin kullanılması önerilmektedir.

**Anahtar Kelimeler:** Bulanık mantık (BM), Hidroksi (HHO) hücresi, Plaka Kombinasyonu

## INTRODUCTION

Fossil fuels currently constitute 82% of the global total primary energy sources and oil makes 31.5 % of this. Of the global oil production, 62.2% is consumed by the transport sector. Thus, the automotive industry is the largest consumer of fossil oil. Studies have also shown that the demand for oil and gas is rising exponentially and indications are that fossil fuels will not outlast the century if current habits are not curtailed. Hence, in response to the growing fuel prices and the increasing pressures for a cleaner "greener" society, the automotive industry has made efforts to reduce emissions and increase fuel efficiency. These efforts have primarily focussed on emissions reductions using catalytic converters, reducing vehicle weight, using alternative structural materials, improving engine management and fuel supply systems, incorporating the stop - start technology and introducing alternative sources of energy such as hydrogen fuel cells, biofuels and others. Governments and municipalities have also made efforts through the development and implementation of legislation. As regulations become more restrictive and global fossil fuel prices increase, the search for more sustainable sources of transportation fuels becomes more urgent. The current research into alternative energy sources for motor vehicles is mainly concentrated around electric/battery powered cars, hydrogen fuel cells, solar and hydrogen powered cars. These technologies, as promising as they may be, will not completely replace the fossil fuelled internal combustion engine within the next few decades. One of the major hindrances will be the lack of supporting infrastructure such as fuel supply and distribution centres. There is therefore potential for a bridging or interim technology that can be incorporated into existing technology using the existing infrastructure, which can lead to greener use of available fossil resources. One such option is the introduction of hydrogen gas into the combustion process of an internal combustion engine (Madyira and Harding, 2014).

Hydrogen has a strong chance to take the place of conventional fossil fuels in traditional internal combustion engines. However, one of the main drawbacks hindering this chance is storage issues of hydrogen due to its extremely low density (about 14 times lower than water in storage conditions). There is also another issue of keeping hydrogen in storage place, due to its extremely high diffusivity. This issue requires higher insulation during carriage to prevent hydrogen diffuse through walls. Liquified hydrogen, despite having higher specific energy than petrol, is disadvantaged in terms of volumetric energetic storage about five times. Yet again its energy density is considerably higher than that of electric batteries, it is still a good candidate for fossil fuel replacement. Enhancing intake air of combustion process with hydrogen can improve flame speed, lean burn ability and flame quenching distance. However, production cost, along with the storage issues makes it a non-feasible approach. Some of the potential difficulties can be eliminated by usage of Brown's Gas or HHO (produced by electrolysis of water). What is more, usage of HHO surpasses reactivity of the natural hydrogen, improving engine emissions, performance and fuel efficiency at expense of power in automotive

electrical system or from generator designed for this purpose in automobile engine (Leelakrishnan et al., 2013).

HHO combustion in engine provides powerful and quick reaction and after release of energy HHO turns into a water vapor as emission. This results in higher torque in engine and easier cooling when compared to other fuels about 10 to 20 times. Considering a conventional combustion engine, temperature after combustion is about 250 F is inferior to the one enhanced with HHO, which reaches 150 F to 200 F due to vapor formation. By attaining lower temperatures, engines can get a longer lifespan by lower temperature change during cycle and lower rate of oil degradation which is also improving oil changing period. This leads to another opportunity of cost saving in maintenance cost and longer service intervals (Chakrapani and Neelamegam, 2011).

HHO gas has an auto ignition temperature about 570°C (1065°F) and has a heating value of 241.8 kJ for a stoichiometric mixture at normal atmospheric pressure. HHO gas can ignite and convert to water vapor, releasing energy at concentration level of 4 to 94 % hydrogen per volume. Flame temperature can vary despite heating value remains same. Flame temperature of 2800°C is attained when combustion occurs under stoichiometric ratio conditions, about 700°C hotter than a hydrogen flame in air (Sakthivel, 2014). This Energy's performance must be increased which is predicted to be more important in the future. One of the methods to determine the effects of the parameters on performance is fuzzy logic method.

In this study, two different plate combinations compared in terms of HHO dry cell performance and fuzzy logic modeling used to estimate of performance HHO dry cell at intermediate values. Unperformed experiments are predicted with RBMTF for current, temperature and flow rate values for every plate's 80 output between 90th and 270th seconds. Performance parameters are plate combination, time, current, temperature and flow rate. Study includes fuzzification of input variables, representation of fuzzy set with 9 linguistic variables, formation of rule basis and a comparison between output values obtained by experiments and by calculation based on generated rules and RBMTF technique. The comparison between experimental data and RBMTF is done by using three different statistical methods. These are, root mean square error (RMSE), mean absolute error (MAE) and the coefficient of multiple determination ( $R^2$ ). Main objective of the study is to present that it is possible to estimate performance of HHO dry cell with a fuzzy logic approach.

## LITERATURE REVIEW

In the existing literature, there have been many investigations on application of fuzzy logic. Some of briefly mentioned below. Keshwani et al. (Keshwani et al., 2008) carried out rule-based Mamdani-type fuzzy modeling of skin permeability. They proposed that potential uses of the presented models include rapid assessment of skin permeability of compounds to identify candidates for transdermal drug delivery and estimate toxicity risks. Shakhawat et al. (Shakhawat et al., 2006) studied fuzzy rule-based modelling for human health risk from naturally occurring radioactive materials in produced water. They concluded that a dual-barrier approach for human health risk assessment from naturally occurring radioactive materials in produced water. Yıldız et al. (Yıldız and Kişoğlu, 2011) examined with the size tables and body size numbers taken from ready-wear enterprises carrying out activities in the women's outside wear field, modelling a common body numbering system was aimed through the fuzzy logic system. They proposed that this modeling will reduce the problems related to consumer products by contributing in a positive sense to the marketing problems and to the competition in the garment industry. Özek et al. (Sinecen and Sinecen, 2004) studied modelling of air conditioning system by fuzzy logic approach, because one of the main problems in control systems is the difficulty to form the mathematical model associated with the control mechanism. They realized that the fuzzy logic without using mathematical model of control system can create control mechanism only with the help of linguistic variables. Tiryaki et al. (Tiryaki and Kazan, 2007) studied about dishwasher which is frequently used in daily life is modelled and simulated by using fuzzy logic. They concluded that if an

appropriate hardware support and appropriate sensors are provided for the dishwasher, with the aim of the fuzzy logic model the washing process may be done without human intervention according to the inputs such as quantity of the dishes, type of the dishes by the machine. Işıktaş et al. (Işıktaş et al., 2016) studied about fuzzy logic modelling of performance HHO dry cell with different type membership functions. They noted that RBMTF which has a triangular membership function has a more better performance than other membership functions for determine performance of HHO dry cell. Ata and Dincer (Ata and Dincer, 2015; Ata and Dincer, 2015; Ata, 2015; Ata and Dincer, 2016 ) studied about rule-based Mamdani-type fuzzy (RBMTF) modeling of performance proton exchange membrane fuel cell with carbon nanotube. They noted that RBMTF can be successfully used for the specification PEM performances with coating carbon nanotube. Kim et al. (Kim and Kim, 1999) examined an electrical modelling of the fuel cell generation system. They used fuzzy logic controller to overcome inherent disadvantages such as uncontrollable large overshoot and large current ripple. They noted that fuzzy controller is very effective in output control and desired operating point operation, which in turn offers high system stability and performance. Tong et al. (Tong et al., 2013) studied about 1 kW PEM fuel cell unit and developed the models of stack voltage, cathode flow, anode flow. They proposed that the power demand of the external load can be provided by the fuel cell stack under the control of a real-time simplified variable universe fuzzy controller.

## MATERIALS AND METHODS

### Experimental Study

Figure 1 shows experimental system for this study. Water tank is used to store water the cells required. Thus the material of the tank needs to have the protection against corrosion. There are three outlets on the water tank. These are the gas inlet that the gas gets back to the tank, the gas outlet that the gas were taken, water outlet that water flows to the cell. Safety tank is an important element and is used to protect the main tank. This element contains water and prevent the flame to reach the main tank. Power supply is an element used to obtain HHO gas. Power supply needs to generate electricity. Stainless steel was chosen as the plate material and the thickness of the plate was 1mm. The dimensions of the plates were 10x10 cm<sup>2</sup>. The plates has 10 cm length and 10 cm width. A piece that have the length of 2 cm was cut off from the corners of the plates. Thus, the power requirement reduced. End plates are selected from mica material. It is chosen to be observed during system operation. Gas inlet was drilled on top of the plates as water inlet was drilled on the bottom of the plates. The diameter of each hole is 8 mm. Seals are selected from plastic. Each gasket has the diameter of 10 cm and the thickness of 2 mm. The gaskets contact with the last plates are 4 mm thick. This is because the water inlet and the gas outlet is to ensure more comfortable and regular gas flow. Current, voltage and temperature were measured for the different plate combination. Tap water was used in the experiments and the system was set to 10 minutes. For each combinations, new cells were prepared. According to experimental work result, current values were increased with decreasing the number of plate. However, the current value did not exceed the highest value of 5.3 A. The reason of that, relation between the active surface area of the plates and the current drawn. It was observed that the highest ratio of the current value of the plate active surface area was 0.1 A/cm<sup>2</sup>. The working temperature is an important parameter in this system and it varies according to the number of plates and current. The temperature was observed to be increased as the current drawn went up. The highest temperature value recorded during the experiments was 38 °C. This value occurred when the highest current value was 5.3 A. The result of experimental work showed the voltage dropped as the number of plates reduced (Dincer et al., 2013).

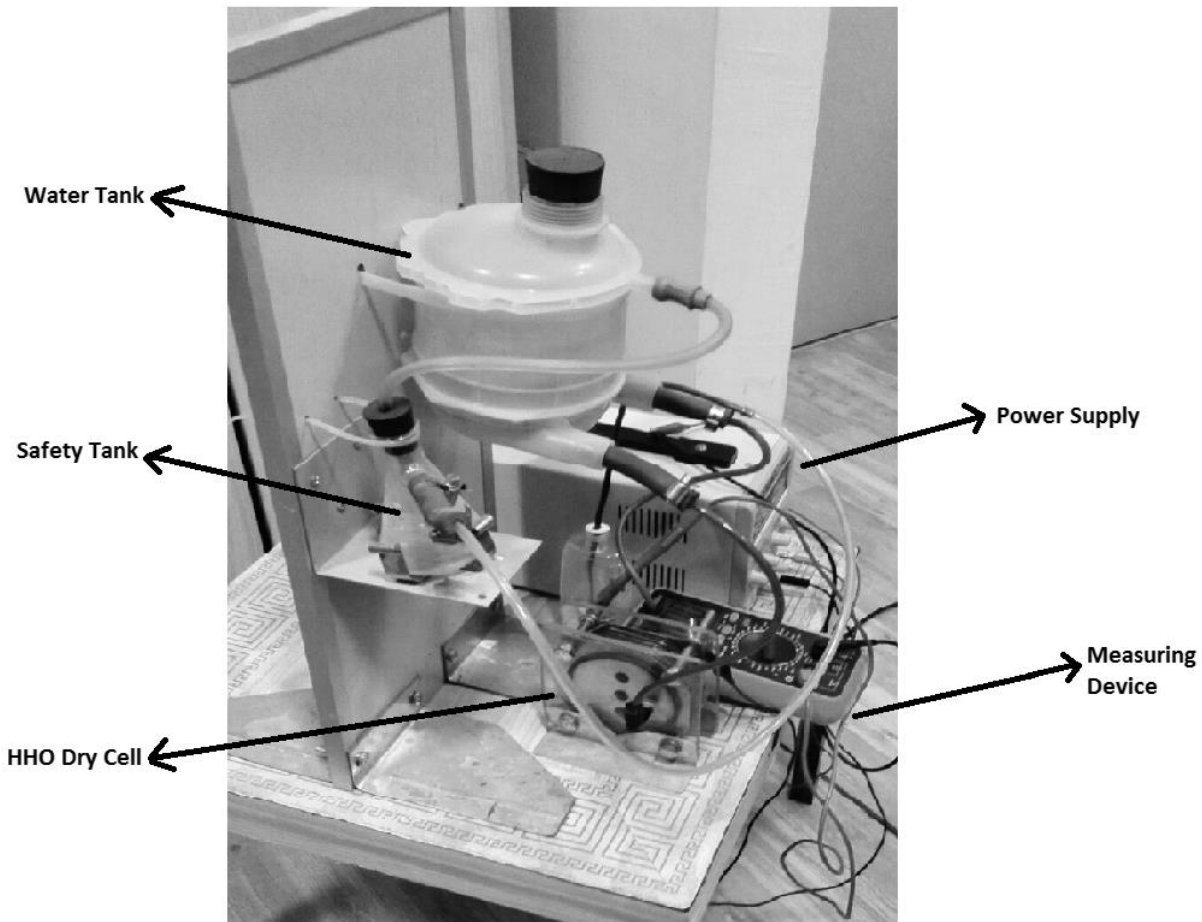


**Figure 1.** Experimental system

### Fuzzy Logic Modeling

Mamdani-type fuzzy logic model is used to evaluate performance of HHO dry cell by this study. Mamdani's method is providing a relatively simple structure for 'min-max' operations, hence it is one of the most commonly used applications in numerous fields requiring specialized knowledge. Mamdani's method is a fuzzy logic method and can be applied in any kind of problem that has an input and output interconnected to each other. Method proposed by Ebrahim Mamdani in 1975 during an attempt to control a steam engine and boiler combination. Method foresees a synthesis of a set of linguistic control rules obtained from experienced human operators. Fuzzy Logic Toolbox explains Mamdani type inference as expectation of output membership functions as fuzzy sets. Mamdani-type fuzzy model is created in the following five steps:

- a) Fuzzification of inputs in antecedent to a degree of membership between 0 and 1
- b) Determining the weights of rules using fuzzy logic.
- c) Application of AND and OR operations
- d) Combining consequences to get an output distribution
- e) Defuzzifying the output distribution (this step is used only if a crisp output is needed)

Advantages of the Mamdani Method as a summary; method is intuitive, well suited for usage of human input, has widespread acceptance (Bölgen, 2010).

## RESULTS AND DISCUSSIONS

HHO gas has substantial advantages when compared to the gasoline due to its high diffusivity. First two of these advantages is rate of formation of homogenous mixture is greater since HHO diffuses faster in mixture. Secondly, HHO can dilute quite fast under circumstances of leakage. Several researches show that 1866 litres of HHO gas is obtained from 1 liter of water, after ignition, the HHO gas returns to original volume after combustion (Sakthivel, 2014).

The aim of this study with the aid of experimental data, HHO dry cell performances in terms of current and temperature were modeled with fuzzy logic modeling technique. In the developed RBMTF system, output parameters A and T were determined using inlet parameters plate number and t.

The following steps to design an fuzzy logic (FL) system:

1. Definition of the control objectives and criteria: What am I trying to control? What do I have to do to control the system? What kind of response do I need? What are the possible (probable) system failure modes?
2. Determination of the input and output relationships. One should choose a minimum number of variables for input to the FL engine (typically error and rate-of-change-of-error).
3. Break the control problem down into FL rules. The problem should be split into a series of IF X AND Y THEN Z rules that define the desired system output response for given system input conditions.
4. Creation of FL membership functions. The memberships defines the meaning (values) of Input/Output terms used in the rules.
5. System test: evaluate the results, tune the rules and membership functions, and retest until satisfactory results are obtained (Esteves, 2009).

In this study, hydroxy cell performances were modeled with a RBMTF modeling technique. Input parameters plate number and time; output parameters current, temperature and flow rate were described by RBMTF if-the rules (Fig. 2). Numerical parameters of input and output variables were fuzzificated as linguistic variables: Very Very Low ( $L_1$ ), Very Low ( $L_2$ ), Low ( $L_3$ ), Negative Medium ( $L_4$ ), Medium ( $L_5$ ), Positive Medium ( $L_6$ ), High ( $L_7$ ), Very High ( $L_8$ ) and Very Very High ( $L_9$ ) linguistic classes (Tables 1 and 2). The 80 values between 90th and 270th seconds, which are not obtained from experimental work for 10x10 cm<sup>2</sup> and 11x11 cm<sup>2</sup> current, temperature and flow rate are predicted by fuzzy logic method. Fig. 3 and Fig. 4 shows respectively, the comparison of experimental data for 10x10 cm<sup>2</sup> and 11x11 cm<sup>2</sup> plate dimensions with fuzzy prediction for the variation of time with plate combination of current, temperature and flow rate values. From a comparison of the experimental results with the results of the fuzzy logic study, one can see that the results are quite compatible.

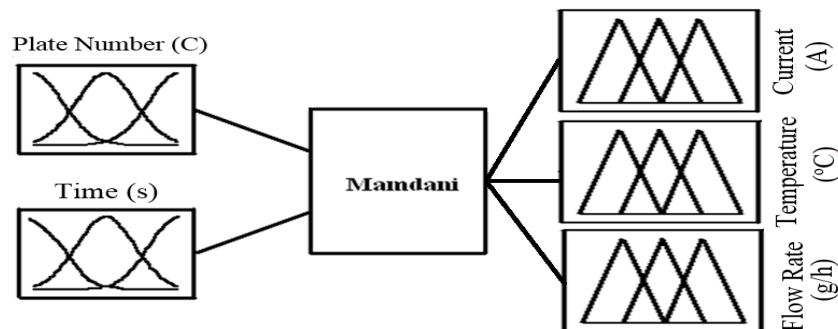


**Figure 2.** Designed fuzzy modeling structure the performance of hydroxy cell performances

**Table 1.** Fuzzy sets of input variables : Plate Number (C) and Time (s)

Membership name	very very low	very low	low	negative medium	medium	positive medium	high	very high	very very high
Plate Number	L <sub>1</sub>	L <sub>2</sub>	L <sub>3</sub>	L <sub>4</sub>	L <sub>5</sub>	L <sub>6</sub>	L <sub>7</sub>	L <sub>8</sub>	L <sub>9</sub>
Time (s)	C <sub>1</sub>	C <sub>2</sub>	C <sub>3</sub>	C <sub>4</sub>	C <sub>5</sub>	C <sub>6</sub>	C <sub>7</sub>	C <sub>8</sub>	C <sub>9</sub>
	t <sub>1</sub>	t <sub>2</sub>	t <sub>3</sub>	t <sub>4</sub>	t <sub>5</sub>	t <sub>6</sub>	t <sub>7</sub>	t <sub>8</sub>	t <sub>9</sub>

**Table 2.** Fuzzy sets of output variables: (a) Current (A), (b) Temperature (°C), (c) Flow Rate (g/h)

a

Membership name	very very low	very low	low	negative medium	medium	positive medium	high	very high	very very high
Current (A)	L <sub>1</sub>	L <sub>2</sub>	L <sub>3</sub>	L <sub>4</sub>	L <sub>5</sub>	L <sub>6</sub>	L <sub>7</sub>	L <sub>8</sub>	L <sub>9</sub>
	A <sub>1</sub>	A <sub>2</sub>	A <sub>3</sub>	A <sub>4</sub>	A <sub>5</sub>	A <sub>6</sub>	A <sub>7</sub>	A <sub>8</sub>	A <sub>9</sub>

b

Membership name	very very low	very low	low	negative medium	medium	positive medium	high	very high	very very high
Temperature (°C)	L <sub>1</sub>	L <sub>2</sub>	L <sub>3</sub>	L <sub>4</sub>	L <sub>5</sub>	L <sub>6</sub>	L <sub>7</sub>	L <sub>8</sub>	L <sub>9</sub>
	T <sub>1</sub>	T <sub>2</sub>	T <sub>3</sub>	T <sub>4</sub>	T <sub>5</sub>	T <sub>6</sub>	T <sub>7</sub>	T <sub>8</sub>	T <sub>9</sub>

c

Membership name	very very low	very low	low	negative medium	medium	positive medium	high	very high	very very high
Flow Rate (g/h)	L <sub>1</sub>	L <sub>2</sub>	L <sub>3</sub>	L <sub>4</sub>	L <sub>5</sub>	L <sub>6</sub>	L <sub>7</sub>	L <sub>8</sub>	L <sub>9</sub>
	FR <sub>1</sub>	FR <sub>2</sub>	FR <sub>3</sub>	FR <sub>4</sub>	FR <sub>5</sub>	FR <sub>6</sub>	FR <sub>7</sub>	FR <sub>8</sub>	FR <sub>9</sub>

The most important factor that affects the performance of the fuzzy logic system is the number of the rules and their accuracy. In this study, there are 2 inputs and 81 rules for the every output of 9x9 matrix and totally 81x3=243 rules are generated. Rules of RBMTF for FR, A, T was given in Tables 3-5, respectively.

**Table 3.** Rules of RBMTF for current (A)

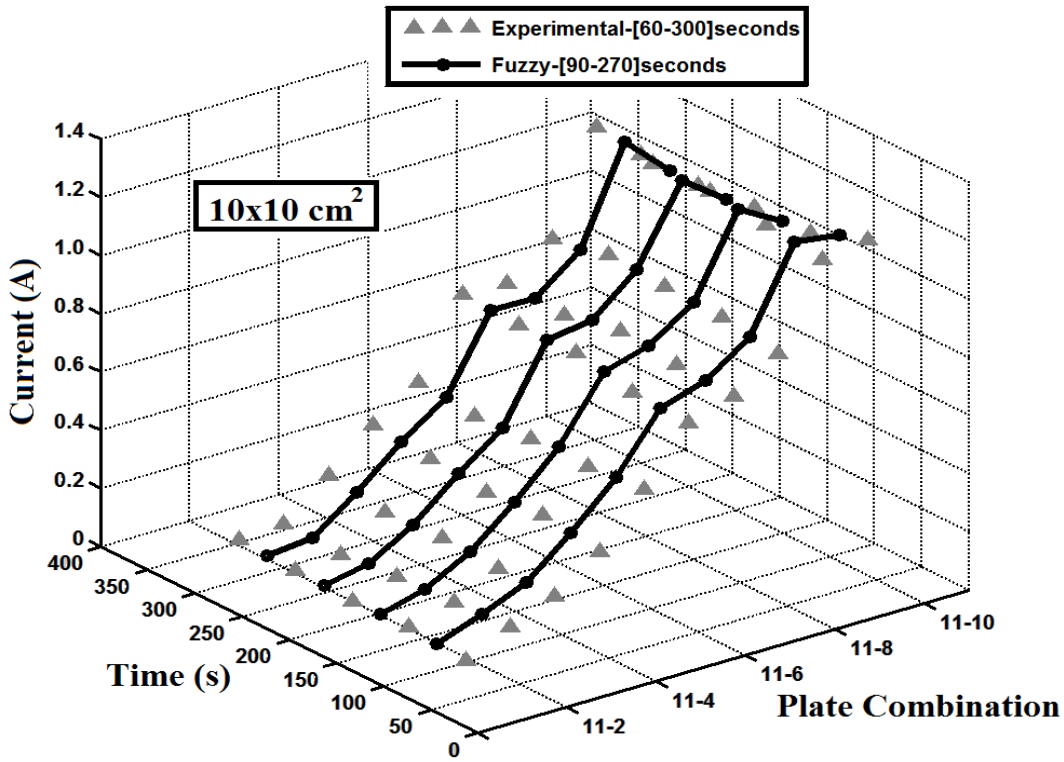
Rule number	C	t	A	Rule number	C	t	A
1	If C is C <sub>1</sub>	and t is t <sub>1</sub>	then A is A <sub>9</sub>	42	If C is C <sub>5</sub>	and t is t <sub>6</sub>	then A is A <sub>9</sub>
2	If C is C <sub>1</sub>	and t is t <sub>2</sub>	then A is A <sub>9</sub>	43	If C is C <sub>5</sub>	and t is t <sub>7</sub>	then A is A <sub>9</sub>
3	If C is C <sub>1</sub>	and t is t <sub>3</sub>	then A is A <sub>9</sub>	44	If C is C <sub>5</sub>	and t is t <sub>8</sub>	then A is A <sub>9</sub>
4	If C is C <sub>1</sub>	and t is t <sub>4</sub>	then A is A <sub>9</sub>	45	If C is C <sub>5</sub>	and t is t <sub>9</sub>	then A is A <sub>9</sub>
5	If C is C <sub>1</sub>	and t is t <sub>5</sub>	then A is A <sub>9</sub>	46	If C is C <sub>6</sub>	and t is t <sub>1</sub>	then A is A <sub>3</sub>
6	If C is C <sub>1</sub>	and t is t <sub>6</sub>	then A is A <sub>9</sub>	47	If C is C <sub>6</sub>	and t is t <sub>2</sub>	then A is A <sub>3</sub>
7	If C is C <sub>1</sub>	and t is t <sub>7</sub>	then A is A <sub>9</sub>	48	If C is C <sub>6</sub>	and t is t <sub>3</sub>	then A is A <sub>4</sub>
8	If C is C <sub>1</sub>	and t is t <sub>8</sub>	then A is A <sub>9</sub>	49	If C is C <sub>6</sub>	and t is t <sub>4</sub>	then A is A <sub>4</sub>
9	If C is C <sub>1</sub>	and t is t <sub>9</sub>	then A is A <sub>9</sub>	50	If C is C <sub>6</sub>	and t is t <sub>5</sub>	then A is A <sub>4</sub>
10	If C is C <sub>2</sub>	and t is t <sub>1</sub>	then A is A <sub>9</sub>	51	If C is C <sub>6</sub>	and t is t <sub>6</sub>	then A is A <sub>5</sub>
11	If C is C <sub>2</sub>	and t is t <sub>2</sub>	then A is A <sub>9</sub>	52	If C is C <sub>6</sub>	and t is t <sub>7</sub>	then A is A <sub>5</sub>
12	If C is C <sub>2</sub>	and t is t <sub>3</sub>	then A is A <sub>9</sub>	53	If C is C <sub>6</sub>	and t is t <sub>8</sub>	then A is A <sub>5</sub>
13	If C is C <sub>2</sub>	and t is t <sub>4</sub>	then A is A <sub>9</sub>	54	If C is C <sub>6</sub>	and t is t <sub>9</sub>	then A is A <sub>5</sub>
14	If C is C <sub>2</sub>	and t is t <sub>5</sub>	then A is A <sub>9</sub>	55	If C is C <sub>7</sub>	and t is t <sub>1</sub>	then A is A <sub>1</sub>
15	If C is C <sub>2</sub>	and t is t <sub>6</sub>	then A is A <sub>9</sub>	56	If C is C <sub>7</sub>	and t is t <sub>2</sub>	then A is A <sub>1</sub>
16	If C is C <sub>2</sub>	and t is t <sub>7</sub>	then A is A <sub>9</sub>	57	If C is C <sub>7</sub>	and t is t <sub>3</sub>	then A is A <sub>1</sub>
17	If C is C <sub>2</sub>	and t is t <sub>8</sub>	then A is A <sub>9</sub>	58	If C is C <sub>7</sub>	and t is t <sub>4</sub>	then A is A <sub>2</sub>
18	If C is C <sub>2</sub>	and t is t <sub>9</sub>	then A is A <sub>9</sub>	59	If C is C <sub>7</sub>	and t is t <sub>5</sub>	then A is A <sub>2</sub>
19	If C is C <sub>3</sub>	and t is t <sub>1</sub>	then A is A <sub>9</sub>	60	If C is C <sub>7</sub>	and t is t <sub>6</sub>	then A is A <sub>2</sub>
20	If C is C <sub>3</sub>	and t is t <sub>2</sub>	then A is A <sub>9</sub>	61	If C is C <sub>7</sub>	and t is t <sub>7</sub>	then A is A <sub>2</sub>
21	If C is C <sub>3</sub>	and t is t <sub>3</sub>	then A is A <sub>9</sub>	62	If C is C <sub>7</sub>	and t is t <sub>8</sub>	then A is A <sub>2</sub>
22	If C is C <sub>3</sub>	and t is t <sub>4</sub>	then A is A <sub>9</sub>	63	If C is C <sub>7</sub>	and t is t <sub>9</sub>	then A is A <sub>2</sub>
23	If C is C <sub>3</sub>	and t is t <sub>5</sub>	then A is A <sub>9</sub>	64	If C is C <sub>8</sub>	and t is t <sub>1</sub>	then A is A <sub>1</sub>
24	If C is C <sub>3</sub>	and t is t <sub>6</sub>	then A is A <sub>9</sub>	65	If C is C <sub>8</sub>	and t is t <sub>2</sub>	then A is A <sub>1</sub>
25	If C is C <sub>3</sub>	and t is t <sub>7</sub>	then A is A <sub>9</sub>	66	If C is C <sub>8</sub>	and t is t <sub>3</sub>	then A is A <sub>1</sub>
26	If C is C <sub>3</sub>	and t is t <sub>8</sub>	then A is A <sub>9</sub>	67	If C is C <sub>8</sub>	and t is t <sub>4</sub>	then A is A <sub>1</sub>
27	If C is C <sub>3</sub>	and t is t <sub>9</sub>	then A is A <sub>9</sub>	68	If C is C <sub>8</sub>	and t is t <sub>5</sub>	then A is A <sub>1</sub>
28	If C is C <sub>4</sub>	and t is t <sub>1</sub>	then A is A <sub>8</sub>	69	If C is C <sub>8</sub>	and t is t <sub>6</sub>	then A is A <sub>1</sub>
29	If C is C <sub>4</sub>	and t is t <sub>2</sub>	then A is A <sub>9</sub>	70	If C is C <sub>8</sub>	and t is t <sub>7</sub>	then A is A <sub>1</sub>
30	If C is C <sub>4</sub>	and t is t <sub>3</sub>	then A is A <sub>9</sub>	71	If C is C <sub>8</sub>	and t is t <sub>8</sub>	then A is A <sub>2</sub>
31	If C is C <sub>4</sub>	and t is t <sub>4</sub>	then A is A <sub>9</sub>	72	If C is C <sub>8</sub>	and t is t <sub>9</sub>	then A is A <sub>2</sub>
32	If C is C <sub>4</sub>	and t is t <sub>5</sub>	then A is A <sub>9</sub>	73	If C is C <sub>9</sub>	and t is t <sub>1</sub>	then A is A <sub>1</sub>
33	If C is C <sub>4</sub>	and t is t <sub>6</sub>	then A is A <sub>9</sub>	74	If C is C <sub>9</sub>	and t is t <sub>2</sub>	then A is A <sub>1</sub>
34	If C is C <sub>4</sub>	and t is t <sub>7</sub>	then A is A <sub>9</sub>	75	If C is C <sub>9</sub>	and t is t <sub>3</sub>	then A is A <sub>1</sub>
35	If C is C <sub>4</sub>	and t is t <sub>8</sub>	then A is A <sub>9</sub>	76	If C is C <sub>9</sub>	and t is t <sub>4</sub>	then A is A <sub>1</sub>
36	If C is C <sub>4</sub>	and t is t <sub>9</sub>	then A is A <sub>9</sub>	77	If C is C <sub>9</sub>	and t is t <sub>5</sub>	then A is A <sub>1</sub>
37	If C is C <sub>5</sub>	and t is t <sub>1</sub>	then A is A <sub>4</sub>	78	If C is C <sub>9</sub>	and t is t <sub>6</sub>	then A is A <sub>1</sub>
38	If C is C <sub>5</sub>	and t is t <sub>2</sub>	then A is A <sub>5</sub>	79	If C is C <sub>9</sub>	and t is t <sub>7</sub>	then A is A <sub>1</sub>
39	If C is C <sub>5</sub>	and t is t <sub>3</sub>	then A is A <sub>7</sub>	80	If C is C <sub>9</sub>	and t is t <sub>8</sub>	then A is A <sub>1</sub>
40	If C is C <sub>5</sub>	and t is t <sub>4</sub>	then A is A <sub>8</sub>	81	If C is C <sub>9</sub>	and t is t <sub>9</sub>	then A is A <sub>1</sub>
41	If C is C <sub>5</sub>	and t is t <sub>5</sub>	then A is A <sub>9</sub>				

Table 4. Rules of RBMTF for temperature ( $^{\circ}\text{C}$ )

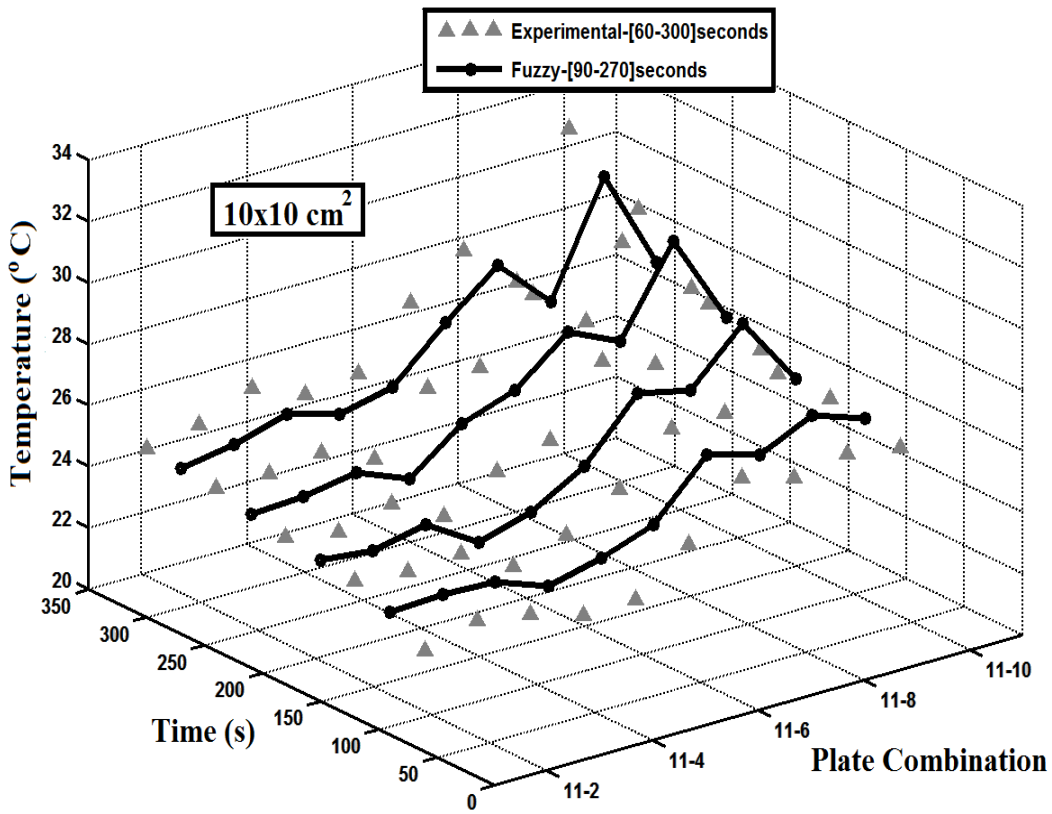
Rule number	C	t	T	Rule number	C	t	T
1	If C is C <sub>1</sub>	and t is t <sub>1</sub>	then T is T <sub>2</sub>	42	If C is C <sub>5</sub>	and t is t <sub>6</sub>	then T is T <sub>7</sub>
2	If C is C <sub>1</sub>	and t is t <sub>2</sub>	then T is T <sub>3</sub>	43	If C is C <sub>5</sub>	and t is t <sub>7</sub>	then T is T <sub>8</sub>
3	If C is C <sub>1</sub>	and t is t <sub>3</sub>	then T is T <sub>3</sub>	44	If C is C <sub>5</sub>	and t is t <sub>8</sub>	then T is T <sub>9</sub>
4	If C is C <sub>1</sub>	and t is t <sub>4</sub>	then T is T <sub>3</sub>	45	If C is C <sub>5</sub>	and t is t <sub>9</sub>	then T is T <sub>9</sub>
5	If C is C <sub>1</sub>	and t is t <sub>5</sub>	then T is T <sub>3</sub>	46	If C is C <sub>6</sub>	and t is t <sub>1</sub>	then T is T <sub>2</sub>
6	If C is C <sub>1</sub>	and t is t <sub>6</sub>	then T is T <sub>3</sub>	47	If C is C <sub>6</sub>	and t is t <sub>2</sub>	then T is T <sub>3</sub>
7	If C is C <sub>1</sub>	and t is t <sub>7</sub>	then T is T <sub>3</sub>	48	If C is C <sub>6</sub>	and t is t <sub>3</sub>	then T is T <sub>3</sub>
8	If C is C <sub>1</sub>	and t is t <sub>8</sub>	then T is T <sub>3</sub>	49	If C is C <sub>6</sub>	and t is t <sub>4</sub>	then T is T <sub>4</sub>
9	If C is C <sub>1</sub>	and t is t <sub>9</sub>	then T is T <sub>4</sub>	50	If C is C <sub>6</sub>	and t is t <sub>5</sub>	then T is T <sub>5</sub>
10	If C is C <sub>2</sub>	and t is t <sub>1</sub>	then T is T <sub>2</sub>	51	If C is C <sub>6</sub>	and t is t <sub>6</sub>	then T is T <sub>5</sub>
11	If C is C <sub>2</sub>	and t is t <sub>2</sub>	then T is T <sub>3</sub>	52	If C is C <sub>6</sub>	and t is t <sub>7</sub>	then T is T <sub>7</sub>
12	If C is C <sub>2</sub>	and t is t <sub>3</sub>	then T is T <sub>3</sub>	53	If C is C <sub>6</sub>	and t is t <sub>8</sub>	then T is T <sub>8</sub>
13	If C is C <sub>2</sub>	and t is t <sub>4</sub>	then T is T <sub>4</sub>	54	If C is C <sub>6</sub>	and t is t <sub>9</sub>	then T is T <sub>9</sub>
14	If C is C <sub>2</sub>	and t is t <sub>5</sub>	then T is T <sub>4</sub>	55	If C is C <sub>7</sub>	and t is t <sub>1</sub>	then T is T <sub>1</sub>
15	If C is C <sub>2</sub>	and t is t <sub>6</sub>	then T is T <sub>4</sub>	56	If C is C <sub>7</sub>	and t is t <sub>2</sub>	then T is T <sub>2</sub>
16	If C is C <sub>2</sub>	and t is t <sub>7</sub>	then T is T <sub>5</sub>	57	If C is C <sub>7</sub>	and t is t <sub>3</sub>	then T is T <sub>2</sub>
17	If C is C <sub>2</sub>	and t is t <sub>8</sub>	then T is T <sub>5</sub>	58	If C is C <sub>7</sub>	and t is t <sub>4</sub>	then T is T <sub>3</sub>
18	If C is C <sub>2</sub>	and t is t <sub>9</sub>	then T is T <sub>6</sub>	59	If C is C <sub>7</sub>	and t is t <sub>5</sub>	then T is T <sub>3</sub>
19	If C is C <sub>3</sub>	and t is t <sub>1</sub>	then T is T <sub>3</sub>	60	If C is C <sub>7</sub>	and t is t <sub>6</sub>	then T is T <sub>3</sub>
20	If C is C <sub>3</sub>	and t is t <sub>2</sub>	then T is T <sub>4</sub>	61	If C is C <sub>7</sub>	and t is t <sub>7</sub>	then T is T <sub>4</sub>
21	If C is C <sub>3</sub>	and t is t <sub>3</sub>	then T is T <sub>4</sub>	62	If C is C <sub>7</sub>	and t is t <sub>8</sub>	then T is T <sub>4</sub>
22	If C is C <sub>3</sub>	and t is t <sub>4</sub>	then T is T <sub>4</sub>	63	If C is C <sub>7</sub>	and t is t <sub>9</sub>	then T is T <sub>5</sub>
23	If C is C <sub>3</sub>	and t is t <sub>5</sub>	then T is T <sub>5</sub>	64	If C is C <sub>8</sub>	and t is t <sub>1</sub>	then T is T <sub>1</sub>
24	If C is C <sub>3</sub>	and t is t <sub>6</sub>	then T is T <sub>5</sub>	65	If C is C <sub>8</sub>	and t is t <sub>2</sub>	then T is T <sub>1</sub>
25	If C is C <sub>3</sub>	and t is t <sub>7</sub>	then T is T <sub>6</sub>	66	If C is C <sub>8</sub>	and t is t <sub>3</sub>	then T is T <sub>1</sub>
26	If C is C <sub>3</sub>	and t is t <sub>8</sub>	then T is T <sub>6</sub>	67	If C is C <sub>8</sub>	and t is t <sub>4</sub>	then T is T <sub>1</sub>
27	If C is C <sub>3</sub>	and t is t <sub>9</sub>	then T is T <sub>7</sub>	68	If C is C <sub>8</sub>	and t is t <sub>5</sub>	then T is T <sub>1</sub>
28	If C is C <sub>4</sub>	and t is t <sub>1</sub>	then T is T <sub>3</sub>	69	If C is C <sub>8</sub>	and t is t <sub>6</sub>	then T is T <sub>2</sub>
29	If C is C <sub>4</sub>	and t is t <sub>2</sub>	then T is T <sub>3</sub>	70	If C is C <sub>8</sub>	and t is t <sub>7</sub>	then T is T <sub>2</sub>
30	If C is C <sub>4</sub>	and t is t <sub>3</sub>	then T is T <sub>4</sub>	71	If C is C <sub>8</sub>	and t is t <sub>8</sub>	then T is T <sub>2</sub>
31	If C is C <sub>4</sub>	and t is t <sub>4</sub>	then T is T <sub>5</sub>	72	If C is C <sub>8</sub>	and t is t <sub>9</sub>	then T is T <sub>2</sub>
32	If C is C <sub>4</sub>	and t is t <sub>5</sub>	then T is T <sub>5</sub>	73	If C is C <sub>9</sub>	and t is t <sub>1</sub>	then T is T <sub>1</sub>
33	If C is C <sub>4</sub>	and t is t <sub>6</sub>	then T is T <sub>6</sub>	74	If C is C <sub>9</sub>	and t is t <sub>2</sub>	then T is T <sub>2</sub>
34	If C is C <sub>4</sub>	and t is t <sub>7</sub>	then T is T <sub>7</sub>	75	If C is C <sub>9</sub>	and t is t <sub>3</sub>	then T is T <sub>2</sub>
35	If C is C <sub>4</sub>	and t is t <sub>8</sub>	then T is T <sub>8</sub>	76	If C is C <sub>9</sub>	and t is t <sub>4</sub>	then T is T <sub>3</sub>
36	If C is C <sub>4</sub>	and t is t <sub>9</sub>	then T is T <sub>9</sub>	77	If C is C <sub>9</sub>	and t is t <sub>5</sub>	then T is T <sub>3</sub>
37	If C is C <sub>5</sub>	and t is t <sub>1</sub>	then T is T <sub>3</sub>	78	If C is C <sub>9</sub>	and t is t <sub>6</sub>	then T is T <sub>3</sub>
38	If C is C <sub>5</sub>	and t is t <sub>2</sub>	then T is T <sub>3</sub>	79	If C is C <sub>9</sub>	and t is t <sub>7</sub>	then T is T <sub>3</sub>
39	If C is C <sub>5</sub>	and t is t <sub>3</sub>	then T is T <sub>4</sub>	80	If C is C <sub>9</sub>	and t is t <sub>8</sub>	then T is T <sub>3</sub>
40	If C is C <sub>5</sub>	and t is t <sub>4</sub>	then T is T <sub>5</sub>	81	If C is C <sub>9</sub>	and t is t <sub>9</sub>	then T is T <sub>3</sub>
41	If C is C <sub>5</sub>	and t is t <sub>5</sub>	then T is T <sub>6</sub>				

**Table 5.** Rules of RBMTF for Flow Rate (g/h)

Rule number	C	t	FR	Rule number	If	C	and	t	then	FR
1	If C is C <sub>1</sub>	and t is t <sub>1</sub>	then FR is FR <sub>1</sub>	42	If C is C <sub>5</sub>	and t is t <sub>6</sub>		then FR is FR <sub>5</sub>		
2	If C is C <sub>1</sub>	and t is t <sub>2</sub>	then FR is FR <sub>1</sub>	43	If C is C <sub>5</sub>	and t is t <sub>7</sub>		then FR is FR <sub>5</sub>		
3	If C is C <sub>1</sub>	and t is t <sub>3</sub>	then FR is FR <sub>1</sub>	44	If C is C <sub>5</sub>	and t is t <sub>8</sub>		then FR is FR <sub>5</sub>		
4	If C is C <sub>1</sub>	and t is t <sub>4</sub>	then FR is FR <sub>1</sub>	45	If C is C <sub>5</sub>	and t is t <sub>9</sub>		then FR is FR <sub>5</sub>		
5	If C is C <sub>1</sub>	and t is t <sub>5</sub>	then FR is FR <sub>1</sub>	46	If C is C <sub>6</sub>	and t is t <sub>1</sub>		then FR is FR <sub>6</sub>		
6	If C is C <sub>1</sub>	and t is t <sub>6</sub>	then FR is FR <sub>1</sub>	47	If C is C <sub>6</sub>	and t is t <sub>2</sub>		then FR is FR <sub>6</sub>		
7	If C is C <sub>1</sub>	and t is t <sub>7</sub>	then FR is FR <sub>1</sub>	48	If C is C <sub>6</sub>	and t is t <sub>3</sub>		then FR is FR <sub>6</sub>		
8	If C is C <sub>1</sub>	and t is t <sub>8</sub>	then FR is FR <sub>1</sub>	49	If C is C <sub>6</sub>	and t is t <sub>4</sub>		then FR is FR <sub>6</sub>		
9	If C is C <sub>1</sub>	and t is t <sub>9</sub>	then FR is FR <sub>1</sub>	50	If C is C <sub>6</sub>	and t is t <sub>5</sub>		then FR is FR <sub>6</sub>		
10	If C is C <sub>2</sub>	and t is t <sub>1</sub>	then FR is FR <sub>2</sub>	51	If C is C <sub>6</sub>	and t is t <sub>6</sub>		then FR is FR <sub>6</sub>		
11	If C is C <sub>2</sub>	and t is t <sub>2</sub>	then FR is FR <sub>2</sub>	52	If C is C <sub>6</sub>	and t is t <sub>7</sub>		then FR is FR <sub>6</sub>		
12	If C is C <sub>2</sub>	and t is t <sub>3</sub>	then FR is FR <sub>2</sub>	53	If C is C <sub>6</sub>	and t is t <sub>8</sub>		then FR is FR <sub>6</sub>		
13	If C is C <sub>2</sub>	and t is t <sub>4</sub>	then FR is FR <sub>2</sub>	54	If C is C <sub>6</sub>	and t is t <sub>9</sub>		then FR is FR <sub>6</sub>		
14	If C is C <sub>2</sub>	and t is t <sub>5</sub>	then FR is FR <sub>2</sub>	55	If C is C <sub>7</sub>	and t is t <sub>1</sub>		then FR is FR <sub>7</sub>		
15	If C is C <sub>2</sub>	and t is t <sub>6</sub>	then FR is FR <sub>2</sub>	56	If C is C <sub>7</sub>	and t is t <sub>2</sub>		then FR is FR <sub>7</sub>		
16	If C is C <sub>2</sub>	and t is t <sub>7</sub>	then FR is FR <sub>2</sub>	57	If C is C <sub>7</sub>	and t is t <sub>3</sub>		then FR is FR <sub>7</sub>		
17	If C is C <sub>2</sub>	and t is t <sub>8</sub>	then FR is FR <sub>2</sub>	58	If C is C <sub>7</sub>	and t is t <sub>4</sub>		then FR is FR <sub>7</sub>		
18	If C is C <sub>2</sub>	and t is t <sub>9</sub>	then FR is FR <sub>2</sub>	59	If C is C <sub>7</sub>	and t is t <sub>5</sub>		then FR is FR <sub>7</sub>		
19	If C is C <sub>3</sub>	and t is t <sub>1</sub>	then FR is FR <sub>3</sub>	60	If C is C <sub>7</sub>	and t is t <sub>6</sub>		then FR is FR <sub>7</sub>		
20	If C is C <sub>3</sub>	and t is t <sub>2</sub>	then FR is FR <sub>3</sub>	61	If C is C <sub>7</sub>	and t is t <sub>7</sub>		then FR is FR <sub>7</sub>		
21	If C is C <sub>3</sub>	and t is t <sub>3</sub>	then FR is FR <sub>3</sub>	62	If C is C <sub>7</sub>	and t is t <sub>8</sub>		then FR is FR <sub>7</sub>		
22	If C is C <sub>3</sub>	and t is t <sub>4</sub>	then FR is FR <sub>3</sub>	63	If C is C <sub>7</sub>	and t is t <sub>9</sub>		then FR is FR <sub>7</sub>		
23	If C is C <sub>3</sub>	and t is t <sub>5</sub>	then FR is FR <sub>3</sub>	64	If C is C <sub>8</sub>	and t is t <sub>1</sub>		then FR is FR <sub>7</sub>		
24	If C is C <sub>3</sub>	and t is t <sub>6</sub>	then FR is FR <sub>3</sub>	65	If C is C <sub>8</sub>	and t is t <sub>2</sub>		then FR is FR <sub>7</sub>		
25	If C is C <sub>3</sub>	and t is t <sub>7</sub>	then FR is FR <sub>3</sub>	66	If C is C <sub>8</sub>	and t is t <sub>3</sub>		then FR is FR <sub>7</sub>		
26	If C is C <sub>3</sub>	and t is t <sub>8</sub>	then FR is FR <sub>3</sub>	67	If C is C <sub>8</sub>	and t is t <sub>4</sub>		then FR is FR <sub>7</sub>		
27	If C is C <sub>3</sub>	and t is t <sub>9</sub>	then FR is FR <sub>3</sub>	68	If C is C <sub>8</sub>	and t is t <sub>5</sub>		then FR is FR <sub>7</sub>		
28	If C is C <sub>4</sub>	and t is t <sub>1</sub>	then FR is FR <sub>5</sub>	69	If C is C <sub>8</sub>	and t is t <sub>6</sub>		then FR is FR <sub>7</sub>		
29	If C is C <sub>4</sub>	and t is t <sub>2</sub>	then FR is FR <sub>4</sub>	70	If C is C <sub>8</sub>	and t is t <sub>7</sub>		then FR is FR <sub>7</sub>		
30	If C is C <sub>4</sub>	and t is t <sub>3</sub>	then FR is FR <sub>4</sub>	71	If C is C <sub>8</sub>	and t is t <sub>8</sub>		then FR is FR <sub>7</sub>		
31	If C is C <sub>4</sub>	and t is t <sub>4</sub>	then FR is FR <sub>4</sub>	72	If C is C <sub>8</sub>	and t is t <sub>9</sub>		then FR is FR <sub>7</sub>		
32	If C is C <sub>4</sub>	and t is t <sub>5</sub>	then FR is FR <sub>4</sub>	73	If C is C <sub>9</sub>	and t is t <sub>1</sub>		then FR is FR <sub>7</sub>		
33	If C is C <sub>4</sub>	and t is t <sub>6</sub>	then FR is FR <sub>4</sub>	74	If C is C <sub>9</sub>	and t is t <sub>2</sub>		then FR is FR <sub>7</sub>		
34	If C is C <sub>4</sub>	and t is t <sub>7</sub>	then FR is FR <sub>4</sub>	75	If C is C <sub>9</sub>	and t is t <sub>3</sub>		then FR is FR <sub>7</sub>		
35	If C is C <sub>4</sub>	and t is t <sub>8</sub>	then FR is FR <sub>4</sub>	76	If C is C <sub>9</sub>	and t is t <sub>4</sub>		then FR is FR <sub>7</sub>		
36	If C is C <sub>4</sub>	and t is t <sub>9</sub>	then FR is FR <sub>4</sub>	77	If C is C <sub>9</sub>	and t is t <sub>5</sub>		then FR is FR <sub>7</sub>		
37	If C is C <sub>5</sub>	and t is t <sub>1</sub>	then FR is FR <sub>6</sub>	78	If C is C <sub>9</sub>	and t is t <sub>6</sub>		then FR is FR <sub>7</sub>		
38	If C is C <sub>5</sub>	and t is t <sub>2</sub>	then FR is FR <sub>5</sub>	79	If C is C <sub>9</sub>	and t is t <sub>7</sub>		then FR is FR <sub>7</sub>		
39	If C is C <sub>5</sub>	and t is t <sub>3</sub>	then FR is FR <sub>5</sub>	80	If C is C <sub>9</sub>	and t is t <sub>8</sub>		then FR is FR <sub>7</sub>		
40	If C is C <sub>5</sub>	and t is t <sub>4</sub>	then FR is FR <sub>5</sub>	81	If C is C <sub>9</sub>	and t is t <sub>9</sub>		then FR is FR <sub>7</sub>		
41	If C is C <sub>5</sub>	and t is t <sub>5</sub>	then FR is FR <sub>5</sub>							



(a)



(b)

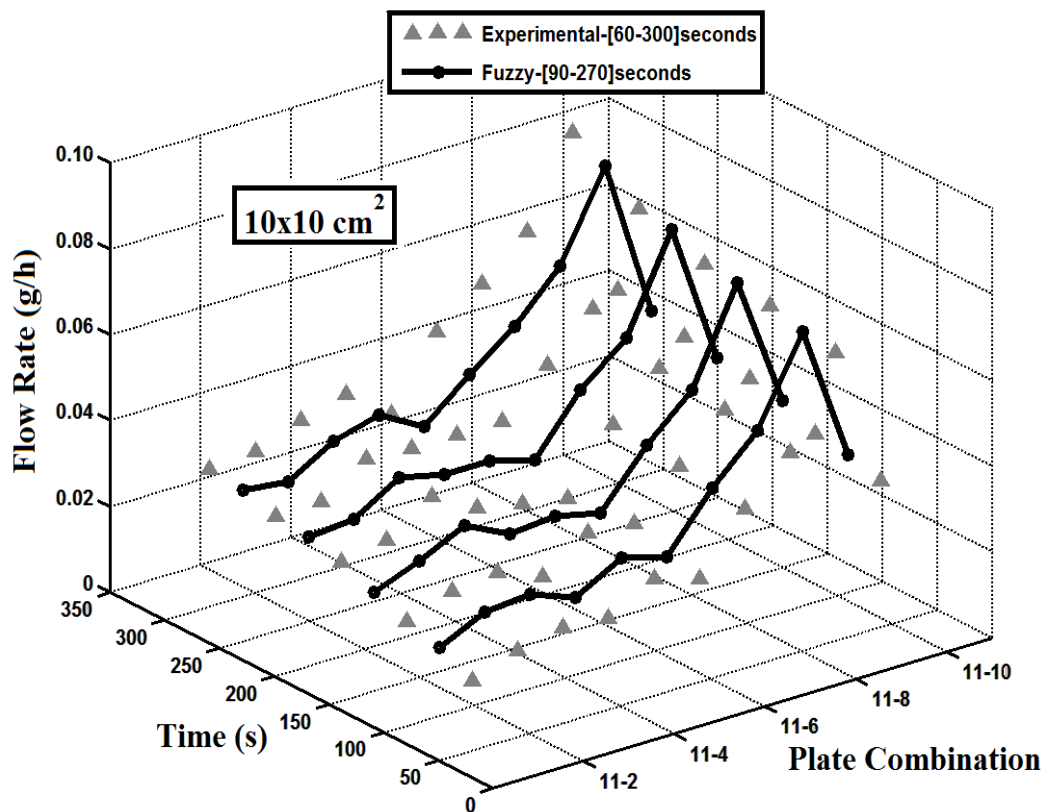
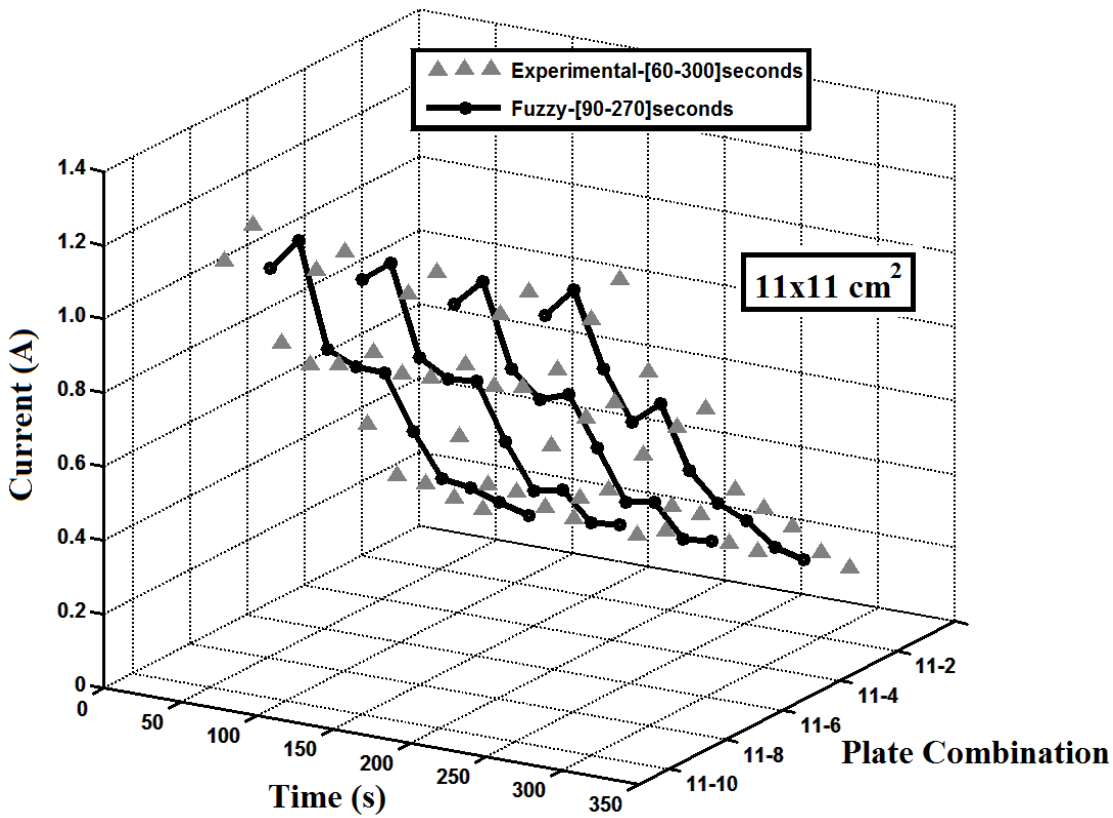


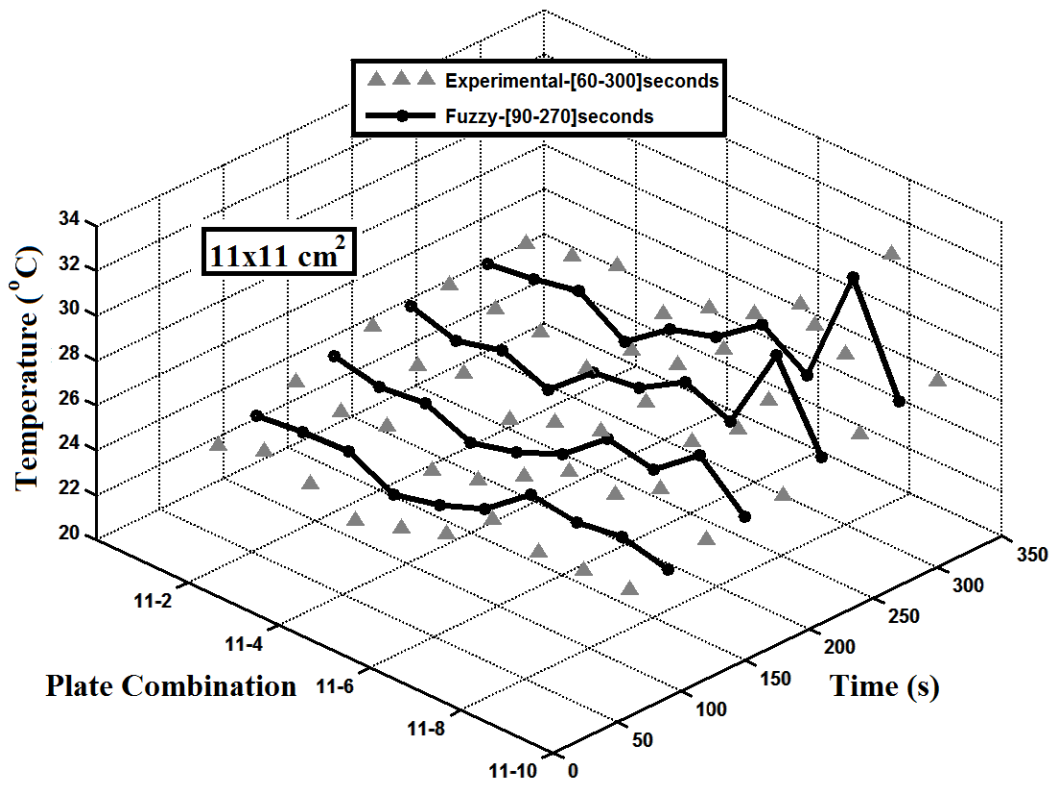
**Figure 3.** Comparison of experimental data of 10x10 cm<sup>2</sup> plate dimension with fuzzy predict for the variation of time with plate combination of output values (a) Current, (b) Temperature, (c) Flow Rate

These figures present that;

- The current value predicted by RBMTF for the 11-2 plate combination and  $t=90$  s is less than the current value from the results of the experimental work for the 11-2 plate combination and  $t=60$  s, but higher than the current value from the results of the experimental work for 11-2 plate combination and  $t=120$ s (Fig.3a).
- The temperature value predicted by RBMTF for the 11-5 plate combination and  $t=210$  s is higher than the temperature value from the results of the experimental work for the 11-5 plate combination and  $t=180$  s, but less than the temperature value from the results of the experimental work for 11-5 plate combination and  $t=240$ s (Fig. 3b).
- The flow rate value predicted by RBMTF for the 11-8 plate combination and  $t=270$  s is higher than the flow rate value from the results of the experimental work for the 11-8 plate combination and  $t=240$  s, but less than the flow rate value from the results of the experimental work for 11-8 plate combination and  $t=300$ s (Fig. 3c).



(a)



(b)

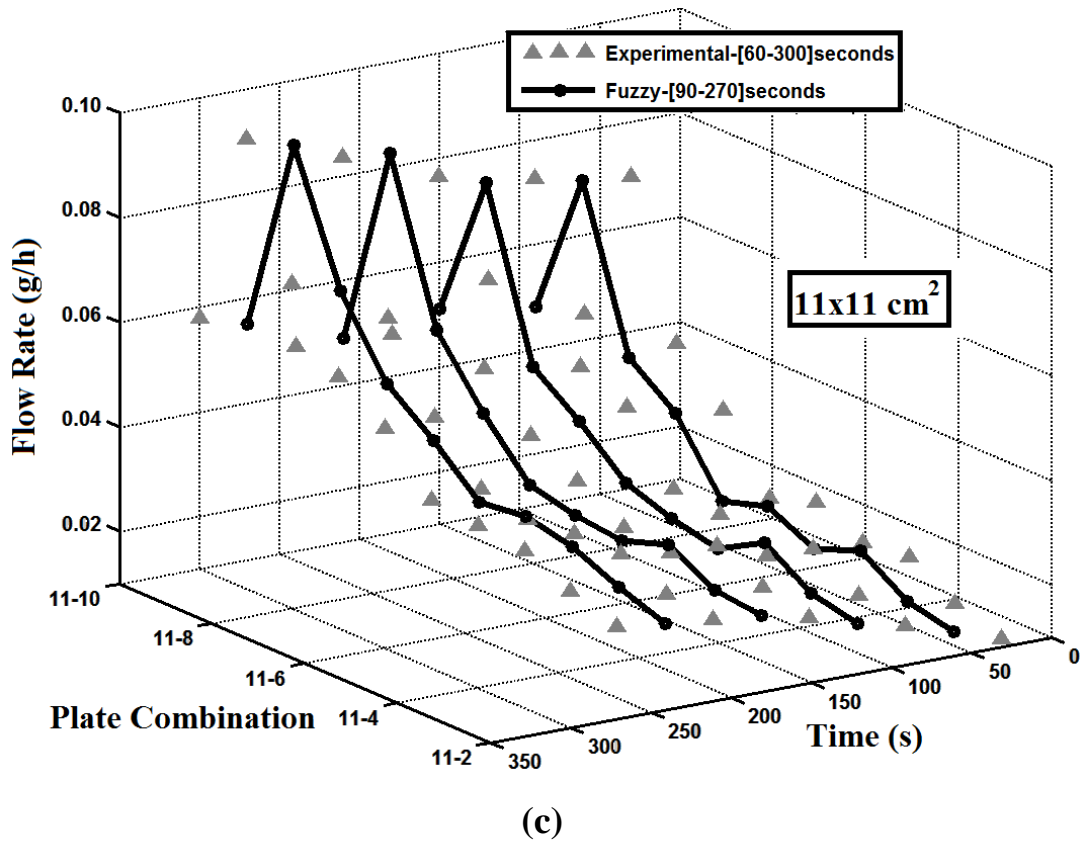


**Figure 4.** Comparison of experimental data of 11x11 cm<sup>2</sup> plate dimension with fuzzy predict for the variation of time with plate combination of output values (a) Current, (b) Temperature, (c) Flow Rate

Fig. 4 shows respectively, the comparison of experimental data for 11x11 cm<sup>2</sup> plate dimensions with fuzzy prediction for the variation of time with plate combination of current, temperature and flow rate values. From a comparison of the experimental results with the results of the fuzzy logic study, one can see that the results are quite compatible.

- The current value predicted by RBMTF for the 11-9 plate combination and t=150 s is less than the current value from the results of the experimental work for the 11-9 plate combination and t=120 s, but higher than the current value from the results of the experimental work for 11-9 plate combination and t=180s (Fig. 4a).
- The temperature value predicted by RBMTF for the 11-6 plate combination and t=210 s is higher than the temperature value from the results of the experimental work for the 11-6 plate combination and t=180 s, but less than the temperature value from the results of the experimental work for 11-6 plate combination and t=240s (Fig. 4b).
- The flow rate value predicted by RBMTF for the 11-3 plate combination and t=270 s is higher than the flow rate value from the results of the experimental work for the 11-3 plate combination and t=240 s, but less than the flow rate value from the results of the experimental work for 11-3 plate combination and t=300s (Fig. 4c).

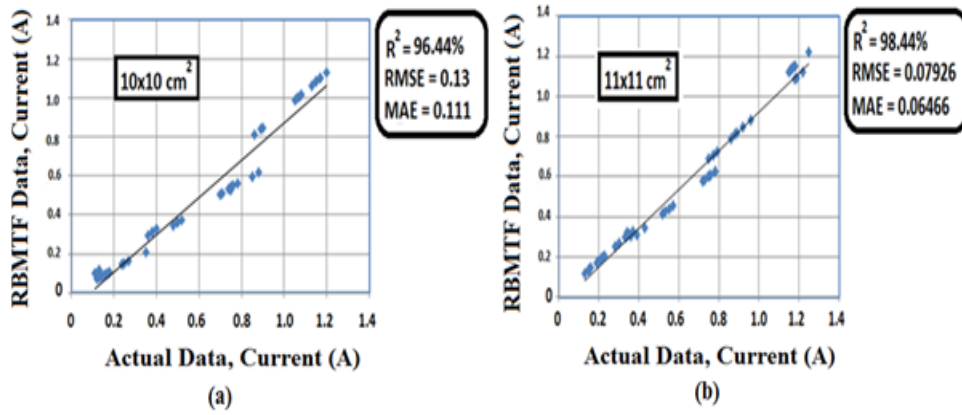
The comparison between experimental data and fuzzy logic is done using statistical methods. This methods include; root mean square error (RMSE), mean absolute error (MAE) and the coefficient of multiple determination (R<sup>2</sup>). Measures of average error or model performance then are based on statistical summaries of t<sub>i</sub> (target value) and o<sub>i</sub> (output value). When Figs. 5-7 and Table 6 are observed, it is found that actual values and the values from fuzzy technique are very close to each other.

$$\text{RMSE} = \sqrt{\frac{1}{N} \sum_{i=1}^N (t_i - o_i)^2} \quad (1)$$

$$\text{MAE} = \frac{1}{N} \sum_{i=1}^N |t_i - o_i| \quad (2)$$

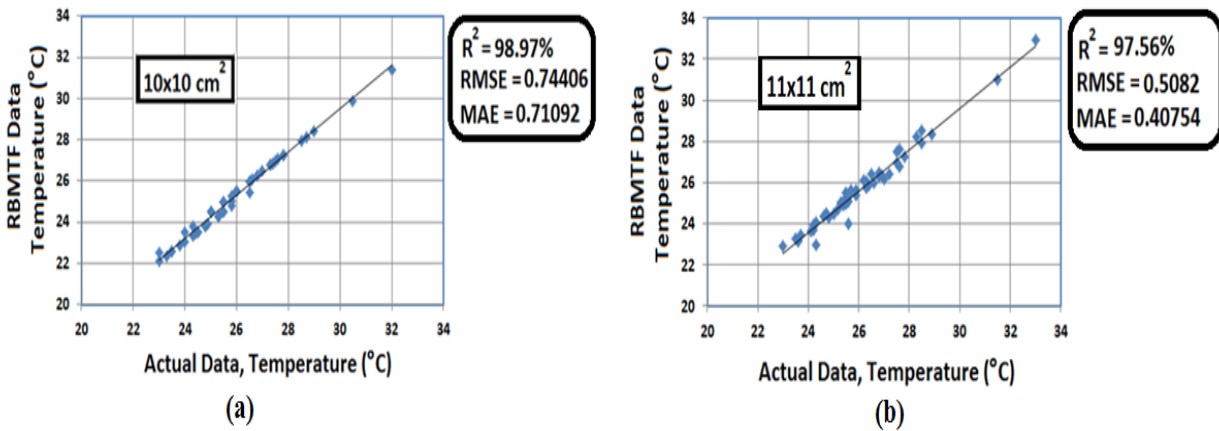
$$R^2 = 1 - \left( \frac{\sum_j (t_i - o_i)^2}{\sum_j (o_i)^2} \right) \quad (3)$$

Fig. 4a and b shows comparison of the actual and RBMTF results for 10x10 cm<sup>2</sup> and 11x11 cm<sup>2</sup> dimension plate current value. For 10x10 cm<sup>2</sup> dimension plate, RMSE, MAE and R<sup>2</sup> for the current is 0.13, 0.111 and 96.44% respectively. For 11x11 cm<sup>2</sup> dimension plate, RMSE, MAE and R<sup>2</sup> for the current is 0.07926, 0.06466 and 98.44% respectively.



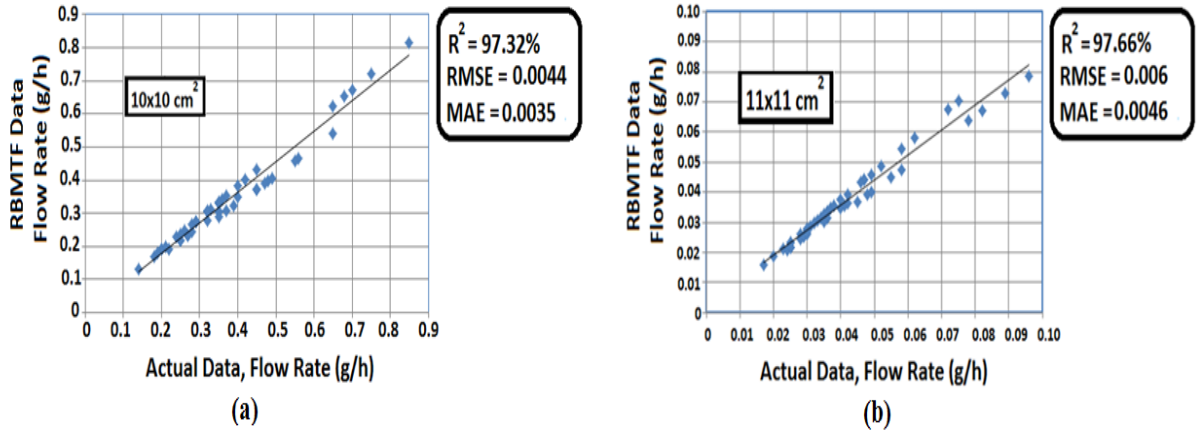
**Figure 5.** Comparison of the actual and RBMTF results for current with three different statistical method (a) 10x10 cm<sup>2</sup> plate dimension, (b) 11x11 cm<sup>2</sup> plate dimension

Fig. 6a and b shows comparison of the actual and RBMTF results for 10x10 cm<sup>2</sup> and 11x11 cm<sup>2</sup> dimension plate temperature value. For 10x10 cm<sup>2</sup> dimension plate, RMSE, MAE and R<sup>2</sup> for the temperature is 0.74406, 0.71092 and 98.97% respectively. For 11x11 cm<sup>2</sup> dimension plate, RMSE, MAE and R<sup>2</sup> for the temperature is 0.5082, 0.40754 and 97.56% respectively.



**Figure 6.** Comparison of the actual and RBMTF results for temperature with three different statistical method (a) 10x10 cm<sup>2</sup> plate dimension, (b) 11x11 cm<sup>2</sup> plate dimension

Fig. 7a and b shows comparison of the actual and RBMTF results for 10x10 cm<sup>2</sup> and 11x11 cm<sup>2</sup> dimension plate flow rate value. For 10x10 cm<sup>2</sup> dimension plate, RMSE, MAE and R<sup>2</sup> for the flow rate is 0.74406, 0.71092 and 98.97% respectively. For 11x11 cm<sup>2</sup> dimension plate, RMSE, MAE and R<sup>2</sup> for the flow rate is 0.5082, 0.40754 and 97.56% respectively.



**Figure 7.** Comparison of the actual and RBMTF results for current with three different statistical method (a) 10x10 cm<sup>2</sup> plate dimension, (b) 11x11 cm<sup>2</sup> plate dimension

**Table 6.** The statistical error values for current (A), temperature (°C), flow rate (g/h)

Parameters	Plate Dimension	RMSE	MAE	R <sup>2</sup>
Current (A)	10x10 cm <sup>2</sup>	0.13	0.111	96.44%
	11x11 cm <sup>2</sup>	0.07926	0.07926	98.44%
Temperature (°C)	10x10 cm <sup>2</sup>	0.74406	0.71092	98.97%
	11x11 cm <sup>2</sup>	0.5082	0.40754	97.56%
Flow Rate (g/h)	10x10 cm <sup>2</sup>	0.0044	0.0035	97.32%
	11x11 cm <sup>2</sup>	0.006	0.0046	97.66%

**CONCLUSIONS**

Artificial intelligence (AI= fuzzy logic, genetic algorithm, neural network etc.) systems are widely accepted as a technology offering an alternative way to tackle complex and ill-defined problems. They can learn from examples, are fault tolerant in the sense that they are able to handle noisy and incomplete data, they are able to deal with nonlinear problems, and, once trained, they can perform prediction and generalization at high speed. They have been used in diverse applications in control, robotics, pattern recognition, forecasting, medicine, power systems, manufacturing, optimization, signal processing, and social=psychological sciences. They are particularly useful in system modeling, such as in implementing complex mappings and system identification. AI systems comprise areas such as expert systems, artificial neural networks, genetic algorithms, fuzzy logic, and various hybrid systems, which combine two or more techniques (Kalogirou, 2003; Dincer et al., 2008). The aim of this article has been to show the possibility of the use of fuzzy logic for the calculation of performance HHO dry cell with different plate

combination. Namely, in this study, the method proposed is an alternative to the methods available for HHO dry cell experimental studies.

In the experimental study, tap water was used and the system was set to 5 minutes. For each combination, new cells were prepared. Current, temperature and flow rate values are determined for every 300 values which are obtained on every plate from 60 th second to 600 th second by 60 second intermittently for 10x10 cm<sup>2</sup> and 11x11 cm<sup>2</sup> plate. HHO dry cell performances in terms of current, temperature and flow rate for 90th-270th seconds by 60 second intermittently can be predicted by using RBMTF model without attempting any experiments. The temperature value predicted by RBMTF for the 11-6 plate combination and t=210s is 26.6 °C. This fuzzy predict value higher than the temperature value from the results of the experimental work for the 11-6 plate combination and t=180 s is 25.5 °C. The estimated value of fuzzy is less than the temperature value from the results of the experimental work for 11-6 plate combination and t=240s is 26.8 °C. The comparison between experimental data and fuzzy logic is done using statistical methods. This methods include; root mean square error (RMSE), mean absolute error (MAE) and the coefficient of multiple determination (R<sup>2</sup>). Their results show very acceptable relations between the results of the developed fuzzy model and the experimental results for HHO dry cell performance.

## REFERENCES

- Ata, S., 2015, PEM Yakıt Hücresinin Membran Performansının Deneysel Olarak İncelenmesi ve Enerji Ayırımı Olayının Bulanık Mantık Yöntemi ile Modellenmesi, Yüksek Lisans Tezi, Selçuk Üniversitesi Fen Bilimleri Enstitüsü, Konya.
- Ata, S., Dincer, K., "Rule-based Mamdani-type Fuzzy Modeling of Performance Proton Exchange Membrane Fuel Cell With Carbon Nanotube", 15th International Multidisciplinary Scientific GeoConference SGEM 2015, Albena, Bulgaria, pp. 487-494, 18-24 June 2015.
- Ata, S., Dincer, K., "Anot Tarafı Karbon Nanotüp İle Kaplanmış PEM Yakıt Hücresi Performansının Bulanık Mantık Yöntemiyle Modellenmesi", Ulusal Hidrojen Teknolojileri Kongresi UHTEK-2015, İstanbul, Türkiye, 20-23 Aralık 2015.
- Ata, S., Dincer, K., "Improving the Performance of Proton Exchange Membrane Fuel Cell Using Fuzzy Logic", 18th International Conference on Energy and Sustainable Development, Paris, France, pp. 16-17, 16-17 May 2016.
- Bölgen, M., 2010, Fuzzy Logic and Data Mining Techniques in Evaluating of Credit Risks of Companies, Master Thesis, Graduate School of Natural and Applied Sciences of Dokuz Eylül University, İzmir.
- Chakrapani, K., Neelamegam, P., 2011, "Optimization of Fuel Consumption Using HHO in HDL Technique Verified in FPGA", Journal of Theoretical and Applied Information Technology, Vol. 31, pp. 140-146.
- Dincer, K., Ongun, R., Dede, O., 2013, "HHO Hücresinin Performansının Deneysel Olarak İncelenmesi", Selçuk Üniversitesi Journal of Technical-Online, Vol. 12 (3), ISSN 1302/6178.
- Dincer, K., Tasdemir, S., Baskaya, S., Ucgul, I., Uysal, B. Z., 2008, "Fuzzy Modeling of Performance of Counterflow Ranque-Hilsch Vortex Tubes with Different Geometric Constructions", Numerical Heat Transfer, Part B: Fundamentals, Vol. 54 (6), pp. 499-517.
- Esteves, R.M., 2009, Data Fusion Algorithms for Assessing Sensors Accuracy in an Oil Production Well - A Bayesian approach, MSc Thesis, University of Stavanger Faculty of Science and Technology.
- İşıқтаş, A., Dincer, K., Ata, S., "Comparison Between the Effects of Different Types of Membership Functions on Fuzzy Logic for Hydroxy Dry Cell Performance", 16th International Multidisciplinary Scientific GeoConference SGEM 2016, Albena, Bulgaria, 28th June - 7th July 2016.
- Kalogirou, S.A., 2003, "Artificial Intelligence for the Modeling and Control of Combustion Processes: A Review", Progress in Energy and Combustion Science, Vol. 29, pp. 515-566.

- Keshwani, D.R., Jones, D. D., Meyer, G.E.R, Brand, M., 2008, "Rule-based Mamdani-type Fuzzy Modeling of Skin Permeability", *Applied Soft Computing*, Vol. 8, pp. 285-294.
- Kim, Y., Kim, S., 1999, "An Electrical Modelling and Fuzzy Logic Control of a Fuel Cell Generation System", *IEEE Transactions on Energy Conversion*, Vol. 14, pp. 239-244.
- Leelakrishnan, E., Lokesh, N., Suriyan, H., 2013, "Performance and Emission Characteristics of Brown's Gas Enriched Air in Spark Ignition Engine", *International Journal of Innovative Research in Science, Engineering and Technology*, Vol. 2, pp. 393-404.
- Madyira, D., Harding, W., "Effect of HHO on Four Stroke Petrol Engine Performance", 9th South African Conference on Computational and Applied Mechanics, 14-16 Jan 2014.
- Özek, A., Sinecen, M., 2004, "Klima Sistem Kontrolünün Bulanık Mantık ile Modellemesi", *Pamukkale Üniversitesi Mühendislik Bilimleri Dergisi*, Vol. 10, pp. 353-358.
- Sakthivel, S., 2014, "An Experimental Assessment of Performance and Exhaust Emission Characteristics by Addition of Hydroxy (HHO) Gas in Twin Cylinder C.I. Engine", *International Journal of Innovative Research in Science, Engineering and Technology*, Vol. 3(2), pp. 60-65.
- Shakhawat, C., Tahir, H., Neil, B., 2006, "Fuzzy Rule-Based Modelling for Human Health Risk from Naturally Occurring Radioactive Materials in Produced Water", *Journal of Environmental Radioactivity*, Vol. 89, pp. 1-17.
- Tiryaki, A.E., Kazan, R., 2007, "Bulaşık Makinesinin Bulanık Mantık ile Modellenmesi", *Mühendis ve Makine*, Vol. 48, pp. 3-8.
- Tong, S.W., Qian, D.W., Fang, J.J., Li, H.X., 2013, "Integrated Modelling and Variable Universe Fuzzy Control of a Hydrogen-Air Fuel Cell System", *International Journal of Electrochemical Science*, Vol. 8(3), pp. 3636-3652.
- Yıldız, Ş., Kişoğlu, S., 2011, "Bulanık Mantık Yaklaşımı ile Hazır Giyimde Beden Numarası Belirleme", *E-Journal of New World Sciences Academy*, Vol. 6, pp. 12-22.



## DESIGN AND IMPLEMENTATION OF AN OPEN ACCESS GEOPORTAL

<sup>1</sup>Fatih SARI

<sup>1</sup>Selçuk Üniversitesi, Çumra Uygulamalı Bilimler Yüksekokulu, Yönetim Bilişim Sistemleri Bölümü

<sup>1</sup>fatih.sari@selcuk.edu.tr

(Geliş/Received:08.01.2017 ; Kabul/Accepted in Revised Form: 29.07.2017 )

**ABSTRACT:** GeoPortal Systems are being considered one of the most important object in interoperability concept for Spatial data Management. With the developing technology of the information age, the need for accessing to spatial data is caused to effort for establishing national, regional and local information systems by institutes and organizations. Sharing and accessing of spatial datasets between institutes and organizations are being more important within interoperability concept. In this study, Open Access GeoPortal System is designed and applied to establish a common platform for institutes/organizations to analyze, interact, view, query and share spatial data. Open Access GeoPortal System, which is aimed to develop effective solutions in the field of using and sharing spatial data and establish interoperability concept, intends to provide an infrastructure for users to realize functions related with spatial data on web without installing any software. Open Access GeoPortal System is providing standardization stage acceleration, interoperability concept establishment and solutions to problems of spatial data thanks to the developed functions and processes which are working on international standardization organizations as like INSPIRE, ISO, W3C and OGC.

**Key Words:** *GeoPortal, Interoperability, Open Source Software Development, Web GIS, Web Services.*

### Açık GeoPortal Sistemi Tasarımı ve Uygulaması

**ÖZ:** GeoPortal sistemleri, Konumsal Veri Altyapıları için birlikte çalışabilirlik kavramını sağlayan en önemli yapılardan birisidir. Teknolojik gelişmeler, kurumların ve organizasyonların bilgiye erişme ihtiyacı, yerel, bölgesel ve ulusal ölçekte bilgi sistemlerinin oluşturulmasına neden olmaktadır. Birlikte çalışılabilirlik kavramı içerisinde kurumlar ve organizasyonlar arasındaki bilgi paylaşımı daha da önemli hale gelmiştir.

Bu çalışmada, kurumlar/organizasyonlar arasında konumsal verinin paylaşımı, analizi, görüntülenmesi ve depolanması için Açık GeoPortal sisteminin tesis edilmesi ve geliştirilmesi gerçekleştirilmiştir. Açık GeoPortal Sistemi, herhangi bir yazılım kurmadan konumsal verinin paylaşımına ve erişimine etkin çözüm getirmek amacı ile birlikte çalışılabilirlik kavramı kurmak için oluşturulmuştur. Açık GeoPortal Sistemi, standartlaşma çalışmalarının hızlanmasına, konumsal verinin paylaşımında yaşanan sorunlara çözüm getirmek amacı ile INSPIRE, ISO, W3C ve OGC organizasyonlarının standartları kullanılarak oluşturulmuştur.

**Anahtar Kelimeler:** *GeoPortal, Birlikte çalışılabilirlik, Açık kaynak kodlu yazılım geliştirme, Web CBS, Web servisleri,*

### INTRODUCTION

Access to spatial data, observations, and analytical results from diverse sources facilitates interdisciplinary and exploratory research, analysis, and decision-making, particularly in the case of geospatial information (Evans and Bambacus, 2005). Since the late 1990s, the geographic industry has

seen increasing interest and activity in the deployment of web sites that provide access to geographic content (Tait, 2005). This is achieved with the development of World Wide Web (WWW) and Geographical Information Systems (GIS) corporation. Geographic portals represent an applied response to this need to disseminate geographic data and leverage the GIS community's substantial investment in GIS capabilities and content (NRC, 1999).

Access, distribution and share of geographic information are the core object of each Spatial Data Infrastructure (SDI) project (Tang and Selwood, 2005). Spatial Data Infrastructure (SDI) are interoperability component for spatial data management and SDI's are the main object to establish interoperability at national, regional and local scales (Cömert, 2004). In (GSDI, 1999) definition, it is clearly defined that one of the main aim of SDI is to "provide instant access to geographic information. The United States National Research Council's Mapping Sciences Committee that first coined the term "spatial data infrastructure" in 1993, defined SDI as "the means to assemble geographic information that describes the arrangement and attributes of features and phenomena on the earth. In more explanatory definition, SDI is a combination of attribute and spatial data, which are coming from distributed databases and data sources, together with technologies, tools and technical structure to provide access to spatial data by users (Masser, 2005). The mentioned tools and technical structures are being GeoPortal systems.

There are many different GeoPortal definitions are available in literature and highlights "accessing spatial data via web" expression. (BEA, 2008) is defined GeoPortal as "a web site which is only one way to access spatial data and its applications". Java Portlet is defined GeoPortal as "personal or common web applications which are combining spatial data from different sources or data providers" (Abdelnur and Hepper, 2003). According to the (ESRI, 2013), GeoPortal is "a system to access spatial data without depending to location, format and data types". Open Geospatial Consortium (OGC) defines GeoPortal as a "human interface to collect online spatial data sources, spatial datasets and services together" (OGC, 2004). (Tang and Selwood, 2005) are defined GeoPortal as a gateway to the SDI systems. Thanks to the developments of web services, SDI implementation is being successful for accessing and sharing data. Because of GeoPortal systems constitute a connection bridge between data producers and users via web services, developing intelligent GeoPortal systems will be visible interface of SDI systems and it is being possible to accomplish the requirements of SDI systems (Iwaniak et al., 2011). Web services are providing advanced information technologies for comprehensive GIS functions to establish interoperability (You et al., 2012). Web services are developing a standardized internet based communication bridge between different institutes and information systems (Alonso et al., 2004), (Zhang and Li, 2005). Thanks to increasing importance and developments of SDI's, accessing to spatial data with web services is raised in last decade (Florczyk et al., 2012).

GeoPortals act as information aggregators providing a single access point to a variety of information sources. Therefore, they have an important role to play as entry points for the discovery, visualization and retrieval of data and services that constitute the geospatial web. This can be called as distributed computing and GeoPortals are the main structure of this concept. Distributed computing has provided the foundational standards and technology on which the Internet and distributed GIS are built. The core object of the distributed GIS and interoperability structures are the internet technology. The internet consists of technology standards, such as, Transmission Control Protocol/Internet Protocol (TCP/IP) and Hyper Text Transport Protocol (HTTP). The internet protocols specify the data transfer between server and client computers as well as software and network infrastructure. Because of GeoPortal systems are providing interoperability, some standards and definitions must be considered for GeoPortal development. U.S. Federal Geographic Data Committee (FGDC), The Open Geospatial Consortium, The International Organization for Standardization (ISO) / Technical Committee 211 (TC211), Open Geospatial Consortium (OGC) and INSPIRE committees are developing standards to establish interoperability platform within GeoPortal concept (Yang et al., 2006; Rautenbach et al., 2013).

In GeoPortal literature, existing GeoPortal systems and their infrastructure are being presented in most of the studies. Earth Science Gateway (ESG) GeoPortal (Bambacus et al., 2007), Knowledge

Annotation Initiative of the Knowledge Acquisition Community (KA2) GeoPortal (Benjamins et al., 1999), Germany Subsurface GeoPortal (DINO) (Lance et al., 2011), The developed GeoPortals around United Kingdom (Beaumont et al., 2005), Multi Agency Geographic Information for the Countryside, (MAGIC) GeoPortal (Askew et al., 2005), Disaster Risk Management Portal (NDRMP) GeoPortal, (Samadzadegan et al., 2008), European GeoPortal and European Spatial Data Infrastructure (ESDI) (Bernard et al., 2005) and INSPIRE GeoPortal (Crompvoets et al., 2004) are examined. Another important field of GeoPortal systems literature are SDI systems. An intelligent GeoPortal system design to provide spatial data to planners is developed by (Iwaniak et al., 2011), the reasons to develop GeoPortals and the importance for SDI projects are presented by (Maguire and Longley, 2005), the benefits of well-designed GeoPortals and the gaining in SDI Systems are detailed by (Tang and Selwood, 2005) and technologies, infrastructures and development stages for SDI Based GeoPortals are detailed by (Yang et al., 2006). Common GeoPortal development systems, technologies and system designs are also being presented in literature. The benefits of Web 2.0 technologies in GeoPortal systems (Bertrand, 2010), The Geospatial Portal Reference Architecture (Liu et al., 2008), A semantic spatial data search tool for E-Government GeoPortal (Wiegand, 2007), GeoPortal development technologies (Tait, 2005), The thematic map production via web services and (Rautenbach et al., 2013), Spatial data integration to GeoPortal (Yang et al., 2007), Resource Description Framework (RDF) tool to search spatial data in GeoPortal (Athanasios et al., 2009) and existing GeoPortals and developing their search and mapping technologies (Frehner and Brandli, 2006).

## OPEN ACCESS GEOPORTAL DESIGN

The main aim of the Open Access Geoportal (OAG) is to establish a platform which is providing tools to access, distribute, share and represent of spatial data through web based GeoPortal interfaces without using any GIS software with developed additional services and interfaces. Within OAG, additional spatial data functions, existing GeoPortal technologies, international standard specifications, developable function for existing GeoPortal interfaces are examined to improve the capability of OAG according to the requirements for spatial data users-providers and additional services are developed.

If have a look to the existing GeoPortals as like Group on Earth Observations (GEO), Ontario Council of University Scholars GeoPortal, National Oceanic and Atmospheric Administration (NOAA), National Geophysical Data Center (NGDC), United Nations World Food Programme SDI-T (WFP), United Nations Environment Programme (UNEP) GeoPortal, Spain IDECLM and HlanData GeoPortals, it seems that, commonly GeoPortal systems are providing view service of spatial data. Although GeoPortal systems are providing legend information of spatial data, styling spatial data or generating symbology with Styled Layer Descriptor (SLD) is being impossible due to the lack of symbology tools.

OAG is developed based on five main services addition to Heron-MC GeoPortal interface. Heron-MC JavaScript Library provides a user interface for the GeoPortal and WebGIS applications. Heron-MC supports a flexible and open source development environment for users and developers. Adding new functions and integrate new services into the client is possible and easy with its flexible structure with JavaScript and HTML programming languages. Additionally, Php programming language can be used for server-side operations scripting. Heron-MC interface is suitable for use as a GeoPortal interface due to the functions of view, query, display attribute data and other tools. The OAG structure is shown in Figure 1.

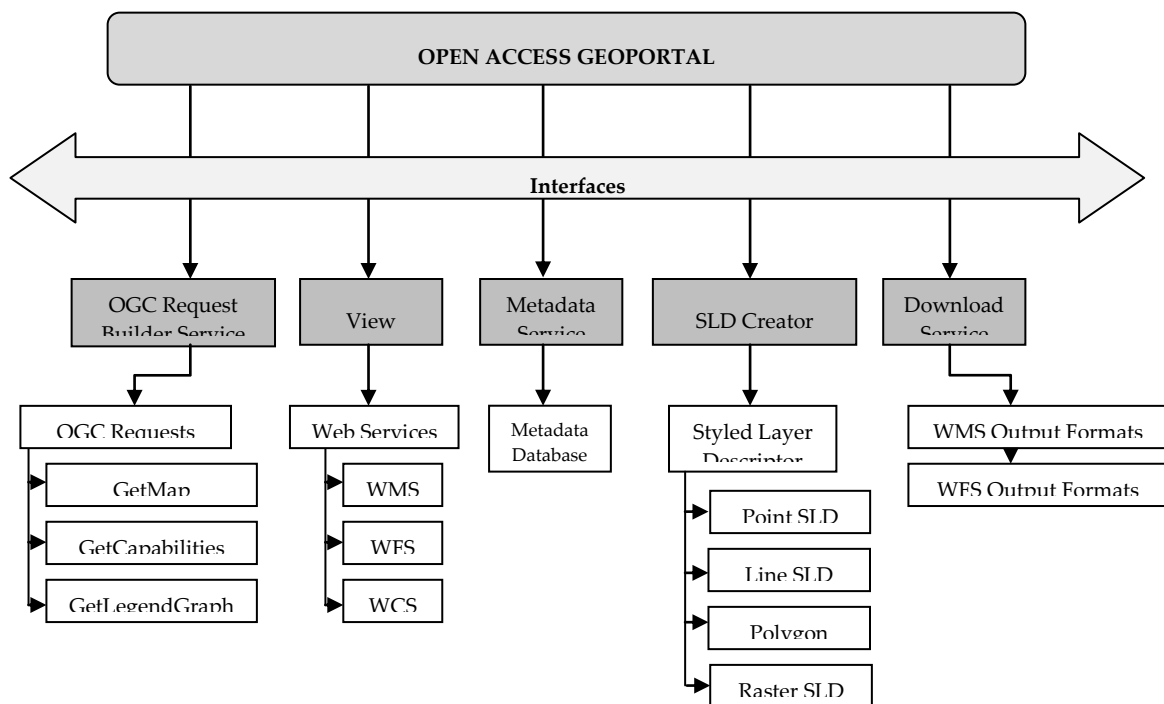


Figure 1. OAG structure

The OAG is being a technical platform between institutes and organizations which are using or producing spatial data together with the implementation of international standards as like OGC, INSPIRE, W3C and ISO. Within OAG, OGC standards are used to develop web services and related functions for spatial data with WMS, WFS and WCS. INSPIRE data specifications are used to define spatial data catalogues and their specifications with Annex-I and Annex-II-III catalogues. W3C standards are used to implement web interfaces and internet protocols for OAG. ISO standards are used to develop metadata service (ISO 19115) within 19100 Geographic Information Standard series. The OAG components, standards, organizations and programming languages according to the developed services are given in Table 1.

Table 1. OAG developing programming languages and open standards

Service	Standard	Organization	Programming Language
<b>View Service (Heron MC)</b>	CSS HTML	W3C	JavaScript
<b>Metadata Service</b>	19115 Metadata XML	ISO W3C	Php, JavaScript
<b>Download Service</b>	WMS WFS WCS OGC Requests XML	OGC W3C	Html, JavaScript, Php
<b>OGC Request Builder Service</b>	OGC Requests WMS WFS WCS 19136 GML SVG	OGC ISO W3C	Html, JavaScript, Php
<b>SLD Creator Service</b>	SLD XML	OGC W3C	Html, JavaScript, Php

View Service

One of the main object of GeoPortal system is the view service. View service is providing to display the web services on a map object. Therefore, instead of searching spatial data through a keyword as like in catalogue GeoPortals, it is being more useful to display web services and interact with them. View service is being GeoPortal interface which include tools and functions to interact with web services. The best way to interact with web services and use all the functions is to utilize the Heron Mapping Client (MC) JavaScript library. The OAG web interface home page and related function replacements are given in Figure 2.

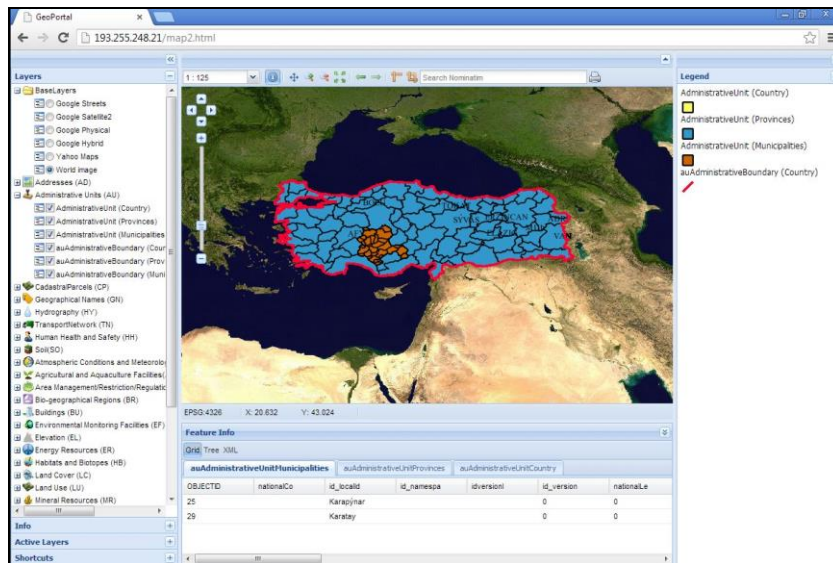


Figure 2. OAG home page

### OGC Request Builder Service

OGC Request Builder Service is developed to provide a user-interface to constitute request for retrieving data according to the user-defined parameters. Commonly in GeoPortal systems, web services are integrated with the default configuration in the fields of symbology, coordinate system and data format which is specified by spatial data authorities. OGC Request Builder Service is developed to provide download option of spatial data according to the user defined parameters within OAG. OGC Request Builder Service web forms for each request are given in Figure 3.



Figure 3. OGC Request Builder Service web forms

OGC Request Builder Service is based on PHP codes which are generating URL for requests according to the user defined parameters via web forms (Figure 3). The parameters are specifying the variables of request and defined in web forms according to the mandatory and optional parameters which is specified in OGC catalogues. The flowchart of the OGC Request Builder Service is given in Figure 4.

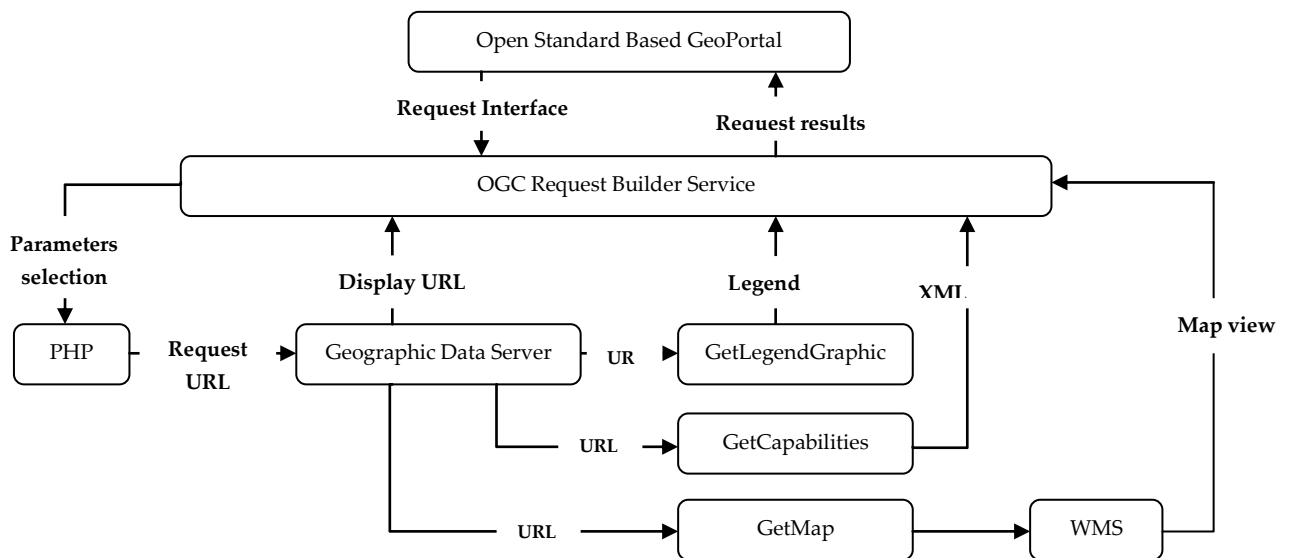


Figure 4. OGC Request Builder Service flowchart

**Download Service**

Download Service is developed to enable download operation spatial data through web services. Spatial data users are usually needs to get data from GeoPortal systems. Because of there are a large amount of spatial data format, software and spatial analysis functions are being used, spatial data should be download It is based on GetMap requests and including WMS, WFS and WCS supported output file formats. The structure is similar with the OGC Request Builder Service in the field of web service URL generating. The only difference is in Download Service, users are not specifying any

parameters to download data. Instead of this, by clicking to the desired file format, download option will be started. Download service interface is developed with Php codes including web service and data format selection. The Download Service web interface is given in Figure 5.

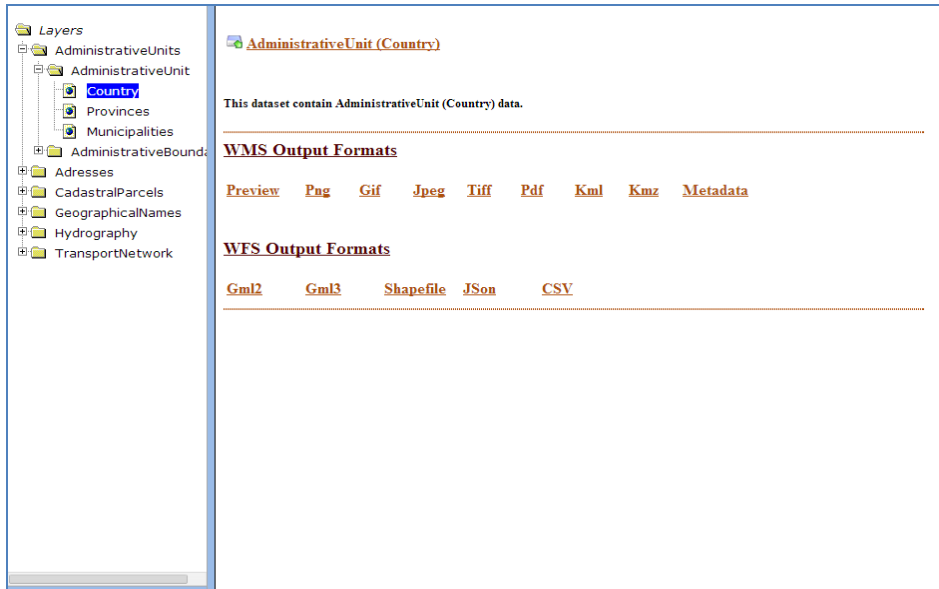


Figure 5. Download Service web interface

When users select data format, GetMap request is constituted with PHP codes and send to server for retrieve data in specified format. The Geographical data server will be processed the request and prepare the file format according to the GetMap request parameters. Download Service structure is given in Figure 6.

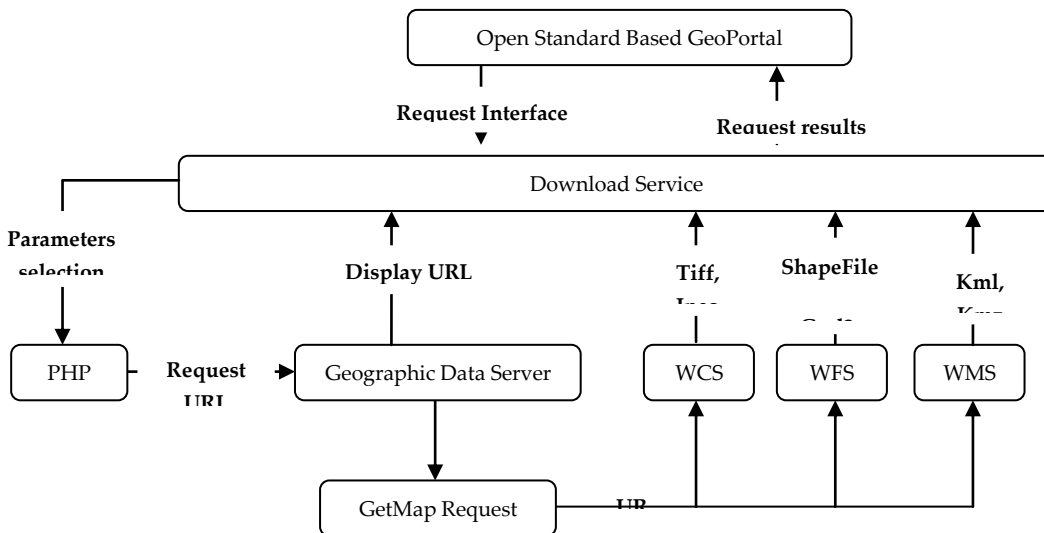


Figure 6. Download Service structure

**Metadata Service**

Metadata service is developed to provide view of metadata for web services via web interface. Because of metadata is including the descriptive information about web services, developed GeoPortal systems should include metadata services to increase the usability of web services in the terms of

interoperability. Metadata service is consisted from a MySQL database to store metadata files and HTML page to display related metadata. The metadata service is based on Php codes which are connect and retrieve metadata information from MySQL database and display on web pages. Metadata Service structure is given in Figure 7.

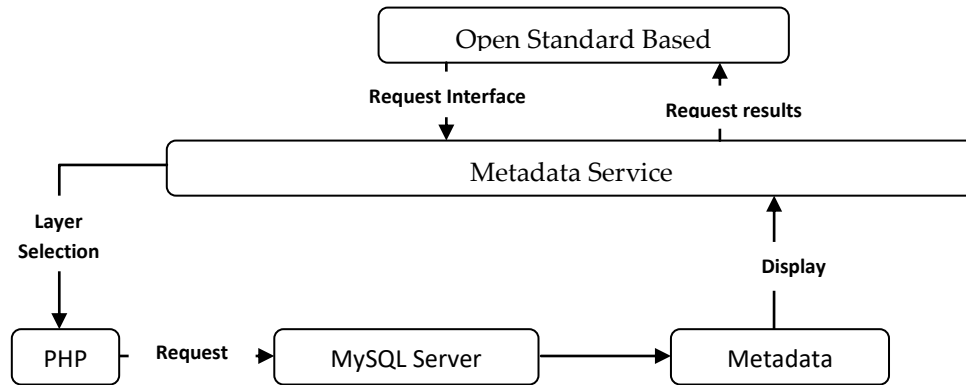


Figure 7. Metadata Service structure

The web page of the metadata service is given in Figure 8 for INSPIRE Administrative Unit thematic scheme.

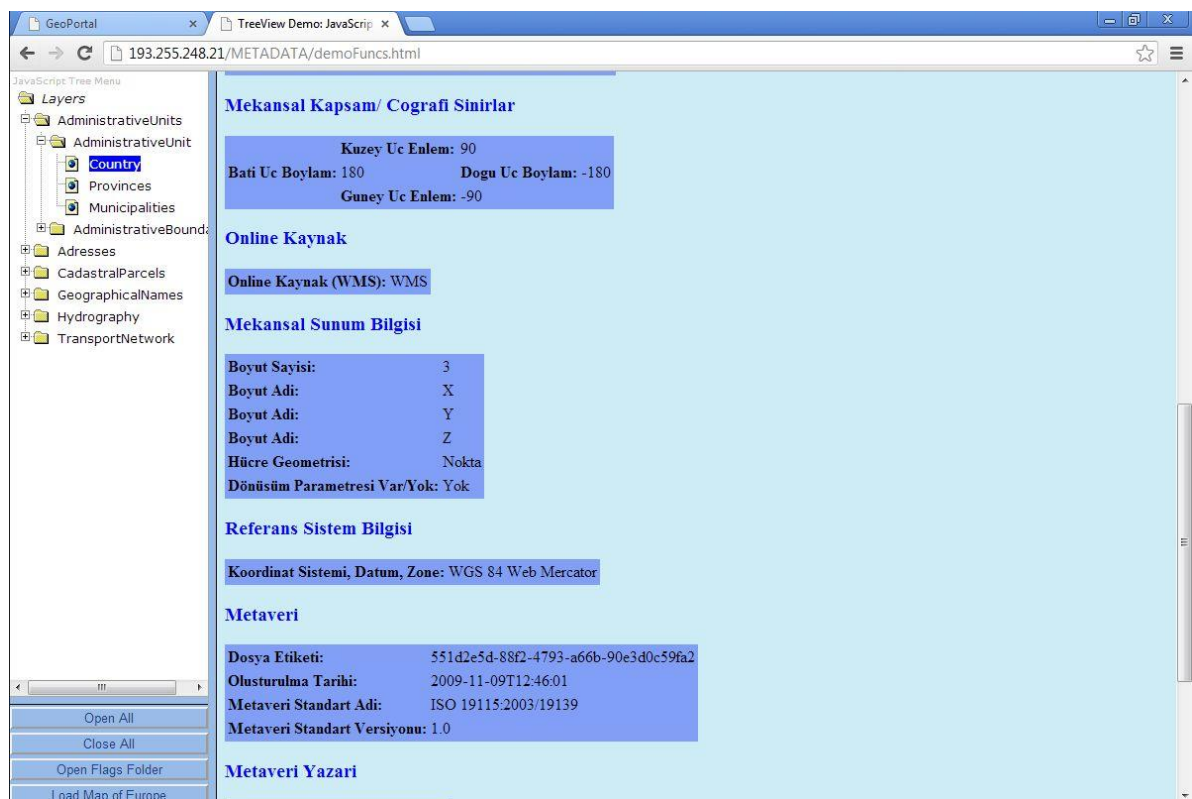


Figure 8. Metadata Service web page

SLD Creator Service

Web service symbology and related SLD files usually are being specified by spatial data authorities, thus, it is being impossible to define or create SLD files within GeoPortal systems. On the other hand, existing GeoPortal Systems are not including SLD creating function and users are unable to view, edit or change the SLD file within GeoPortal interfaces. Therefore, SLD files which are created by desktop GIS systems are couldn't be used in GeoPortal systems. SLD Creator Service is consist from user forms to select variables for each parameter of SLD files which are given in Figure 9.



Figure 9. SLD Service Web forms a) Line SLD b)Point SLD c) Polygon SLD d) Raster SLD

SLD is XML based files and define the variables between tags and can define point, polyline, polygon, raster files and their label options. Symbol styles, colors, sizes, placements, label fields, label

styles and related parameters can be defined with SLD files according to the point, polyline, polygon and raster data types. When users specified the parameters, PHP codes are generated the SLD files with inserting each variable into related tags. SLD Creator Service structure is given in Figure 10.

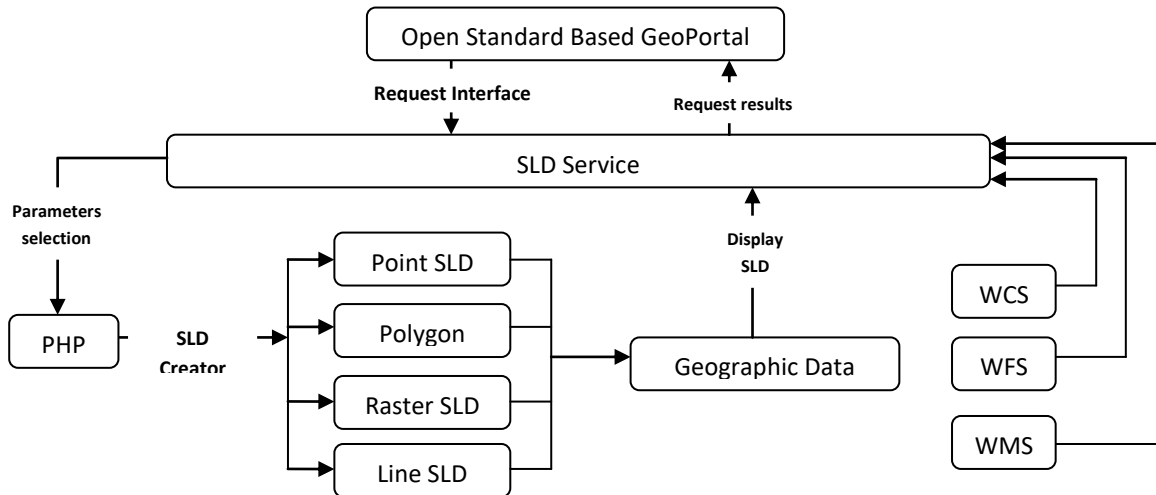


Figure 10. SLD Service structure

## RESULT AND DISCUSSION

OAG presenting a gateway to the distributed GIS due to the interoperability components and representing a reference GeoPortal application. One of the main obstacles of establishing GeoPortal is the status of spatial data. The solution of spatial data quality depends to INSPIRE and ISO standards to be understood by data providers. Before constituting GeoPortal systems, INSPIRE and ISO standards must be applied to spatial datasets. Addition to this, generating incomplete attribute data and metadata is required together with spatial data. This situation is also provide accurate and up-to-dated spatial data infrastructure and will contribute to OAG establishing concept. Reliable and up-to-dated spatial data will increase decision-making quality and decision support system applications. Standardization policies and applications should be started in every institute and then at national scales, spatial data should be integrated into NSDI.

### Discussion

OAG implementation can be useful in environmental monitoring such as meteorological monitoring, air quality, geological changes, agriculture management, water resources and urban settlements. OAG can be modified according to the requirements and aims of the projects. Thus, it is being possible to interact with spatial data and increase the usability of spatial data.

One of the main obstacles of establishing GeoPortal in Turkey is the status of spatial data. The solution of spatial data quality depends to INSPIRE and ISO standards to be understood by data providers. Before constituting GeoPortal systems, INSPIRE and ISO standards must be applied to spatial datasets. Addition to this, generating incomplete attribute data and metadata is required together with spatial data. This situation is also provide accurate and up-to-dated NSDI spatial data infrastructure and will contribute to Turkey National GIS (TNGIS) establishing concept. Reliable and up-to-dated spatial data will increase decision-making quality and decision support system applications. Standardization policies and applications should be started in every institute and then at national scales, spatial data should be integrated into NSDI.

Because of GeoPortal systems are the main component of interoperability concept, as mentioned in TNGIS policies, Turkey should establish national GeoPortal system to provide accessibility of spatial data for every institute and data users. GeoPortal systems will contribute to interoperability concept in Turkey both accessibility to spatial data and the quality requirements of each spatial datasets all around Turkey.

## REFERENCES

- Abdelnur, A., Hepper, S., 2003, *Java Portlet Specification*, Version 1.0, Status: FCS Specification, Specification Lead: Sun Microsystems, Inc., Release: August 29.
- Alonso, G., Casati, F., Kuno, H., Machiraju, V., 2004, *Web Services. Concepts, Architectures and Applications*, Springer, Berlin/Heidelberg.
- Askew, D., Evans, S., Matthews, R., Swanton, P., 2005, "MAGIC: a Geoportal for the English Countryside", *Computers, Environment and Urban Systems*, Vol. 29, pp. 71–85.
- Athanasis, N., Kalabokidis, K., Vaitis, M., Soulakellis, N., 2009, "Towards a Semantics-Based Approach in the Development of Geographic Portals", *Computers & Geosciences*, Vol. 35, pp. 301–308.
- Bambacus, M., Yang, C., Evans, J., Cole, M., Alameh, N., Marley, S., 2007, "An Interoperable Portal Supporting Prototyping Geospatial Applications", *URISA Journal*, Vol. 19(2), pp.15-21.
- BEA, 2008, *BEA WebLogic Portal, Portal Development Guide*, BEA Systems, Inc.
- Beaumont, P., Longley, P.A., Maguire, D.J., 2005, "Geographic Information Portals - a UK Perspective", *Computers, Environment and Urban Systems*, Vol. 29, pp. 49–69.
- Benjamins, R. Fensel, D., Decker, S., 1999, "KA2: Building Ontologies for the Internet: A Midterm Report", *International Journal of Human Computer Studies*, Vol. 51(3), pp. 687.
- Bernard, L., Kanellopoulos, I., Annoni, A., Smits, P., 2005, "The European Geoportal—One Step Towards the Establishment of a European Spatial Data Infrastructure", *Computers, Environment and Urban Systems*, Vol. 29, pp. 15–31.
- Bertrand De Longueville, 2010, "Community-Based Geoportals: The Next Generation? Concepts and Methods for The Geospatial Web 2.0." *Computers, Environment and Urban Systems*, Vol. 34, pp. 299–308.
- Cömert, Ç., 2004, "Web Services and National Spatial Data Infrastructures", *International Society of Photogrammetry and Remote Sensing, XXth Congress, Commission IV, WG IV/4, Spatial Data Infrastructure*, Istanbul, Turkey, 12-23 July 2004.
- Crompvoets, J., Wachowicz, M., Bree, F., Bregt, A., 2004, "Impact Assessment of The Inspire Geo-Portal", *10th EC GI & GIS Workshop, ESDI State of the Art*, Warsaw, Poland, 20-25 June 2004.
- ESRI, 2013, *GIS Portal Technology*, ESRI White Paper, <http://www.esri.com/library/whitepapers/pdfs/geospatial-portal-technology.pdf>, (10.10.2016).
- Evans, J.D., Bambacus, M.J., 2005, "NASA's Earth-Sun System Gateway: an Open Standards-Based Portal to Geospatial Data and Services", *Geoscience and Remote Sensing Symposium, IGARSS '05, Proceedings 2005 IEEE International*, Seoul, Korea, 25-29 July 2005.
- Florczyk, A.J., Noguera, J., Zarazaga-Soria, F.J., Bejar, R., 2012, "Identifying Ortho images in Web Map Services", *Computers & Geosciences*, Vol. 47, pp. 130–142.
- Frehner, M., Brandli, M., 2006, "Virtual Database: Spatial Analysis in a Web-based Data Management System for Distributed Ecological Data", *Environmental Modelling & Software*, Vol. 21, pp. 1544–1554.
- GSDI, 1999, *The Strategic Imperative of a Global Spatial Data Infrastructure*, <http://www.gsdidocs.org/docs1999/stratim.html>, (07.10.2016).
- Iwaniak, A., Kaczmarek, I., Kubik, T., Łukowicz, J., Paluszynski, W., Kourie, D., Cooper, A., Coetsee, S., 2011, "An Intelligent Geoportal For Spatial Planning, Intelligent geoportal for spatial planning", *25th International Cartographic Conference (ICC 2011)*, Paris, France, 3-8 Jul 2011.

- Lance, K.T., Georgiadou, Y.P., Bregt, A.K., 2011, "Evaluation of the Dutch Subsurface Geoportal: What Lies Beneath?", *Computers, Environment and Urban Systems*, Vol. 35, pp. 150–158.
- Liu, L., Li, D., Shao, Z., 2008, "Design and Implementation of a Geospatial Portal", *Geoinformatics 2008 and Joint Conference on GIS and Built Environment: Geo-Simulation and Virtual GIS Environments*.
- Maguire, D.J., Longley, P.A., 2005, "The Emergence of Geoportals and Their Role in Spatial Data Infrastructures", *Computers, Environment and Urban Systems*, Vol. 29, pp. 3–14.
- Masser, I. 2005, *GIS Worlds: Creating Spatial Data Infrastructures*, Redlands: ESRI Press.
- National Research Council, 1999, *Distributed Geo libraries: Spatial Information Resources*, National Academy Press: Washington, DC.
- OGC, 2004. *Geospatial Portal Reference Architecture*, A Community Guide to Implementing Standards-Based Geospatial Portals, Version: 0.2, OGC 04-039, OGC Discussion Paper.
- Rautenbach, V., Coetzee, S., Iwaniak, A., 2013, "Orchestrating OGC Web Services to Produce Thematic Maps in a Spatial Information Infrastructure", *Computers, Environment and Urban Systems*, Vol. 37, pp. 107–120.
- Samadzadegan, F., Saeedi, S., Alvand, A., 2008, "Design and Implementation of a Service Oriented Geospatial Portal for Disaster Risk Management", *Tenth International Conference for Spatial Data Infrastructure*, St. Augustine, Trinidad, 25-29 February 2008.
- Tait, M.G., 2005, "Implementing Geoportals: Applications of Distributed GIS", *Computers, Environment and Urban Systems*, Vol. 29, pp. 33–47.
- Tang, W., Selwood, J., 2005, "Spatial Portals: Adding Value To Spatial Data Infrastructures", *ISPRS Workshop on Service and Application of Spatial Data Infrastructure*, XXXVI(4/W6), Hangzhou, China, 14- 16 October 2005.
- Wiegand, N., 2007, "Semantic Web for Geospatial E-Government Portal", *The Proceedings of the 8th Annual International Digital Government Research Conference*, Philadelphia, 20-23 May 2007.
- Yang, P.C., Cao, Y., Evans, J., Kafatos, M., Bambacus, M., 2006, "Spatial Web Portal for Building Spatial Data Infrastructure", *Journal of The International Association of Chinese Professionals in Geographic Information Sciences*, Vol. 6, pp. 38-43.
- Yang, C., Evans, J., Cole, M., Alameh, N., Marley, S., Bambacus, M., 2007, "The Emerging Concepts and Applications of the Spatial Web Portal", *PE&RS*, Vol. 73(6), pp. 691-698.
- You, L., Gui, Z., Guo, W., Shen, S., Wu, H., 2012, "A Geospatial Web Services Composition Framework Supporting Real-Time Status Monitoring", *ISPRS Annals of the Photogrammetry, Remote Sensing and Spatial Information Sciences*, Volume I-4, 2012 XXII ISPRS Congress, Melbourne, Australia, 25 August – 01 September 2012.
- Zhang, C., Li, W., 2005, "The Roles of Web Feature and Web Map Services in Real-time Geospatial Data Sharing for Time critical Applications", *Cartography and Geographic Information Science*, Vol. 32 (4), pp. 269-283.



## A FAST BISECTION BASED ANALYZER DESIGN FOR THE DETERMINATION OF MODES IN CIRCULAR WAVEGUIDES

<sup>1</sup>Coşkun DENİZ

<sup>1</sup>Adnan Menderes University, Department of Electrical and Electronics Engineering, Aytepe Campus, Aytepe-09010, Aydın, TURKEY

<sup>1</sup>cdeniz@adu.edu.tr

(Geliş/Received: 06.04.2017; Kabul/Accepted in Revised Form: 21.07.2017)

**ABSTRACT:** Determination of zeros of Bessel functions and their derivatives are essential in the TE and TM modes supported by the circular waveguides. However, since these functions are conventionally defined as infinite series, fast calculation of their numerical values and zeros with reliable accuracy requires improved numerical techniques or approximations. Moreover, modes are usually sorted by human inspection and instant retrieval of correctly ordered modes becomes essential especially for higher mode-index values. Here, a fast-computational algorithm design based on the numerical Bisection method to determine the sorted TE and TM mode solutions of the circular waveguides is presented. Our suggestion involves: i) determination of the critical points close to the zeros of Bessel functions and their derivatives within the user selected sampling width (typically =0.01), ii) application of the numerical Bisection method to these functions one after another to scan up to the user selected maximum index number by using these critical points up to maintain the user selected sensitivity values, iii) Bubble sorting of the unified roots matrix, iv) scan the bubble sorted roots matrix to decide the mode type. As a result, our design finds the related TE and TM modes along with the cut-off and propagating wave frequencies in the correct order with a very fast calculation by the user controlled Computable Document File (CDF) environment.

**Key Words:** Bessel functions, Circular waveguides, Computable document file (CDF), Cylindrical waveguides, Real time computation, TE modes, TM modes,

### Dairesel Dalga Kılavuzlarının Modlarını Belirlemede İkiye Bölme Temelli Hızlı Bir Analizör Tasarımı

**ÖZ:** Dairesel dalga kılavuzlarının desteklediği TE ve TM modlarının belirlenmesinde, Bessel fonksiyonlarının ve türevlerinin sıfırlarının bulunması elzemdir. Ancak, bu fonksiyonlar konvansiyonel olarak sonsuz seri şeklinde tanımlandığından, sayısal değerlerinin ve sıfırlarının hızlı ve makul güvenilirlikte hesaplanması, geliştirilmiş sayısal teknikleri ya da yaklaşım yapmayı gerektirir. Ayrıca, modlar genellikle insan tarafından kontrol edilerek sıralandırılır ve özellikle yüksek mod endekslerinde, doğru olarak sıralanmış modlara anında erişim önemlidir. Burada, sıralanmış modları hızlı olarak hesaplayan, sayısal yöntemlerden ikiye bölme (Bisection) temeline dayanan bir algoritma tasarımı sunulmaktadır. Önerimiz şu hususları içermektedir: i) Bessel fonksiyonlarının ve türevlerinin sıfırlarına yakın kritik noktaların, kullanıcı tarafından seçilen örnekleme genişliğine göre (tipik olarak=0.01) belirlenmesi, ii) Kullanıcı tarafından seçilen hassasiyet değeri elde edilinceye kadar, bu kritik noktaları kullanarak, kullanıcı tarafından seçilen maksimum indeks değerine kadar taranan bu fonksiyonlara ardışık olarak sayısal ikiye bölme yönteminin uygulanması, iii) Birleştirilmiş kökler matrisinin köpük sıralaması (bubble sorting), iv) köpük sıralaması yapılmış kökler matrisinin taranarak mod tipinin belirlenmesi. Neticede, tasarımı hızlı bir hesaplamayla, ilgili modları, kesim frekansları ve ilerleyen

dalga frekansları ile birlikte doğru sıralanmış olarak, kullanıcı kontrollü hesaplanabilir doküman dosyası (CDF) ortamında bulunmaktadır.

**Anahtar Kelimeler:** Bessel fonksiyonları, Dairesel dalga kılavuzları, Hesaplanabilir doküman formatı, Lindirik Dalga kılavuzları, Gerçek zamanlı hesaplama, TE modları, TM modları.

## INTRODUCTION

The circular waveguide, occasionally used as an alternative to the rectangular waveguide, is constructed from a single, enclosed conductor and supports transverse electric (TE) and transverse magnetic (TM) modes (Balanis, 1989; Beattie, 1958; Cheng, 1989; Kushwaha *et al*, 2014; Sekeljic, 2010; Deniz, 2016; Deniz, 2017). Each mode has a characteristic cut-off frequency, below which electromagnetic energy is severely attenuated as typical to the other waveguides. Circular waveguide's round cross section makes it easy to machine and it is often used to feed conical horns. Moreover, very low attenuation of their  $TE_{0n}$  modes also makes it popular in engineering applications (Balanis, 1989; Cheng, 1989). These modes are conventionally given by the  $\chi'_{mn}$  values for the  $TE_{mn}$  mode and  $\chi_{mn}$  values for the  $TM_{mn}$  mode where the first one is the  $n$ th zero of derivative of the first kind of Bessel functions with index  $m$ , namely  $J'_m(x)$ , and the second one is the  $n$ th zero of the first kind of Bessel functions with index  $m$ , namely  $J_m(x)$ , respectively (Balanis, 1989; Beattie, 1958; Cheng, 1989; Kushwaha *et al*, 2014; Sekeljic, 2010; Deniz, 2016; Deniz, 2017). Bessel functions have infinite zeros in the entire domain or finite zeros in a given subdomain; like trigonometric functions, Airy functions, etc., and finding their zeros as accurate and as fast as possible is essential here for the circular waveguides. Since analytical solutions in finding roots of such functions is always not possible, various numerical and approximation techniques are being improved (Abuelma'atti, 1999; Blachman and Mousavinezhad, 1986; Deniz, 2016; Deniz, 2017; Harrison, 2009; Luke, 1975; Millane and Eads, 2003; Newman, 1984; Waldron, 1981). For the Bessel functions of the first kind and their derivatives, we have the following conventional analytic expressions in the form of infinite series (Abramowitz and Stegun, 1965; Arfken and Weber, 2005; Bell, 1968; Boas, 2006; Korenev, 2002; Watson, 1995):

$$J_m(x) = \sum_{k=0}^{\infty} \frac{(-1)^k}{k! \Gamma(k+m+1)} \left(\frac{x}{2}\right)^{2k+m}, m \in \mathbb{R}^+ \quad (1a)$$

$$J'_m(x) = \frac{dJ_m(x)}{dx} = \frac{J_{m-1}(x) - J_{m+1}(x)}{2} = \frac{m}{2} J_m(x) - J_{m+1}(x) \quad (1b)$$

where  $J_m(x)$  &  $J'_m(x)$  are the Bessel functions of first kind and their derivatives with index  $m$  and  $\Gamma$  is the gamma function. Their values for negative index values are also defined as well as their integral forms and approximate forms under special cases (such as asymptotic, large Bessel indices, etc.) (Abramowitz and Stegun, 1965; Arfken and Weber, 2005; Bell, 1968; Boas, 2006; Korenev, 2002; Watson, 1995). We can also see that their exact analytical calculations as well as finding their zeros are impractical but can be calculated by some approximations such as asymptotic approximations, approximations for large Bessel indices, etc. Today's advanced computation software, such as Mathematica, Maple, Matlab, etc., can find their numerical values and zeros by some approximations within the desired sensitivity (Richards, 2002; Wolfram, 2003; Wolfram, 2017a). Besides the determination of these zeros, their sorting, fast and accurate ordering is also important for designing and analyzing the circular waveguides.

Here we suggest a very fast and accurate algorithm design based on the conventional Bisection method to find and sort the zeros of Bessel functions of first kind and their derivatives to represent the solutions of the circular waveguides. For the root finding part, our suggestion employs the conventional numerical Bisection technique given in the fundamental textbooks regarding numerical methods such as in (Chapra and Canale, 2014; Hamming, 1987; Hoffman, 2001). It is also applicable to the other similar functions involving oscillatory zeros obeying the Intermediate Value Theorem (IVT) in a given domain.

General view of our design while operating is given in Figure 1. It runs under the Mathematica CDF (Computable Document Format) player, which is a free-software downloadable from the Wolfram’s web page given in (Wolfram, 2017b). General properties of the CDF are given in (Guillermo and León, 2017; Hastings et al., 2016; Hong, 2016; Wellin, 2016; Wolfram, 2017b; Wolfram, 2017c; Wolfram Research, 2017) and some of the sample applications are available in (Al-Shamali, 2015; Beaulieu, 2012; Deshmukh, 2012; Hollingsworth and Narayanan, 2016; Jones, 2014; Kahle, 2014; Russel, 2013; Selinger, 2016; Tasgal and Band, 2015). To summarize, it can be coded to have a user console enabling real time computations. Moreover, once it is coded on Mathematica software, it can be easily converted to a CDF file which runs under the free CDF player without requiring any other software purchasing (Guillermo and León, 2017; Hastings et al., 2016; Hong, 2016; Wellin, 2016; Wolfram, 2017a; Wolfram, 2017b; Wolfram, 2017c; Wolfram Research, 2017).

Our Bisection-based algorithm involves two main stages. In the first stage, we use iterations by the desired scanning step (typically=0.01) to scan the related Bessel functions of first kind first and then its derivative to determine the critical points near the zeros for both roughly. These critical points are then instantaneously being processed by the conventional Bisection technique given in (Chapra and Canale, 2014; Hamming, 1987; Hoffman, 2001) to determine the related zeros in the second stage. In effect, we have very fast and accurate results since the iteration number for the desired accuracy level is very low (typically=5 iterations for the sensitivity set value=0.0001). Once these roots are found, they are unified and the conventional Bubble Sorting, which is normally known to be not much fast and practical (Arora et al, 2012; Astrachan, 2003; Cormen et al, 2009; Khairullah, 2013; Rohil and Manisha, 2014) is applied. Though, we have very fast and accurate modes in the correct order. Sorted and unified roots matrix is then re-scanned to determine the related mode type to be assigned for each. In effect, we have very fast and correctly ordered modes with the related cut-off and propagating wave frequency values. As seen in Figure 1, user console involves guide radius, operation frequency, relative permittivity and permeability values of the medium, maximum Bessel index value, Bisection precision value, count step value and an update button. When the update button is pushed, user selected values are entered.

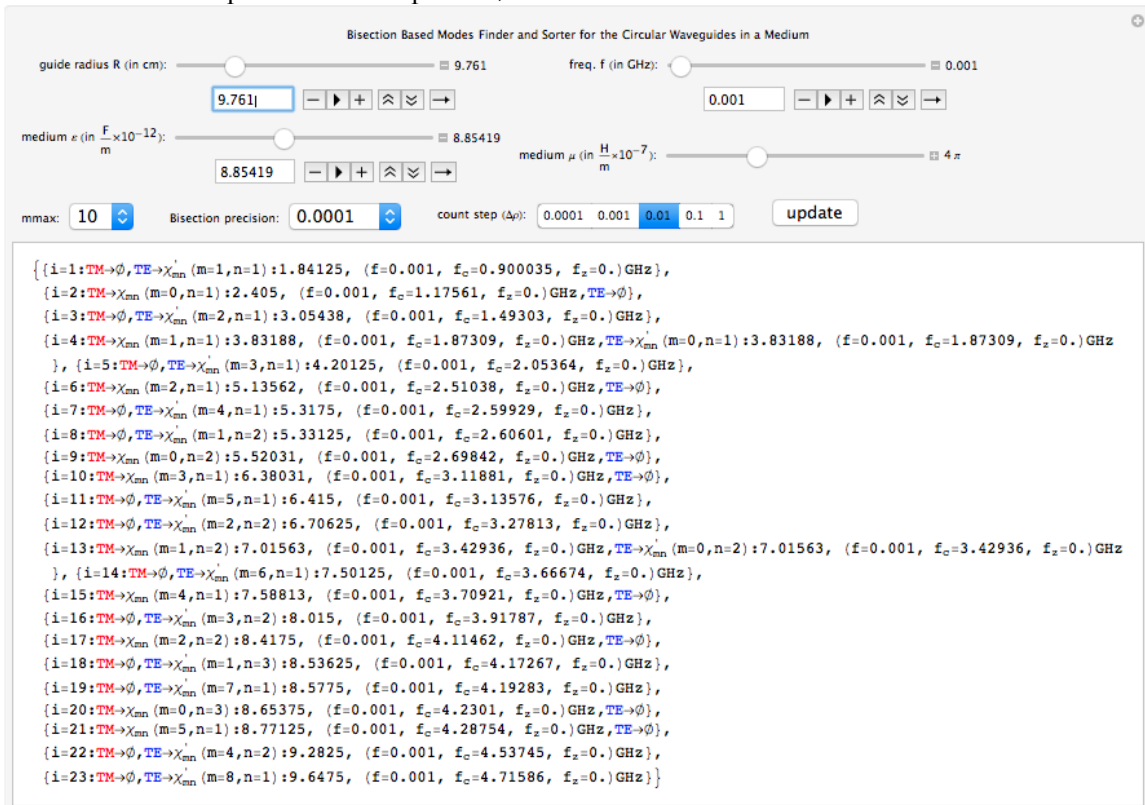


Figure 1. General appearance of our analyzer while running

Applications of the Bessel functions and their zeros to determine the modes of circular waveguides is being summarized in Chapter 2. Bisection method and our suggested algorithm regarding the numerical root finding based on the conventional Bisection method is being presented in Chapter 3 and their application to specific circular waveguide is being presented and discussed in Chapter 4.

## CIRCULAR WAVEGUIDES

General properties of the  $TE$  and  $TM$  modes given in (Balanis, 1989; Cheng, 1989; Deniz, 2017; Kushwaha *et al*, 2014) can be summarized as follows:

### TE Modes

The Transverse Electric to  $z$ , ( $TE^z$ ) modes, can be derived by letting the vector potential  $\mathbf{A}$  and  $\mathbf{F}$  be equal to the followings:

$$\mathbf{A} = 0 \quad (2a)$$

$$\mathbf{F} = \mathbf{a}_z F_z(\rho, \phi, z) \quad (2b)$$

from which we have

$$\nabla^2 F_z(\rho, \phi, z) + \beta^2 F_z(\rho, \phi, z) = 0 \quad (3a)$$

whose solution gives:

$$F_z(\rho, \phi, z) = [A_1 J_m(\beta_\rho \rho) + B_1 Y_m(\beta_\rho \rho)] \times [C_2 \cos(m\phi) + D_2 \sin(m\phi)] \times [A_3 e^{-j\beta_z z} + B_3 e^{j\beta_z z}] \quad (3b)$$

where

$$\beta_\rho^2 + \beta_z^2 = \beta^2 \quad (4)$$

and  $J_m$  &  $Y_m$  are the Bessel functions of first and second kind respectively. Constants:  $\{A_1, B_1, C_2, D_2, A_3, B_3, m, \beta_\rho, \beta_z\}$  can be calculated by using the following boundary conditions:

$$E_\phi(\rho = a, \phi, z) = 0 \quad (5a)$$

$$E_z(\rho = a, \phi, z) = 0 \quad (5b)$$

from which we get

$$F_z(\rho, \phi, z) = A_{mn} J_m(\beta_\rho \rho) \times [C_2 \cos(m\phi) + D_2 \sin(m\phi)] \times A_3 e^{-j\beta_z z} \quad (6)$$

Then, the electric field component  $E_\phi^+$  can be calculated from

$$E_\phi^+(\rho, \phi, z) = \frac{1}{\epsilon} \frac{\partial F_z^+(\rho, \phi, z)}{\partial \rho} \quad (7a)$$

and by applying the boundary condition for  $E_\phi^+$  in (5a), we get:

$$E_\phi^+(\rho = a, \phi, z) = 0 \Rightarrow J'_m(\beta_\rho a) = 0 \Rightarrow \beta_\rho = \frac{\chi'_{mn}}{a} \quad (7b)$$

where  $\chi'_{mn}$  represents the  $n$ th zero ( $n = 1, 2, 3, \dots$ ) of the derivative of the Bessel function  $J_m(x)$  of the first kind of order  $m$  ( $m = 0, 1, 2, 3, \dots$ ). The smallest value of  $\chi'_{mn}$  corresponds to  $\chi'_{11} = 1.8412$  ( $m = 1, n = 1$ ). Using (4) and (7b),  $\beta_z$  of the  $mn$  mode can be written as follows:

$$(\beta_z)_{mn} = \begin{cases} \sqrt{\beta^2 - \beta_\rho^2} = \sqrt{\beta^2 - \left(\frac{\chi'_{mn}}{a}\right)^2}, & \beta > \beta_\rho = \frac{\chi'_{mn}}{a} \\ 0, & \beta = \beta_c = \beta_\rho = \frac{\chi'_{mn}}{a} \\ -j\sqrt{\beta_\rho^2 - \beta^2} = j\sqrt{\left(\frac{\chi'_{mn}}{a}\right)^2 - \beta^2}, & \beta < \beta_\rho = \frac{\chi'_{mn}}{a} \end{cases} \quad (8a)$$

where Cut-off is defined when  $\beta_{z(mn)} = 0$ , namely:

$$\beta_c = \omega_c \sqrt{\mu\epsilon} \Rightarrow (f_c)_{mn} = \frac{\chi'_{mn}}{2\pi a \sqrt{\mu\epsilon}} \quad (8b)$$

where  $(f_c)_{mn}$  is the cut-off frequency above which the related  $TE$  mode propagates with the guide wavelength:

$$\lambda_g = \frac{2\pi}{(\beta_z)_{mn}} \quad (8c)$$

### TM Modes

Similarly, the Transverse Magnetic to  $z$ , ( $TM^z$ ) modes, can be derived by letting the vector potential  $\mathbf{A}$  and  $\mathbf{F}$  be equal to the followings:

$$\mathbf{F} = 0 \quad (9a)$$

$$\mathbf{A} = \mathbf{a}_z A_z(\rho, \phi, z) \quad (9b)$$

from which we have

$$\nabla^2 A_z(\rho, \phi, z) + \beta^2 A_z(\rho, \phi, z) = 0 \quad (10a)$$

whose solution gives:

$$A_z(\rho, \phi, z) = [A_1 J_m(\beta_\rho \rho) + B_1 Y_m(\beta_\rho \rho)] \times [C_2 \cos(m\phi) + D_2 \sin(m\phi)] \times [A_3 e^{-j\beta_z z} + B_3 e^{j\beta_z z}] \quad (10b)$$

where

$$\beta_\rho^2 + \beta_z^2 = \beta^2 \quad (11)$$

and  $J_m$  &  $Y_m$  are the Bessel functions of first and second kind respectively. Constants:  $\{A_1, B_1, C_2, D_2, A_3, B_3, m, \beta_\rho, \beta_z\}$  can be calculated by using the following boundary conditions:

$$E_\phi(\rho = a, \phi, z) = 0 \quad (12a)$$

$$E_z(\rho = a, \phi, z) = 0 \quad (12b)$$

from which we get

$$A_z^+(\rho, \phi, z) = B_{mn} J_m(\beta_\rho \rho) \times [C_2 \cos(m\phi) + D_2 \sin(m\phi)] \times A_3 e^{-j\beta_z z} \quad (13a)$$

Then, the electric field component  $E_z^+$  can be calculated from

$$E_z^+(\rho, \phi, z) = -j \frac{1}{\omega \mu \epsilon} \left( \frac{\partial^2}{\partial \rho^2} + \beta^2 \right) A_z^+(\rho, \phi, z) \quad (13b)$$

and by applying the boundary condition in (12b) to (13b), we get

$$E_z(\rho = a, \phi, z) = 0 \Rightarrow J_m(\beta_\rho) = 0 \Rightarrow \beta_\rho = \frac{\chi_{mn}}{a} \quad (13c)$$

where  $\chi_{mn}$  represents the  $n$ th zero ( $n = 1, 2, 3, \dots$ ) of the Bessel function  $J_m(x)$  of the first kind of order  $m$  ( $m = 0, 1, 2, 3, \dots$ ). The smallest value of  $\chi_{mn}$  corresponds to  $\chi_{01} = 2.4049$  ( $m = 0, n = 1$ ).

Using (13c) and (11),  $\beta_z$  of the  $mn$  mode can be written as follows:

$$(\beta_z)_{mn} = \begin{cases} \sqrt{\beta^2 - \beta_\rho^2} = \sqrt{\beta^2 - \left(\frac{\chi_{mn}}{a}\right)^2}, & \beta > \beta_\rho = \frac{\chi_{mn}}{a} \\ 0, & \beta = \beta_c = \beta_\rho = \frac{\chi_{mn}}{a} \\ -j\sqrt{\beta_\rho^2 - \beta^2} = j\sqrt{\left(\frac{\chi_{mn}}{a}\right)^2 - \beta^2}, & \beta < \beta_\rho = \frac{\chi_{mn}}{a} \end{cases} \quad (14)$$

where Cut-off is defined when  $\beta_{z(mn)} = 0$ , namely:

$$\beta_c = \omega_c \sqrt{\mu \epsilon} \Rightarrow (f_c)_{mn} = \frac{\chi_{mn}}{2\pi a \sqrt{\mu \epsilon}} \quad (15)$$

where  $(f_c)_{mn}$  is the cut-off frequency above which the related  $TM$  mode propagates with the guide wavelength given in equation (8c). Since the cut-off frequencies of the  $TE_{0n}$  and  $TM_{1n}$  modes are identical ( $\chi'_{0n} = \chi_{1n}$ ), they are referred to also as degenerate modes.

## DETERMINATION OF THE MODES

### The Bisection method

The conventional Bisection technique, based on the Intermediate Value Theorem, is also called as Binary-search method and it is applicable if  $f(\rho)$  is a continuous function defined on the interval  $[a, b]$ , with  $f(a)$  and  $f(b)$  of opposite sign as follows (Chapra and Canale, 2014; Hamming, 1987; Hoffman, 2001):

**Theorem 1 (IVT):** Assume  $f: IR \rightarrow IR$  is a continuous function and there are two real numbers  $a$  and  $b$  such that  $f(a) \times f(b) < 0$ . Then  $f(\rho)$  has at least one zero between  $a$  and  $b$ .

The Intermediate Value Theorem implies that a number  $c$  exists in  $(a, b)$  with  $f(c) = 0$ . Although the procedure will work in most of the cases when there is more than one root in the interval  $(a, b)$ , we assume for simplicity that the root in this interval is unique for now. The method calls for a repeated halving (or bisecting) of sub-intervals of  $[a, b]$  and, at each step, locating the half containing  $c$  until the desired precision ( $\approx prec$ ) is attained. To begin, set  $a_1 = a$  and  $b_1 = b$ , and let  $p_1$  be the midpoint of  $[a, b]$ ; that is,

$$c_1 = a_1 + \frac{b_1 - a_1}{2} = \frac{a_1 + b_1}{2} \quad (16)$$

Then the calculation involves the following procedures:

- i) If  $|f(c_1)| \leq prec$ , then  $c = c_1$ , and we are done, root= $c$ .
- ii) If  $f(p_1) \neq 0$ , then  $f(p_1)$  has the same sign as either  $f(a_1)$  or  $f(b_1)$ .
- iii) If  $f(p_1)$  and  $f(a_1)$  have the same sign,  $p(p_1, b_1)$ . Set  $a_2 = c_1$  and  $b_2 = b_1$ .
- iv) If  $f(p_1)$  and  $f(a_1)$  have opposite signs,  $p(a_1, p_1)$ . Set  $a_2 = a_1$  and  $b_2 = c_1$ .
- v) Continue the same process to interval  $[a_2, b_2]$  and reapply with  $r$  iterations until  $|f(c \leftarrow c_r)| \leq prec$ , root= $c$ .

Flowchart of the Bisection algorithm used here is given in Figure 2. The dashed rectangle is our addition here to reject the roots found but out of the guide radius  $R$ . This modified Bisection module is used in our suggested algorithm whose flowchart is given in Figure 3 to find the root (which is guaranteed to exist by the IVT given above) in the determined  $[a, b]$  interval instantaneously.

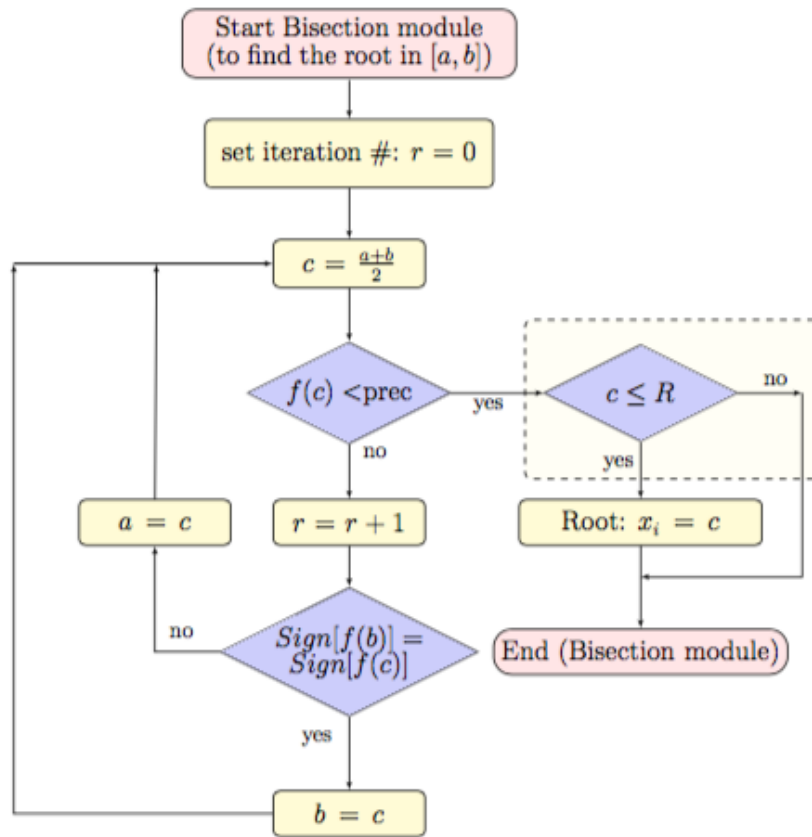


Figure 2. Flowchart of the Bisection algorithm to calculate the root of  $f(x)$  between  $a$  &  $b$  by  $r$  iterations.

**Our Suggestion**

The flowchart of our suggestion is given in figure 3. User enters the following parameters: Guide radius ( $R$ ), frequency ( $freq$ ), medium permittivity and permeability ( $\epsilon, \mu$ ), Bisection precision ( $prec$ ) and, count step ( $\Delta\rho$ ). Bisection method discussed above operates in the determination of one zero between the end points  $[a, b]$  where  $f(a)$  &  $f(b)$  are in opposite signs satisfying the IVT as discussed. Since we study the functions with more than one zero, we suggest first to determine such critical points  $[a_n, b_n]$  as follows:

$$[a_n, b_n] = [k, a_n + \Delta m] \tag{17a}$$

where  $\Delta\rho$  is the count step selected by the user (default value is set to 0.01) and  $k$  scans the domain

of the guide radius  $[0, R]$  in  $\Delta\rho$  steps. Here we determine the critical point pairs  $\{a_n, b_n\}$  obeying the IVT as follows:

$$\text{Sign}[f(a_n)] \times \text{Sign}[f(b_n)] \leq 0 \quad (17b)$$

By this suggestion, the application of the Bisection method can be started within very close critical point pairs  $\{a_n, b_n\}$ . So, less iteration steps are needed in the application of the Bisection method. Since the  $n$ th zeros of  $J'_m(x)$  &  $J_m(x)$  are searched to determine the modes  $\chi'_{mn}$  &  $\chi_{mn}$  in each application of the Bisection method, the user initially enters the maximum value of  $m$  ( $=m_{max}$ ), hence we have:  $m = 0, 1, 2, \dots, m_{max}$ . Once all the parameters are been entered and activated by the update button by the user,  $\chi'_{m \times 1}$  matrix for the roots of  $J'_m(\rho)$  and similarly,  $\chi_{m \times 1}$  matrix for the roots of  $J_m(\rho)$  are defined in order that final results for the roots can be assigned to these matrices. So, starting from  $k = 0$  and  $f(\rho) = J'_{m=0}(\rho)$ , all the roots are found and assigned to the related elements of matrix  $\chi'_{0 \times 1}$ . When  $k$  reaches  $R$ , it is complete and it repeats for  $f(\rho) = J_{m=0}(\rho)$  from  $k = 0$  up to  $k = R$  and all the roots are found and assigned to the related elements of matrix  $\chi_{0 \times 1}$ . Then the same procedure continues for the next  $m$  value with  $m = 1$  and repeats up to  $m = m_{max}$  to find and assign all the roots to the related matrices in the following order:

$$\left\{ \chi'_m = (\chi'_{m1} \ \chi'_{m2} \ \dots \ \chi'_{mn} \ \dots \ \chi'_{m_{max}l})^T, \ \chi_m = (\chi_{m1} \ \chi_{m2} \ \dots \ \chi_{mn} \ \dots \ \chi_{m_{max}l})^T \right\}, \quad \begin{matrix} m = 0, 1, 2, \dots, m_{max} \\ n = 1, 2, 3, \dots, l \end{matrix} \quad (18)$$

Note that  $l$  is a relatively big number (typically 50 or more) regarding the maximum root number in  $0 \leq \rho \leq R$  and  $0 \leq m \leq m_{max}$ , which is not known at the beginning and the blocks marked by (\*) are not necessary if any matrix predefinition is not required by the programming language in use or by the preference of the programmer. Deletion of the non-assigned elements to reduce the matrices at the end of this module is also optional. The outputs at the end of this module for a relatively small guide radius ( $R = 7 \text{ cm}, m_{max} = 10$ ) is given as an example as follows:

$$R = 7 \text{ cm}, m_{max} = 10 \Rightarrow \begin{cases} m = 0 \Rightarrow \chi'_0 = (3.83188), \chi_0 = (2.405 \ 5.52031)^T \\ m = 1 \Rightarrow \chi'_1 = (1.84125 \ 5.33125)^T, \chi_1 = (3.83188) \\ m = 2 \Rightarrow \chi'_2 = (3.05438 \ 6.70625)^T, \chi_2 = (5.13562) \\ \quad m = 3 \Rightarrow \chi'_3 = (4.20125), \chi_3 = (6.38031) \\ \quad \quad m = 4 \Rightarrow \chi'_4 = (5.3175), \chi_4 = \phi \\ \quad \quad \quad m = 5 \Rightarrow \chi'_5 = (6.415), \chi_4 = \phi \end{cases} \quad (19)$$

Note that for  $5 < m \leq m_{max} = 10$ ,  $\chi_m$  or  $\chi'_m$  exceeds  $R = 7 \text{ cm}$ .

### Sorting Module

Flow chart algorithm for our sorting module is given in figure 4. We prefer the conventional Bubble sorting given in (Arora *et al*, 2012; Astrachan, 2003; Cormen *et al*, 2009; Khairullah, 2013; Rohil and Manisha, 2014). For small guide radius value given above we have the following operations:

$$\bar{\chi} = \bigcup_{m=0}^{m_{max}} (\chi'_m \cup \chi_m) \quad (20a)$$

$$R = 7 \text{ cm}, m_{\max} = 10 \Rightarrow \bar{\chi} = \begin{pmatrix} 3.83188 \\ 2.405 \\ 5.52031 \\ 1.84125 \\ 5.33125 \\ 3.05438 \\ 6.70625 \\ 5.13562 \\ 4.20125 \\ 6.38031 \\ 5.3175 \\ 6.415 \end{pmatrix}, M = \begin{pmatrix} 1.84125 \\ 2.405 \\ 3.05438 \\ 3.83188 \\ 4.20125 \\ 5.13562 \\ 5.3175 \\ 5.33125 \\ 5.52031 \\ 6.38031 \\ 6.415 \\ 6.70625 \end{pmatrix} \quad (20b)$$

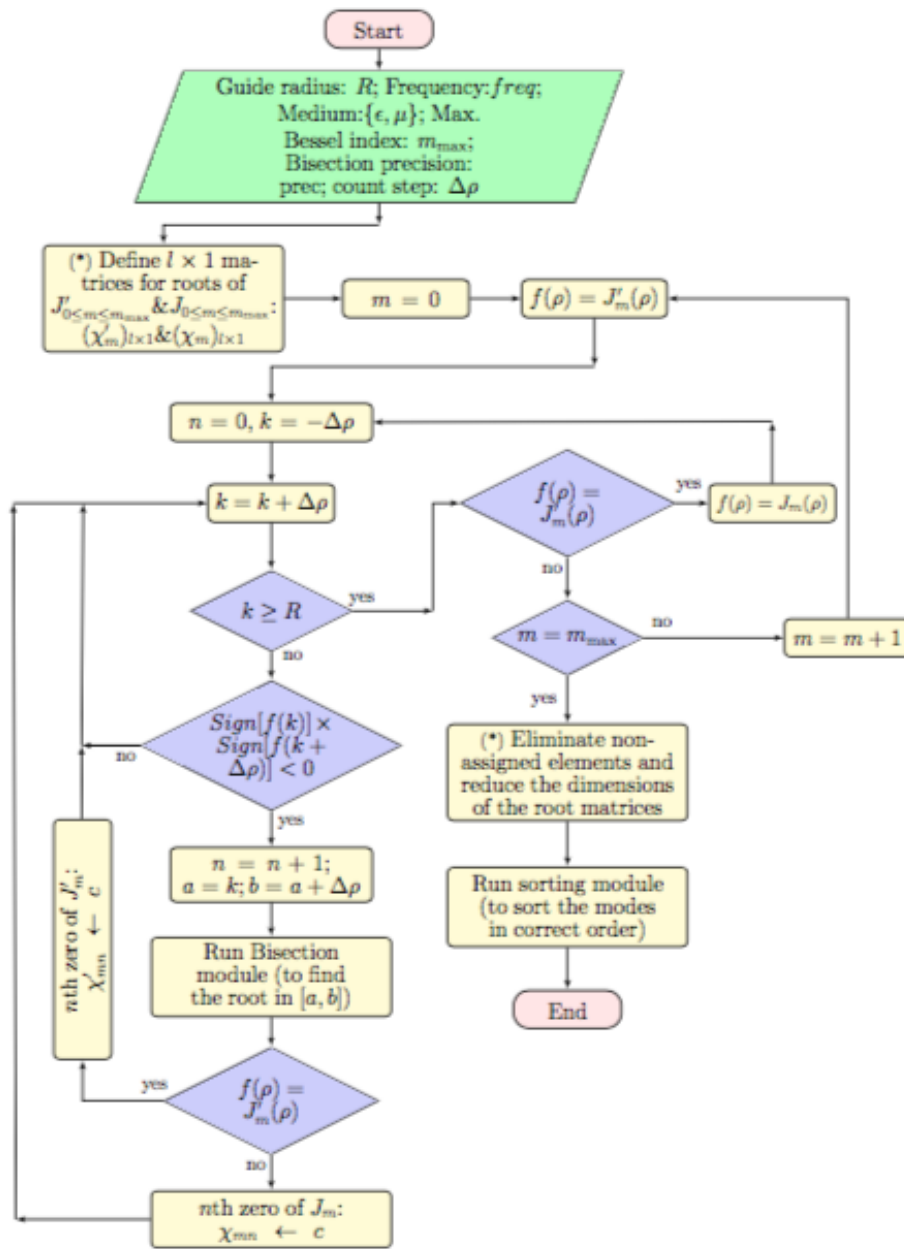


Figure 3. Flowchart of the suggested algorithm to calculate and sort the zeros of  $J'_m(\rho)$  and  $J_m(\rho)$  in the given interval:  $\rho_{\min} \leq \rho \leq \rho_{\max}$ . (\*): optional.

Unsorted roots (both for  $\chi'_m$  and  $\chi_m$ ) are assigned to column matrix  $\bar{\chi}$  and they are sorted in the column matrix  $\mathbf{M}$ . Indice  $i$  scans from 0 up to  $\dim(\mathbf{M})$  and each time indice  $m$  scans from 0 up to  $m_{max}$  and  $M_i \in \chi'_m$  is checked. If it is true, row number of element  $M_i$  in  $\chi'_m$  is assigned as indice  $n$  of the  $\chi'_{mn}$ . If it is false,  $M_i \in \chi_m$  is checked and if it is true, row number of element  $M_i$  in  $\chi_m$  is assigned as indice  $n$  of the  $\chi_{mn}$ . Note that  $\chi'_{01} = \chi_{11} = 3.83188$  in our simplified illustration. It is due to the fact that (Balanis, 1989; Beattie, 1958; Cheng, 1989; Deniz, 2016; Deniz, 2017; Kushwaha *et al*, 2014; Sekeljic, 2010):

$$\chi'_{0n} = \chi_{1n} \quad (21)$$

where the related TM and TE modes are common. Such common modes are also detected by the sequential checking in our design.

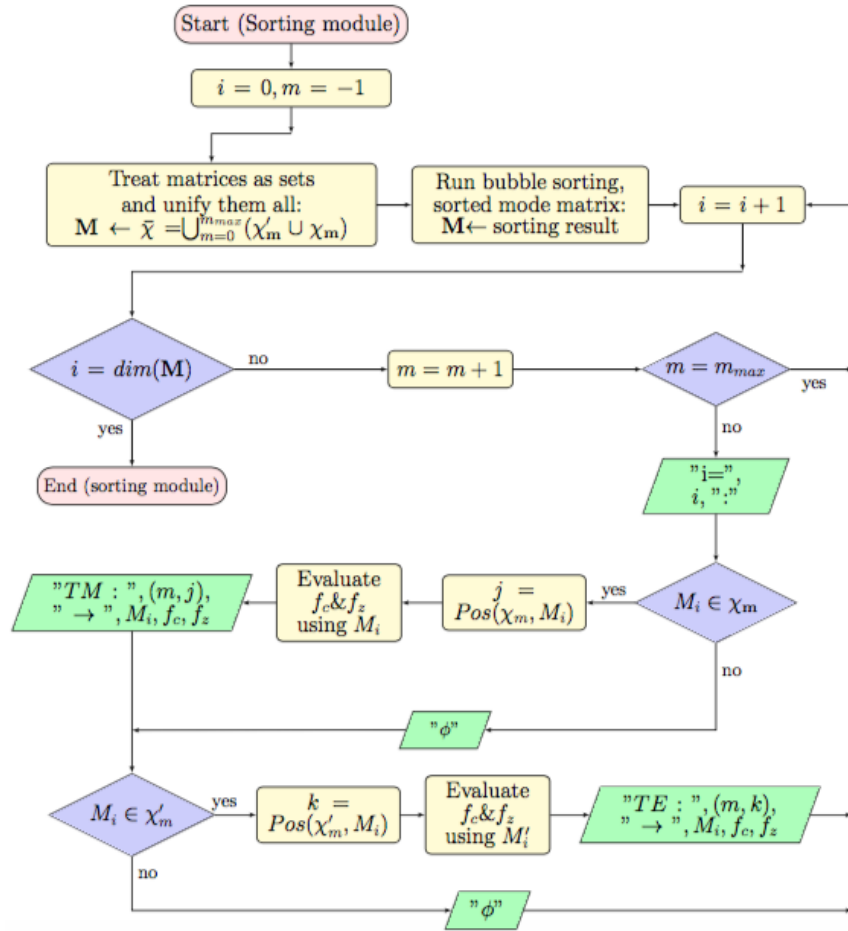


Figure 4. Flowchart of the sorting module

## RESULTS AND CONCLUSION

Results for relatively large parameters are given in Table 1. They are in agreement with the results given in (Balanis, 1989; Beattie, 1958; Cheng, 1989; Deniz, 2016; Deniz, 2017; Kushwaha *et al*, 2014; Sekeljic, 2010) and in the correct order as in (Beattie, 1958), where the first 700 zeros are listed in the correct order as a reference table. Note that results in (Beattie, 1958) with as much as first 700 modes are sorted by the inspection of the author, obviously requiring a great effort without using any sorting algorithm for quick access for practical applications. Although we use here a slow and impractical Bubble sorting as discussed in (Arora *et al*, 2012; Astrachan, 2003; Cormen *et al*, 2009; Khairullah, 2013; Rohil and Manisha, 2014), we have very fast and accurate results in the correct mode orders as aimed here. It is enabled by the use of the suggested algorithm running under the free Mathematica CDF player

which offers a real time computation with the user console. Our simplified illustration for selected parameters  $R = 7 \text{ cm}$ ,  $m_{max} = 10$  given in Section 3.3 can be followed and verified from Table 1 between the index numbers  $i = 1$  and  $i = 12$ .

It is obvious that as the selected parameter  $m_{max}$  increases, the maximum  $m$  value of  $\chi_{mn}$  and  $\chi'_{mn}$  to be found and sorted increases and similarly, as the parameter  $R$  increases maximum  $n$  value of  $\chi_{mn}$  and  $\chi'_{mn}$  to be found and sorted increases, too. However, as seen in our algorithm in Figure 3, both parameters are checked and Bisection method is applied provided that  $k < R$  and  $m < m_{max}$  holds. All the first  $n' \rightarrow n$ th roots of  $J'_m(\rho)$  are first determined until  $k = R$  is reached then  $k \rightarrow 0$  and all the first  $n$ th roots of  $J_m(\rho)$  are then obtained until  $k = R$  is reached again by the Bisection method. When both are completed,  $m$  is increased by one and it repeats again. Then it sequentially continues until  $m = m_{max}$  is reached ( $m = m_{max}$  is included). So, our design finds the roots in the following orders:

$$\begin{aligned}
m = 0: & \chi'_{01}, \chi'_{02}, \chi'_{03}, \dots, \chi'_{0n'}, \chi_{01}, \chi_{02}, \chi_{03}, \dots, \chi_{0n}, \\
m = 1: & \chi'_{11}, \chi'_{12}, \chi'_{13}, \dots, \chi'_{1n}, \chi_{11}, \chi_{12}, \chi_{13}, \dots, \chi_{1n}, \\
m = 2: & \chi'_{21}, \chi'_{22}, \chi'_{23}, \dots, \chi'_{2n'}, \chi_{21}, \chi_{22}, \chi_{23}, \dots, \chi_{2n} \\
& \vdots \\
m = m_{max}: & \chi'_{m_{max}1}, \chi'_{m_{max}2}, \chi'_{m_{max}3}, \dots, \chi'_{m_{max}n'}, \chi_{m_{max}1}, \chi_{m_{max}2}, \chi_{m_{max}3}, \dots, \chi_{m_{max}n}
\end{aligned} \tag{22}$$

Each root is assigned to the related matrix as given in (18). Note that maximum root number of  $J'_m(\rho)$  is denoted by  $n'$  but maximum root number of  $J_m(\rho)$  by  $n$  here since they may not be equal, though both are counted by the same dummy index  $n$  and when  $k = R$  is reached for either one (for  $J'_m(\rho)$  or  $J_m(\rho)$  in the related loop), corresponding  $n$  value for that loop determines the maximum root numbers (say,  $n \rightarrow n'$  for  $J'_m(\rho)$  and  $n$  for  $J_m(\rho)$ ). Also note that predefined dimensions of matrices ( $\chi'_m$  and  $\chi_m$ ) are large when compared to  $n$  and  $n'$  values, namely:  $n \leq l$  and  $n' \leq l$ .

As the radius ( $R$ ) increases, zeros of Bessel functions and their derivatives get closer so, choosing small count step values ( $\Delta\rho$ ) prohibits a missing root. On the other hand, too small count step values cause great iteration numbers to scan, which means a decrease in the calculation speed, for small  $R$  values. For this reason, parameter: "count step values ( $\Delta\rho$ )" is introduced in the user console as seen in Figure 1. For large  $R$  values, greater  $\Delta\rho$  parameter to scan can be chosen to avoid a missing root by the user. Similarly, the "Bisection precision" parameter is essential as seen in Figure 1 and in Figure 2. Bisection method sequentially repeats until  $prec < f(c)$  and this means that smaller  $prec$  parameters cause greater iteration numbers and hence a reduction in speed. Note that, in order to detect and find a root (whatever the precision parameter is),  $\Delta\rho$  parameter should not cause a missing root by the IVT given in Theorem 1 above. Moreover, as the radius increases, choosing lower precision values are advantageous since then the higher order roots get closer. Optimum values of  $\Delta\rho$  and  $prec$  values for user selections are introduced in the user console.

Our sorting module whose flowchart is given in Figure 4 also increases the calculation speed since the unified sorted matrix  $\mathbf{M}$  is used to compare with the related  $\chi'_m$  and  $\chi_m$  matrices to determine their positions (and hence their correct orders). Even though a relatively impractical and slow sorting method (the Bubble sorting) is used here, in effect, related modes and propagating wave frequencies are found accurately and in the correct order with a very fast and instantaneous calculation.

**Table 1.** Results for the parameters:  $R=20\text{cm}$ ,  $m_{max} = 20$ ,  $prec = 0.0001$ ,  $\Delta\rho = 0.01$

i	TM ( $\chi_{mn}$ )	TE ( $\chi'_{mn}$ )	i	TM ( $\chi_{mn}$ )	TE ( $\chi'_{mn}$ )
1	-	(1,1): 1.84125	51	(4,3): 14.3725	-
2	(0,1): 2.405	-	52	(10,1): 14.475	-
3	-	(2,1): 3.05438	53	-	(3,4): 14.5863
4	(1,1): 3.83188	(0,1): 3.83188	54	(2,4): 14.7963	-
5	-	(3,1): 4.20125	55	(7,2): 14.8213	-
6	(2,1): 5.13562	-	56	-	(1,5): 14.8638
7	-	(4,1): 5.3175	57	-	(13,1): 14.9275
8	-	(1,2): 5.33125	58	(0,5): 14.9312	-
9	(0,2): 5.52031	-	59	-	(6,3): 15.2681
10	(3,1): 6.38031	-	60	-	(9,2): 15.2863
11	-	(5,1): 6.415	61	(11,1): 15.5894	-
12	-	(2,2): 6.70625	62	(5,3): 15.7006	-
13	(1,2): 7.01563	(0,2): 7.01563	63	-	(4,4): 15.9638
14	-	(6,1): 7.50125	64	-	(14,1): 15.975
15	(4,1): 7.58813	-	65	(8,2): 16.0375	-
16	-	(3,2): 8.015	66	(3,4): 16.2238	-
17	(2,2): 8.4175	-	67	-	(2,5): 16.3475
18	-	(1,3): 8.53625	68	-	(10,2): 16.4475
19	-	(7,1): 8.5775	69	(1,5): 16.4706	(0,5): 16.4706
20	(0,3): 8.65375	-	70	-	(7,3): 16.5294
21	(5,1): 8.77125	-	71	(12,1): 16.6988	-
22	-	(4,2): 9.2825	72	(6,3): 17.0038	-
23	-	(8,1): 9.6475	73	-	(15,1): 17.0213
24	(3,2): 9.76125	-	74	(9,2): 17.2413	-
25	(6,1): 9.93625	-	75	-	(5,4): 17.3125
26	-	(2,3): 9.96938	76	-	(11,2): 17.6006
27	(1,3): 10.1738	(0,3): 10.1738	77	(4,4): 17.6163	-
28	-	(5,2): 10.5194	78	-	(8,3): 17.7738
29	-	(9,1): 10.7125	79	-	(3,5): 17.7888
30	(4,2): 11.065	-	80	(13,1): 17.8013	-
31	(7,1): 11.0863	-	81	(2,5): 17.9594	-
32	-	(3,3): 11.3463	82	-	(1,6): 18.015
33	(2,3): 11.6197	-	83	-	(16,1): 18.065
34	-	(1,4): 11.7063	84	(0,6): 18.0713	-
35	-	(6,2): 11.735	85	(7,3): 18.2875	-
36	-	(10,1): 11.7712	86	(10,2): 18.4338	-
37	(0,4): 11.7913	-	87	-	(6,4): 18.6375
38	(8,1): 12.225	-	88	-	(12,2): 18.745
39	(5,2): 12.3388	-	89	(14,1): 18.8994	-
40	-	(4,3): 12.6819	90	(5,4): 18.9806	-
41	-	(11,1): 12.8275	91	-	(9,3): 19.005
42	-	(7,2): 12.9325	92	-	(17,1): 19.105
43	(3,3): 13.015	-	93	-	(4,5): 19.1963
44	-	(2,4): 13.1706	94	(3,5): 19.4094	-
45	(1,4): 13.3238	(0,4): 13.3238	95	-	(2,6): 19.5125
46	(9,1): 13.3544	-	96	(8,3): 19.555	-
47	(6,2): 13.5894	-	97	(1,6): 19.6163	(0,6): 19.6163
48	-	(12,1): 13.8775	98	-	(13,2): 19.8825
49	-	(5,3): 13.9875	99	-	(7,4): 19.9413
50	-	(8,2): 14.115	100	(15,1): 19.995	-

**REFERENCES**

Abramowitz, A., Stegun, I.A., 1965, *Handbook of Mathematical Functions, with Formulas, Graphs, and Mathematical Tables*, 3rd Printing with Corrections, Vol. 55 of NBS Applied Mathematics Series, Superintendent of Documents, US Government Printing Office, Washington DC, pp. 355 – 479.

- Abuelma'atti, M. T., 1999, "Trigonometric Approximations for Some Bessel functions", *Active and Passive Elec. Comp.*, Vol. 22, pp. 75-85.
- Al-Shamali, F., 2015, "Interactive CDF Diagrams in Introductory Physics Course", *Proceedings of 20th International Conference on Multimedia in Physics Teaching and Learning*, LMU Munich, p. 77.
- Arfken, H.J., Weber, G.B., 2005, *Mathematical Methods for Physicists* (6<sup>th</sup> ed.), Elsevier Academic Press, pp. 675–686.
- Arora, N., Kumar, S., Tamta, V.K., 2012, "A Novel Sorting Algorithm and Comparison with Bubble Sort and Insertion Sort", *International Journal of Computer Applications*, Vol. 45(1), pp. 31-32.
- Astrachan, O., 2003, "Bubble Sort: An Archaeological Algorithmic Analysis", *SIGCSE '03 Proceedings of the 34th SIGCSE Technical Symposium on Computer Science Education*, NY, pp. 1-5.
- Balanis, C., 1989, *Advanced Engineering Electromagnetics* (2<sup>nd</sup> ed.), Wiley, NY, pp. 483–500.
- Beattie, C. L., 1958, "Table of First 700 Zeros of Bessel Functions" —  $J_1(x)$  and  $J_1'(x)$ , *Bell System Technical Journal*, Vol. 37, pp. 689-697.
- Beaulieu, J.R., 2012, *A Dynamic, Interactive Approach to Learning Engineering and Mathematics*, MSc. Thesis in Mechanical Eng., Virginia Polytechnic Institute and State University, Blacksburg, VA.
- Bell, W.W., 1968, *Special Functions for Scientists and Engineers*, D. Van Nostrand Compant Ltd., London, pp. 92-110.
- Blachman, N. M., Mousavinezhad, S. H., 1986, "Trigonometric Approximations for Bessel functions", *EEE Transactions on Aerospace and Electronic Systems*, Vol. AES-22(1), pp.2-7.
- Boas, L.M., 2006, *Mathematical Methods in the Physical Sciences* (3<sup>rd</sup> ed.), Wiley, NY, pp. 587–606.
- Chapra, S., Canale, R., 2014, *Numerical Methods for Engineers* (7<sup>th</sup> ed.), WCB/McGraw-Hill, NY, pp. 148-154.
- Cheng, D. K., 1989, *Field and Wave Electromagnetics* (2<sup>nd</sup> ed.), Addison-Wesley, London, pp. 562-572.
- Cormen, T. H., Leiserson, C. E., Rivest, R. L., Stein, C., 2009, *Introduction to Algorithms* (3<sup>rd</sup> ed.), MIT Press, USA, p. 40.
- Deniz, C., 2016, "A Secant Based Roots Finding Algorithm Design and its Applications to Circular Waveguides", *IOSR Journal of Electrical and Electronics Engineering*, Vol. 11(6), Ver. III, pp. 84-91.
- Deniz, C., 2017, "A Newton Raphson Based Roots Finding Algorithm Design and its Applications to Circular Waveguides", *El-Cezeri Journal of Science and Engineering*, Vol. 4(1), pp. 32-45.
- Deshmukh, S., 2012, *Illustration of Fundamentals of Vibrations Using Computable Document Format*, MSc. Thesis in Mechanical Eng., The University of Texas At Arlington.
- Guillermo, J., León, S., 2017, *Mathematica Beyond Mathematics: The Wolfram Language in the Real World*, CRC press- Taylor & Francis group, NY.
- Hamming, R. W., 1987, *Numerical Methods for Scientists and Engineers* (2<sup>nd</sup> Revised ed., Dover Books on Mathematics), Dover Publications, NY, pp. 68-72.
- Harrison, J., 2009, "Fast and Accurate Bessel Function Computation", *Computer Arithmetic-proc. of 19<sup>th</sup> IEEE symp. on Computer Arithmetic*, Portland-Oregon, pp. 104-113.
- Hastings, C., Mischo, K., Morrison, M., 2016, *Hands-On Start to Wolfram Mathematica: And Programming with the Wolfram Language*, 2<sup>nd</sup> ed., Wolfram Media Inc., Canada.
- Hoffman, J.D., 2001, *Numerical Methods for Engineers and Scientists*, (2<sup>nd</sup> ed.), Marcel Dekkel, NY-Basel, pp. 141-154.
- Hollingsworth, M.L. and Narayanan, N.H., 2016, "Building a Better eTextbook", *Bulletin of the IEEE Technical Committee on Learning Technology*, Vol. 18, No. 2/3, pp. 14-17.
- Hong, W., 2016, *Art of Mathematics*, Dorrance Publishing, Pittsburg, pp. 165–166.
- Jones, J., 2014, *The Technical and Social History of Software Engineering*, Pearson, NJ, pp. 201-203.
- Kahle, D., 2014, "Animating Statistics: A New Kind of Applet for Exploring Probability Distributions", *Journal of Statistics Education*, Vol. 22, No. 2, pp. 1-21.
- Khairullah, Md., 2013, "Enhancing Worst Sorting Algorithms", *International Journal of Advanced Science and Technology*, Vol. 56, pp. 13-26.

- Korenev, B.G., 2002, *Bessel Functions and Their Applications*, Taylor and Francis, NY.
- Kushwaha, R. K., Srivastava, S., Chaurasiya, V., 2014, "A Novel Approach to Analyze a Circular Waveguide in Air and Dielectric Medium", *SOP Transactions on Wireless Communications*, Vol. 1, No. 2, pp. 1-18.
- Luke, Y. L., 1975, *Approximation of Special Functions*, Academic Press, NY.
- Millane R. P., Eads, J. L., 2003, "Polynomial Approximations to Bessel Functions", *IEEE Transactions on Antennas and Propagation*, Vol. 51(6), pp. 1398-1400.
- Newman, J. N., 1984, "Approximations for the Bessel and Struve functions", *Mathematics of Computation*, Vol. 43(168), pp. 551-556.
- Richards, D., 2002, *Advanced Mathematical Methods with Maple*, Cambridge University Press, UK, pp. 325-331.
- Rohil, H., Manisha, 2014, "Run Time Bubble Sort—An enhancement of Bubble Sort", *International Journal of Computer Trends and Technology (IJCTT)*, Vol. 14(1), pp. 36-38.
- Russel, D. A., 2013, "Creating Interactive Acoustics Animations using Mathematica's Computable Document Format", *Proceedings of Meetings on Acoustics*, Vol. 19, 025006.
- Sekeljic, N., 2010, "Asymptotic Expansion of Bessel Functions; Applications to Electromagnetics", *Dynamics at the Horsetooth, Focused Issue: Asymptotics and Perturbations*, Vol. 2A, pp. 1-11.
- Selinger, J. V., 2016, *Introduction to the Theory of Soft Matter from Ideal Gases to Liquid Crystals*, Springer, OH-USA.
- Tasgal, R. S., Band, Y.B., 2015, "Sound Waves and Modulational Instabilities on Continuous-Wave Solutions in Spinor Bose-Einstein Condensates", *Physical Review*, A 91, 013615, pp. 1-15.
- Waldron, R.A., 1981, "Formulas for Computation of Approximate Values of Some Bessel Functions", *Proceedings of the IEEE*, Vol. 69, pp. 1686-1588.
- Watson, G. N., 1995, *A Treatise on the Theory of Bessel Functions*, (2<sup>nd</sup> ed.), Cambridge University Press, NY.
- Wellin, P., 2016, *Essentials of Programming in Mathematica*, 1st ed., Cambridge, Cambridge University Press, pp. 449-493.
- Wolfram, S., 2003, *The Mathematica Book* (5<sup>th</sup> ed.), Wolfram Media Inc., 5th edition, USA, pp. 29-35 & pp. 102-110.
- Wolfram, S., 2017a, *Wolfram Documentation Center, BesselJ*, <http://reference.wolfram.com/mathematica/ref/BesselJ.html> (accessed in 22 February 2017).
- Wolfram, S., 2017b, *Wolfram CDF player*, <https://www.wolfram.com/cdf-player/> (accessed in 22 February 2017).
- Wolfram, S., 2017c, *Computable Document Format*, <http://www.wolfram.com/events/siam-2016/files/CDF-4.pdf> (accessed in 22 February 2017).
- Wolfram Research, Inc., 2017, *Mathematica*, Version 11.1, Champaign, IL.



## A K-MEANS CLUSTERING BASED SHAPE RETRIEVAL TECHNIQUE FOR 3D MESH MODELS

<sup>1</sup>Mohammadhassan REZAEI, <sup>2</sup>Erkan GUNPINAR

<sup>1,2</sup>Istanbul Technical University, School of Mechanical Engineering, Inonu Caddesi, No: 65, Gumussuyu, 34437, Istanbul, TURKEY

<sup>1</sup>mohrezaei86@gmail.com, <sup>2</sup>gunpinar@itu.edu.tr

(Geliş/Received: 14.04.2017; Kabul/Accepted in Revised Form: 03.07.2017)

**ABSTRACT:** Due to the large size of shape databases, importance of effective and robust method in shape retrieval has been increased. Researchers mainly focus on finding descriptors which is suitable for rigid models. Retrieval of non-rigid models is a still challenging field which needs to be studied more. For non-rigid models, descriptors that are designed should be insensitive to different poses. For non-rigid model retrieval, we propose a new method which first divides a model into clusters using geodesic distance metric and then computes its descriptor using the area of these clusters. A skeleton-based K-means clustering method is utilized for dividing the model into clusters. Each cluster is represented by an area based descriptor which is invariant to scale and orientation. Articulated objects from human to animals are employed in this study's experiments for the validation of the proposed retrieval algorithm.

**Key Words:** Geodesic distance, K-means clustering, Mesh skeleton, Shape retrieval,

### Üç Boyutlu Çözüm Ağları için K-Means Kümeleme Tabanlı Şekil Araması

**ÖZ:** Şirketlerin veri tabanlarında çok fazla şekil bulunmaktadır. İstenilen şekillerin bu veri tabanından bulunup getirilmesi için etkili ve güçlü şekil arama metodlarının kullanılması gerekmektedir. Araştırmacılar genelde rijit (esnemeyen) modellere uygun geometrik tanımlayıcılar üzerine odaklanmışlardır. Rijit olmayan modellerin bulunması daha zor olmakta ve bu konuda daha çok çalışılması gerekmektedir. Rijit olmayan modeller için tasarlanan geometrik tanımlayıcılar değişik model pozlarında (insan modeli için yürüme, oturma gibi pozlar) çalışabilmesi gerekmektedir. Rijit olmayan model araması için, öncelikle model jeodezik metrik kullanarak parçalara bölünür. Sonra her bir parçanın alanı toplam alana bölünerek geometrik tanımlayıcı hesaplar. İskelet-bazlı K-means metodu kullanarak model parçalara ayrılmıştır. Her parça alan-bazlı tanımlayıcılar kullanılarak tanımlanmıştır. Bu tanımlayıcıların ölçek ve oryantasyon değişikliklerine hassasiyeti yoktur. Çalışmanın testlerinde insandan hayvanlara eklemli canlılar kullanılmış, önerilen model arama metodunun performansı doğrulanmıştır.

**Anahtar Kelimeler:** Jeodezik uzaklık, K-means kümeleri, Çözüm ağı iskeletleri, Model bulma,

### INTRODUCTION

With the increase in the number of 3-D models in the internet or company databases, accessing desired models from databases in a shorter time becomes an open issue for research. In the last years, some 3D model search engines have been designed for accessing 3D models in databases consisting of huge data sets. Some famous search engines are Princeton University search Engine (Min *et al.*, 2003), Taiwan National University shape retrieval engine (Shen *et al.*, 2003) and FOX-Mier shape retrieval engine (Ansary *et al.*, 2007). In shape retrieval, model features should be found which describe the model well which are called *shape descriptors*. Some of the descriptors proposed in literature are accurate, but

utilizing them in real time is time consuming. On the other side, there are some descriptors which are fast, but not robust. Researchers try to design a descriptor and balance the speed and robustness at the same time.

In a shape retrieval engine, an input model, called *query*, is selected and similar models to the query are listed among the models in model database. Utilizing directly the retrieval algorithm on 3D models in database is time consuming, therefore we first have a preprocessing step called *off-line step* in which descriptors for the query and datasets are calculated. Comparison between the query descriptor and the descriptors for models of datasets are then made in an on-line step. Search engine retrieves all similar models to the query via using pre-computed descriptors. The descriptor suggested in this paper is insensitive to different model poses and is invariant when the model is rotated, translated or scaled.

The proposed algorithm consists of three main steps. First, a 3D mesh model is partitioned into clusters via a K-means clustering technique. Geodesic distance is utilized during the clustering step. As K-means algorithm is sensitive to the initial seeds given, K-Furthest seeds are computed by means of the mesh skeleton. Model descriptor is defined based on surface area of the clusters which is not sensitive to different model poses. Models are finally retrieved using their descriptors. We form a model database for the validation of the proposed algorithm which consists of the models especially from Princeton University Benchmark.

## RELATED WORKS

3D shape retrieval methods can be divided into three main categories: Feature-based techniques, graph-based techniques and view-based techniques. Here, we outline some of the proposed techniques in these categories. Paquet et al. (2000) used cord histograms. Cords were defined as the connecting center of the model to the center of each triangle faces. Zhang and Chen (2001) used surface properties like area, volume and istatistical moment to create global feature descriptors. Convex-hull based descriptors were introduced by Corney et al. (2002). Hull crumbliness, hull packing and hull compactness were defined as descriptors in their paper. Extended Gaussian Image (EGI) method was defined for the first time by Horn (1984). In this histogram-based method, normal vector of each triangle was mapped on the Gaussian sphere. Complex extended Gaussian image (CEGI) was then generalized by Kang and Ikeuchi (1991) which took the distance of faces to the origin also into consideration. Kazhdan et al. (2004) used a mirroring descriptor in their work. They calculated global descriptor by measuring the reflective symmetry of each plane of 3-D model according to the position of model's center. Osada et al.(2002) brought distribution concept to global dissimilarity descriptors. They first extracted descriptor based on area, volume or distance. Difference of distributions then showed the amount of dissimilarity between 3D models. Ohbuchi et al. (2002) created shape histograms along with the principal axis of 3D model. They used properties such as the moment of inertia, average distance from surface to the principal axis and distance variation to the principal axis for creating histograms. Ip et al. (2002) applied the shape distribution approach for the CAD models by reforming Osada's  $D2$  function. This method was only useful for volume models and not for soup models. Sector and shells based disstribution histograms were used by Ankerst et al. (1999). 3D models were divided into different spatial parts by using singly concentric shells and sectors. These sector and shell unites were corresponding with each bin in the shape histogram. Vranic et al. (2001) presented a ray-based descriptor which first found the spherical extent function of the model and then created descriptor by calculating spherical harmonics of that function. The method was not rotation invariation and needs pose normalization. Kazhdan et al. (2003) described a rotation invariant method for representing 3D models. In this method, by means of concentric spheres, spherical harmonic was constructed.

For graph-based techniques, reeb graphs and skeleton-based methods are the most popular. Mathematically, *reeb graphs* are a kind of skeleton which describe a 3D model topologically by using a scalar function. In reeb graphs, quotient function,  $f$ , play an important role for creating graphs. Biasotti et al. (2003) showed that applying various quotient function led to different reeb graphs and choosing

suitable quotient function has crucial effect in matching result. Hilaga et al. (2001) used integral geodesic distance as a quotient function. Bespalov et al. (2003) implemented Hilaga’s procedure on solid models. They concluded that reeb graph matching method was sensitive to topology of 3D models and more work should be done to enhance the method. For skeleton-based techniques, Sundar et al. (2003) used models skeleton for retrieving the models. They first voxelized 3D shape object and they then used Gagvani’s *Volume Thinning* algorithm (Gagvani and Silver, 1999). Sundar et al. (2003) tried to find similarity of two 3D shapes by comparing their skeletal graph by detecting the maximum cardinality, minimum weight matching between two corresponding graph. Funkhouser et al. (2003) used a view based technique for shape retrieval. They applied a two dimensional sketch as a query. Chen et al. (2003) and Shen et al. (2003) utilized a view-based technique for retrieving 3D objects by noticing the fact that 3D models are similar if they look same from all points of view.

Our technique takes different approach than the shape retrieval techniques in the literature which utilize a single cluster (i.e., whole model). However, we generate different clusters and the descriptor is defined on these clusters. We believe that it is advantageous because main focus of researchers in previous works was to finding descriptors which represent 3-D model globally. One of the weak point is that some of the retrieved models for the input model (query) are completely different, but they are globally similar to the query according to the descriptor used. To avoid this problem, we proposed a new method which divides models into clusters first and computes then descriptors on these clusters. Furthermore, using geodesic metric for K-means clustering rather than Euclidean metric makes our method insensitive to different poses.

**PROPOSED METHOD**

**Overview**

In this section, we describe the flow of the proposed method. Figure 1 illustrates the main steps of the proposed algorithm. The skeleton of a given 3D mesh model is first computed. Two furthest points on the skeleton are then found. Two corresponding points on the mesh for these two points is calculated which are assigned as the first two seed points that will be used in the *K-means* clustering algorithm. Other *k-2* seed points are then found. In the next step, *K-means* algorithm is utilized to partition the mesh into vertex clusters by using *k* seed points. *K* is a user-defined integer input. The mesh model is simplified using an area based shape descriptor which is a fingerprint of the model. The descriptor carries the important information of the model which is used to compare it with other shapes. Therefore, similarity rate between models is computed based on this shape descriptor.

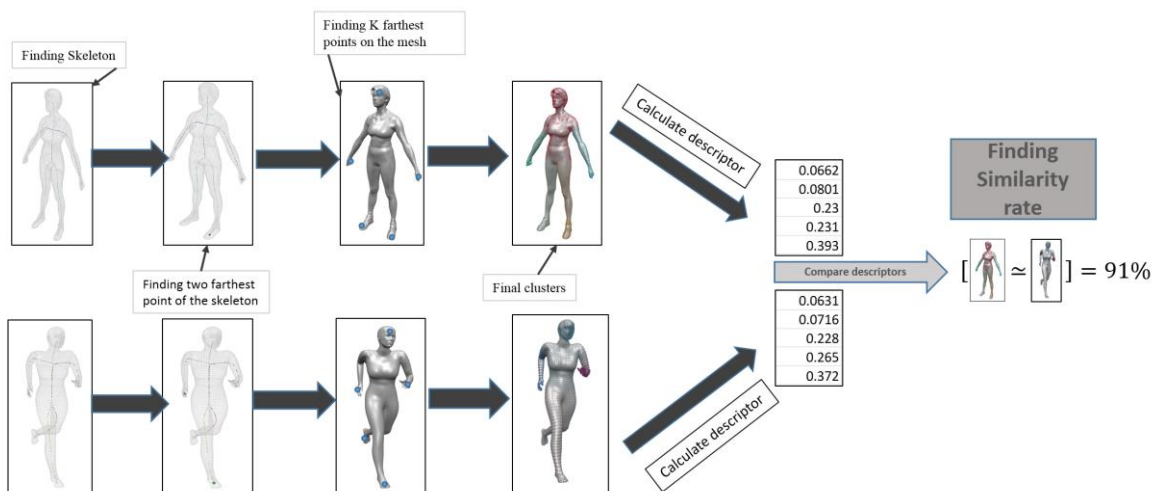


**Figure 1.** Flow of the proposed technique

### K-means Clustering

A mesh,  $M$ , is partitioned into  $k$  sub-meshes or clusters,  $\{M_1, M_2, \dots, M_k\}$ . A cluster,  $M_i$ , consists of a set of vertices and a cluster center (or centroid),  $\mu_i$ , where  $i$  is integer between 1 and  $k$ . Furthermore, any two cluster,  $M_u$  and  $M_v$ , do not share the same vertex (i.e.,  $M_u \cap M_v = \emptyset$ ). To find clusters, objective function in Formula 1 is utilized which aims to minimize the total sum of the squared distance for all vertices in each cluster with its centroid center.

$$\min \sum_{i=1}^k \sum_{x \in M_i} \|x - \mu_i\|^2 \quad (1)$$

Exact solution for this problem is NP hard. Lloyd's clustering technique (Lloyd, 1982) is used extensively by many scientists and researchers in different fields (Herwig *et al.*, 1999; Agarwal and Nabil, 2004; Gibou and Fedkiw, 2005) which our technique utilize as well. Partitioning and cluster center update phases are iterated until the cluster centers do not move anymore or if their move is negligible.

Pseudo-code for the Lloyd's *K-means* clustering technique is as follows:

1. Select  $k$  vertices randomly in the mesh as initial centroids or seeds
2. Assign each mesh vertex to the closest centroid.
3. Compute mean of each cluster and select the vertex in the cluster that is closest to the mean as new centroid.
4. Iterate line 2 and 3.
5. If the centroid positions do not change anymore, algorithm stops.
6.  $K$  number of clusters are obtained.

*K-means* clustering has a rather high speed, however this algorithm is sensitive to initial seed points (i.e., centroids) or initial centers. We tried to solve this problem by making use of mesh skeleton which will be described in the next section. Another important issue is to use of an appropriate distance metric. Geodesic distance is utilized to compute distance between two points which is the shortest path between the points on the surface model. Figure 2 shows Geodesic and Euclidean distance on a 3D mesh model.

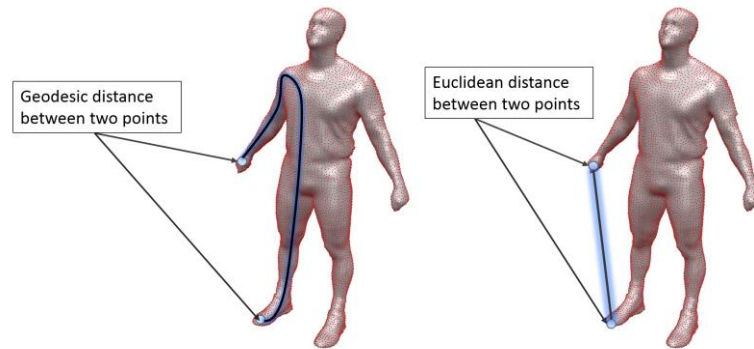


**Figure 2.** Geodesic and Euclidean distance on the 3D model

### Skeleton-based K-means Partitioning

Weak point of K-means clustering is its sensitivity to the selected initial seed points. Shape retrieval method that will be detailed in Section 3.4 closely depends on the quality of generated clusters. Our aim is to cluster models in the way that clusters are similar in similar models. To achieve this, initial seed points should be approximately at the same position for similar models. One way is to select  $k$  furthest points on the mesh. This has, however, high computational cost for a model with a large number of vertices if Geodesic distance computation is utilized. Suppose we have a 3D model with  $n$  mesh vertices.

For finding two furthest vertices in the mesh, Geodesic distance between  $\frac{n*(n-1)}{2}$  vertex pairs should be checked. The 3D models used in our work have mostly more than 5000 points and finding two furthest vertex for a model can take even a few days. To overcome this problem, we first create the skeleton of 3D model and then compute two furthest points in the skeleton which can help in finding two furthest points in the mesh. The problem of finding two furthest points can be solved just in a few seconds even for models with 10000 points.

There are several techniques (Au *et al.*, 2008, Dey and Sun, 2006; Gagvani and Silver, 1999; Sundar *et al.* 2003; Tagliasacchi *et al.*, 2012) existing in literature to compute the skeleton of a given shape represented using 3D mesh. The technique (Tagliasacchi *et al.*, 2012) of Andrea Tagliasacchi *et al.* is utilized to compute the skeleton for a shape represented using 3D mesh because of its high computational speed and the ability to produce good results. The method creates skeleton curve by using *Mean Curvature Flow* (MCF), which is negative gradient flow of the area. Area of the mesh becomes smaller by iteratively contracting mesh vertices towards the positions where curvature is maximum. Another advantage of the MCF-based methods is that it can automatically compute skeleton by just adjusting a few number of user-defined parameters (Au *et al.*, 2008; Tagliasacchi *et al.*, 2012).

The computed skeleton is represented using an undirected graph with positive weights. A graph  $G = (V, E)$  consists of a set of vertices  $V$  and a set of edges  $E \subseteq V \times V$  which are unordered pair of  $V$ . In undirected graphs all the edges are bidirectional. Figure 3 illustrates a undirected graph.

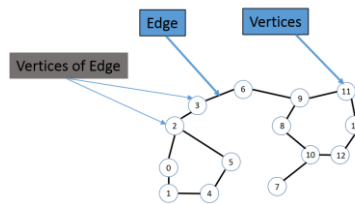


**Figure 3.** An undirected graph with 15 vertices and 15 edges.

The problem to find two furthest points in an undirected graph can be formulated as a single-source shortest path problem which can be solved by the Dijkstra's algorithm (Dijkstra, 1959). Let  $s$  and  $t$  be the source and target vertex, respectively. All possible shortest paths in the graph are computed first. A path connecting two vertices ( $s$  and  $t$ ) with maximum weight (sum of all the edges of shortest path) will then be selected. These two vertices are the two furthest vertices in the skeleton. A pseudo-code for finding the shortest path from a source vertex,  $s \in V$ , to another vertices,  $v \in V$ , is given in below:

```

function Dijkstra(Graph, source):
  for each vertex v in Graph: // setting all vertex except source vertex to infinity
    set dist[v] to infinity
    set previous[v] undefined
  end for
  set dist[source] to 0 // distance from source vertex to itself is zero
  Q : the set of all vertices of Graph
  while Q is not empty // so long as queue is not empty
    set u to the vertex in Q with smallest distance in dist[u]
    remove u from Q
    if dist[u] is infinity
      break // all remaining vertices are inaccessible from source
    end if
    for each neighbor v of u:
      W= dist[u] + dist_between(u, v) ;
      if W < dist[v]
        dist[v] := W ;
        previous[v] := u ;
        decrease-key v in Q // reorder v in the queue
      end if
    end for
  end while
  return dist
End of function

```

Next, other  $k-2$  seeds will be found to complete the seed set  $S = \{s_1, s_2, s_3, \dots, s_k\}$  which will be used to start  $K$ -means clustering algorithm.  $s_1$  and  $s_2$  denote the first two seed points that are computed with the help of the model skeleton in the previous step. Our objective is to find these points which are well distributed on the model. In other words, the seeds should be evenly spaced which we call *space-filling* seeds. Therefore, minimum pairwise distance between seeds is maximized. A greedy approach is chosen to find other seeds. To find the  $i^{th}$  seed where  $2 < i \leq k$  and  $i$  is integer, the vertex  $v \in V$  in the mesh should maximize the following equation:  $\min \{Dist(v, s_1), Dist(v, s_2), \dots, Dist(v, s_{i-1})\}$  and is selected as the  $i^{th}$  seed  $s_i$ . The seed selections will be performed until finding  $k$  seeds on the 3D mesh model. Effect of initializing  $K$ -means clustering with Skeleton-based  $k$  seeds and randomly selected seeds are given in Figure 4. Former one can generate similar clusters for the models in same groups. However, the latter one does not achieve similar clusters.

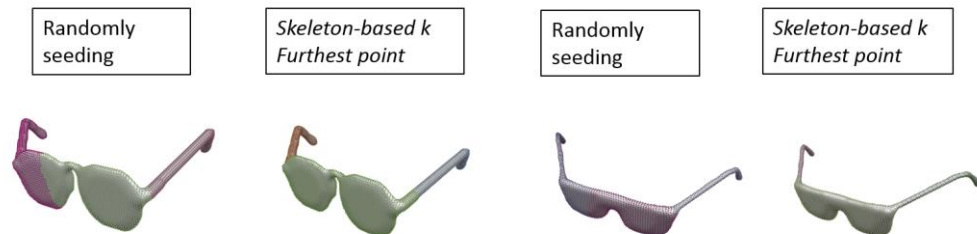


**Figure 4.** Clusters in the left image are obtained starting with random seeds. Clusters in the right image are obtained using the seeds generated by our method.



**Table 1.** Retrieving results of different queries for the most similar models

<i>Input model</i>	<i>Number of clusters</i>	<i>Retrieved models respectively from most to least similarity rate</i>									
	K=3	 99%	 91%	 91%	 86%	 86%	 85%	 83%	 79%	 79%	 79%
	K=5	 96.5%	 96%	 95.3%	 95%	 94.5%	 94.4%	 92%	 91.3%	 90.9%	 90.6%
	K=6	 97.9%	 97%	 96%	 95.9%	 95%	 94.5%	 94.2	 94%	 93.3%	 93.1%
	K=5	 97.9%	 97.7%	 97.7%	 97.6%	 97.1%	 97%	 96.2%	 96%	 96%	 95.7%
	K=9	 99.1%	 98%	 97.5%	 96.3%	 96%	 94%	 94%	 92%	 91.8%	 91.8%

Table 2 shows the most dissimilar models to the query. For the eyeglass model, all of the most dissimilar models are octopuses with 57.8%, 59.5%, 60% and 62.4% dissimilarity rates. For the woman model, cylindrical model and panda are the most dissimilar retrieved models with 81% of similarity rates. For the hand model, the camel is the most dissimilar model, and most of the octopus models are the last 10 dissimilar models to the input hand model. According to the results in Table 2, by increasing the number of clusters, dissimilarity rate difference between most similar and the least similar model to the query decreases. For example; for the eyeglass model with the K=3 setting, similarity rate difference between the most similar (99%) and the most dissimilar model (57.8%) is 42.2%. However, this difference decreases to 18% for the hand model with the K=6 setting and to 16% for the octopus model with the K=9 setting.

**Table 2.** Retrieving results of different queries for the least similar models

<i>Input model</i>	<i>Number of clusters</i>	<i>Least similar models to the query</i>									
	K=3	 68%	 68%	 67%	 67%	 67%	 67%	 62.4%	 60%	 59.5%	 57.8%
	K=5	 85%	 85%	 84.4%	 83%	 82%	 82%	 81.3%	 81.3%	 81%	 81%
	K=6	 90.5%	 90.4%	 90.3%	 90.2%	 88.7%	 88.5%	 86.5%	 84.5%	 84%	 79.9%
	K=5	 90%	 90%	 89.8%	 89.7%	 89.5%	 89.5%	 86.8%	 85.9%	 82.2%	 79.2%
	K=9	 88.7%	 88.4%	 88%	 87.8%	 87.85	 87.7%	 87.6%	 87.4%	 87.4%	 86.7%

**Parameter tuning:** Here, we will show the effect of choosing different number of clusters ( $K$ ) on the same group of models (eyeglasses). Experiments are done for the  $K$  values of 3, 5, 7 and 9. The retrieval results are arranged in Table 3. Average similarity rate for different number of clusters are approximately same in most of the cases. It seems that the  $K=3$  setting gives satisfactory results for the eyeglass model and it is not required to increase the number of clusters. Note that if the number of clusters increase, more computation time is needed.

**Table 3.** Effect of selecting different number of clusters on the similarity rate for the eyeglass model

<i>Input model</i>	<i>Number of clusters</i>	<i>Similarity rate</i>		
	K=3	 91%	 99%	 91%
	K=4	 82%	 95%	 88.4%
	K=5	 90%	 96%	 90%
	K=6	 93.9%	 96.9%	 90.6%
	K=9	 87.8%	 96.8%	 91.6%

The woman model is used to test the effect of selecting different number of clusters,  $K$ , on the similarity rate. Table 4 summarizes these results. According to Table 4, results with the  $K=6$  setting seems better than the  $K=3$  setting, but more computation time is required for this setting. Finding optimum number of clusters will be our future goal, but we recommend to select a fewer number of clusters as much as possible.

**Table 4.** Effect of selecting different number of clusters on the similarity rate for the woman model

<i>Input model</i>	<i>Number of clusters</i>	<i>Similarity rate</i>		
	K=3	 99%	 94%	 96.7%
	K=4	 99%	 88%	 98.5%
	K=5	 94.5%	 91%	 91%
	K=6	 97.6%	 96.1%	 97%
	K=9	 95%	 93%	 96.5%

**Computational time:** Time required for clustering and descriptor computation is shown in Table 5. With the increase in the number of clusters ( $K$ ), computational time for both of these steps increase. Ratio of clustering time to descriptor time decreases when  $K$  increases. For example, the ratio for  $K=3$  is 0.75, whereas it increases to 1.18 for  $K=9$ . The reason behind this is that finding  $K$  furthest points on the mesh is computed based on the Geodesic distance which takes higher time. For a human model, clustering time is from 11.4 minutes to 52.9 minutes. Time taken for computing descriptor is from 15.2 to 44.6 minutes.

The woman and octopus model contains approximately 5600 and 6000 mesh vertices, respectively. Computational time for both clustering and descriptor again increases. It can be observed that computation time for models with approximately same number of points are approximately same. For octopus model, clustering time changes from 12.8 to 57.1 minutes. Ratio of clustering time to descriptor

time for the octopus model with the  $K=3$  setting is 0.86, whereas it increases to 1.21 for the  $K=9$  setting which is closed to those of the woman model, 0.75 and 1.18, respectively. The chair model consists of 8600 mesh vertices, and therefore computational time increases significantly. Clustering time for the  $K=3$  setting increases from 12.8 minutes to 24.5 when compared to the octopus model. For the descriptor calculation stage, it increases from 14.8 to 34.4 minutes. Ratio of the clustering time to the descriptor time for the  $K=3$  setting is 0.71, whereas it increases to 1.17 for the  $K=9$  setting. When compared to the previous models, they are approximately same. According to the results, it can be concluded that the ratio of clustering time to the descriptor time for different models with same number of clusters is approximately same also for the models consisting of different number of mesh vertices. Finally, the online step, finding the most similar models based on the precomputed descriptors, for the model retrieval takes less than a minute for the test cases in this work.

**Table 5.** Computational time for the proposed technique

Model	Number of clusters	Clustering time (in minutes )	Time for descriptor computation (in minutes )
	$K=3$	11.4	15.2
	$K=5$	21.8	24
	$K=7$	35.7	33.7
	$K=9$	52.9	44.6
	$K=3$	12.8	14.8
	$K=5$	24.1	26.8
	$K=7$	38.4	37.4
	$K=9$	57.1	46.9
	$K=3$	24.5	34.4
	$K=5$	48.8	53.2
	$K=7$	77	79
	$K=9$	117	100

## CONCLUSION AND FUTURE WORKS

In this paper, we present a new method for retrieving 3D models represented using meshes. The models are divided into clusters by applying skeleton-based K-means partitioning method. In an off-line step, model descriptors are computed which are based on the cluster areas. In an online step, similarity rate between the query and other models in database is computed and similar models to the query are retrieved from the database. Performance of the proposed retrieval technique is shown via several experiments where rigid and non-rigid models are utilized. According to the results, the proposed method is successful in terms of its retrieving performance. Furthermore, it has been shown that the method is invariant to different model poses, and therefore can be used for non-rigid models.

As a future work, the proposed clustering method will be improved in order to achieve a less computation time in off-line step. One way for this can be to find an optimum number of clusters required for the K-means clustering method. The proposed algorithm fails in some cases even though it works well in most cases according to experiments. Using different geometric descriptors jointly instead of just one simple descriptor can lead to better retrieving performance. Additionally, it will be interesting to study on the automatic setting for the  $k$  value that is used in the clustering algorithm. Finally, we would like to extend our model retrieval technique for quadrilateral meshes (generated using mixed-integer quadrangulation (Bommes *et al.*, 2009) which are segmented into quad partitions using motorcycle graph (Eppstein *et al.*, 2008; Bommes *et al.*, 2009; Gunpinar *et al.*, 2013; Gunpinar *et al.*, 2014a; Gunpinar *et al.*, 2014b).

## REFERENCES

- Agarwal, P. K., Mustafa, N. H., "K-means Projective Clustering" ,In *Proceedings of The Twenty-Third ACM SIGMOD-SIGACT-SIGART Symposium on Principles of Database Systems* , ACM, Paris, France, pp. 155-165, 14 – 16 June 2004.
- Ankerst, M., Kastenmüller, G., Kriegel, H. P. , Seidl, T., "3D Shape Histograms for Similarity Search and Classification in Spatial Databases" , In *International Symposium on Spatial Databases*, pp. 207-226, Springer Berlin Heidelberg, July 1999.
- Ansary, T. F., Vandeborre, J. P., Daoudi, M., "3d-Model Search Engine from Photos" , In *Proceedings of the 6th ACM international conference on Image and video retrieval*, Amsterdam, The Netherlands, pp. 89-92, ACM, 09 - 11 July 2007.
- Au, O. K. C., Tai, C. L., Chu, H. K., Cohen-Or, D., Lee, T. Y., 2008, "Skeleton Extraction by Mesh Contraction" , *ACM Transactions on Graphics (TOG)*, Vol.27 (3), 44.
- Bespalov, D., Regli, W. C., Shokoufandeh, A., "Reeb Graph Based Shape Retrieval for CAD" , In *ASME 2003 International Design Engineering Technical Conferences and Computers and Information in Engineering Conference* , Chicago, Illinois, USA, pp. 229-238, American Society of Mechanical Engineers, 2–6 September 2003.
- Biasotti, S., Marini, S., Mortara, M., Patane, G., Spagnuolo, M., Falcidieno, B., "3D Shape Matching Through Topological Structures" , In *International Conference on Discrete Geometry for Computer Imagery* ,pp. 194-203, Springer Berlin Heidelberg, November 2003.
- Bommes, D., Zimmer, H., Kobbelt, L., 2009, "Mixed-integer Quadrangulation" , *ACM Transactions on Graphics (TOG)*, Vol.28 (3), 77.
- Chen, D. Y., Tian, X. P., Shen, Y. T., Ouhyoung, M., 2003, "On Visual Similarity Based 3D Model Retrieval" ,In *Computer Graphics Forum*, Vol. 22, No. 3, pp. 223-232, Blackwell Publishing, Inc, September 2003.
- Corney, J., Rea, H., Clark, D., Pritchard, J., Breaks, M., MacLeod, R., 2002, "Coarse Filters for Shape Matching" , *IEEE Computer Graphics and Applications*, Vol. 22(3), pp. 65-74, 2002.
- Dey, T. K., Sun, J., "Defining and Computing Curve-Skeletons with Medial Geodesic Function" , In *Symposium on Geometry Processing*, Vol. 6, pp. 143-152, June 2006.
- Dijkstra, E. W. 1959, "A Note on Two Problems in Connexion with Graphs" , *Numerische Mathematik*, Vol. 1(1), pp. 269-271.
- Eppstein, D., Goodrich, M. T., Kim, E., Tamstorf, R., 2008, "Motorcycle Graphs: Canonical Quad Mesh Partitioning" , In *Computer Graphics Forum* , Vol. 27, No. 5, pp. 1477-1486, Blackwell Publishing Ltd , July 2008.
- Funkhouser, T., Min, P., Kazhdan, M., Chen, J., Halderman, A., Dobkin, D., Jacobs, D., 2003, "A Search Engine for 3D Models" , *ACM Transactions on Graphics (TOG)*, Vol. 22(1), pp. 83-105.
- Gagvani, N., Silver, D. 1999, "Parameter-Controlled Volume Thinning" , *Graphical Models and Image Processing*, Vol. 61(3), pp. 149-164.

- Gibou, F., Fedkiw, R., "A fast hybrid k-means level set algorithm for segmentation", In *4th Annual Hawaii International Conference on Statistics and Mathematics*, Honolulu, Hawaii, pp. 281-291, 9-11 January 2005.
- Gunpinar, E., Suzuki, H., Ohtake, Y., Moriguchi, M. 2013, "Generation of Bi-Monotone Patches from Quadrilateral Mesh for Reverse Engineering", *Computer-Aided Design*, Vol. 45(2), pp. 440-450.
- Gunpinar, E., Moriguchi, M., Suzuki, H., Ohtake, Y., 2014a, "Feature-Aware Partitions from the Motorcycle Graph", *Computer-Aided Design*, Vol. 47, pp. 85-95.
- Gunpinar, E., Moriguchi, M., Suzuki, H., Ohtake, Y. 2014b, "Motorcycle Graph Enumeration from Quadrilateral Meshes for Reverse Engineering", *Computer-Aided Design*, Vol. 55, pp. 64-80.
- Herwig, R., Poustka, A. J., Müller, C., Bull, C., Lehrach, H., O'Brien, J. 1999, "Large-Scale Clustering of cDNA-Fingerprinting Data", *Genome Research*, Vol. 9(11), pp. 1093-1105.
- Hilaga, M., Shinagawa, Y., Kohmura, T., Kunii, T. L., "Topology Matching for fully Automatic Similarity Estimation of 3D shapes", In *Proceedings of the 28th Annual Conference on Computer Graphics and Interactive Techniques*, Los Angeles, CA, USA, pp. 203-212, ACM, 12 - 17 August 2001.
- Horn, B. K. P., 1984, "Extended Gaussian Images", *Proceedings of the IEEE*, Vol. 72(12), pp. 1671-1686.
- Ip, C. Y., Lapadat, D., Sieger, L., Regli, W. C., "Using Shape Distributions to Compare Solid Models", In *Proceedings of the Seventh ACM Symposium on Solid Modeling and Applications*, Saarbrücken, Germany, pp. 273-280, ACM, 17 - 21 June 2002.
- Kang, S. B., Ikeuchi, K., "Determining 3-D Object Pose Using the Complex Extended Gaussian Image", In *Computer Vision and Pattern Recognition, 1991. Proceedings CVPR'91, IEEE Computer Society Conference on*, pp. 580-585, IEEE, June 1991.
- Kazhdan, M., Chazelle, B., Dobkin, D., Funkhouser, T., Rusinkiewicz, S., 2004, "A Reflective Symmetry Descriptor for 3D models", *Algorithmica*, Vol. 38(1), pp. 201-225.
- Kazhdan, M., Funkhouser, T., Rusinkiewicz, S., "Rotation Invariant Spherical Harmonic Representation of 3D Shape Descriptors", In *Symposium on Geometry Processing*, Vol. 6, pp. 156-164, June 2003.
- Lian, Z., Godil, A., Bustos, B., Daoudi, M., Hermans, J., Kawamura, S. Dp Suetens, P., 2011, "Shape Retrieval on Non-rigid 3D Watertight Meshes", In *Eurographics Workshop on 3D Object Retrieval (3DOR)*.
- Lloyd, S. 1982, "Least Squares Quantization in PCM", *IEEE transactions on Information Theory*, Vol. 28(2), pp. 129-137.
- Min, P., Halderman, J. A., Kazhdan, M., Funkhouser, T. A., "Early Experiences with a 3D Model Search Engine", In *Proceedings of the Eighth International Conference on 3D Web Technology*, St. Malo, France, pp. 7-ff, ACM, 09 – 12 March 2003.
- Ohbuchi, R., Otagiri, T., Ibato, M., Takei, T., 2002, "Shape-Similarity Search of Three-Dimensional Models Using Parameterized Statistics", In *Computer Graphics and Applications, 2002. Proceedings, 10th Pacific Conference on*, pp. 265-274, IEEE.
- Osada, R., Funkhouser, T., Chazelle, B., Dobkin, D., 2002 "Shape distributions", *ACM Transactions on Graphics, (TOG)*, 21(4), 807-832.
- Paquet, E., Rioux, M., Murching, A., Naveen, T., Tabatabai, A., 2000, "Description of Shape Information for 2-D and 3-D Objects", *Signal Processing: Image Communication*, Vol. 16(1), pp. 103-122.
- Shen, Y. T., Chen, D. Y., Tian, X. P., Ouhyoung, M., 2003, "3D Model Search Engine based on Lightfield Descriptors", In *Proc. Eurographics*, Granada, Spain, 1–6 September 2003.
- Shilane, P., Min, P., Kazhdan, M., Funkhouser, T., "The Princeton Shape Benchmark", In *Shape Modeling Applications, 2004. Proceedings*, Genova, Italy, pp. 167-178, IEEE, 7-9 June 2004.
- Sundar, H., Silver, D., Gagvani, N., Dickinson, S., "Skeleton Based Shape Matching and Retrieval", In *Shape Modeling International*, Seoul, South Korea, pp. 130-139, IEEE, 12-15 May 2003.
- Tagliasacchi, A., Alhashim, I., Olson, M., Zhang, H., "Mean Curvature Skeletons", In *Computer Graphics Forum*, Vol. 31, No. 5, pp. 1735-1744, Blackwell Publishing Ltd, August 2012.

- Vranic, D. V., Saupe, D., Richter, J., "Tools for 3D-Object Retrieval: Karhunen-Loeve Transform and Spherical Harmonics", *In Multimedia Signal Processing, 2001 IEEE Fourth Workshop on* (pp. 293-298), Cannes, France, 3-5 Oct. 2001.
- Zhang, C., Chen, T., 2001, "Efficient Feature Extraction for 2D/3D Objects in Mesh Representation", *In Image Processing, 2001. Proceedings. 2001 International Conference on*, Thessaloniki, Greece, Vol. 3, pp. 935-938, 7-10 Oct. 2001.

## A STUDY FROM JUNK MARKET TO THE PRODUCTION OF 5.25% EFFICIENT DYE-SENSITIZED SOLAR CELLS

<sup>1</sup>Sunay TURKDOGAN

<sup>1</sup>Department of Electrical and Electronics Engineering and Department of Energy Systems Engineering, Faculty of Engineering, University of Yalova, Yalova, 77200, Turkey

<sup>1</sup>[sunay.turkdogan@yalova.edu.tr](mailto:sunay.turkdogan@yalova.edu.tr)

(Geliş/Received: 20.04.2017; Kabul/Accepted in Revised Form: 10.07.2017)

**ABSTRACT:** This paper reveals that having limited facilities is just an excuse not to do any experimental research in most of the universities and institutions all over the world. This may sound impractical for developed countries; however, it is one of the most fundamental problems for underdeveloped and even for some of the developing countries. In this paper, a study of building a laboratory mostly using homemade devices from junks is explained. This paper might be a good and encouraging reference especially for low-income countries, some universities/institutions with very limited budget around the world as well as some students/researchers who want to have their own tools to conduct a research. After a brief explanation to build some of the tools using junks, the production of dye-sensitized solar cells using homemade equipments with up to 5.25% power conversion efficiency (PCE) will be demonstrated under AM1.5 simulated light emission. Structural, electrical and photovoltaic properties of the fabricated devices will also be investigated using scanning electron microscopy (SEM), X-ray diffraction spectroscopy (XRD), and current-voltage (IV) characterization tools in this paper.

**Key Words:** Dye-sensitized solar cells, Homemade, Optical tachometer, Oven, Photovoltaics (PV), , Spin coater / centrifuge.

### Hurda Pazarından %5.25 Verimli Boya Duyarlı Güneş Hücrelerinin Üretimine Uzanan Bir Çalışma

**ÖZ:** Bu çalışma birçok üniversite ve kurumda sınırlı donanımına sahip olmanın herhangi bir deneysel araştırma yapılmaması için sadece bir bahane olduğunu ortaya koymaktadır. Bu, gelişmiş ülkeler için garip gelebilir; ancak, az gelişmiş ve bazı gelişmekte olan ülkeler için bile en temel sorunlarından biridir. Bu yazıda, çoğunlukla atık/hurda ev cihazları kullanarak bir laboratuvar oluşturma çalışması ve bu laboratuvardaki cihazları kullanarak boya duyarlı güneş hücrelerinin üretimi anlatılmaktadır. Bu çalışmanın özellikle düşük gelirli ülkeler, çok sınırlı bir bütçeye sahip üniversiteler ve araştırma yapmak isteyen öğrenciler ve araştırmacılar için tetikleyici ve cesaret verici bir referans olacağı düşünülmektedir. Hurda malzemeler kullanılarak tasarlanan bazı cihazların kısaca açıklanmasından sonra, AM1.5 benzetimi altında %5.25 güç dönüşüm verimliliğine (PCE) sahip boya duyarlı güneş hücrelerinin üretimi ev yapımı ekipmanlar kullanılarak gösterilecektir. Üretilen cihazların yapısal, elektriksel ve fotovoltaiik özellikleri taramalı elektron mikroskopu (SEM), X-ışınları difraksiyonu (XRD), akım-gerilim (IV) karakterizasyon araçları kullanılarak bu çalışmada araştırılmıştır.

**Anahtar Kelimeler:** Boya Duyarlı Güneş Hücreleri, Ev Yapımı, Optik Takometre, Etüv, Fotovoltaiik, Spin Kaplayıcı / Santrifüj.

## INTRODUCTION

Studying/working in highly prestigious universities/institutions is the most valuable asset in people's life as they provide all the necessary facilities and opportunities to conduct world-class research. However the situation in other universities/institutions in a developing stage is not the same because there is not enough budget to purchase all necessary tools to conduct all kinds of research on faculty members' or students' demands. As an author of this paper after the utilization of the world's most advanced laboratories and developing the first semiconductor based monolithic multicolor lasers (Fan et al., 2013; Turkdogan, 2012; Fan et al., 2015; Turkdogan, 2015;) and LEDs (Turkdogan, 2016) in those labs, the limited budget related difficulties were met in a very young university and the story of building the cost effective equipments/tools using junks and their use to build practical devices were essentially drove us to conduct this research.

In this paper, a few homemade devices along with few commercial ones were employed. Centrifuge, magnetic stirrer and spin coater were designed using high rpm brushless HDD motor with the control circuits and the optical tachometer was designed using Arduino Nano Board. In addition to those a homemade furnace was also designed by transforming a regular residential-type salvage oven into a precisely temperature controllable scientific grade furnace via PID temperature controller (REX-C100), solid-state relay (FOTEK SSR-40A) and K-type thermocouple. Although all these devices are enough to conduct a research on an emerging technology of dye-sensitized solar cells and some others, we are also developing new equipments such as DC magnetron sputter coater, PID controlled split hinge tube furnace and pyranometer from junks. Our aim by designing such low cost tools is to bring the science and research for everyone at anywhere. After building all these tools, we are going to employ them to create new projects in the field of photonics/optoelectronics and those are going to bring high value-added devices. In the literature there are similar works explaining the production of scientific grade equipments from junks (Bianchi et al., 2006; El-Agez and Taya, 2014) but this paper is going to be its first kind explaining the production of more than one equipment as well as their use to fabricate/construct a practical device.

In addition to explaining the development of the equipments from junks, the secondary aim of this research is to build dye-sensitized solar cells with relatively high power conversion efficiency (PCE). The increasing demand for energy forces us to seek new energy sources and those should come from clean energy sources for a sustainable world. Sun is the main source of all renewable energies (wind, tides, biomass, hydro and solar) with the exception of geothermal and among all these options solar energy is the most dependable and able to cover the world energy demand (Ellabban et al., 2014; Gevorkian, 2007). The energy emitted by sun in just one hour is able to meet the world's annual energy demand. Since it has that huge potential, a great number of people are working on the improvement of photovoltaic cells, which directly transform sun light into electricity. In order to bring the cost of electricity produced by PV cells down new materials and device architectures should be used or the efficiency of current commercial cells should be increased by some techniques because the cost of energy produced by PV cells is still high compared to the energy produced from conventional sources (IEA, 2014; Feldman, 2014; Shankleman and Martin, 2017). PV cells are grouped as 1st generation (sc-Si, poly-Si, a-Si), 2nd generation (Thin films - CdTE, CIGS) and 3rd generation (Nanostructure based, Organic, Perovskite, Dye-sensitized, CZTS solar cells) and each cell technology has its own advantages and disadvantages compared to each other (Parida et al., 2011). Since the fabrication process of the DSSCs are relatively easy (Gratzel, 2003) compared to the widely used 1st and 2nd generation solar cells such as sc-Si, poly-Si, CdTe thin film, a dye-sensitized solar cell is going to be built using the aforementioned equipments as a proof of concept. Although DSSCs are not comparable with the current commercial PV cells at the current stage they show a great promise as they are less sensitive to impurities, temperature and angle of incident light, they have relatively high PCE and they can be fabricated with low cost on either flexible or rigid substrates (Jose et al., 2009).

## MATERIALS AND METHOD

The details of designing homemade equipments from junks and fabrication of dye-sensitized solar cells with the characterization methods will be given in the subsections below.

### Building a Homemade PID Controlled Laboratory Oven

A must have laboratory ovens provide uniform temperature throughput and can be used for various applications such as drying, curing, annealing, and so on with the temperature range over 350°C. In order to build an oven which is needed for synthesizing the materials and annealing the samples in our case a salvage residential type oven was purchased from a junk market for \$4. The analog thermometer of the oven was broken, but the heating elements were in a working condition. That was what we actually needed because temperature could be controlled via PID controller (REX-C100) and a K-type thermocouple more precisely. In order to do that K-type thermocouple (\$4) was inserted into center of the oven from the top side (see Fig. 1a-b) and the temperature value was read by a PID controller (\$14 w/ SSR). PID controller keeps the set value inside the oven by switching on and off the solid state relay which supplies energy to the heating elements. Bottom and top resistances of the oven are connected in series to lower the flowing current through the heating elements and therefore this slow down the heating up rate compared to only one-resistance or parallel resistances in use (1000W vs. 2000W & 4000W). The control circuit is suitable to control the temperature between 25-1000°C, but due to the type of heating elements used in the oven our controllable temperature range is limited between 25-350°C. Instead of buying an oven for \$1000 we paid only \$22 in total and designed a precisely temperature controllable oven which can be comparable to the commercial ones.

### Building a Homemade Spin Coater

Spin coater is a widely used tool especially in semiconductor processing and it is used to deposit uniform thin films to a flat substrate through the centrifugal force. When the substrate is rotated at high rpms, the substance (coating material) is spread over by centrifugal force and the thickness of the uniform coating becomes inversely proportional to the square root of the spinning speed (Scriven, 1988). The thickness also depends on the viscosity of the coating materials. Commercial spin coaters usually cost thousands of dollars. In order to design a homemade spin coater with very low cost a 3-phase 9600rpm brushless DC motor recovered from a junk HDD was used as a main part. Motor was controlled using an Electronic Speed Controller (ESC) (XXD HW30A) which is widely used among hobbyists. In order to control ESC we employed an inexpensive servo motor tester (HJ Digital Servo Tester/ESC), which has a reading on it depending on the pulse-duty ratio of the signal sent to servos or ESCs. By connecting all these together as illustrated in the bottom of Fig. 1c and placing all the electronics inside a plastic box and high rpm motor on top of the box with a CD case with holes on it to introduce the coating material, a spin coater was built with extremely low cost. (HDD: 1\$, ESC: 6\$, Servo Tester: 6\$, Plastic Box: 2\$, CD case: 0.5\$, power switch: 0.5\$, 12V power supply: 2\$ and 18\$ in total compared to thousands of dollars) With our spin coater, double-sided tape should be used to fix the substrate to the rotor, but a chuck with a groove to secure the substrate is another option for a vacuum free spin coater.

### Building Homemade Centrifuge and Magnetic Stirrer

Centrifuge machine is another tool widely used in laboratories. It puts an object in rotation around a fixed axis. Sedimentation principle is the main working principle in which the centripetal acceleration causes denser substances and particles to move outward in the radial direction while the less dense objects are displaced and move to the center. In our case a laboratory centrifuge is used to sediment the

synthesized powder which will be dissolved in another solvent and used to be coated on the substrate. In order to design a centrifugal machine the spin coater was utilized because the idea is the same but the only difference is the purpose. Instead of putting substrates onto a spinning plane we need to put vials in an angle and pointing outward direction to utilize the centrifugal force. Since a spin coater was already designed, we used the same device, but converted it to a centrifuge by placing the neck of a plastic bottle with some holes on it to hold the vials as seen in Fig. 1c-d. In order to keep the balance and eliminate any vibration we need to put the same amount of sample to the opposite slots. Since 5lt plastic water bottle is free of charge cost of the centrifuge also came out free. In addition to all those, a strong magnet recovered from a junk HDD was attached to the rotor and with the help of a stage (CD case) to hold the beakers over the magnet spin coater was utilized as a magnetic stirrer. In another words the cost of spin coater, centrifuge and magnetic stirrer all able to spin up to 9600rpm is 18\$ in total.

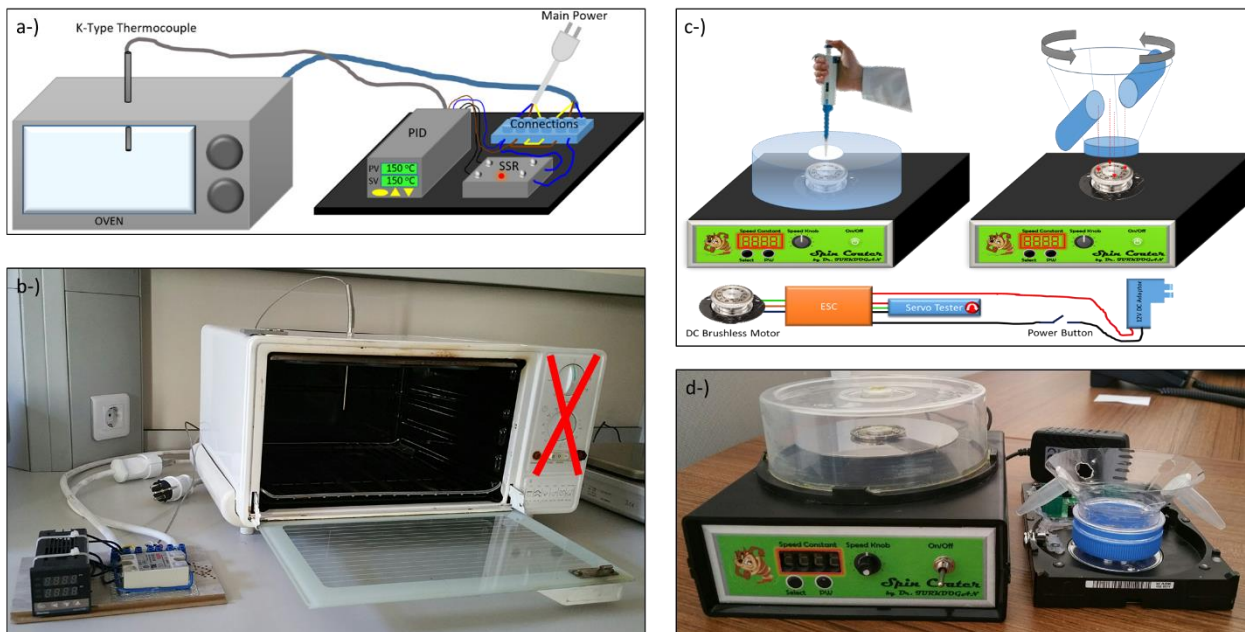


**Figure 1.** Schematic illustrations and real color images of homemade laboratory oven (a-b), spin coater and centrifuge (c-d). Bottom part of (c) shows the electronic control diagram of spin coater, centrifuge and magnetic stirrer.

### Designing an Optical Tachometer using a Microprocessor

In order to measure the rotation speed of the spin coater and centrifuge an optical tachometer was designed utilizing Arduino microcontroller with two resistors and IR LED-photodiode pair taken from a salvage computer mouse. As mentioned in the previous paragraphs 3 phase brushless DC motor recovered from a junk HDD is controlled using an ESC which is widely used among hobbyists. In order to control ESC we employed an inexpensive servo motor tester, which has a reading on it depending on the pulse-duty ratio of the signal sent to servos or ESCs. For the sake of easiness, this value was aimed to be taken as a reference to give speed information. In order to do the transformation an optical tachometer was needed. Figure 2 shows the circuit diagram of the optical tachometer designed and it basically measures how many transition from high to low occurs in a second and then transforms this value by multiplying by 60 to get rpm value by considering the number of triggering black tapes adhered on the spinning plane. This value was reflected on either LCD display or PC serial monitor. Since a black sticky tape was placed on the rotating reflective plane and so that for each rotation we get a trigger from high to low and by utilizing Arduino's interrupt function rpm value was figured out. The photodiode in the circuit was used in photoconductive mode and therefore it was reverse biased and the current flowing from the PD due to incident IR light is transformed into processable voltage signal via

resistors connected in series to PD. Besides fixed resistor a trimpot was also used to adjust the detection sensitivity of the transition from reflective to dark surface(s). The codes used with Arduino are given in Appendix 1 and by using those codes and given circuit diagram everyone can build their own optical tachometer for various purposes.

Figure 2b shows the captured oscilloscope screens of Pin D2 (Interrupt 0) when the spin coater was spinning at 3600 and 9600 rpms, respectively. As seen from the curves when the reflective surface faces the PD, signal at “pin D2” becomes logic “HIGH” and when it faces dark sticky tape the same pin changes the logic status and becomes “LOW”. As shown in Fig. 2b as the spinning speed increases the number of transition in a given time increases and this is reflected in terms of RPMs on the serial monitor (Figure 2b insets). By utilizing the designed optical tachometer a number of values read in the servo tester were tested and their real rpm values saved. By plotting rotation speed vs. Servo tester reading in Fig. 2c we figured out their dependence and any rotation speed required by user can be found in terms of servo tester reading value using the extrapolated formula and adjusted accordingly.

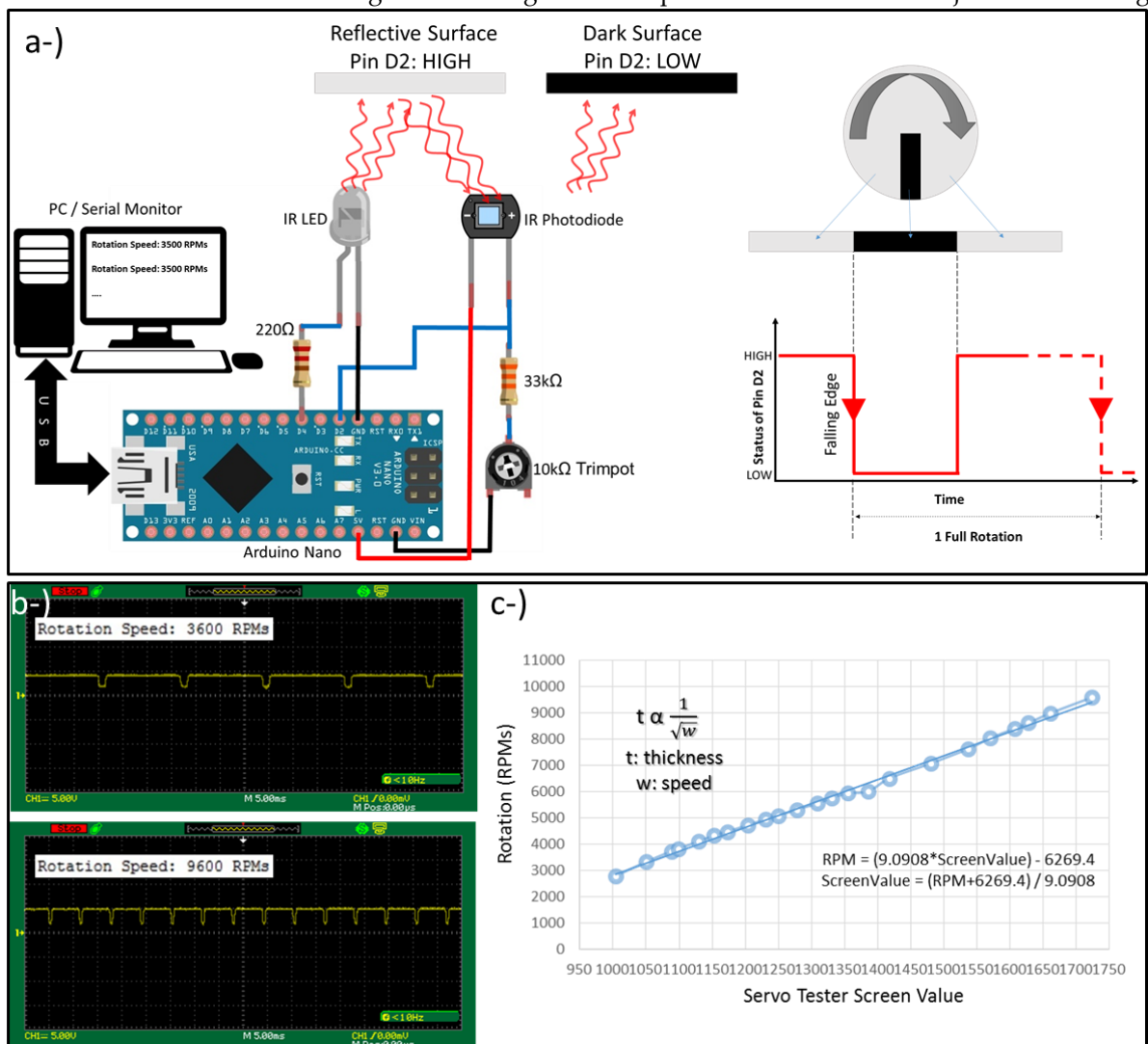


**Figure 2.** (a) Schematic of the optical tachometer with the illustration of photodetectors’s signal as PD facing the reflective and dark surfaces on the spinning plane. (b) Pin D2’s signal input taken from the Oscilloscope screen when the spin coater rotates at 3600rpms and 9600rpms, respectively. Insets with white background show the serial monitor output. (c) Rotation speed of the spin coater as a function of servo tester’s set value.

The way we followed in this research is somewhat indirect, but we are planning to design a motor driver circuit, which is going to give an option of putting the required rotation speed directly.

### Fabrication of Dye-Sensitized Solar Cells

In order to fabricate a dye-sensitized solar cell within the scope of this paper TiO<sub>2</sub> and ZnO tandem layers as photoanode and conventional Pt counter electrodes were employed. ZnO nanostructures were hydrothermally synthesized and Titanium(IV) Oxide nanoparticles purchased from Sigma Aldrich was used as is. Zinc Nitrate hexahydrate was used as a source material for ZnO and 60mg of Zn(NO<sub>3</sub>)<sub>2</sub> · 6H<sub>2</sub>O was dissolved in 40ml deionized water under magnetic stirring. A few drops of Ammonia were added into the solution to adjust the pH level to 10 and then the whole solution was poured into a Teflon lined stainless steel autoclave (Kilic et al., 2012; Kilic and Çelik, 2015). ZnO nanoparticles were synthesized at 200°C for the course of 8 hours. Precipitated products after the growth of ZnO were centrifuged at 5400rpm for 10min to obtain ZnO powder. The collected powder at the bottom of the vials was dried at 100°C for an hour in the oven and then both TiO<sub>2</sub> nanoparticles and ZnO powder were dissolved by Nitric Acid in the milk consistency to be coated on the ITO layer. Since the work function of TiO<sub>2</sub> is smaller than that of ZnO (Ji et al., 2012), TiO<sub>2</sub> layer was first coated via spin coater rotating at 4000rpm for 2 min and then annealed at 300°C for half an hour. After that ZnO was spin coated over ITO/TiO<sub>2</sub> at 5000rpm for about 2min and followed by annealing at 300°C for an hour. N719 dye molecules were adsorbed by the photoanode and KI/I<sub>3</sub> electrolyte was used as redox couples. To construct the cell (ITO/TiO<sub>2</sub>/ZnO/N719) / (Pt/ITO) layers were sandwiched by binder clips (see Fig. 4b) and electrolyte was introduced between counter electrode and sensitized photoanode by capillary force and cell became ready for the IV measurements.

### Characterization Methods

The structural properties of the samples were carried out using scanning electron microscope (SEM-FEI QUANTA FRG 450) at 15kV and chemical compositions of the constituent materials were figured out using energy dispersive spectroscopy (EDS) detector embedded in the SEM microscope. Crystallographic properties, phases and structural quality were investigated by x-ray diffraction (XRD-Panalytical Empyrean diffractometer) studies using CuK $\alpha$  radiation ( $\lambda = 1.5406 \text{ \AA}$ ). Measurements to figure out the electrical and photovoltaic properties were performed using Keithley 2400 SourceMeter under dark and AM 1.5 simulated light emission.

## RESULTS AND DISCUSSION

SEM images in Fig.3a-b show the typical morphologies of TiO<sub>2</sub> nanoparticles and synthesized ZnO nanostructures. As seen in Fig. 3a the coated spherical particles are 20-30nm in diameter and 3D ZnO nanostructures seen in Fig. 3b have 3D flower-like morphology and the size ranges from 500nm to 2 $\mu$ m. By changing the pH value of the solution before hydrothermal growth morphology of the structures can be tuned. EDS analysis result in Fig.3d proved that the prepared hybrid photoanode has the composition of Zn, O and Ti; however, since the penetration depth of electrons is around 1 $\mu$ m in the EDS analysis we see only a tiny bit amount of Ti which comes from the bottom layer of TiO<sub>2</sub>. If we exclude the Ti peak we can say that the products are perfectly stoichiometric and have no significant defects. XRD spectra in Fig. 3c show that photoanode constituent materials, TiO<sub>2</sub> and ZnO, exhibit sharp peaks therefore very high crystalline quality and the characteristic peaks of TiO<sub>2</sub> and ZnO films are centered at 25.17, 37.7, 47.81 degrees and 31.59, 34.19, 36.05 degrees, respectively. Those peaks are well matched with the diffraction lines of the materials seen in the literature (Downs and Hall-Wallace, 2003) and correspond respectively to (210), (102), and (321) for TiO<sub>2</sub> and to (100), (002) and (101) for ZnO.

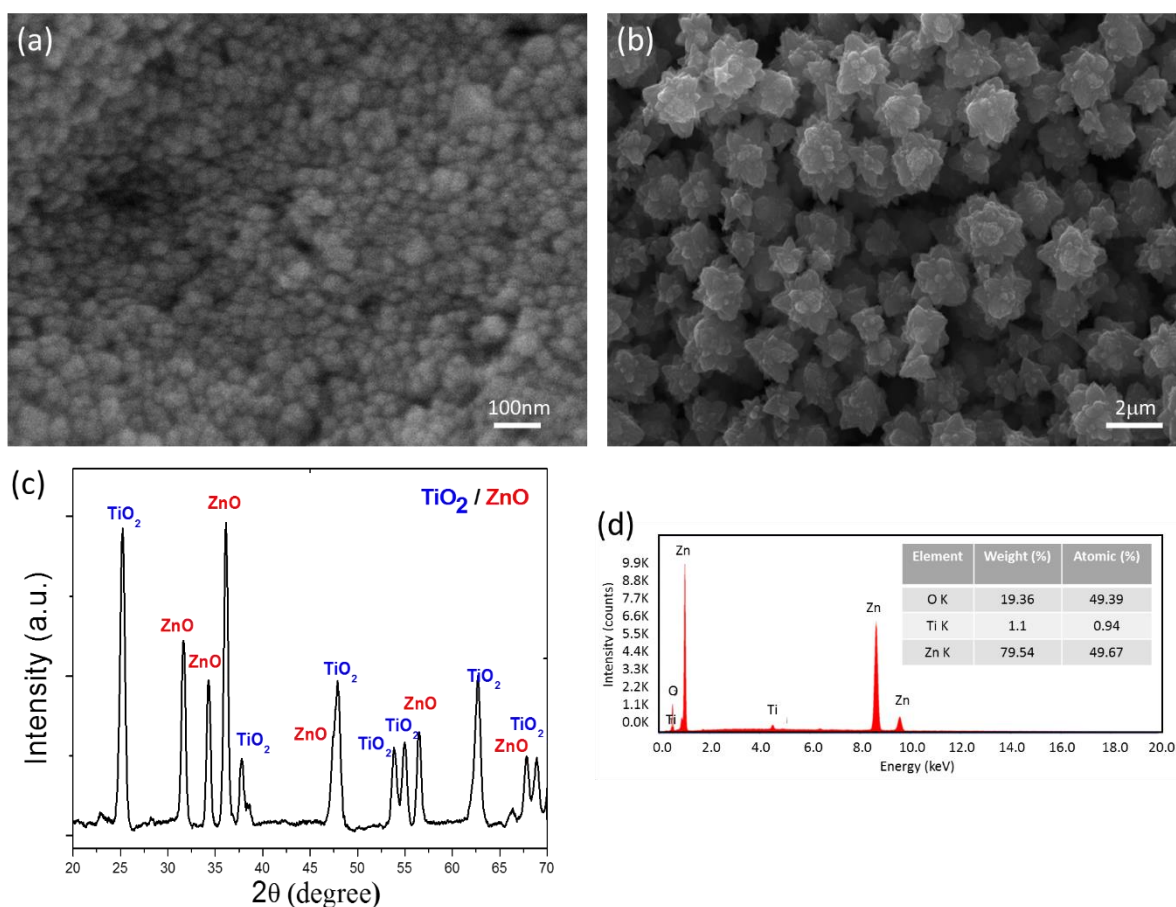


**Figure 3.** Top view SEM images of (a) TiO<sub>2</sub> and (b) ZnO nanostructures. (c) XRD spectra of TiO<sub>2</sub>/ZnO hybrid structures in the photoanode region where we see the characteristic peaks of both TiO<sub>2</sub> and ZnO. (d) EDS spectra of TiO<sub>2</sub>/ZnO hybrid structures with the quantification results that prove the formation of ZnO on top of TiO<sub>2</sub>.

Photovoltaic properties of DSSC constructed with ITO/TiO<sub>2</sub>/ZnO/N719 photoanode and Pt/ITO CE were investigated under solar simulator with AM1.5G simulated solar radiation. The layers and band alignment (Ji et al., 2012) with the movement of electrons as a result of photon absorption is shown in Fig. 4a and constructed solar cell's real color image is seen in Fig. 4b. Photovoltaic properties of the cell are very promising and it exhibits 5.25% power conversion efficiency. Although it is not the upper limit of DSSC technology (the highest efficiency is 11.9% (Green et al., 2017)) it is relatively high considering that the cells were fabricated with very low cost and using homemade laboratory equipments. IV measurements of the cells with 0.25 cm<sup>2</sup> active surface area (mask with 0.25 cm<sup>2</sup> holes was used) were performed and all the photovoltaic properties is given in Table 1. It is worth to note that the role of ZnO on top of TiO<sub>2</sub> is to increase the conductivity and charge collection efficiency through the interface engineering and it is believed to be the reason of getting relatively high efficiency from such cells. On the other hand 3D ZnO structures with many branches provide a large surface area for the adsorption of dye molecules and therefore increased number of photon absorber molecules with a better band alignment cause to increase the short circuit current of the cells. In Fig. 4c Rseries resistance was indicated and that would be fixed using some intermediate materials such as graphene and carbon nanotube in both photoanode and CE region to decrease the transition resistance and increase the conductivity. Researchers around the world utilized those and the results show a great improvement on the PCE of the solar cells (Sun et al., 2010; Yang et al., 2010; Yang et al., 2013; Kilic et al., 2016).

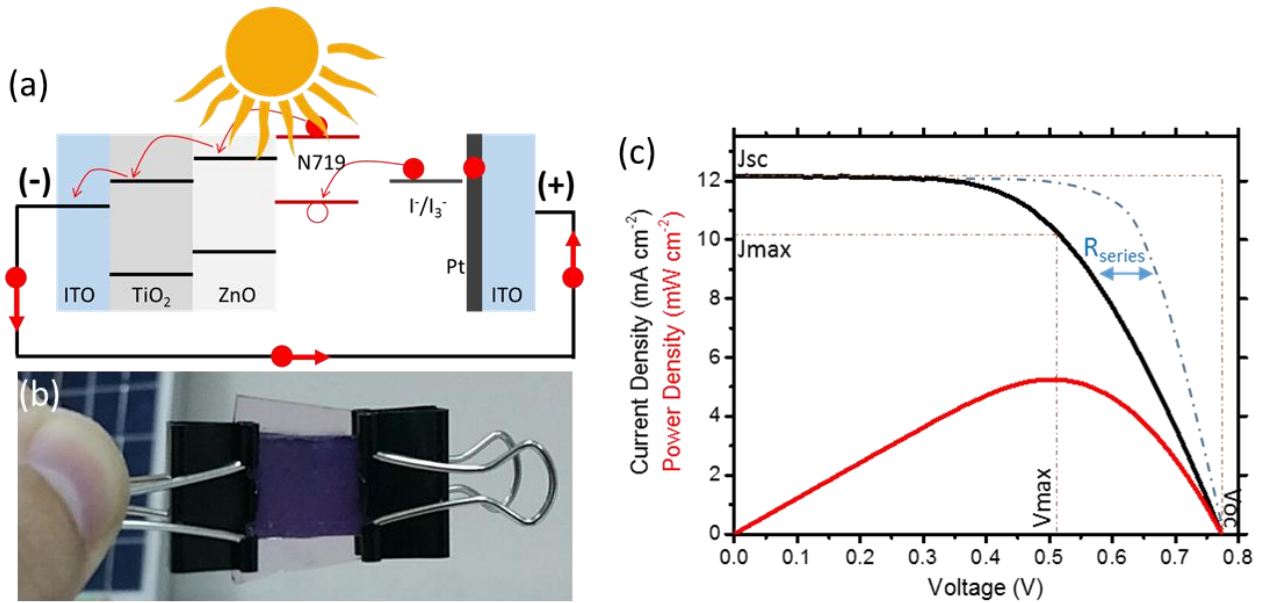


**Figure 4.** (a) Schematic illustration of TiO<sub>2</sub>/ZnO hybrid structure based DSSC w/ Pt counter electrode (b) Real color image of the constructed cell. (c) JV and PV curves of the corresponding solar cell with the indication of some important parameters.

**Table 1.** Photovoltaic properties of DSSCs based on TiO<sub>2</sub>/ZnO photoanode w/ Pt counter electrode under AM 1.5G simulated light emission (100mW/cm<sup>2</sup>).

Voc (V)	Jsc (mA/cm <sup>2</sup> )	Vmax (V)	Jmax (mA/cm <sup>2</sup> )	FF (%)	Efficiency (%)
0.77	12.1392	0.51	10.3046	56.22	5.25

**CONCLUSION**

We highly believe that this work is going to encourage a great number of people and stimulate them to initiate a research in different fields in which case they do not have enough facility. It is believed to be a valuable guiding reference for diverse communities. This work is of great interest for the development of new equipments, tools as well as functional devices in many areas. Although we utilized the homemade equipments for dye-sensitized solar cells, they are of more great interest for the production of other emerging solar cell technologies such as perovskites and organics. We brought the cost of the aforementioned devices down to tens of dollars compared to thousands of dollars. This study not only bring the price of laboratory equipments down to several dollars but also become an encouraging and explanatory guide for a wide community. In addition to encouraging the people to be more creative and producing inexpensive convenient devices this paper reveals important results for the clean and green energy future. DSSCs with TiO<sub>2</sub>/ZnO tandem construction was demonstrated with 5.25% PCE and they show a great promise to replace the conventional energy sources; however, the drawbacks of DSSCs in general should be addressed before commercialization and we need to work further to optimize our cells to increase the conversion efficiency.

## ACKNOWLEDGEMENT

We would like to thank Assoc. Prof. Dr. Bayram KILIC for his encouragement on this exciting research and having fruitful discussions about dye-sensitized solar cells.

## REFERENCES

- Bianchi, R. F., Panssiera, M. F., Lima, J. P. H., Yagura, L., Andrade, A. M., Faria, R. M., 2006, "Spin Coater based on Brushless DC Motor of Hard Disk Drivers", *Progress in Organic Coatings*, Vol. 57, No. 1, pp. 33-36.
- Downs, R. T., Hall-Wallace, M., 2003, "The American Mineralogist Crystal Structure Database", *American Mineralogist*, Vol. 88, pp. 247-250.
- El-Agez, T. M., Taya, S. A., 2014 "Design of a Spectroscopic Ellipsometer by Synchronous Rotation of the Polarizer and Analyzer in Oppositedirections", *Microwave and Optical Technology Letters*, Vol. 56, No. 12, pp. 2822–2826.
- Ellabban, O., Abu-Rub, H., Blaabjerg, F., 2014, "Renewable Energy Resources: Current Status, Future Prospects and Their Enabling Technology", *Renewable and Sustainable Energy Reviews*, Vol. 39, pp. 748–764.
- Fan, F., Liu, Z., Yin, L., Nichols, P. L., Ning, H., Turkdogan, S., Ning, C. Z., 2013, "Simultaneous Two-Color Lasing in a Single CdSSe Heterostructure Nanosheet", *Semiconductor Science and Technology*, Vol. 28, No. 6, pp. 065005.
- Fan, F., Turkdogan, S., Liu, Z., Shelhammer, D., Ning, C. Z., 2015, "A Monolithic White Laser", *Nature Nanotechnology*, Vol. 10, No. 9, pp. 796-803.
- Feldman, D., 2014, Photovoltaic (PV) Pricing Trends: Historical, Recent, And Near-Term Projections, <https://escholarship.org/uc/item/06b4h95q>
- Gratzel, M., 2003, "Dye-sensitized Solar Cell", *Journal of Photochemistry and Photobiology C*, Vol. 4, pp. 145–153.
- Gevorkian, P., 2007, *Sustainable Energy Systems Engineering: The Complete Green Building Design Resource*, McGraw Hill Professional.
- Green, M. A., Emery, K., Hishikawa, Y., Warta, W., Dunlop, E. D., 2017, "Solar Cell Efficiency Tables (Version 49)", *Progress in Photovoltaics: Research and Applications*, Vol. 25, pp. 3-13.
- IEA, 2014, *Technology Roadmap: Solar Photovoltaic Energy*.
- Jose, R., Thavasi, V., Ramakrishna, S., 2009, "Metal Oxides for Dye - Sensitized Solar Cells", *Journal of the American Ceramic Society*, Vol. 92, no. 2, pp. 289-301.
- Ji, I., Park, M. J., Jung, J. Y., Choi, M. J., Lee, Y. W., Lee, J. H., Bang, J. H., 2012, "One-dimensional Core/Shell Structured TiO<sub>2</sub>/ZnO Heterojunction for Improved Photoelectrochemical Performance", *Bulletin of the Korean Chemical Society*, Vol. 33, No. 7, pp. 2200-2206.
- Shankleman, J., Martin, C., 2017, "Solar Could Beat Coal to Become the Cheapest Power on Earth". *Bloomberg View, Bloomberg LP*, Retrieved 3 January 2017.
- Kilic, B., Omay, D., Kosa, E., Trabzon, L., Kizil, H., 2012, "Growth of ZnO Nanostructures on Biopolymer Films", *Journal of Materials Science and Engineering A*, Vol. 2, No. 12A, pp. 761.
- Kılıç, B., Çelik, V., 2015, "Self-assembled Growth of Tandem Nanostructures based on TiO<sub>2</sub> Mesoporous/ZnO Nanowire Arrays and Their Optoelectronic and Photoluminescence Properties", *Applied Physics A*, Vol. 119, No. 2, pp. 783-790.
- Kilic, B., Turkdogan, S., Astam, A., Ozer, O. C., Asgin, M., Cebeci, H., Urk, D., Mucur, S. P., 2016, "Preparation of Carbon Nanotube/TiO<sub>2</sub> Mesoporous Hybrid Photoanode with Iron Pyrite (FeS<sub>2</sub>) Thin Films Counter Electrodes for Dye-Sensitized Solar Cell", *Scientific Reports*, Vol. 6, pp. 27052.
- Levelized Cost and Levelized Avoided Cost of New Generation Resources, US Energy Information Administration, Annual Energy Audit 2016, 5 Aug. 2016.

- Parida, B., Iniyan, S., Goic, R., 2011, "A Review of Solar Photovoltaic Technologies", *Renewable and Sustainable Energy Reviews*, Vol. 15, no. 3, pp. 1625-1636.
- Scriven, L. E., 1988, "Physics and Applications of Dip Coating and Spin Coating", *In MRS Proceedings*, Vol. 121, pp. 717.
- Sun, S., Gao, L., Liu, Y., 2010, "Enhanced Dye-Sensitized Solar Cell using Graphene-TiO<sub>2</sub> Photoanode Prepared by Heterogeneous Coagulation", *Applied Physics Letters*, Vol. 96, No. 8, pp. 083113.
- Turkdogan, S., 2012, *Nanowire Synthesis and Characterization: Erbium Chloride Silicate and Two Segment Cadmium Sulfide-Cadmium Selenide Nanowires and Belts*, Master Thesis, Arizona State University, Electrical Engineering, Tempe.
- Turkdogan, S., 2015, *Growth and Characterization of Multisegment Chalcogenide Alloy Nanostructures for Photonic Applications in a Wide Spectral Range*, PhD Dissertation, Arizona State University, Electrical Engineering, Tempe.
- Turkdogan, S., Fan, F., Ning, C. Z., 2016, "Color-Temperature Tuning and Control of Trichromatic White Light Emission from a Multisegment ZnCdSSe Heterostructure Nanosheet", *Advanced Functional Materials*, Vol. 26, No. 46, pp. 8521-8526.
- Yang, N., Zhai, J., Wang, D., Chen, Y., Jiang, L., 2010, "Two-dimensional Graphene Bridges Enhanced Photoinduced Charge Transport in Dye-Sensitized Solar Cells", *ACS Nano*, Vol. 4, No. 2, pp. 887-894.
- Yang, Z., Liu, M., Zhang, C., Tjiu, W. W., Liu, T., Peng, H., 2013, "Carbon Nanotubes Bridged with Graphene Nanoribbons and Their Use in High - Efficiency Dye - Sensitized Solar Cells", *Angewandte Chemie International Edition*, Vol. 52, No. 14, pp. 3996-3999.

## APPENDICES

### Appendix 1. Arduino codes for the optical tachometer

```
#define irLED 4 // The Infrared LED is connected to pin#4
volatile byte intNum; // "volatile" should be used with interrupts
unsigned int rpm; //rpm might be either negative or positive
int mtime=1000; //Measurement time in which number of interrupts were detected. Min detectable rpm
                becomes 60*1000/mtime.
int ntape=1; //Number of tape on a rotating plane
void int_count() // Counting the number of interrupts
{
intNum++; //each interrupt increases the intNum by 1
}
void setup()
{
Serial.begin(9600);
attachInterrupt(0, int_count, FALLING); //IR dedector is connected to pin 2 which is interrupt 0. Triggers
                when it goes from HIGH to LOW and calls int_count.
pinMode(irLED, OUTPUT); // Make irLED pin output
digitalWrite(irLED, HIGH); // Turn on IR LED
intNum = 0;
rpm = 0;
}
void loop()
{
delay(mtime); // Update RPM every defined millisecond (mtime)
detachInterrupt(0); // During the calculations we do not process interrupts
```

```
rpm = (60 * 1000 * intNum / mtime / ntape); // Calculates the rotation per minute depending on the
      measure time and # of triggering tapes on the spinning plane.
Serial.print("Rotation Speed: ");
Serial.print(rpm);
Serial.println(" RPMs");
Serial.println();
intNum = 0;
attachInterrupt(0, int_count, FALLING); //Restart the interrupt processing
}
```

## KİTOSAN KAPLI KAOLİN BONCUKLARIN SULU ÇÖZELTİLERDEN KROM(VI) UZAKLAŞTIRILMASINDA ADSORBAN OLARAK KULLANIMI

<sup>1</sup>Şerife PARLAYICI, <sup>2</sup>Türkan ALTUN

<sup>1,2</sup>Selçuk Üniversitesi, Mühendislik Fakültesi, Kimya Mühendisliği Bölümü, KONYA

<sup>1</sup>serifeparlayici@selcuk.edu.tr, <sup>2</sup>turkanaltun@selcuk.edu.tr

(Geliş/Received: 25.04.2017 ; Kabul/Accepted in Revised Form: 14.07.2017 )

**ÖZ:** Filtrasyon, iyon değişimi, kimyasal çöktürme ve membran sistemleri gibi fizikokimyasal prosesler ağır metaller içeren atık suların saflaştırılmasında kullanılmaktadır. Adsorpsiyon metodu daha ekonomiktir ve diğer proseslere göre bazı üstünlüklere sahiptir. Son yıllarda araştırmacılar düşük maliyetli ve kolayca elde edilebilen adsorbanların elde edilmesi yönünde çalışmalar yapmaktadırlar. Bu çalışmada, sulu çözeltilerden Cr(VI) iyonlarının giderilmesinde düşük maliyetli adsorban olarak hazırlanan kitosan kaplı kaolin kompozit boncukların kullanımı araştırılmıştır. Kitosan kaplı kaolin kürecikleri kullanarak sulu çözeltiden Cr(VI) adsorpsiyonu üzerine pH, sorbent dozu, başlangıç metal konsantrasyonu ve temas süresinin etkileri sistematik olarak incelendi. Çözeltinin pH'sı 2-6 aralığında değiştirilmiş ve kitosan kaplı kaolin boncukları ile Cr(VI) adsorpsiyonunun pH'ya bağlı olduğu tespit edilmiştir. Denge verilerini tanımlamak için Langmuir ve Freundlich adsorpsiyon izoterm modelleri uygulanmıştır. Verilerin Langmuir modele uygun olduğu görülmüş ve 120 dk. temas süresince kitosan kaplı kaolin boncukların Cr(VI) için maksimum adsorpsiyon kapasitesi 31,98 mg/g olarak bulunmuştur.

**Anahtar Kelimeler:** Adsorpsiyon, Kaolin, Kitosan, Krom, İzoterm.

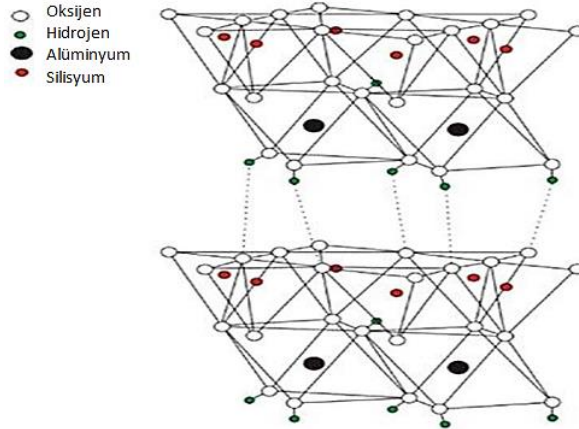
### Removal Of Chromium (VI) From Aqueous Solutions Using Chitosan Coated Kaoline Beads As Adsorbent

**ABSTRACT:** Various physicochemical process such as filtration, ion exchange, chemical precipitation, and membran systems are used in treatment of waste waters including heavy metals. Among these processes, adsorption technique is more economical process and has some advantages over the other techniques. Recently, researchers have many studies on the low cost and easily obtainable adsorbents. In this study, the use of chitosan coated kaoline composite beads as low-cost adsorbent to removal of Cr(VI) ions from the aqueous solutions has been investigated. The effects of pH, sorbent dosage, initial metal concentration and contact time on the adsorption of Cr(VI) from aqueous solution using the chitosan coated kaoline beads were studied systemically. The pH of the solution was varied over a range of 2-6 and the adsorption of Cr(VI) ions on chitosan coated kaoline beads was determined to be pH-dependent. The Freundlich and Langmuir adsorption isotherm models were applied to describe equilibrium data. The data fitted well with Langmuir model and maximum adsorption capacity of chitosan-coated kaoline beads was determined to be 31,98 mg/g for Cr(VI) at 120 sec. of contact time.

**Keywords:** Adsorption, Kaoline, Chitosan, Chromium, Isotherm.

## GİRİŞ (INTRODUCTION)

Krom, bakır, kurşun gibi ağır metal kirliliği; membran, çöktürme, ters osmoz, indirgeme, filtrasyon, çözücü ekstraksiyonu gibi çeşitli yöntemlerle giderilebilir (Rengaraj ve diğ., 2001; Yurlova ve diğ., 2002; Tao ve diğ., 2014; Benito ve Ruiz, 2002; Ramos ve diğ., 1994). Bu proseslerin maliyetinin yüksek olması, ikincil kirliliğe sebep olması, düşük metal konsantrasyonları için etkili olmamaları gibi dezavantajları vardır. Adsorpsiyon bu metotlarla karşılaştırıldığı zaman, ağır metallerin atık sulardan uzaklaştırılmasında daha etkili ve ekonomik olduğu görülmektedir (Altun ve diğ., 2016). Bu sebeple son yıllarda düşük maliyetli adsorbanların araştırılması yönünde çalışmalar artmıştır. Ağır metal gideriminde hindistancevizi kabuğu, üzüm atığı, badem kabukları, doğal killer, kaktüs yaprakları, çamların yaprakları, mısır koçanı, kül-kömür karışımı, silikajeller vb. gibi malzemeler adsorban olarak kullanılabilir. Bu düşük maliyetli adsorban maddeler arasında killer, doğada bol miktarda bulunmaktadır. Ayrıca iyon değişim potansiyeli yüksek olduğu için iyi adsorplama özelliğine sahiptir. Killerin adsorpsiyon yeteneği minerallerinin yapısında sahip oldukları yüklerden kaynaklanmaktadır. Bunun yanında yapılarının gözenekli olması ve yüzey alanlarının büyük oluşundan kaynaklanmaktadır. Bu sebeplerden dolayı killer, sulu çözeltilerinden ağır metallerin gideriminde yaygın olarak kullanılmaktadır. Killerle yapılan adsorpsiyon işlemleri yaygın olarak kullanılmakta olan aktif karbona kıyasla çok daha ekonomiktir. Kaolin, kil mineralleri sınıflandırması içinde bir grup kil mineralidir (Bailey, 1980). Kaolin, granit kayalardan elde edilen bir kil türüdür.  $Al_2O_3 \cdot 2SiO_2 \cdot 2H_2O$  molekül formülüne sahip olup tabakalı yapısı birbirini takip eden  $[Si_2O_5]^{2-}$  ve  $[Al_2(OH)_4]^{2+}$  tabakalarının istiflenmesiyle oluşur. Kaolinin kristal yapısı bir sekizyüzlü ve bir de dörtyüzlüden oluşan birbirine bağlı iki tabakadan meydana gelmektedir (Şekil 1.).

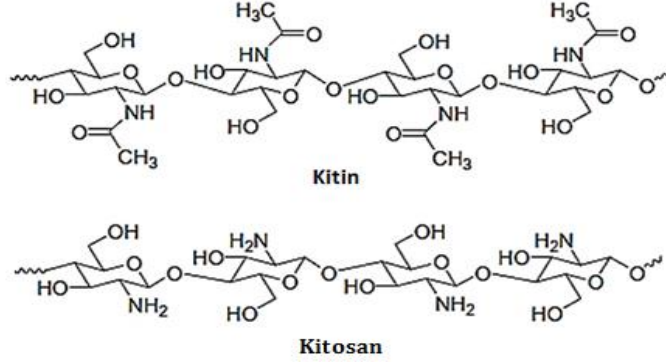


Şekil 1. Kaolinin kristal yapısı (Cheng ve ark., 2012)

Figure 1. The crystal structure of kaolin (Cheng et al., 2012)

Son yıllarda biyobozunur polimer-kil karışımları hazırlanarak bu polimerlerin özellikleri iyileştirilmektedir. Bu amaçla bentonit, montmorillonit, sepiolit gibi killer daha çok tercih edilmektedir. Bu konularda yapılan çalışmalar günümüzde önemli ölçüde artmıştır. Biyobozunur polimer olarak kitosan, bilimsel çalışmalarda büyük ilgi çekmektedir. Kitosan kimyasal yapısı selüloza benzeyen doğada selülozdan sonra en çok bulunan, N-asetil-D-glukopiranoz olup kitinin deasetillenmiş ürünüdür (Demir ve Seventekin, 2009) (Şekil 2). Kitin mikroorganizmalar ve fungi hücre duvarında, böceklerde, yengeç ve karides kabuklu hayvanların dış iskeletlerinde bol miktarda bulunabilen doğal bir polimerdir. Kitosan, biyolojik olarak parçalanabilirliği, toksik olmaması, biyoyumluluğu, doğal olarak elde edilebilmesi, bol bulunması, düşük maliyetli olması, kimyasal ve fiziksel özellikleri bakımından üstün özelliklere sahip olmasından dolayı tıp,

ziraat, kozmetik, kağıt ve tekstil başta olmak üzere daha bir çok çeşitli endüstriyel sektörde ve akademik araştırmalarda yaygın olarak kullanılmaktadır.



Şekil 2. Kitin ve kitosanın kimyasal yapısı (Sajomsang, 2010)

Figure 2. Chemical structures of chitin and chitosan(Sajomsang, 2010)

Son yıllarda yapılan çalışmalarda killer, metal adsorplama kapasitelerini arttırmak için çeşitli modifikatörlerle modifiye edilmektedir. Diğer taraftan kitosan her tekrarlayan birimlerinde reaktif gruplara sahip olmasından dolayı kolayca modifikasyona uğrayabilmektedir. Bu çalışmada kil olarak kaolin, biyobozunur polimer olarak kitosan kullanılmıştır. Adsorbent olarak hazırlanan bu yeni polimer kil kompoziti ile sulu ortamdan Cr(VI) iyonlarının adsorpsiyonu incelenmiştir.

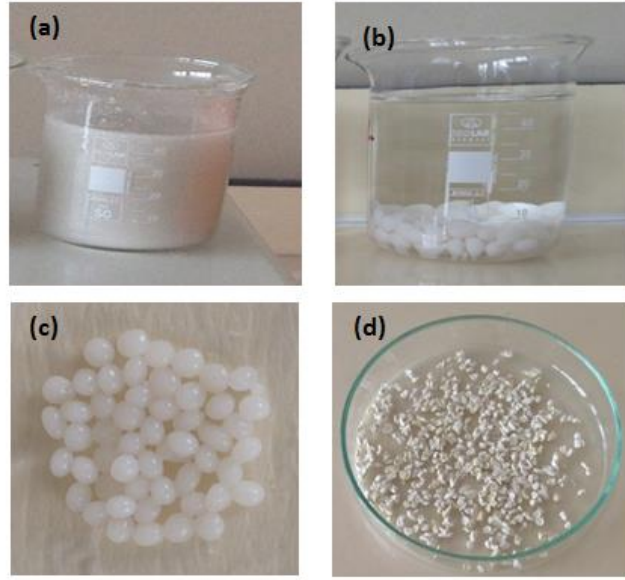
## MATERYAL ve YÖNTEM (MATERIALS and METHOD)

### Materyal (Material)

Bu çalışmada, Merck firmasından temin edilen kaolin ile Sigma Aldrich firmasından temin edilen kitosan adsorban madde hazırlanmasında kullanılmıştır. Çalışmada kullanılan kimyasal maddeler analitik saflıkta olup, Merck firmasından satın alınmıştır. Deneylerde NaOH, HCl, H<sub>2</sub>SO<sub>4</sub>, H<sub>3</sub>PO<sub>4</sub>, K<sub>2</sub>Cr<sub>2</sub>O<sub>7</sub>, 1,5-difenilkarbazit, oksalik asit ve aseton kimyasalları kullanılmıştır. Cr(VI) stok çözeltisi K<sub>2</sub>Cr<sub>2</sub>O<sub>7</sub>'den hazırlanmıştır.

### Kitosan Kaplı Kaolin Boncukları Hazırlanması (Preparation of Chitosan Coated Kaoline Beads)

Kitosan kaplı kaolin boncukları (Kts/Kao) hazırlanmasında kaolin 0,2 M oksalik asitte 12 saat 250 rpm'de çalkalanmıştır. Asitle muamele edilmiş kaolin mavi bant süzgeç kağıdında süzülüş, saf su ile birkaç kez yıkanmış ve etüvde 70 °C'de kurutulmuştur. Diğer taraftan kitosan 0,2 M oksalik asitte 5 saat manyetik karıştırıcı ile karıştırılmıştır. Hazırlanan kitosan jeli, 1:1 g kitosan/g kaolin oranında olacak şekilde asitle muamele edilmiş kaolin yavaş yavaş eklenmiş ve 5 saat boyunca manyetik karıştırıcıda karıştırılmıştır. Elde edilen karışım 0,7 M NaOH banyosuna peristaltik pompa ile damlalar halinde 5 cm yükseklikten damlatılmış ve bir gece NaOH banyosunda bekletilerek (Kts/Kao) boncukları elde edilmiştir (Şekil 3.). Oluşan (Kts/Kao) boncukları süzülüş, saf su ile pH nötr olana kadar yıkanmış ve etüvde 70 °C'de sabit tartıma gelinceye kadar kurutulmuştur.



**Şekil 3.** (Kts/Kao) boncukları fotoğrafı **a)** (Kts/Kao) karışımı **b)** NaOH banyosu **c)** yaş hali **d)** kuru hali  
*Figure 3.* Photograph of (Cts/Kao) beads **a)** (Cts/Kao) mixture **b)** NaOH bath **c)** wet **d)** dry

#### Kesikli Kap Adsorpsiyon Çalışması (Batch Adsorption Studies)

Konsantrasyon değişiminin adsorpsiyona etkisini araştırma için stok Cr(VI) çözeltisinden farklı konsantrasyonlarda hazırlanarak 0,1'er gram (Kts/Kao) boncukları üzerine eklenmiştir. Çalkalayıcıda oda sıcaklığında 2 saat boyunca tutulmuştur. Dengeye gelen Cr(VI)-(Kts/Kao) karışımı süzülerek adsorban ve çözelti ayrılmıştır. Çözelti fazında dengedeki Cr(VI) iyon konsantrasyonu UV-Visible spektrofotometre (Shimadzu UV-1700) ile tayin edilmiştir. 0,5 gr 1,5-difenil karbazit 100 ml asetonda çözülmüştür. 1 ml Cr(VI) çözeltisi 1 ml 0,2 N'lik H<sub>2</sub>SO<sub>4</sub> ilave edilmiş üzerine 1 ml 1,5-difenil karbazit çözeltisi eklendikten sonra saf su ile 50 ml'ye seyreltilerek 540 nm dalga boyunda okuma işlemi yapılmıştır (Gilcreas ve diğ., 1965; Snell ve Snell, 1959). Adsorban fazında tutulan Cr(VI) konsantrasyonları Eşitlik 1. ile hesaplanmıştır:

$$q_e = \frac{V}{W}(C_0 - C_e) \quad (1)$$

Bu denklemde C<sub>0</sub> sulu fazdaki başlangıç metal konsantrasyonunu, C<sub>e</sub> denge anındaki metal konsantrasyonunu, V sulu fazın hacmini, W ise kuru adsorbanın kütesini göstermektedir. Metal adsorpsiyon miktarları Freundlich ve Langmuir izotermlerinden (Eşitlik 2, 3) faydalanılarak hesaplanmıştır.

$$\log q_e = \log k + \frac{1}{n} \log C_e \quad (2)$$

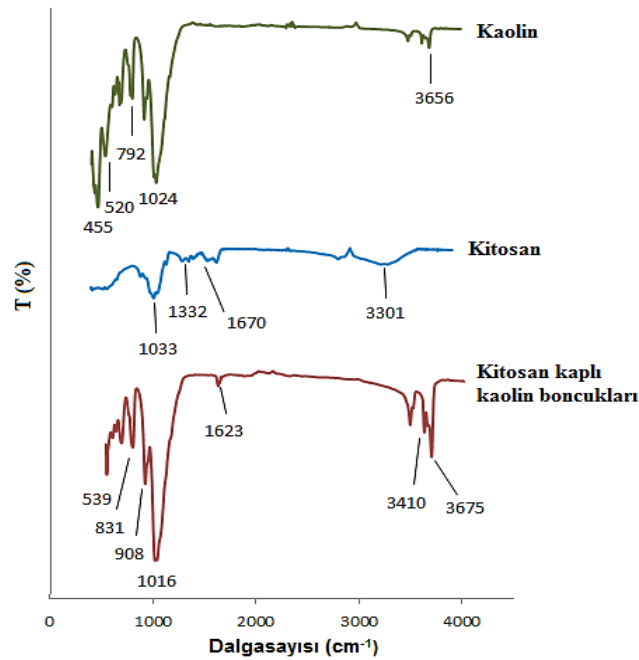
$$\frac{C_e}{q_e} = \frac{C_e}{A_s} + \frac{1}{K_b A_s} \quad (3)$$

Freundlich izotermindeki  $n$  sabit bir değeri,  $k$  adsorpsiyon kapasitesini, Langmuir izotermindeki  $A_s$  adsorpsiyon kapasitesini,  $K_b$  ise adsorpsiyon enerjisiyle ilgili bir sabiti göstermektedir. İzoterm sabitleri, grafiklerin doğru denklemleri ve eğimlerinden hesaplanarak, dengede; (Kts/Kao) boncukların Cr(VI) adsorpsiyon kapasitesi sonuçlar ve tartışma bölümünde verilmiştir.

## SONUÇLAR ve TARTIŞMA (RESULTS and DISCUSSIONS)

### (Kts/Kao) Karakterizasyonu ((Cts/Kao) Characterization)

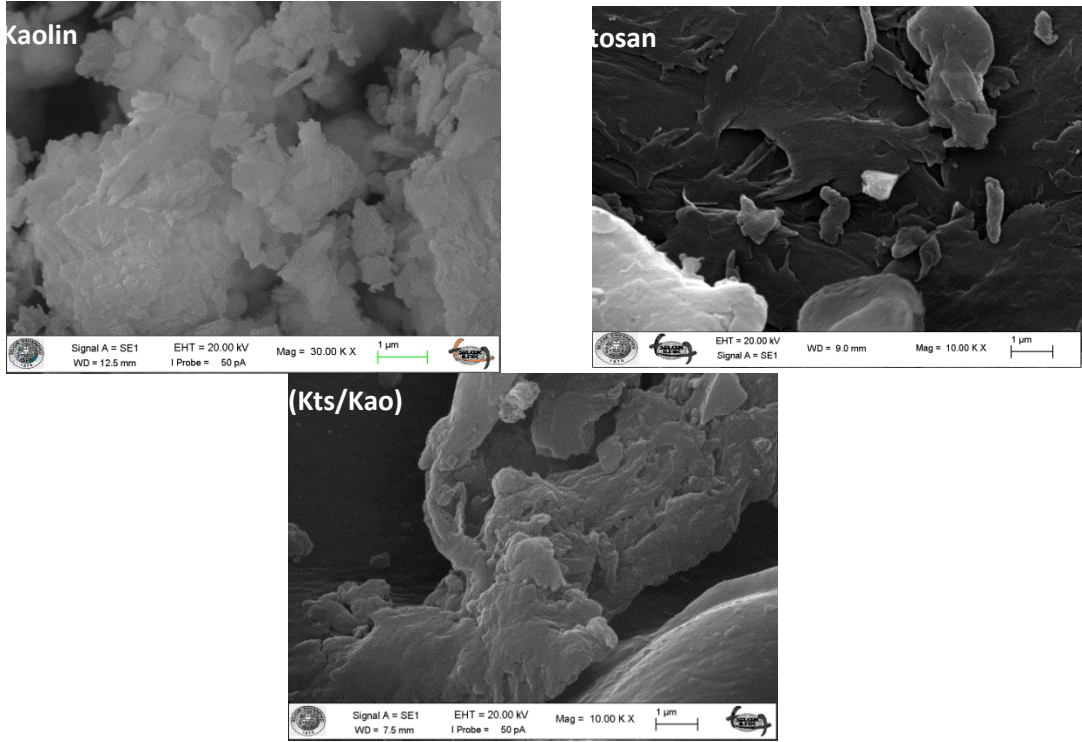
Kitosan, kaolin ve Kts/Kao boncukları FT-IR (Bruker VERTEX 70) spektrumu Şekil 4.'de verilmiştir. Kitosan FTIR spektrumunda; 3378  $\text{cm}^{-1}$ 'de geniş bandın yüzeydeki hidsoksil ( $-\text{OH}$ ) gruplarından kaynaklanmaktadır (Tiwari ve Shukla, 2009). 1658  $\text{cm}^{-1}$  de  $-\text{NH}$  bandından ve 1562  $\text{cm}^{-1}$  de  $-\text{NH}_2$  eğilme bandlarından kaynaklanmaktadır (Nghah ve Fatinathan, 2008). Kitosan yapısındaki alkol gruplarının COH titreşimlerini 1378  $\text{cm}^{-1}$ 'deki band göstermektedir. Diğer taraftan kaolinin FTIR spektrumunda; 3685, 3620 ve 3484  $\text{cm}^{-1}$ 'deki bandlar kaolinin Si-O-Al yüzeyine zayıf olarak hidrojen bağı ile bağlı su moleküllerindeki  $-\text{OH}$  gruplarının gerilme titreşimlerinden kaynaklanmaktadır. 1022  $\text{cm}^{-1}$  de gözlenen şiddetli bandlar tetrahedral tabakadaki Si-O-Si gruplarının Si-O gerilim titreşiminden kaynaklanmaktadır. 789  $\text{cm}^{-1}$ 'de gözlenen band Si-O-Al (oktahedral) bükülme titreşiminin, 533 ve 462  $\text{cm}^{-1}$ 'de gözlenen bandlar ise Si-O-Si bükülme titreşimlerine aittir (Sari ve Tuzen, 2014). Kts/Kao boncukları FTIR spektrumunda ise; 3675  $\text{cm}^{-1}$ 'de geniş band yüzeydeki hidroksil  $-\text{OH}$  gruplarından kaynaklanmaktadır. 3477  $\text{cm}^{-1}$  deki pik amin fonksiyonel gruplarındaki  $-\text{N}-\text{H}_2$  gerilim titreşimini göstermektedir. 1655  $\text{cm}^{-1}$  deki bantlar amid grubundaki  $-\text{N}-\text{H}_2$  gerilim titreşiminden kaynaklanmaktadır (Nghah ve Fatinathan, 2008; Zhou ve diğ., 2014). 1031  $\text{cm}^{-1}$  civarındaki bant kitosan yapısındaki C-N gerilme titreşiminden ve 908 ve 831  $\text{cm}^{-1}$ 'deki bantlar, kaolin yapısındaki  $-\text{Si}-\text{OH}$  ve  $-\text{Al}(\text{OH})_3$  gerilme titreşimlerine, 539  $\text{cm}^{-1}$ 'de gözlenen bandlar ise Si-O-Si bükülme titreşimlerine aittir (Sari ve Tuzen, 2014).



Şekil 4. Kaolin, Kitosan ve (Kts/Kao) FTIR spektrumu

Figure 4. FTIR Spectra of chitosan, kaolin and (Cts/Kao)

Çalışmada kullanılan (Kts/Kao) kompozitinin yüzey yapısı taramalı elektron mikroskobu (SEM) (ZEİSS LS-10) ile incelenmiş ve Şekil 5'de görüntüleri verilmiştir. (Kts/Kao) yüzeyindeki porlu gözenek mikrofotografikte açıkça görünmektedir. Kompozitin iç yüzeyi ve dış yüzeyi benzer yapıdadır ve yüzey morfolojisi birbirine benzemektedir. Şekil 5'de kitosanın yüzeyinin girinti çıkıntı ve oyukların az olduğu görülmektedir. Kompozit oluşturulduktan sonraki SEM görüntüsünde ise hazırlanan kompozitin yapısındaki kitosanın lifli yapısıyla kaolinin girinti çıkıntılı yapısı ile yeni tabakalı girinti çıkıntılı bir yapı oluşturularak kitosana kıyasla yüzey alanının arttığı görülmektedir.

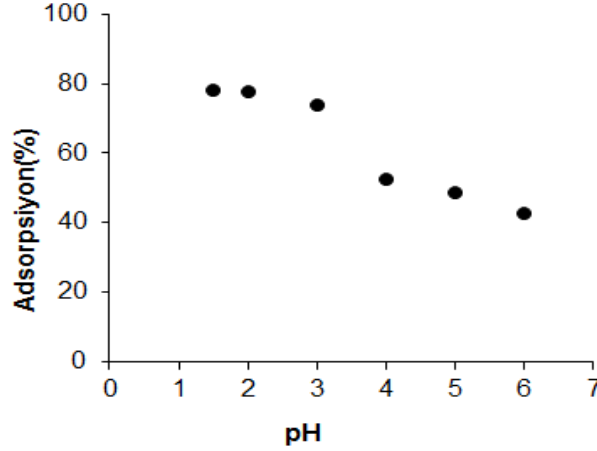


Şekil 5. SEM görüntüleri

Figure 5. SEM images

#### Çözelti pH'ının Etkisi (Effect of solution pH)

Kesikli kap çalışmalarının başlangıç kısmında (Kts/Kao) boncukları ile sulu çözeltilerden Cr(VI) uzaklaştırılmasında çözelti pH'ının etkisi incelenmiştir. Hazırlanan bu çözeltilerin pH'ları 0,1 M'lik HCl ve 0,1 M'lik NaOH çözeltileri ile 2,0-6,0 arasında ayarlanmıştır. Adsorbanın Cr(VI) adsorplama miktarı çözeltinin pH'sından çok etkilendiği görülmüştür.



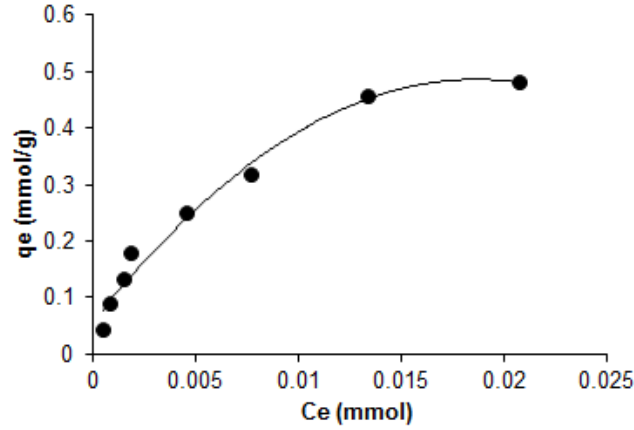
**Şekil 6.** (Kts/Kao) boncuklarıyla Cr(VI) adsorpsiyonuna pH'nin etkisi (Adsorpsiyon şartları: Cr(VI) konsantrasyonu,  $10^{-3}$  mol/L; adsorbent dozu, 2g/L; temas süresi, 2 saat; sıcaklık,  $25 \pm 1$  °C).

*Figure 6.* Effect of pH on the adsorption of Cr(VI) by (Kts/Kao) beads. (Adsorption conditions: concentration of Cr(VI),  $10^{-3}$  mol/L; adsorbent dosage, 2g/L; contact time, 2 h; temperature,  $25 \pm 1$  °C).

Cr(VI) iyonlarının adsorpsiyonu üzerine çözelti pH'sının etkisi, Şekil 6'de verilmiştir. Şekilden de görüleceği gibi maksimum Cr(VI) adsorpsiyonu pH 2,0 civarında gerçekleşmiştir. pH < 2 değerinde dahi Cr(VI) tutunması yüksek olup pH > 3 da metal tutunması %75'den %50 civarına hızla düşmüştür. Kompozit adsorban bünyesinde bulunan amino ve hidroksil grupları, metal iyonlarının adsorpsiyonunda etkilidir (Teng ve diğ., 2001). Cr(VI) adsorpsiyonunda yüzey adsorpsiyonu, iyon değiştirme, kimyasal adsorpsiyon ve kompleks oluşum gibi mekanizmalar da olmaktadır. Cr(VI) asidik ortamda Cr(III)'e dönüşerek adsorbanda bulunan fonksiyonel gruplarındaki protonları sökerek adsorban yüzeyine katılmaktadır. Yang ve diğ. (2016) hazırladıkları manyetik kitosan adsorbani ile Cr(VI) uzaklaştırma pH çalışmasında, ortam pH'ını 3-5 arasında değiştirmişler ve bizim çalışmamıza benzer sonuçlar bulmuşlardır.

#### **Adsorpsiyon İzotermi (Adsorption Isotherm)**

Cr(VI) gideriminde  $K_2Cr_2O_7$ 'den hazırlanan farklı konsantrasyonlardaki çözeltiler (Kts/Kao) boncukları ile muamele edilerek, adsorpsiyon çalışmaları gerçekleştirilmiş ve çözeltide kalan Cr(VI) miktarları UV-Vis. spektrofotometresi ile tayin edilmiştir. Cr(VI) iyonlarının (Kts/Kao) boncukları üzerindeki adsorpsiyonu; Şekil 7.'de kompozit adsorban üzerindeki adsorpsiyon izotermelerini göstermektedir. Adsorpsiyon izotermi gram (Kts/Kao) miktarının adsorplayabildiği Cr(VI) miktarının çözelti ortamında kalan Cr(VI) miktarına karşı grafik çizilerek elde edilmiştir.



**Şekil 7.** (Kts/Kao) adsorpsiyon izotermi (Adsorpsiyon şartları: adsorban dozu, 2g/L; pH 2; temas süresi, 2 saat; sıcaklık,  $25 \pm 1$  °C).

*Figure 7.* Adsorption isotherm for (Kts/Kao) (Adsorption conditions: adsorbent dosage, 2g/L; pH 2; contact time, 2 h; temperature,  $25 \pm 1$  °C).

Cr(VI) iyonlarının (Kts/Kao) ile adsorpsiyonu sonucu hesaplanan izoterm parametreleri Tablo 1 de verilmiştir. Freundlich izotermi için, Eşitlik 2 kullanılarak k ve n parametreleri hesaplanmıştır. Freundlich izotermindeki k adsorpsiyon kapasitesini gösterirken, n sabit bir değerdir.  $1/n$  değerinin 0.1–1.0 arasında olması adsorpsiyonun elverişli olduğu anlamına gelmektedir. (Erdem ve diğ., 2004).  $1/n$  değeri 0,60'dır ve (Kts/Kao)'nin Cr(VI) adsorplamaya elverişli olduğunu göstermektedir. Langmuir izotermi için ise Eşitlik 3 kullanılarak  $A_s$  ve  $K_b$  parametreleri hesaplanmıştır. Langmuir izotermindeki  $A_s$  adsorpsiyon kapasitesi,  $K_b$  sabiti adsorpsiyon enerjisiyle ilgili bir sabittir. Sonuçlardan proses için Langmuir adsorpsiyon izotermi daha uygun olduğu görülmektedir. Langmuir adsorpsiyon izotermine göre (Kts/Kao) boncuklarının maksimum Cr(VI) adsorpsiyon kapasitesi 31,98 mg/g olarak bulunmuştur. Sonuç olarak; Kts/Kao boncuklarının literatürdeki çoğu adsorbana göre daha yüksek adsorplama kapasitesine sahip olduğu için Cr(VI) gideriminde uygun adsorban olabileceği düşünülebilir.

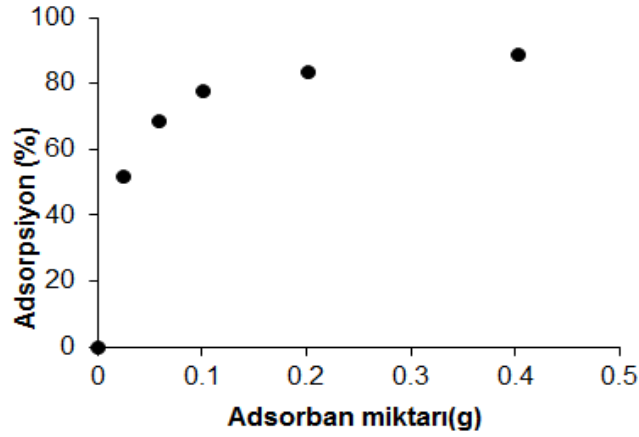
**Tablo 1.** (Kts/Kao) boncuklarının Cr(VI) iyonları adsorpsiyonunda Langmuir ve Freundlich izoterm parametreleri

*Table 1.* Parameters of Langmuir and Freundlich isotherms for adsorption of Cr(VI) on (Kts/Kao) beads

Langmuir			Freundlich		
$A_s$	$K_b$	$R^2$	k	n	$R^2$
0.62	2.64	0.982	5.98	1.66	0.953

#### Adsorban Miktarının Etkisi (Effect of Adsorbent Amount)

Hazırlanan Cr(VI) çözeltileri farklı miktarlarda (0,025-0,4g) tartılan (Kts/Kao) boncukları ile ayrı ayrı muamele edilmiştir. Şekil 8'da adsorban miktarına karşı Cr(VI) iyonlarının adsorpsiyonu görülmektedir. Grafikten görüldüğü gibi adsorban miktarı artarken Cr(VI) iyonları adsorpsiyonu artmakta, belirli bir değerden sonra bir plato değerine ulaşmaktadır. Bu plato değerinden sonra adsorban miktarının artması adsorpsiyonu önemli derecede etkilememektedir.



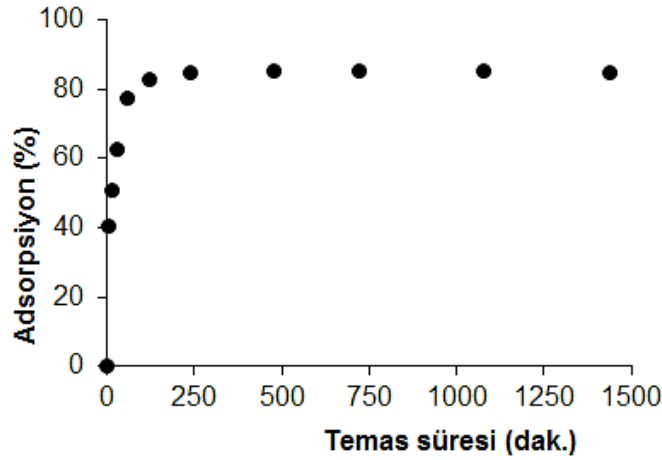
**Şekil 8.** (Kts/Kao) boncuklarıyla Cr(VI) adsorpsiyonunda adsorban miktarının etkisi (Adsorpsiyon şartları: Cr(VI) konsantrasyonu,  $10^{-3}$  mol/L; pH 2; temas süresi, 2 saat; sıcaklık,  $25 \pm 1$  °C).

*Figure 8.* Effect of adsorbent amount on the adsorption of Cr(VI) by (Kts/Kao) beads. (Adsorption conditions: concentration of Cr(VI),  $10^{-3}$  mol/L; pH 2; contact time, 2 h; temperature,  $25 \pm 1$  °C).

Mekonnen ve diğ. (2015) ve Al-Afy ve diğ. (2014) ise farklı adsorban miktarına karşı Cr(VI) uzaklaştırma çalışmalarında adsorpsiyonun önce hızlı arttığını belirli bir değerden sonra bir plato değerinden sonra sabit kaldığı görülmüştür. Şekil 8.'de görüldüğü gibi Cr(VI) iyonlarının (Kts/Kao) ile adsorpsiyonu 0,1 grama kadar artmıştır. (Kts/Kao) için Cr(VI) adsorban miktarının artırılması ile % 50-82 adsorpsiyon görülmüştür. Yapılan çalışma sonucu optimum adsorban miktarı 0,1 gram olarak belirlenmiştir. Adsorpsiyon bir yüzey olayıdır ve verim yüzey alanıyla doğru orantılıdır. Cr(VI) giderimindeki artış, adsorban miktarının artırılması ile daha fazla yüzey alanı oluşacağından adsorplanan Cr(VI) miktarının artışına dayandırılabilir (Özer ve diğ., 1997; Hamadi ve diğ., 2004). Elde edilen sonuçlar literatürde farklı adsorbanlarla yapılan çalışmalarla uyum içerisinde olduğu görülmüştür (Guo ve diğ., 2002).

#### **Temas Süresinin Etkisi (Effect of contact time)**

Cr(VI) çözeltisi üzerine (Kts/Kao) ilave edilerek 5, 15, 30, 60, 120, 240, 480, 720, 1080 ve 1440 dk. temas süreleri boyunca metal tutma miktarları incelenmiştir. Çalışmanın temas süresine karşı yüzde adsorpsiyon grafiği Şekil 9'de görülmektedir. Zamanla adsorpsiyonun belli bir süre arttığı, sonra bir plato değerine ulaştığı ve plato değerinden sonra adsorpsiyonun sabit kaldığı görülmüştür.



**Şekil 9.** (Kts/Kao) boncuklarıyla Cr(VI) adsorpsiyonunda temas süresinin etkisi (Adsorpsiyon şartları: Cr(VI) konsantrasyonu,  $10^{-3}$  mol/L; pH 2; adsorban dozu, 2g/L; sıcaklık,  $25 \pm 1$  °C).

*Figure 9.* Effect of contact time on adsorption of Cr(VI) by (Kts/Kao) beads. (Adsorption conditions: concentration of Cr(VI),  $10^{-3}$  mol/L; pH 2; adsorbent dosage, 2g/L; temperature,  $25 \pm 1$  °C).

Şekil 9'da görüldüğü gibi Cr(VI) iyonlarının (Kts/Kao) boncukları ile tutulmasında dengeye 120 dakikada erişilmiştir. Reaksiyonun 5-30 dakika arasında Cr(VI) adsorplanması hızla artmış, 30-120 dakika arasında artış yavaşlamış ve 120 dakikada dengeye ulaşılmıştır. Başta adsorpsiyonun hızlı olması, ilk aşamada Cr(VI) iyonlarının tutulması için kompozit yüzeyindeki adsorpsiyon merkezlerinin serbest olması sebebiyle Cr(VI) iyonlarının bu merkezlerle kolayca etkileşebilmesinden kaynaklanmaktadır. İlk aşamadan sonra adsorpsiyonun daha yavaş gerçekleşmesi ise yüzeydeki merkezlerin işgal edildikçe Cr(VI) iyonlarının iç yüzeye daha yavaş difüzyonu sebebiyle olabilir (Ghaedi ve diğ., 2012). Belirli bir süreden sonra adsorbanın maksimum adsorplama kapasitesine ulaşıldığı için temas süresinin artmasıyla verimde herhangi bir değişikliğin olmaması dengenin kurulduğu gösterir. 120 dakikadan sonra temas süresinin arttırılması ile adsorpsiyonda fazla bir değişiklik gözlemlenmemiştir. Bundan dolayı (Kts/Kao) boncukları adsorban olarak kullanıldığında Cr(VI) iyonlarının adsorpsiyonunda optimum temas süresi 120 dk. olarak belirlenmiştir. Bu durum temas süresinin adsorpsiyon prosesini belli bir değere kadar etkilediğini göstermektedir (Akgül ve diğ., 2006). Popuri ve diğ. (2009) temas süresine karışı ağır metal uzaklaştırma çalışmalarını yaparken adsorpsiyonun önce hızlı arttığını ve yaklaşık 180 dakika civarında bir plato değerine ulaştığı belirlemiştir.

## SONUÇLAR (CONCLUSIONS)

Bu çalışmada, (Kts/Kao) kompoziti hazırlanmış ve Cr(VI)'nın adsorpsiyonunda adsorban olarak kullanımı incelenmiştir. Zaman çalışmaları incelendiğinde 120 dakika sonra adsorplanacak Cr(VI) miktarının yaklaşık yarısı ilk 5-30 dakikada adsorplandığı görülmüştür. Başka bir deyişle adsorplanma başlangıçta çok hızlıdır. 120 dakikadan sonra ise denge derişiminde önemli bir değişiklik olmadığı için dengeye gelme süresi 120 dakika olarak belirlenmiştir. (Kts/Kao)'un Cr(VI) adsorpsiyonunun asidik şartlarda çok daha fazla olduğu rapor edilmiştir. Optimum adsorban miktarı 0,1 gram olarak belirlenmiştir. Kts/Kao üzerinde Cr(VI) adsorpsiyon verileri Freundlich ve Langmuir denklemlerinde değerlendirilmiş bu izoterm modellerinin adsorpsiyon sabitleri Tablo 1.'de verilmiştir. İki model için bulunan  $R^2$  değerleri incelendiğinde Kts/Kao üzerinde Cr(VI)'nın adsorpsiyon izotermi Langmuir modeline uyduğu görülmüştür. Langmuir izoterm modeli genellikle belirli sayıda benzer yerler içeren yüzeyler üzerinde tek tabaka adsorpsiyonu için geçerlidir (Jain, 2001). Maksimum Cr(VI) adsorpsiyon kapasitesi 31.98 mg/g olarak

bulunmuştur. Sonuçlardan, hazırlanan çevre dostu (Kts/Kao) kompoziti ile sulu ortamlardan yüksek verimlilikle Cr(VI) iyonlarının giderilebileceği görülmektedir.

#### KAYNAKLAR (REFERENCES)

- Akgül, M., Karabakan, A., Acar, O., Yürüm, Y., 2006, "Removal of Silver (I) from Aqueous Solutions with Clinoptilolite", *Microporous and Mesoporous Materials*, Vol. 94, pp. 99-104.
- Al-Afy, N., Hijazi, A., Rammal, H., Reda, M., Annan, H., Toufaily, J., 2013, "Adsorption of Chromium (VI) from Aqueous Solutions by Lebanese Prunusavium Stems" *American Journal of Environmental Engineering*, Vol. 3, pp. 179-186.
- Altun, T., Parlayıcı, S., Pehlivan, E., 2016, "Hexavalent Chromium Removal Using Agricultural Waste Rye Husk", *Desalination and Water Treatment*, Vol. 57, pp. 17748-17756.
- Bailey, S.-W., 1980, "Structures of Layer Silicates, In: Crystal Structures of Clay Minerals and Their X-ray Identification (eds. G.W.Brindley and G.Brown)", *ch.1, Mineralogical Society*, London.
- Benito, Y., Ruiz, M.L., 2002, "Reverse Osmosis Applied to Metal Finishing Wastewater", *Desalination*, Vol. 142, pp. 229-234.
- Cheng, H., Liu, Q., Yang, J., Ma, S., Frost, R. L., 2012, "The Thermal Behavior of Kaolinite Intercalation Complexes-A review", *Thermochimica Acta*, Vol. 545, pp. 1-13.
- Demir, A., Seventekin, N., 2009, "Kitin, Kitosan ve Genel Kullanım Alanları", *Tekstil Teknolojileri, Elektronik Dergisi*, Vol. 3, pp. 92-103.
- Erdem, E., Karapınar, N., Donat, R., 2004, "The Removal of Heavy Metal Cations by Natural Zeolite", *Journal of Colloid and Interface Science*, Vol. 280, pp. 309-314.
- Ghaedi, M., Biyareh, M. N., Kokhdan, S. N., Shamsaldini, S., Sahraei, R., Daneshfar, A., Shahriyar, S., 2012, "Comparison of the Efficiency of Palladium and Silver Nanoparticles Loaded on Activated Carbon and Zinc Oxide Nanorods Loaded on Activated Carbon as New Adsorbents for Removal of Congo Red from Aqueous Solution: Kinetic and Isotherm Study", *Materials Science and Engineering: C*, Vol. 32, pp. 725-734.
- Gilcreas F. W., Tarars M. J., Ingols R. S., 1965, "Standard Methods for The Examination of Water and Wastewater", *12th ed. New York, American Public Health Association (APHA) Inc.*, 213 s.
- Guo, Y., Qi, J., Yang, S., Yu, K., Wang, Z., Xu, H., 2002, " Adsorption of Cr(VI) on Micro- and Mesoporous Rice Husk-Based Active Carbon", *Materials Chemistry and Physics*, Vol. 78, pp.132-137.
- Hamadi, N. K., Swaminathani, S., Chen, X. D., 2004, "Adsorption of Paraquat Dichloride from Aqueous Solution by Activated Carbon Derived from Used Tire", *Journal of Hazardous Materials*, Vol. 112, pp. 133-141.
- Jain, C. K., 2001, "Adsorption of Zinc Onto Bed Sediments of the River Ganga; Adsorption Models and Kinetics", *Hydrological Sciences Journal des Sciences Hydrologiques*, Vol. 46, pp. 419-434.
- Mekonnen, E., Yitbarek, M., Soreta, T. R., 2015, "Kinetic and Thermodynamic Studies of the Adsorption of Cr(VI) onto Some Selected Local Adsorbents", *South African Journal of Chemistry*, Vol. 68, pp. 45-52.
- Ngah, W. S., Fatinathan, S., 2008, "Adsorption of Cu(II) İons in Aqueous Solution Using Chitosan Beads, Chitosan-GLA Beads and Chitosan-Alginate Beads", *Chemical Engineering Journal*, Vol. 143 No. 1-3, pp. 62-72.
- Özer, A., Özer, D., Ekiz, H.-İ., Aksu, Z., Kutsal, T., Çağlar, A., 1997, "Demir (III) İyonlarının Schizomeris leibleinii'ye Adsorpsiyonu", *Doğa -Tr. J. of Eng. and Env. Sci.* Vol. 21, pp. 183-188.
- Popuri, S. R., Vijaya, Y., Boddu, V. M., Abburi, K., 2009, "Adsorptive Removal of Copper and Nickel İons from Water Using Chitosan Coated PVC Beads", *Bioresource Technology*, Vol. 100, pp. 194-199.
- Ramos, R.-L., Juarez Martinez, A., Guerra Coronado, R.-M., 1994, "Adsorption of Chromium (VI) from Aqueous Solutions on Activated Carbon", *Water Science and Technology*, Vol. 30 (9), pp. 191-197.

- Rengaraj, S., Yeon, K. H., Moon, S. H., 2001, "Removal of Chromium from Water and Wastewater by Ion Exchange Resins", *Journal of Hazardous Materials*, , Vol. 87, pp. 273–287.
- Sajomsang, W., 2010, "Synthetic Methods and Applications of Chitosan Containing Pyridylmethyl Moiety And Its Quaternized Derivatives: A review", *Carbohydrate Polymers*, Vol. 80 (3), pp. 631-647.
- Sari, A., Tuzen, M., 2014, "Cd(II) Adsorption from Aqueous Solution by Raw and Modified Kaolinite", *Applied Clay Science*, pp. 63–72.
- Snell, F. D., Snell C. T., 1959, *Colorimetric Method of Analysis*, 2, third ed. D. Van Nostrand Company, New York, Toronto.
- Tao, H., Chao, Y., Xue-hui, R., Ji-de, W., Chun-ge, N., Xin-tai, S., 2014, "Facile Additive-Free Synthesis of Iron Oxide Nanoparticles for Efficient Adsorptive Removal of Congo Red and Cr(VI)". *Applied Surface Science*, Vol. 292, pp. 174–180.
- Teng, W. L., Khor, E., Tan, T. K., Lim, L. Y., Tan, S. C., 2001, "Concurrent Production of Chitin from Shrimp Shells and Fungi", *Carbohydrate Research*, Vol. 332, pp. 305–316.
- Tiwaril, A., Shukla, S. K., 2009, "Chitosan-g-polyaniline: A Creatine Amidinohydrolase Immobilization Matrix for Creatine Biosensor", *Express Polymer Letters*, Vol. 3, No. 9, pp. 553–559.
- Yang W. C., Tang Q. Z., Dong S. Y. , Chai L. Y., Wang H. Y., 2016, "Single-Step Synthesis of Magnetic Chitosan Composites and Application for Chromate (Cr(VI)) Removal", *Journal of Central South University*, Vol. 23, pp. 317–323.
- Yurlova, L., Kryvoruchko, A., Kornilovich, B., 2002, " Removal of Ni (II) Ions from Wastewater by Micellar-Enhanced Ultrafiltration", *Desalination*, Vol. 144, pp. 255–260.
- Zhou, Z., Lin, S., Yue, T., Lee, T. C., 2014, "Adsorption of Food Dyes from Aqueous Solution by Glutaraldehyde Cross-Linked Magnetic Chitosan Nanoparticles", *Journal of Food Engineering*, Vol. 126, pp. 133–141.



## INVESTIGATION OF SURFACE ROUGHNESS AND MICROHARDNESS IN BALL BURNISHING PROCESS OF AZ31B MAGNESIUM ALLOY

**Berat Baris BULDUM**

<sup>1</sup>Mersin University, Department of Mechanical Engineering, Mersin, TURKEY

<sup>1</sup>barisbuldum@mersin.edu.tr

(Geliş/Received: 07.06.2017; Kabul/Accepted in Revised Form: 12.07.2017)

**ABSTRACT:** Magnesium alloys which are lightweight and high strength materials have some limitations due to their insufficient corrosion resistance and low surface quality. To overcome these limitations, especially improving surface properties ball burnishing process was applied to magnesium alloy with different parameters like force, number of passes, feed rate and speed. For reducing number of experiments Taguchi method was used and optimum burnishing condition was determined according to S/N ratios. The results of surface roughness and hardness tests show that feed rate and force was found significant parameters for improving surface quality. When lower feed rate and higher force parameters was chosen best surface roughness value was obtained.

**Key Words:** Ball Burnishing, Magnesium alloy, Surface roughness, Taguchi.

### AZ31B Magnezyum Alaşımının Bilyalı Parlatma Yöntemi ile Mikrosertlik ve Yüzey Pürüzlülüğünün Araştırılması

**ÖZ:** Hafif ve yüksek dayanımlı malzemelerden olan magnezyum alaşımları, yetersiz korozyon direnci ve düşük yüzey kalitesi nedeniyle bazı sınırlamalara sahiptir. Bu sınırlamaların üstesinden gelmek, özellikle yüzey özelliklerini iyileştirmek için, ilerleme hızı, devir, kuvvet ve paso sayısı gibi farklı parametrelerle bilyalı parlatma işlemi uygulanmıştır. Deney sayısını azaltmak için Taguchi yöntemi kullanılmış ve S/N oranlarına göre en iyi parlatma koşulları belirlenmiştir. Yüzey pürüzlülüğü ve sertlik testlerinin sonucunda ilerleme hızı ve kuvvetin yüzey kalitesini iyileştirmede önemli parametreler olduğu bulunmuştur. Düşük ilerleme hızı ve yüksek kuvvet parametreleri seçildiğinde en iyi yüzey pürüzlülüğü değeri elde edilmiştir.

**Anahtar Kelimeler:** Bilyalı Parlatma, Magnezyum alaşımı, Yüzey pürüzlülüğü, Taguchi

### INTRODUCTION

Magnesium is of interest as a construction material because of its very low density and good strength. Magnesium alloys are very attractive materials for engineering applications, such as biomaterial, automobile and aero industries due to their advantages like lightweight, high strength and high specific stiffness. Thus, they have recently been increasing the interest as base materials in many applications, in particular, they are considered to be replacing aluminum alloys in the automotive industries (Cui *et al.*, 2015; Fouad, 2011). The attractive mechanical properties of Mg and its alloys increase their use in industry but, their applications are often limited because of their unsatisfactory corrosion performance and poor surface properties. To overcome the limitation of these deficiencies, the surface properties of Mg alloys, therefore need to be improved. Surface modification is a common way to improve the surface properties. Surface properties have, importance for better product life of several

machines and structural parts that are used for engineering applications (Fouad and El Batanouny, 2011; Pu *et al.*, 2012)

Nowadays manufacturing industry is showing more interest in dimensional precision and surface treatments. Schematic representation of the formation of surface roughness was shown in figure 1. To improve product quality, traditional surface treatments like honing, grinding and lapping are used. But these chip removal processes depend on skill and experience of the operator. To overcome these problems, ball burnishing process is used for better surface roughness which is chip-less, simple and short processing times application. Ball burnishing is a cold working process that obtains better surface roughness using plastic deformation without material loss (Aldas *et al.*, 2014; Kulekci *et al.*, 2014; John *et al.*, 2016; Sagbas, 2011).

Burnishing is a surface finish treatment to cause residual stresses on material surfaces and to improve surface qualities. The enhancement in surface values include increase in surface hardness, reduction in surface roughness, the production of compressive residual stresses which are favorable for cold work hardening of the surface, improves tensile strength and corrosion resistance, also maintains dimensional stability fatigue life as result of the produced compressive residual stress (Hassan *et al.*, 1996; Revankar *et al.*, 2014).

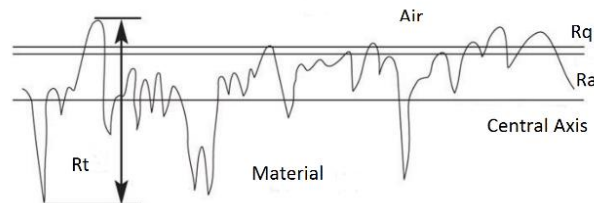


**Figure 1.** Schematic representation of the formation of surface roughness (Hiegemann *et al.*, 2016)

Hassan *et al.* were used ball-burnishing process in order to improve the surface hardness and roughness of brass alloys. They were investigated the effect of different forces and a number of tool passes. The results obtained from the wear tests show that the burnishing process was improved the wear resistance of the brass alloys (Hassan and Al-Dhifi, 1999). El-Axira *et al.* were studied four ball burnishing parameters for aluminum alloy 2014 which is the depth of penetration, feed rate, a number of passes and burnishing speed. A remarkable increasing surface microhardness in specimens was obtained (El Axir *et al.*, 2008). Hassan *et al.* were examined the surface roughness, proof stress, hardness, fatigue strength and ultimate tensile before and after burnishing properties of non-ferrous metals. The results were showed some recuperation on these properties due to the burnishing process (Hassan and Al-Bsharat, 1996). Shiou *et al.* were investigated the optimal surface parameters for the NAK80 mold tool steel via using the Taguchi's L18 orthogonal table. The burnished surface roughness of the samples were enhanced from about  $Ra$   $0.06 \mu\text{m}$  to  $0.016 \mu\text{m}$  in average using the determined optimal parameters (Shiou and Cheng, 2008). Hassan *et al.* were studied the effects of the force and the number of passes on the surface hardness and roughness of aluminum and brass. They were obtained that improvements in the surface roughness and increases in the surface hardness values (Hasan, 1997). Rodriguez *et al.* was used a finite element model of ball-burnishing to find out and estimate residual stress values. They were found that burnishing is an economical and possible process for the quality improvement of materials, not only in surface roughness but in compressive residual stresses as well (Rodriguez *et al.*, 2012).

The scope of this investigation optimum burnishing parameters of AZ31B mg alloys were determined. The effects of different passes, forces, feed rate, and speed were examined using Taguchi method.

## MATERIAL AND METHOD

In this study, AZ31B Mg alloys were used as a workpiece material. The chemical composition of this alloy is as shown in Table 1. AZ31B was chosen because of magnesium alloys are very attractive materials for engineering applications, such as biomaterial, automobile and aero industries due to their advantages like lightweight, high strength and high specific stiffness.

### Design of the Taguchi's Orthogonal Array

The traditional experiments process are too complicated and not easy to use. And also machining process period is important for manufacturer. When the number of parameters is more a large number of experiments have to be realized. Because of this problems Taguchi leads the use of orthogonal arrays to research all parameters with a small number of experiments. Taguchi proposed signal to noise (S/N) ratio for defining optimum parameters of experiments. Experiments design problems can be divided into the smaller the better type, the larger the better type and the nominal the-best type. The signal to noise (S/N) ratio was used for optimizing a treatment for product design.

**Table 1.** Chemical composition of AZ31B Mg alloy

Component	Al	Zn	Mn	Fe	Si	Cu	Ni
%	8.73	0.56	0.23	0.0026	0.021	0.0018	0.0009

The surface roughness value of the burnished surface throughout the optimum parameters should be smaller than nonburnished surface and the hardness value should be bigger than nonburnished surface. Consequently, for surface roughness smaller the better type (equation 1), for surface hardness larger the better type (equation 2) is available. The S/N ratio,  $\eta$ , is defined by the following equations:

$$\eta = -10 \log_{10} \left[ \frac{1}{n} \sum_{i=1}^n y_i^2 \right] \quad (1)$$

$$\eta = -10 \log_{10} \left[ \frac{1}{n} \sum_{i=1}^n \frac{1}{y_i^2} \right] \quad (2)$$

where  $n$  is the number of the experiment and  $y_i$  is the results of the experiments under different parameters (El Axir and Ibrahim, 2005; Shiou and Hsu, 2008; Ibrahim *et al.*, 2009; Gomez-Gras *et al.*, 2015).

The effects of some parameters can be determined efficiently using Taguchi design. The essential burnishing parameters having important effects on surface roughness are speed, feed rate, forces and a number of passes. Consequently, speed, feed rate, a number of passes and force, were selected as four experimental parameters (Table 2). Two levels for a number of passes and three level of other parameters (feed rate, speed, force) were selected. The  $L_{18}$  orthogonal array (Table 3) was chosen for one two level and three three-level factors of the ball burnishing process.

### Sample and Analyses

AZ31B Mg alloys (Yuanhong Alloy Materials Co.,Ltd, China), were used in the experiments, which was commercially bought as 50 mm diameter and approximate length of 300 mm bars to using a test specimen. Samples were cut from these bars, then each sample was machined to a diameter of 25 mm and divided into nine regions. The burnishing tool was attached to a Liouy Hsing GNC-450L CNC lathe

(figure 2), which the operation is performed. Four parameters were adjusted for experiments. Then burnishing process are carried out on the turned surface by varying the force (50, 150, 250 N), feed rate (0.1, 0.25, 0.5 mm/dk), speed (200, 400, 600 rpm), a number of passes.

**Table 2.** The value of using parameters for ball burnishing process

P	F (N)	V (rpm)	f (mm/min)
1	50	200	0.1
2	150	400	0.25
-	250	600	0.5

Therefore, nine burnishing operations were developed for each of the two specimens. The surface roughness of all the burnished work pieces was determined using surface roughness tester (Mitutoyo, SurfTest SJ 201). To determining surface roughness quality, three measurements were taken at different points of the specimen in Ra ( $\mu\text{m}$ ) values and their averages were calculated. The hardness of each sample was determined using vickers test machine (Tronic, Digital Microhardness Tester DHV-1000). Testing load of 1 kg load was applied.

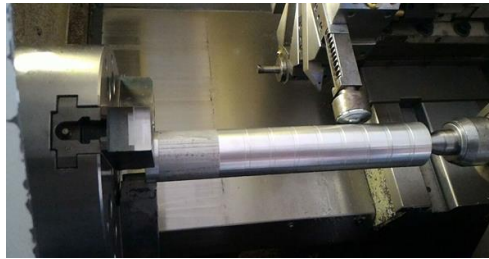


**Figure 2.** The photograph of the AZ31B Mg alloy ball burnishing process

The solid model of the ball burnishing tool is shown in figure 3a. The schematic view of work piece material shown in figure 3b. Figure. 4a and Figure 4b show the photographs of the surface roughness tester and vickers hardness machine used in the present work.

**Table 3.** Taguchi design of experiments

	P	F (N)	V (rpm)	f (mm/dk)
1	1	1	1	1
2	1	1	2	2
3	1	1	3	3
4	1	2	1	1
5	1	2	2	2
6	1	2	3	3
7	1	3	1	2
8	1	3	2	3
9	1	3	3	1
10	2	1	1	3
11	2	1	2	1
12	2	1	3	2
13	2	2	1	2
14	2	2	2	3
15	2	2	3	1
16	2	3	1	3
17	2	3	2	1
18	2	3	3	2

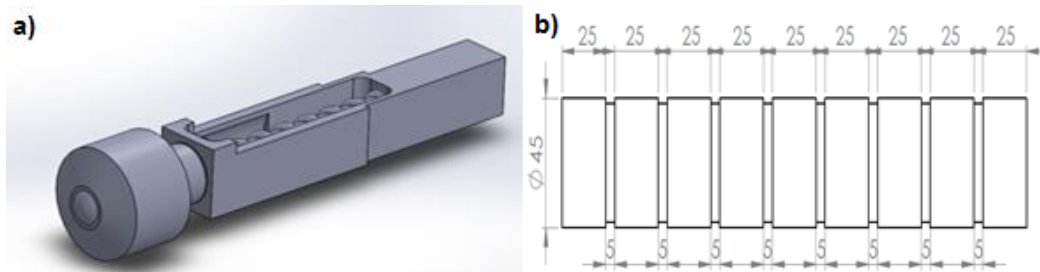


**Figure 3.** a) Solid model of ball burnishing tool b) Schematic view of the specimens

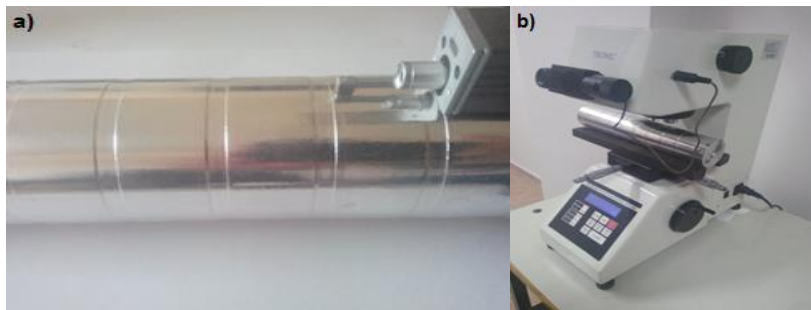


**Figure 4.** a) The photograph of the surface roughness measuring test b) The photograph of the Vickers microhardness test

## RESULT AND DISCUSSION

In the present study the effect of the different parameters (force, speed, feed rate and number of passes) on surface roughness and vickers hardness of AZ31B Mg alloys were performed. For investigating feed rate, speed and force three different level were applied. For number of passes 1 and 2 passes were studied. Researching all this parameters 54 experiments were required. But using Taguchi experimental design the study was made efficient. 3 factor 3 level and 1 factor 2 level Taguchi mixed design were selected. By this way number of experiment were reduced from 54 to 18 using  $L_{18}$  orthogonal array.

S/N values were calculated for defining optimum parameters of burnishing process. Smaller is the better type were used for surface roughness and larger is the better type were used for vickers hardness. Taguchi  $L_{18}$  orthogonal array design, surface roughness and hardness values also S/N ratios are seen in Table 4.

**Table 4.** Taguchi L<sub>18</sub> orthogonal array, measured values and S/N ratios

Num. Of exp.	Passes	Force (N)	Speed (rpm)	Feed rate (mm/dk)	Surface rough.	Hardness (HV)	S/N ratio of surface rough.	S/N ratio of hardness
1	1	50	200	0.1	0.483	81.273	6.31B2	47.763
2	1	50	400	0.25	0.551	79.097	5.155	47.520
3	1	50	600	0.5	0.677	82.953	3.390	47.921
4	1	150	200	0.1	0.355	79.810	8.990	47.602
5	1	150	400	0.25	0.475	82.870	6.466	47.920
6	1	150	600	0.5	0.639	81.360	3.882	47.765
7	1	250	200	0.25	0.382	81.347	8.31B9	47.757
8	1	250	400	0.5	0.539	84.290	5.356	48.062
9	1	250	600	0.1	0.31B6	86.473	10.009	48.288
10	2	50	200	0.5	0.550	77.343	5.183	47.329
11	2	50	400	0.1	0.419	79.156	7.540	47.521
12	2	50	600	0.25	0.508	79.026	5.885	47.503
13	2	150	200	0.25	0.399	80.206	7.982	47.656
14	2	150	400	0.5	0.539	80.306	5.352	47.644
15	2	150	600	0.1	0.344	82.420	9.226	47.864
16	2	250	200	0.5	0.485	78.566	6.264	47.450
17	2	250	400	0.1	0.333	83.753	9.541	48.009
18	2	250	600	0.25	0.390	82.486	8.142	47.872

Calculated S/N values for each factor effecting of surface roughness are shown in Table 5. Highest values were chosen for defining minimum surface roughness. Therefore A2, B3, C1, D1 were determined optimum choice for the best surface roughness (Table 5). S/N ratios data for surface roughness were seen on the graph in figure 5. According to Figure 5 when applying force (250 N) and number of passes (2) level be maximum also speed (200 rpm) and feed rate (0.1 mm/min) level be minimum the best surface roughness value was obtained. Calculated S/N values for each factor effecting of vickers hardness are shown in Table 6. Highest values were chosen for defining maximum hardness. Therefore A1, B3, C3, D1 were determined optimum choice for the best hardness (Table 6).

**Table 5.** Optimum S/N ratios for surface roughness

factor/level	1	2	3
Passes (A)	6.431B	<b>7.235</b>	
Force (B)	5.578	6.983	<b>7.938</b>
Speed (C)	<b>7.175</b>	6.568	6.755
Feed rate (D)	<b>8.603</b>	6.991	4.905

S/N ratios data for vickers hardness were seen on the graph in figure 6. According to Figure 6 when applying force (250 N) and speed (600 rpm) level be maximum also number of passes (1) and feed rate (0.1 mm/min) level be minimum the best vickers hardness value was obtained. But all of factors and levels, there is no significant changing on hardness values.

**Table 6.** Optimum S/N ratios for hardness

Factor/level	1	2	3
Passes (A)	<b>47.844</b>	47.650	
Force (B)	47.592	47.742	<b>47.907</b>
Speed (C)	47.593	47.779	<b>47.869</b>
Feed rate (D)	<b>47.841</b>	47.707	47.695

As is seen from Fig 7a when applying force increasing and feed rate decreasing surface roughness was improved. A few changing was obtained on surface roughness using different forces. But especially feed rate was defined impressive factor for surface roughness.

As shown in fig 7b when using speed are raising surface roughness was reached slightly better value. But decreasing feed rate significant changing on surface roughness was observed. The increasing number of passes 1 to 2 the surface roughness was decreased. This is similarly the results of experiments by Revankar et al (Revankar *et al.*, 2014). But differently further increasing number of passes they were found decreasing on surface roughness values (Fouad, 2011). When the force increasing from 50 N to 250 N the burnishing process resulting in an enhanced surface roughness. The reason for this decreasing on surface roughness with increasing force due to increased pressure between specimen and ball. Therefore the plastic deformation region broadens and raising metal diffusion was filled emptiness on specimen (Nemat and Lyons, 2000; De Lacalle *et al.*, 2007; Klocke *et al.*, 2009; Tadic *et al.*, 2013). The raise on the speed level surface roughness decreasing with an effect of temperature and vibration the increasing of speed beyond a certain limit may influence of metal flow on specimen leading to raising surface roughness (El-Taweel and El-Axir, 2009).

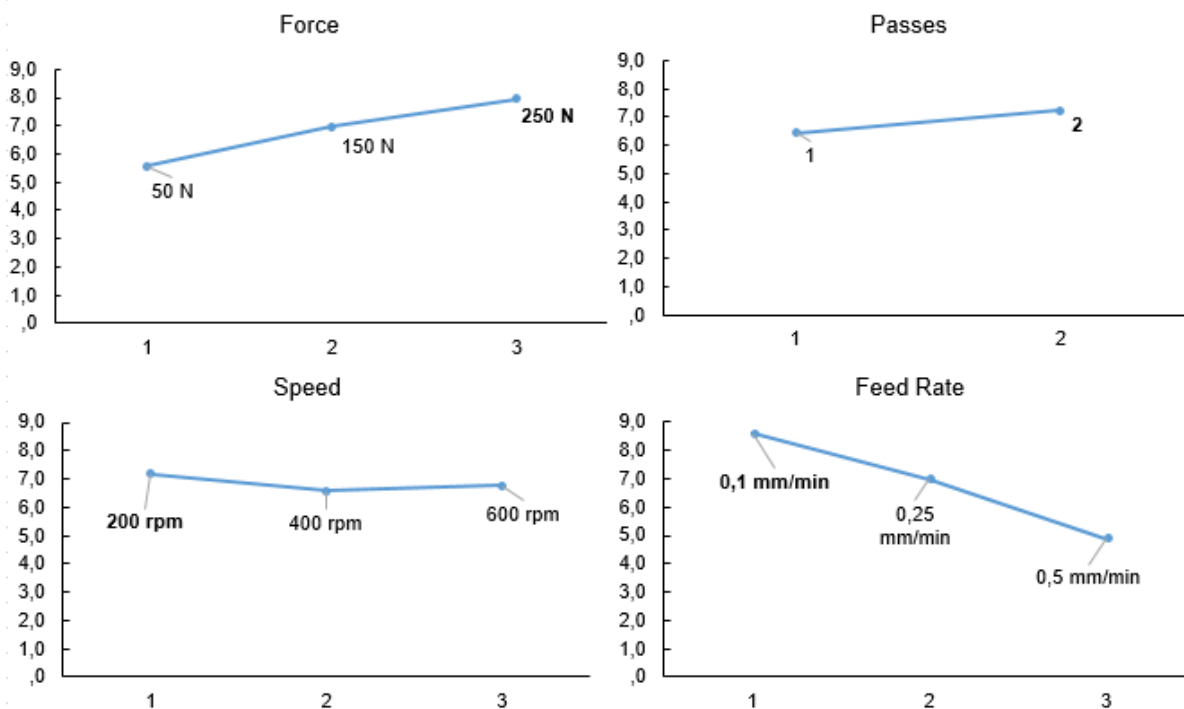


Figure 5. Plots of S/N ratios for surface roughness

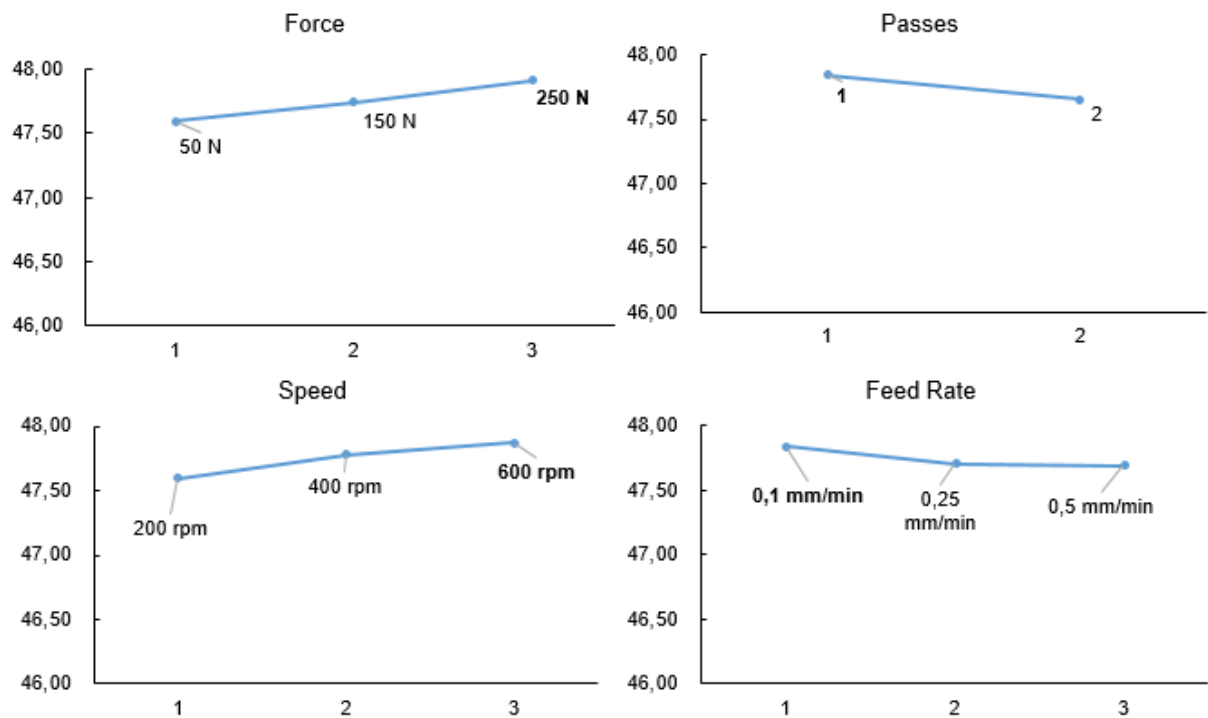


Figure 6. Plots of S/N ratios for hardness

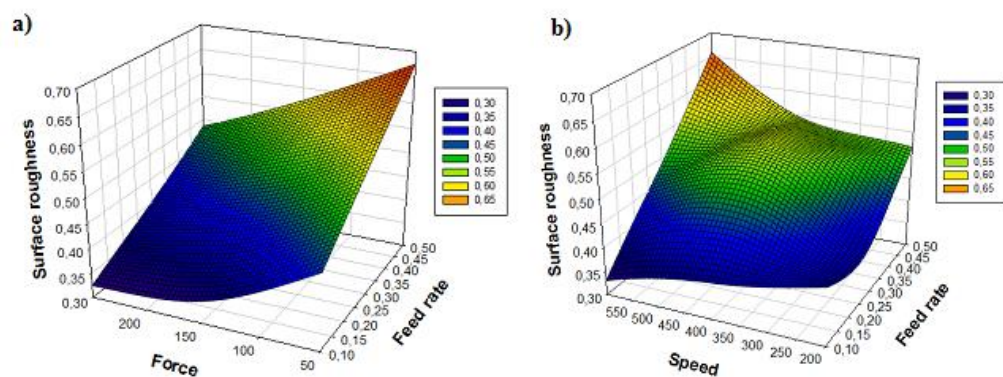


Figure 7 a) Effect of burnishing force and burnishing feed rate on surface roughness b) Effect of burnishing speed and burnishing feed rate on surface roughness

Surface roughness improve the increasing feed rate was caused gradually decreasing on surface roughness this is because deformation of the specimen is bigger and metal flow is equal at lower feed (El-Axir, 2000). For evaluating effect of number of passes on hardness value 2 level was selected. From 1 to 2 passes hardness value decreasing because of much more stiffening and as a result of flaking of the surface due to more repeated ball contact on the same sample surface (El-Axir *et al.*, 2008). An increase in force from 50 N to 250 N the hardness gradually increases. Because of the rise in metal flow that cause to an improve deformation and fill the cavity on workpiece (Nemat and Lyons, 2000). When applying speed increases the hardness value is increases from 200 rpm to 600 rpm. This results of experiments similarly results of experiments performed by Nemat. Also Nemat was found further increase of speed will caused decreasing surface hardness due to vibration and short contact time between ball and workpiece at higher speeds (Nemat and Lyons, 2000). According to our results, feed rate increases from 0,1 mm/min to 0,5 mm/min the hardness decreases because of the low deformation and irregular metal

flow (El-Axir *et al.*, 2008). The optimal results of each factor, both surface roughness and hardness was shown in table 7.

**Table 7.** Optimal values of parameters

factor/ level	Num. of passes	Force	Speed	Feed rate
Surface roughness	2	3	1	1
Hardness	1	3	3	1

## CONCLUSION

In this study, effecting of burnishing parameter like feed rate, force, speed and number of passes on surface roughness and hardness of AZ31B Mg alloys was investigated. The results show that applying force and feed rate was determined significant factor on surface roughness. Increasing number of passes was improved surface roughness but it was caused deteriorate on hardness. The raise in force was enhanced both surface roughness and hardness. The lower level of feed rate was reached better surface roughness and hardness values. The increasing on speed was promoted surface hardness however this increasing was resulted decreasing on surface roughness. In our experiments, optimum results for surface roughness was defined as the burnishing force of 250 N, the burnishing feed rate of 0,1 mm/min, the burnishing speed of 200 rpm and burnishing passes of 2. For surface hardness, the burnishing force of 250 N, burnishing feed rate of 0,1 mm/min, burnishing speed of 600 rpm and burnishing passes of 1 was obtained best results.

## REFERENCES

- Aldas, K., Özkul, I., Eskil, M., 2014, "Prediction of Surface Roughness in Longitudinal Turning Process by a Genetic Learning Algorithm", *Materials Testing*, Vol. 56, pp. 375-380.
- Cui, Z., Shi, H., Wang, W., Xu, B. 2015, "Laser Surface Melting az31bb Magnesium Alloy with Liquid Nitrogen-Assisted Cooling", *Transactions of Nonferrous Metals Society of China*, Vol. 25, pp. 1446-1453.
- De Lacalle, L. N., Lamikiz, A., Sanchez, A., Arana, J. L., 2007, "The Effect of Ball Burnishing on Heat-Treated Steel and Inconel 718 Milled Surfaces", *The International Journal of Advanced Manufacturing Technology*, Vol. 32, pp. 958-968.
- El-Axir, M., 2000, "An Investigation into Roller Burnishing", *International Journal of Machine Tools and Manufacture*, Vol. 40, pp. 1603-1617.
- El-Axir, M. H., Ibrahim, A., 2005, "Some Surface Characteristics due to Center Rest Ball Burnishing", *Journal of Materials Processing Technology*, Vol. 167, pp. 47-53.
- El-Axir, M., Othman, O., Abodiena, A., 2008, "Improvements in Out-of-Roundness and Microhardness of Inner Surfaces by Internal Ball Burnishing Process", *Journal of Materials Processing Technology*, Vol. 196, pp. 120-128.
- El-Taweel, T., El-Axir, M., 2009, "Analysis and Optimization of The Ball Burnishing Process Through the Taguchi Technique", *The International Journal of Advanced Manufacturing Technology*, Vol. 41, pp. 301-310.
- Fouad, Y., 2011, "Fatigue Behavior of a Rolled AZ31B Magnesium Alloy after Surface Treatment by EP and BB Conditions", *Alexandria Engineering Journal*, Vol. 50, pp. 23-27.
- Fouad, Y., El Batanouny, M., 2011, "Effect of Surface Treatment on Wear Behavior of Magnesium Alloy AZ31B", *Alexandria Engineering Journal*, Vol. 50, pp. 19-22.

- Gomez-Gras, G., Travieso-Rodriguez, J. A., Jerez-Mesa, R., 2015, "Experimental Characterization of the Influence of Lateral Pass Width on Results of a Ball Burnishing Operation", *Procedia Engineering*, Vol. 132, pp. 686-692.
- Hassan, A. M., 1997, "The Effects of Ball-and Roller-Burnishing on the Surface Roughness and Hardness of Some Non-Ferrous Metals", *Journal of Materials Processing Technology*, Vol. 72, pp. 385-391.
- Hassan, A. M., Al-Bsharat, A. S., 1996, "Improvements in Some Properties of Non-Ferrous Metals by the Application of the Ball-Burnishing Process", *Journal of Materials Processing Technology*, Vol. 59, pp. 250-256.
- Hassan, A. M., Al-Dhifi, S. Z., 1999, "Improvement in the Wear Resistance of Brass Components by the Ball Burnishing Process", *Journal of Materials Processing Technology*, Vol. 96, pp. 73-80.
- Hiegemann, L., Weddeling, C., Tekkaya, A. E., 2016, "Analytical Contact Pressure Model for Predicting Roughness of Ball Burnished Surfaces", *Journal of Materials Processing Technology*, Vol. 232, pp. 63-77.
- Ibrahim, A. A., Rabbo, S. M., El-Axir, M. H., Ebied, A. A., 2009, "Center Rest Balls Burnishing Parameters Adaptation of Steel Components Using Fuzzy Logic", *Journal of Materials Processing Technology*, Vol. 209, pp. 2428-2435.
- John, M. R. S., Wilson, A. W., Bhardwaj, A. P., Abraham, A., Vinayagam, B. K., 2016, "An Investigation of Ball Burnishing Process on CNC Lathe Using Finite Element Analysis", *Simulation Modelling Practice and Theory*, Vol. 62, pp. 88-101.
- Klocke, F., Backer, V., Wegner, H., Feldhaus, B., Baron, H. U., Hessert, R., 2009, "Influence of Process and Geometry Parameters on the Surface Layer State After Roller Burnishing of In718", *Production Engineering*, Vol. 3, pp. 391-399.
- Kulecki, M. K., Akkurt, A., Esme, U., Ozkul, I., 2014, "Multiple Regression Modeling and Prediction of the Surface Roughness in the Wedm Process", *Materiali in Tehnologije*, Vol.48, pp. 9-14.
- Nemat, M., Lyons, A., 2000, "An Investigation of the Surface Topography of Ball Burnished Mild Steel and Aluminium", *The International Journal of Advanced Manufacturing Technology*, Vol. 16, pp. 469-473.
- Pu, Z., Outeiro, J. C., Batista, A. C., Dillon, Jr. O. W., Puleo, D. A., Jawahir, I. S., 2012, "Enhanced Surface Integrity of AZ31BB Mg Alloy by Cryogenic Machining Towards Improved Functional Performance of Machined Components", *International Journal of Machine Tools and Manufacture*, Vol. 56, pp. 17-27.
- Revankar, G. D., Shetty, R., Shrikantha, S., Vinayak, R., Gaitonde, N., 2014, "Analysis of Surface Roughness and Hardness in Ball Burnishing of Titanium Alloy", *Measurement*, Vol. 58, pp. 256-268.
- Rodriguez, A., Lopez de Lacalle, L. N., Celaya, A., Lamikiz, A., Albizuri, J., 2012, "Surface Improvement of Shafts by the Deep Ball-Burnishing Technique", *Surface and Coatings Technology*, Vol. 206, pp. 2817-2824.
- Sagbas, A., 2011, "Analysis and Optimization of Surface Roughness in The Ball Burnishing Process Using Response Surface Methodology and Desirability Function", *Advances in Engineering Software*, Vol. 42, pp. 992-998.
- Shiou, F., Cheng, C., 2008, "Ultra-precision Surface Finish of NAK80 Mould Tool Steel Using Sequential Ball Burnishing and Ball Polishing Processes" *Journal of Materials Processing Technology*, Vol. 201, pp. 554-559.
- Shiou, F. J., Hsu, C. C., 2008, "Surface Finishing of Hardened and Tempered Stainless Tool Steel using Sequential Ball Grinding, Ball Burnishing and ball Polishing Processes on a Machining Centre", *Journal of Materials Processing Technology*, Vol. 205, pp. 249-258.
- Tadic, B., Todorovic, P. M., Luzanin, O., Miljanic, D., Jeremevic, B. M., Bogdanovic, B., Vukelic, D., 2013, "Using Specially Designed High-Stiffness Burnishing Tool to Achieve High-Quality Surface Finish", *The International Journal of Advanced Manufacturing Technology*, Vol. 67, pp. 601-611.

## BAĞLAYICI OLARAK PİROLİTİK SIVI KULLANILAN MgO-C REFRAKTER TUĞLALARIN MEKANİK ÖZELLİKLERİNİN İNCELENMESİ

<sup>1</sup>Tuba BAHTLI, <sup>2</sup>Veysel Murat BOSTANCI, <sup>3</sup>Derya Yeşim HOPA, <sup>4</sup>Şerife Yalçın YASTI

<sup>1</sup>Necmettin Erbakan Üniversitesi, Mühendislik-Mimarlık Fakültesi, Metalurji ve Malzeme Mühendisliği Bölümü, KONYA

<sup>2</sup>Necmettin Erbakan Üniversitesi, Fen Bilimleri Enstitüsü, Makine Mühendisliği A.B.D., KONYA

<sup>3</sup>Afyon Kocatepe Üniversitesi, Mühendislik Fakültesi, Kimya Mühendisliği Bölümü, AFYONKOCATEPE

<sup>4</sup>Selçuk Üniversitesi, Güzel Sanatlar Fakültesi, Seramik Bölümü, KONYA

<sup>1</sup>taksoy@konya.edu.tr, <sup>2</sup>vmuratb@hotmail.com, <sup>3</sup>dyhopa@aku.edu.tr, <sup>4</sup>syasti@selcuk.edu.tr

(Geliş/Received: 07.07.2017; Kabul/Accepted in Revised Form: 25.07.2017)

**ÖZ:** Bu çalışmada, 500 °C sıcaklık, 15 °C/dk ısıtma hızı ve 0,5 lt/dk azot akış hızı piroliz parametrelerinde lastik atığının pirolizi sonucu elde edilen ve %10' luk H<sub>2</sub>SO<sub>4</sub> çözeltisi ile iki defa ekstraksiyon işlemi uygulanarak kükürt miktarı düşürülen pirolitik sıvı, MgO-C refrakter tuğlada bağlayıcı olarak kullanılmıştır. Üretilen refrakter malzemelerin, açık gözenek (%), yoğunluk ve soğuk basma mukavemet (SBM) değerleri, üç noktalı eğme mukavemet değerleri ve elastik modülü belirlendikten sonra üretilen refrakter malzeme, refrakter sektöründe kullanılan ve fenolik reçine ile üretilen MgO-C refrakter tuğlaların özellikleri ile kıyaslanmıştır. Ayrıca, taramalı elektron mikroskobu (SEM) ile mikroyapı görüntüleri incelenerek, görüntüler mekanik özellikleri ile ilişkilendirilmiş, X-ışınları floresans (XRF) spektroskopisi ile elementel analizleri ve X-ışını kırınım yöntemi (XRD) ile de faz analizleri gerçekleştirilmiştir.

**Anahtar Kelimeler:** Gaz kromatografisi-Kütle spektroskopisi (GC-MS), Mekanik, MgO-C, Piroliz, Refrakter, Yoğunluk,

### Investigation of The Mechanical Properties of MgO-C Refractory Bricks by Incorporation of Pyrolytic Liquid as Binder

**ABSTRACT:** In this study, pyrolytic liquid obtained at 500 °C temperature, 15 °C /min. heating rate and 0,5 lt/min. nitrogen flow rate pyrolysis parameters and then 2 times extraction with 10% H<sub>2</sub>SO<sub>4</sub> solution to decrease sulfur content was used as a binder in MgO-C refractory brick. Open porosity (%), density, cold compressive strength (CCS) and three point bending strength and elastic modulus values of the produced refractory materials were determined, and were compared with the properties of MgO-C refractory bricks produced by incorporation of phenolic resin in the refractory sector. In addition, microstructure images by scanning electron microscopy (SEM) were investigated and correlated with the mechanical properties of those refractories. Elemental analysis by X-ray fluorescence (XRF) spectroscopy and phase analysis by X-ray diffraction (XRD) were performed.

**Key Words:** Gas chromatography-Mass spectroscopy (GC-MS), Mechanics, MgO-C, Pyrolysis, Refractor, Density.

### GİRİŞ (INTRODUCTION)

Manyezit karbon tuğlalar, genel olarak içeriğinde manyezit ve %5-20 arasında karbon içeren şekilli refrakter ürünlerdir. Bazik oksijen fırınları, çelik döküm potaları ve elektrik ark ocakları, manyezit karbon tuğlaların başlıca kullanım alanlarıdır. Yüksek refrakterlikleri, cüruf atağına ve termal şoklara

karşı dirençleri ile diğer alternatiflerinden daha üstün özelliklere sahip olan Mg-C tuğlalar, 1970'li yılların sonunda bulunmuş olup gelişimi günümüzde hala devam etmektedir (Timuçin ve diğ., 2014).

Grafit, magnezya refrakterlere aşağıdaki iki önemli özelliğe sahip olması nedeniyle ilave edilmektedir:

- a) Cüruf tarafından ıslatılmaması
- b) Yüksek termal şok mukavemetine sahip olması

Grafit, yüzey enerjisinin düşük olması nedeniyle eriyikler tarafından ıslanmazlık özelliğine sahiptir. Islanmazlık özelliği, grafitin eriyikle temas ettiğinde ortaya çıkan temas açısının  $\theta > 90^\circ$  olmasından kaynaklanmaktadır. Bu özelliği nedeniyle grafit cüruftan etkilenmez ve tuğladaki magnezya fazını cüruf korozyonundan korur. Tuğlada bulunan magnezya fazı refraktere yüksek mukavemet sağladığından, çok farklı iki malzeme (grafit ve magnezya) birbirini tamamlayıcı özellik göstermiş olur (Özgen, 1988). Ayrıca, grafitin yüksek bir ısı iletkenliğe sahip olması, magnezya-grafit kompozit refrakterlerin termal şoklara yüksek direnç göstermesini sağlamaktadır (Yazla, 1984).

Lastikler; ağırlıkça %60-65 oranında kauçuk, %25-35 karbon siyahı, geri kalanı hızlandırıcı ve dolgu maddelerinden oluşan termoset polimerlerdir (Leung ve Wang, 1998). Hızlandırıcılar organik kükürt bileşimidir ve lastiğin kükürt içeriği hızlandırıcılardan kaynaklanmaktadır. Vulkanizasyon reaksiyonu sırasında, elastomer moleküler zincirleri arasında çapraz bağlanmalar meydana gelir ve bunun sonucunda üç boyutlu bir kimyasal ağ yapısı oluşur. Oluşan üç boyutlu ağ yapısı içerisinde birleşmiş olan elastomerlerden; katı, çözünmeyen ve erimeyen termoset polimer üretilmektedir (Isayev, 2005).

Üretimi pek çok reaksiyon ile gerçekleştirilen lastiklerin kullanım sonrasında değerlendirilmesi konusunda birçok uygulama mevcuttur. Atık lastiklerin geri kazanım yöntemlerinden başlıcaları; enerji üretimi amacıyla güç santrallerinde (termik değerlendirme) kullanım, lastik üretim sürecinde kullanım, çimento fırınlarında kullanım ve hammaddesel kullanımdır (Gönüllü, 2004). Atık lastiklerin hammadde olarak değerlendirilmesi için kullanılan, termal distilasyon olarak da adlandırılan piroliz yöntemi, atık lastiklerden yakıt ve petrokimyasal maddeler üretimine olanak tanıyan, oksijensiz bir atmosferde ısı etkisiyle kimyasal bağların kırılması işlemidir (Wampler, 2007).

Piroliz ile biyokütle ya da polimer gibi maddeler oksijensiz ortamda genellikle 300-650 °C aralığında belirli bekleme sürelerinde termokimyasal olarak bozundurulmaktadır. Bu süreç sırasında büyük karmaşık hidrokarbon zincirleri kısmen küçük ve basit yapılara kırılarak gaz, sıvı ve char (katı) olmak üzere üç temel ürüne dönüşür. Ağır hidrokarbonlar içeren sıvı ürün genelde pirolitik yağ olarak adlandırılmaktadır. Lastik üretiminde ilave edilen organik kükürt, piroliz sonrası sıvı ürün içerisinde yer almaktadır. Pirolitik yağ içerisindeki kükürtün giderilmesine yönelik olarak çeşitli asitlerle kimyasal ekstraksiyon yoluyla kükürt giderimi birçok çalışmada ele alınmıştır (Aydın ve İlkılıç, 2012; Ahmad ve Ahmad, 2013; Unapumnuk ve diğ., 2008). Literatürdeki çalışmalara göre sülfirik asit, asetik asit, formik asit, hidrojen peroksit asitlerinin tek başına veya karışımlarının belli oranlarının, sıvı ürünün kükürt gideriminde etkili olduğu görülmektedir.

Bu çalışmada atık lastiklerin hammadde olarak değerlendirilmesi amacıyla, lastiklere %10'luk sülfirik asit ile 2 kere ekstraksiyon işlemi uygulanmıştır. İşlemler sonucunda kükürt giderimi yapılan pirolitik sıvı MgO-C refrakter tuğlada bağlayıcı olarak kullanılmış, üretilen ürünlerin % açık gözenek, yoğunluk, SBM, üç noktalı eğme mukavemet değerleri belirlenmiş, SEM ile mikroyapıları karakterize edilmiştir.

## MALZEME VE METOD (MATERIAL AND METHODS)

### Refrakter Malzemelerin Üretimi ve Şekillendirme (Refractory Material Production and Shaping)

DeneySEL çalışmalarda kullanılan fenolik reçine Çukurova Kimya Sanayi A.Ş. tarafından temin edilmiştir. Bağlayıcı olarak kullanılan pirolitik sıvı ise, lastik atığının 500 °C sıcaklık, 15 °C/dk. ısıtma hızı ve 0,5 lt/dk. azot akış hızı piroliz parametrelerinde elde edilmiş, kükürt miktarını düşürmek amacıyla 2 defa %10' luk H<sub>2</sub>SO<sub>4</sub> çözeltisi ile ekstraksiyon işlemi uygulanmıştır.

Piroliz sonrası elde edilen sıvı ürüne piknometre ile yoğunluk tayini, pH tayini ve viskozite tayini Afyon Kocatepe Üniversitesi Kimya Mühendisliği Bölümü laboratuvarında gerçekleştirilmiştir. Viskozite tayini için Fungilab marka, Smart series model dönel viskozimetre kullanılmıştır. Sıvı ürünün kükürt miktarı, Afyon Kocatepe Üniversitesi Teknoloji Uygulama ve Araştırma Merkezi (TUAM) bünyesinde yer alan Met marka Multilab model cihazda IR adsorpsiyon prensibi kullanılarak gerçekleştirilmiştir. Sıvı ürünün içerdiği kimyasal bileşikler Anadolu Üniversitesi Bitki İlaç ve Bilimsel Araştırmalar Merkezi (BİBAM) bünyesindeki gaz kromatografisi-kütle spektroskopisi (GC/MS) cihazı kullanılarak (Agilent HP-5MS) belirlenmiştir. GC/MS analizinde, sıvı ürün aseton ile çözülüp 0,20 µm'lik filtreden süzöldükten sonra GC/MS sistemi ile aşağıdaki şartlarda analiz edilmiştir. Çizelge 1'de yer alan analiz koşulları uygulanmıştır.

**Çizelge 1.** GC/MS koşulları

*Table 1. GC/MS conditions*

Kolon	Agilent HP-5MS (30 m uzunluk, 0,32 mm iç çap, 0,25 µm film kalınlığı)
<b>GC/MS koşulları</b>	
Enjeksiyon sıcaklığı: 250°C	MSD sıcaklığı: 280°C
İyonizasyon modu: EI	Elektron enerjisi: 70 ev
Kütle aralığı: 35- 675 m/z	Fırın sıcaklık programı: 45°C' de tutulma süresi 4 dk.; 3°C/dk. ısıtma hızıyla 280 °C' ye ısıtma, 280 °C' de 30 dk. tutulma.
Taşıyıcı gaz: Helyum	

MgO, karbon kaynağı olarak pul grafit, bağlayıcı olarak reçine ve/veya pirolitik sıvı kullanılarak Çizelge 2'de belirtilen kompozisyonlar reçetelerine uygun şekilde tartılarak hazırlanmıştır.

**Çizelge 2.** Kompozisyon reçetesi

*Table 2. Composition prescription*

	1-4 mm MgO	0-1 mm MgO	Toz MgO	Pul Grafit	Reçine	Sıvı Atık	Novalak	Hegzamin	Antioksidan
RS1	%50	%30	%10	%10	%2	%0	%2	%0,02	%1
RS2	%50	%30	%10	%10	%0	%2	%2	%0,02	%1
RS3	%50	%30	%10	%10	%1,33	%0,66	%2	%0,02	%1

Çizelge 2'de belirtilen kompozisyonlar 100 tonluk (241 bar) preste:

i) 5 adet 50 mm × 50 mm × 50 mm ebatında kare prizma şeklinde refrakter malzemeler 100 MPa (62 bar) basınç uygulanarak, ve

ii) Aynı kompozisyona sahip refrakter malzemeler 25 mm × 25 mm × 150 mm ebatlarında çubuk olacak şekilde 100 MPa (92 bar) basınç uygulanarak şekillendirilmiştir. Şekillendirme sonucunda her bir numune numaralandırılıp temperlemeye hazır hale getirilmiştir.

### Temperleme (Tempering)

Şekillendirilen numuneler Necmettin Erbakan Üniversitesi Kimya Bölümü laboratuvarında Nabertherm N11/R model kül fırını içerisinde 250 °C'de 3 saat bekletilerek temperlenmiştir. Temperlemede 5°C/dk.'lık ısıtma hızı kullanılmıştır. Temperlenmiş numunelerden her bir kompozisyon için Liya marka halkalı değirmende öğütme yapılmış ve Fore marka elek cihazında 63 mikron altına elenmiştir. Elenen 63 mikron altı tozlar faz analizleri (XRD) ve kimyasal analizleri (XRF) Kütahya Dumlupınar Üniversitesi bünyesindeki İleri Teknoloji Tasarım Ar. Ge. ve Uy. Merkezi'nde (İLTEM) gerçekleştirilmiştir.

**% Açık Gözenek ve Yoğunluk Ölçümü (% Open Porosity and Density Measurement)**

Çizelge 2’de belirtilen kompozisyonlardan 3’er parça kesilmiştir. Atık malzemelerin kaynama ile kayıba uğramasını ve dağılmasını engellemek için kaynatmak yerine 24 saat boyunca oda sıcaklığındaki suda bekletilerek porların su ile dolması sağlanmıştır. Daha sonra Archimedes düzeneğinde, suda bekletilen numunelerin su içerisindeki ağırlıkları belirlenmiştir (Wb). Sudan çıkarılan numunelerin yüzeyi kâğıt mendil ile silinerek yüzeylerindeki suyu alınıp, yaş ağırlıkları hassas terazi yardımıyla tespit edilmiştir (Wc). Son aşama olarak parçalar etüvde kurutulduktan sonra, kuru ağırlıkları hassas terazide tartılarak belirlenmiştir (Wa). % görünen porozite ve bulk yoğunluk aşağıdaki eşitlikler kullanılarak hesaplanmıştır (British Standard Testing of Engineering Ceramics, 1989):

$$\% \text{ Görünen Porozite} = [(Wc - Wa) / (Wc - Wb)] * 100 \quad (1)$$

$$\text{Yığınsal (Bulk) Yoğunluk} = [Wa / (Wc - Wb)] \quad (2)$$

**Mekanik Özelliklerin Belirlenmesi (Determination of Mechanical Properties)**

- **Soğuk Basma Mukavemeti (Cold compressive strength):** Her bir kompozisyona ait 50 mm × 50 mm × 50 mm (en × boy × yükseklik) ebatında şekillendirilen 5’er adet kare prizma numuneye Liya marka basma test cihazında soğuk basma testi yapılmıştır.

- **3 Nokta Eğme Testi (3 Point Bending Test):** 25mm × 25mm × 150mm (genişlik × kalınlık × uzunluk) çubuk şeklinde üretilen malzemelerden her kompozisyon için 5’er adet numuneye, ASTM C1161-90’a uygun olarak Shimadzu AGS-X marka cihazda üç nokta eğme deneyi uygulanmış ve sonuçların ortalaması alınmıştır. Örnekler destekler arası uzaklık L=125 mm ve numunenin ortasından yükleme hızı 0,15 MPa/sn. olacak şekilde yükleme yapılmıştır. 3-nokta eğme testi ile mukavemet ve elastik modül sıra ile aşağıdaki eşitlikler kullanılarak belirlenmektedir (Köksal, 2009):

$$\text{Mukavemet: } \sigma = \frac{3}{2} \times \frac{P \times L}{W \times D^2} \quad (3)$$

$$\text{Elastik modül: } E = \frac{L^3}{4 \times W \times D^3} \times m \quad (4)$$

P : Kırılma yükü (N)

L : Destekler arası mesafe (m)

W : Numunenin genişliği (m)

D : Numunenin kalınlığı (m)

m : Gerilme-deformasyon ( $\sigma - E$ ) eğrisinin eğrisi eğimi (N/m)

**SONUÇLAR ve TARTIŞMALAR (RESULTS and DISCUSSIONS)****Reçine ve Pirolitik Sıvı Ürünlerinin Yoğunluk, Viskozite, pH, GC-MS Sonuçları (Density, Viscosity, pH, GC-MS Results of Resin and Pyrolytic Liquid Products)**

Çukurova Kimya Sanayi A.Ş. tarafından temin edilen fenolik reçinenin yoğunluğu 1,22 g/ml, 28 °C’de viskozitesi 2200 cST, ph değeri ise 8,31 olarak ölçülmüştür. Fenolik reçinenin bileşik içeriği GC-MS analizi sonucunda Çizelge 3’te belirtilmiştir. Bu bileşiğin en yüksek piki C<sub>13</sub>H<sub>12</sub> 2-(4-Hidroksibenzil)fenol (% 32,7) olarak belirlenmiştir.

**Çizelge 3.** Fenolik reçineye ait GC-MS sonucu*Table 3. GC-MS result of Phenolic resin*

RT (Alıkonma zamanı dk)	Pik Alan %	Bileşik	Kapalı Formül
5,94	1,29	3-Etiltoluen	C <sub>9</sub> H <sub>12</sub>
6,248	25,73	1,2,4-Trimetilbenzen	C <sub>9</sub> H <sub>12</sub>
6,711	1,58	Dietilenglikol	C <sub>4</sub> H <sub>10</sub> O
6,814	1,48	2-Etiltoluen	C <sub>9</sub> H <sub>12</sub>
11,556	0,63	m-Propiltoluen	C <sub>10</sub> H <sub>14</sub>
12,068	0,57	2-Metil-p-etiltoluen	C <sub>10</sub> H <sub>14</sub>
13,74	0,59	o-Simen	C <sub>10</sub> H <sub>14</sub>
25,506	5,1	Dodekametilsikloheksasiloksan	C <sub>12</sub> H <sub>36</sub>
31,434	3,81	1,1,3,3,5,5,7,7,9,9,11,11-Dodekametilheksasiloksan	C <sub>12</sub> H <sub>38</sub>
36,505	0,79	Bis[1,4]benzodithiino[2,3-b:2',3'-e]piridin	C <sub>17</sub> H <sub>9</sub>
39,714	7,8	(3,5-Dimetillfenoksi)(dimetil)fenisilan	C <sub>16</sub> H <sub>20</sub>
45,033	7,59	2,2'-Metilendifenol	C <sub>13</sub> H <sub>12</sub>
45,74	32,7	2-(4-Hidroksibenzil)fenol	C <sub>13</sub> H <sub>12</sub>
47,283	10,32	Fenol, 4,4'-metilen bis-	C <sub>13</sub> H <sub>12</sub>

**Çizelge 4.** Bir kere ekstraksiyon sonrası pirolitik sıvı ürünün GC-MS analizi*Table 4. GC-MS results of pyrolytic liquid after once extraction*

RT (Alıkonma zamanı dk)	Pik Alan %	Bileşik	Kapalı Formül
6,129	0,41	Stiren	C <sub>8</sub> H <sub>8</sub>
9,005	1,04	dl-Limonen	C <sub>10</sub> H <sub>16</sub>
9,315	1,13	Benzen, 1-etil-3-metil-	C <sub>9</sub> H <sub>12</sub>
10,057	0,53	1,3-Siklopentadien	C <sub>5</sub> H <sub>6</sub>
15,362	1,54	Terpilonen	C <sub>10</sub> H <sub>16</sub>
16,349	0,39	Benzen, 1-metil-4-(1-metilpropil)	C <sub>11</sub> H <sub>16</sub>
20,083	0,15	2,2-Dimetilinden, 2,3-dihidro-	C <sub>11</sub> H <sub>14</sub>
20,58	0,37	1H-İnden, 2,3-dihidro-1,2-dimetil-	C <sub>11</sub> H <sub>14</sub>
21,899	1,01	1,3-Benzotiazol	C <sub>7</sub> H <sub>5</sub> NS
23,247	1,21	1H-İnden, 1,3-dimetil-	C <sub>11</sub> H <sub>12</sub>
31,169	1,69	α-Selinen	C <sub>15</sub> H <sub>24</sub>
34,059	0,73	Naftalen, 1,2-dihidro-2,5,8-trimetil-	C <sub>13</sub> H <sub>16</sub>
34,434	0,73	Pentadekan	C <sub>15</sub> H <sub>32</sub>
38,131	0,72	1H-Tieno[3,4-d]imidazol-4-propanoik asit, heksahidro-2-okzo-	C <sub>8</sub> H <sub>12</sub> N <sub>2</sub>
42,261	0,67	n-Heptadekan	C <sub>17</sub> H <sub>36</sub>
42,665	1,17	Naftalen, 1,2,3,4-tetrametil-	C <sub>14</sub> H <sub>16</sub>
49	1,73	Sikloheptan	C <sub>7</sub> H <sub>14</sub>
49,498	0,82	Heptadekannitril	C <sub>16</sub> H <sub>31</sub> N
56,136	0,66	Heptadekannitril	C <sub>17</sub> H <sub>33</sub> N
61,261	1,24	Benzenamin	C <sub>6</sub> H <sub>7</sub> N
63,373	0,36	1,4-Benzendiamine	C <sub>6</sub> H <sub>8</sub> N <sub>2</sub>
67,332	0,32	Pentakosan	C <sub>25</sub> H <sub>52</sub>
69,932	0,28	Hezakosan	C <sub>26</sub> H <sub>54</sub>
70,811	0,13	1H-İmidazol-4-metanol	C <sub>4</sub> H <sub>6</sub> N <sub>2</sub>
77,212	0,85	Stigmast-5-en-3-ol, (3.beta.)-	C <sub>29</sub> H <sub>50</sub> O
80,455	0,59	4.alfa.-Metilkoleston-7-en-3-on	C <sub>28</sub> H <sub>46</sub> O
81,5	0,61	Ergosta-4,6,22-trien-3.beta.-ol	C <sub>28</sub> H <sub>44</sub> O
83,864	0,23	Tetratriakontan	C <sub>34</sub> H <sub>70</sub>
103,678	0,36	Heptan, 1,7-dibromo-	C <sub>7</sub> H <sub>14</sub> Br

500 °C sıcaklık, 15 °C/dk. ısıtma hızı ve 0,5 l/dk. azot akış hızı parametrelerinde elde edilen sıvı ürünün yoğunluğu 0,79, viskozitesi 274 cST, pH değeri 6,1 ve kükürt miktarı % 1,56 olarak ölçülmüştür.

Bir kere %10' luk H<sub>2</sub>SO<sub>4</sub> çözeltisi ile ekstraksiyon işlemi ile kükürt miktarı düşürülmüş olan sıvının yoğunluğu 0,95 g/ml, viskozitesi 45,2 cST, pH değeri ise 6,7 olarak ölçülmüştür. Viskozite değerine

bakılacak olursa, piroliz sonrası sıvıya göre daha yoğun fakat fenolik reçineden daha akışkan bir sıvı elde edildiği görülmektedir. Kükürt analizi sonucu kükürt miktarı % 1,18 olarak belirlenen sıvıya ait GC-MS sonucu da Çizelge 4'te belirtilmiştir.

İkinci kez %10' luk H<sub>2</sub>SO<sub>4</sub> çözeltisi ile ekstraksiyon işlemi uygulanarak kükürt giderimi yapılan pirolitik sıvının yoğunluğu 0,98 g/ml, viskozitesi 351,4 cST, ph değeri ise 5,8 olarak ölçülmüştür. Bu sıvıya ait kükürt analiz sonucu % 1,08'dir ve GC-MS sonucu Çizelge 5'te verilmiştir.

**Çizelge 5.** İkinci kez ekstraksiyon sonrası pirolitik sıvı ürünün GC-MS analizi

*Table 5. GC-MS results of pyrolytic liquid after second extraction*

RT (Alıkonma zamanı dk)	Pik Alan (%)	Bileşik	Kapalı Formül
6,366	0,43	Stiren	C <sub>8</sub> H <sub>8</sub>
9,033	16,87	dl-Limonen	C <sub>10</sub> H <sub>16</sub>
9,343	1,16	Benzen, 1-etil-3-metil-	C <sub>9</sub> H <sub>12</sub>
10,237	1,18	1,3-Sikloheksadien	C <sub>6</sub> H <sub>8</sub>
15,397	0,93	Terpinolen	C <sub>10</sub> H <sub>16</sub>
20,119	0,48	1H-İnden, 2,3-dihidro-1,2-dimetil-	C <sub>11</sub> H <sub>14</sub>
20,616	0,35	2,2-Dimetilinden, 2,3-dihidro-	C <sub>11</sub> H <sub>14</sub>
23,283	1,58	1H-İnden, 1,3-dimetil-	C <sub>11</sub> H <sub>12</sub>
31,197	1,58	α-Selinen	C <sub>15</sub> H <sub>24</sub>
34,102	0,66	Naftalen, 1,2-dihidro-2,5,8-trimetil-	C <sub>13</sub> H <sub>16</sub>
34,462	0,72	Pentadekan	C <sub>15</sub> H <sub>32</sub>
42,297	0,65	n-Heptadekan	C <sub>17</sub> H <sub>36</sub>
42,7	1,08	Naftalen, 1,2,3,4-tetrametil-	C <sub>14</sub> H <sub>16</sub>
47,976	0,5	Pentakloroanilin	C <sub>6</sub> H <sub>2</sub> Cl <sub>5</sub>
48,596	1,78	Sikloheptan	C <sub>7</sub> H <sub>14</sub>
49,533	0,7	Hekzadekannitril	C <sub>16</sub> H <sub>31</sub> N
55,177	0,22	Dietil 2,2'-(metilendisülfonedil)diasetat	C <sub>9</sub> H <sub>16</sub> O <sub>4</sub> S <sub>2</sub>
56,179	0,68	Heptadekannitril	C <sub>17</sub> H <sub>33</sub> N
61,75	0,26	Bisnorbiotin	C <sub>8</sub> H <sub>12</sub> N <sub>2</sub> O <sub>3</sub> S
67,387	0,27	Pentakosan	C <sub>25</sub> H <sub>52</sub>
69,974	0,36	Hekzakosan	C <sub>26</sub> H <sub>54</sub>
70,7	0,34	Pentakloroaminobenzen	C <sub>6</sub> H <sub>2</sub> Cl <sub>5</sub>
70,86	0,14	1H-İmidazol-4-metanol	C <sub>4</sub> H <sub>6</sub> N <sub>2</sub>
71,43	1,39	Stigmast-5-en-3-ol, (3.beta.)-	C <sub>29</sub> H <sub>50</sub> O
78,89	0,29	2,3,4,5,6-Pentaklorobenzenamin	C <sub>6</sub> H <sub>2</sub> Cl <sub>5</sub> N
80,534	0,55	4.alfaa.-Metilkoleston-7-en-3-on	C <sub>28</sub> H <sub>46</sub> O
81,01	0,73	Benzenamin, 2,3,4,5,6-pentakloro-	C <sub>6</sub> H <sub>2</sub> Cl <sub>5</sub> N
81,56	0,56	Ergosta-4,6,22-trien-3.beta.-ol	C <sub>28</sub> H <sub>44</sub> O
83,94	0,44	Tetratriakontan	C <sub>34</sub> H <sub>70</sub>

GC-MS sonuçları değerlendirildiğinde, sülfirik asit ile ekstraksiyon işlemi sıvı ürüne 1 defa ve 2 defa uygulandığında kükürt içerikli bileşenlerin türünde farklılıklar olduğu görülmüştür. 1 yıkama uygulanan sıvı üründe 1 tür kükürt içerikli bileşik varken (1,3-Benzotiazol; alıkonma zamanı 21,899. dk); 2 yıkama uygulanan üründe 2 farklı bileşik tespit edilmiştir (Dietil 2,2'-(metilendisülfonedil)diasetat ve Bisnorbiotin; alıkonma zamanları sırasıyla 55,177. dk ve 61,75.dk) (Çizelge 4, 5). Ancak, 1 yıkama olan üründeki bileşiklerin miktarlarıyla ilgili bilgi veren pik alan 2 yıkama uygulanan sıvıdaki iki bileşiğin pik alanları toplamından daha yüksektir. 1 yıkama yapılan sıvı üründeki kükürt içerikli bileşik 1,3-Benzotiazol için pik alan %1,01 iken; 2 yıkama yapılan üründeki kükürt içerikli bileşikler olan Dietil 2,2'-(metilendisülfonedil)diasetat (% pik alanı 0,22) ve Bisnorbiotin (% pik alanı 0,26) için pik alanlar

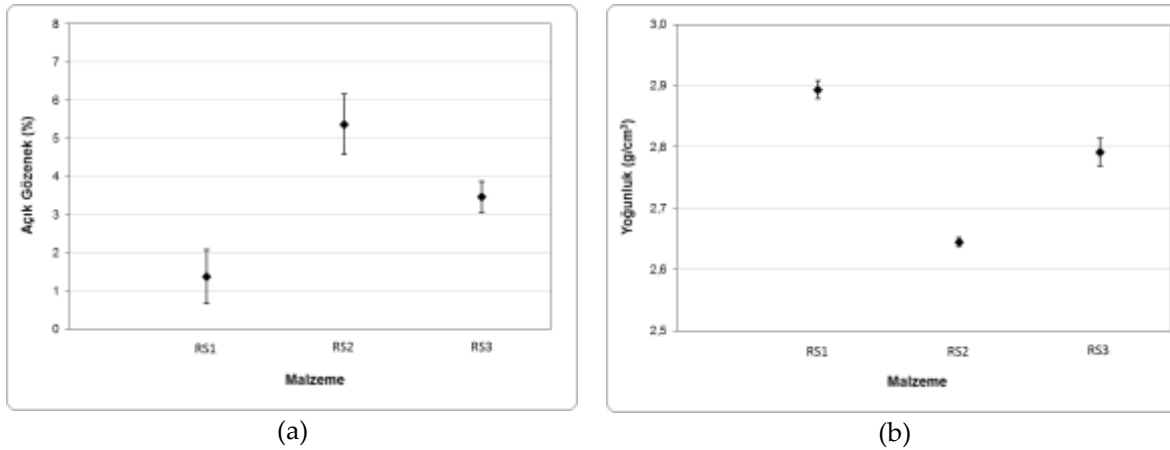
toplamı %0,48' dir (Çizelge 4, 5). Bu durum, kükürt ölçüm sonuçlarını doğrular niteliktedir. 2 yıkama uygulanması kükürt miktarını 1 yıkamaya göre düşürmektedir.

GC-MS sonuçlarında görülen bir diğer farklılık ise 1 ve 2 yıkama uygulanan sıvıların büyük molekül içeriğindeki farklılıklardır. Her iki sıvının  $C_{20}$ - $C_{34}$  arasında büyük moleküller içerdiği görülmektedir. Ancak, bu aralıktaki büyük moleküllerin pik alanları toplamı karşılaştırıldığında 2 yıkama sonrası sıvıda pik alan değerinin (%3,57) 1 yıkamaya göre (%2,88) yüksek olduğu görülmektedir. Buna göre, sülfirik asit ile ekstraksiyon işleminin büyük moleküllerin oluşumunu sağladığı söylenebilir. GC-MS sonuçlarından görülen karbon zincirlerindeki uzama, sıvıların fiziksel özelliklerine de yansımaktadır. Sülfirik asit ile ekstraksiyon sonrası uzun moleküllü zincirlerin artması nedeniyle sıvı viskozitelerinde yükselme görülmektedir. Şöyle ki, iki yıkama sonrası kinematik viskozite 398 cST değerine kadar çıkmıştır.

### Kompozisyonların % Açık Gözenek ve Yoğunluk Tayini (% Open Porosity and Density Values of Compositions)

MgO ile belirli oranlarda karıştırılan grafit, pirolitik sıvı ve fenolik reçine ilaveleriyle hazırlanan kompozisyonlara ait % açık gözenek ve yoğunluk grafikleri Şekil 1'de verilmiştir.

Kompozisyonların yoğunluk değerleri, açık gözenek miktarı azaldıkça artmaktadır. En yüksek yoğunluk değeri grafit ve reçine ile elde edilen RS1 numunesidir. Grafit ve reçine içeren kompozisyonların da genel olarak yoğunluk değerleri daha yüksektir. Pirolitik sıvı girdisi arttıkça üretilen kompozisyonların yoğunluk değeri de azalmaya başlamıştır. En düşük yoğunluk ve en yüksek % açık gözenek miktarına RS2 kompozisyonunda ulaşılmıştır.



Şekil 1. Kompozisyonların a) % açık gözenek ve b) yoğunluk grafikleri

Figure 1. a) % open porosity and b) density graphs of compositions

### XRD ve XRF Analiz Sonuçları (Results of XRD and XRF Analysis)

Temperlenmiş numunelerin kimyasal analizleri (XRF) Çizelge 6'da verilmiştir. XRF analizi ile C tespit edilemediğinden dolayı, geriye kalan elementlerin toplamı % 100 olacak şekilde hesaplanmıştır. Tüm malzemelerin en yüksek oranda kimyasal bileşeni MgO'dur. Genel olarak sıvı atık girdisi olan malzemelerde daha yüksek oranda  $Al_2O_3$ ,  $SiO_2$  ve  $SO_3$ 'e rastlanmıştır, diğer oksitlerin/elementlerin yüzdeleri grafit ve reçine kullanılan malzemeler ile yaklaşık değerlerdedir. RS2'nin  $SiO_2$  miktarı, RS1'den %0,5 daha düşüktür.

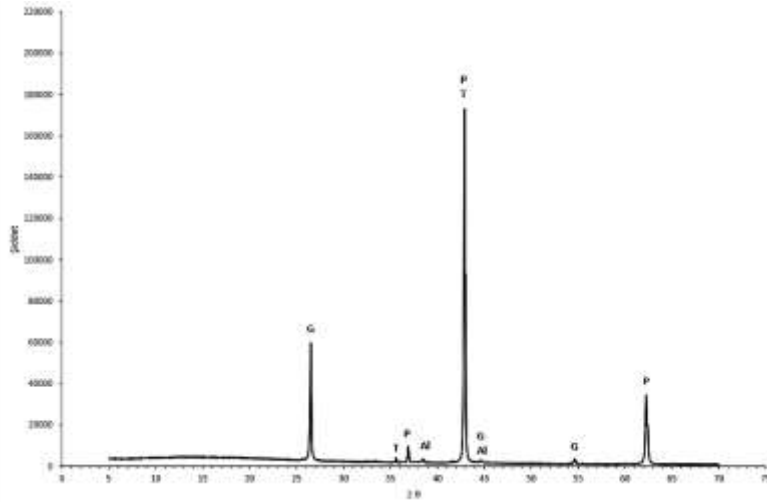
**Çizelge 6.** Kompozisyonların XRF analizleri*Table 6. XRF analysis of compositions*

Oksit/Element Adı	Oksit/Element Miktarı (%)		
	RS1	RS2	RS3
<b>MgO</b>	86,52	88,32	83,56
<b>Al<sub>2</sub>O<sub>3</sub></b>	5,64	6,33	7,62
<b>SiO<sub>2</sub></b>	2,91	2,41	3,15
<b>CaO</b>	2,50	1,37	2,75
<b>Fe<sub>2</sub>O<sub>3</sub></b>	1,60	0,72	1,87
<b>SO<sub>3</sub></b>	0,30	0,37	0,48
<b>Na<sub>2</sub>O</b>	0,19	0,23	0,17
<b>P<sub>2</sub>O<sub>5</sub></b>	0,11	0,07	0,14
<b>MnO</b>	0,09	0,04	0,08
<b>Cl</b>	0,06	0,01	0,08
<b>K<sub>2</sub>O</b>	0,05	0,04	0,06
<b>CuO</b>	-	0,08	-
<b>TiO<sub>2</sub></b>	0,03	0,01	0,04

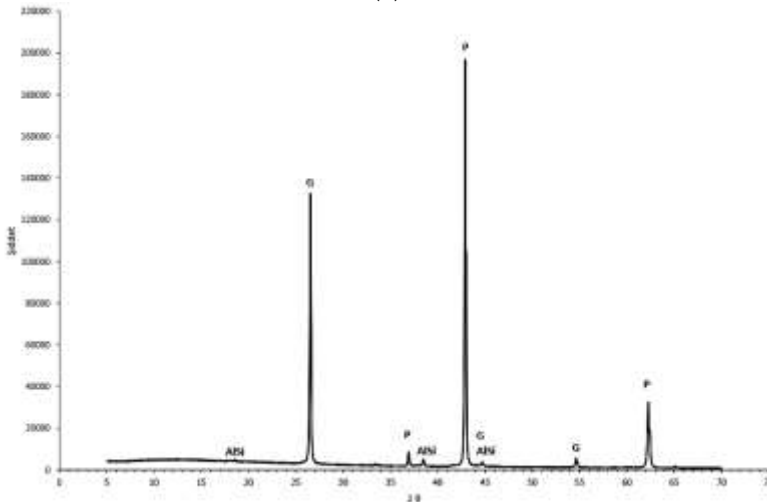
Temperlenmiş kompozisyonların faz analizleri (XRD) Çizelge 7’de ve Şekil 2’de belirtilmiştir. XRD sonuçları incelendiğinde, tüm kompozisyonlar için ana fazların Periklas (MgO) ve Karbon olduğu gözlenmiştir. Özellikle pirolitik sıvı ürününün kullanıldığı malzemelerde Çizelge 6’da görüldüğü üzere yüksek oranlarda Al ve Si elementlerinin fazlarına rastlanmıştır.

**Çizelge 7.** Kompozisyonların XRD analiz sonuçları*Table 7. XRD analysis of compositions*

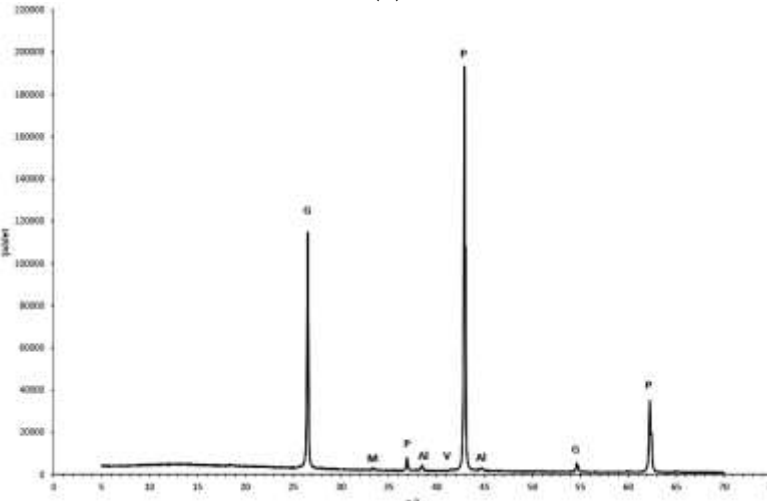
Mineral Adı	Mineral miktarı (%)		
	RS1	RS2	RS3
Periklas (MgO)	65,6	47,5	47,8
Grafit (C)	32,8	-	51,2
Grafit 2H (C)	-	52,4	-
Troilit (FeS)	1,5	-	-
Alüminyum (Al)	0,1	-	0,8
Alüminyum Silisyum (3,85/0,15)	-	0,1	-
Vüstit (FeO)	-	-	0,2



(a)



(b)



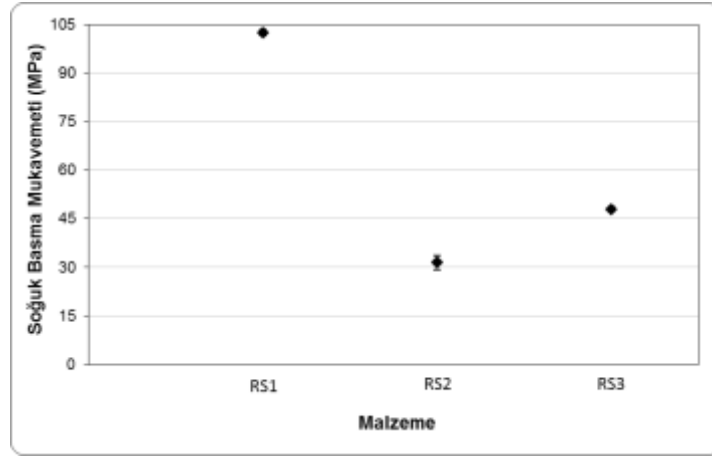
(c)

**Şekil 2.** Üretilen kompozisyonların XRD analizi grafikleri a) RS1, b) RS2 ve c) RS3 (G: Grafit, P: Periklas, T: Troilit, Al: Alüminyum, AlSi: Alüminyum silisyum (3,85/0,15), M: Moissanit, V: Vüstit)

*Figure 2.* XRD graphs of produced compositions a) RS1, b) RS2 and c) RS3 (G: Graphite, P:Periclase, T: Troilite, Al: Aluminum, AlSi: Aluminum silicon (3.85/0.15), M: Moissanite V: Wustite)

### Kompozisyonların Soğuk Basma Mukavemeti Sonuçları (Cold Compressive Strength Results of Compositions)

50 mm × 50 mm × 50 mm (en × boy × yükseklik) ebatında şekillendirilen kompozisyonlara ait soğuk basma mukavemeti (SBM) grafiği Şekil 3'te verilmiştir.



Şekil 3. Kompozisyonların soğuk basma mukavemeti grafikleri

Figure 3. Cold compressive strength graphs of compositions

Grafik incelendiğinde en yüksek mukavemet değerinin grafit ve reçine ile üretilen RS1 kompozisyonuna ait olduğu görülmüştür. Soğuk basma mukavemetlerini kıyaslayacak olursak RS1(Grafit+Reçine) > RS3(Grafit+ Reçine+Sıvı) > RS2(Grafit+Sıvı). Bağlayıcı olarak fenolik reçine ve pirolitik sıvı kullanılan kompozisyonların SBM değerlerini kıyaslar isek sıvı girdisi artmaya başladıkça SBM değeri düşmektedir. Başka bir ifade ile, reçine ve grafit girdileri ile üretilen kompozisyonların soğuk basma mukavemet değerleri yüksek iken pirolitik sıvı girdileri ile azalmaktadır.

Tüm kompozisyonlar için yoğunluk değeri arttıkça ve % açık gözenek değeri azaldıkça (Şekil 1) SBM değerinin de arttığı (Şekil 3) ve dolayısı ile gözenegın SBM üzerine olumsuz etki ettiği gözlenmiştir.

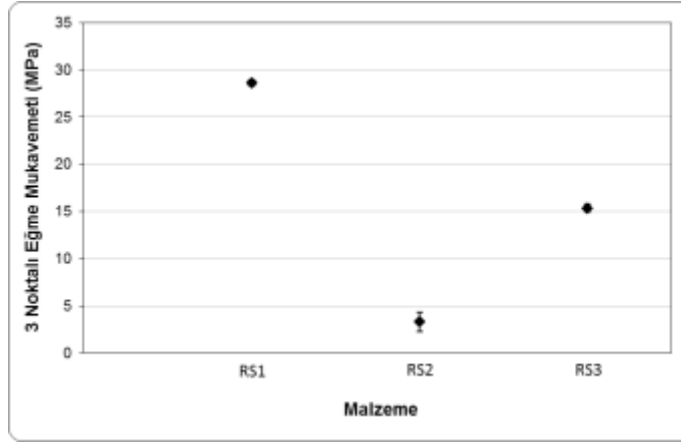
### Çizelge 8. Kompozisyonların % açık gözenek, yoğunluk, S.B.M. sonuçları

Table 8. % open porosity, density and ccs results of compositions

	Açık Gözenek (%)	Arşimet Yoğunluğu (g/cm <sup>3</sup> )	Soğuk Basma Mukavemeti (MPa)
RS1	1,37	2,89	102,50
RS2	5,37	2,64	31,49
RS3	3,47	2,79	47,97

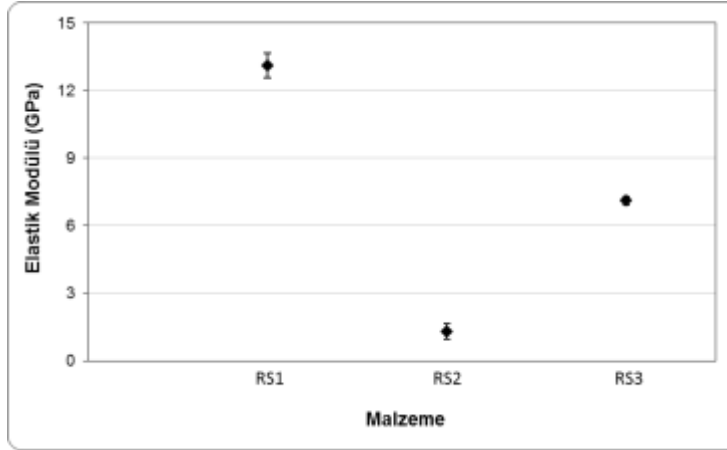
### 3 Nokta Eğme Testi Sonuçları (3 Point Bending Test Results)

25mm × 25mm × 150mm (genişlik × kalınlık × uzunluk) çubuk şeklinde üretilen ve temperlenen her bir kompozisyon için eğme mukavemeti değerlerini gösteren grafik Şekil 4'te verilmiştir. Soğuk basma mukavemeti ile benzer sonuçlar gözlenmiştir. Reçine ve grafit girdileri ile üretilen RS1 kompozisyonunun eğme mukavemeti de soğuk basma mukavemet değerine benzer şekilde en yüksek iken pirolitik sıvı girdileri ile eğme mukavemet değerleri SBM değerlerinde olduğu gibi azalmaya başlamaktadır. Reçine ve grafit kullanılan malzemelerin elastik modülü değerleri yüksek iken, lastik atığının pirolizi sonucu elde edilen sıvı ürünün kullanılması ile üretilen MgO-C refrakter kompozisyonlarının elastik modülü değerleri daha düşüktür. En yüksek elastik modülü değerine RS1 kompozisyonunda, en düşük elastik modülü değerlerine ise RS2 malzemelerinde ulaşılmıştır.



Şekil 4. Kompozisyonların 3 nokta eğme testi grafiği  
Figure 4. 3 Point bending test graphs of compositions

Kompozisyonların 3 noktalı eğme testi ile belirlenen elastik modülü değerleri Şekil 5'te belirtilmiştir.



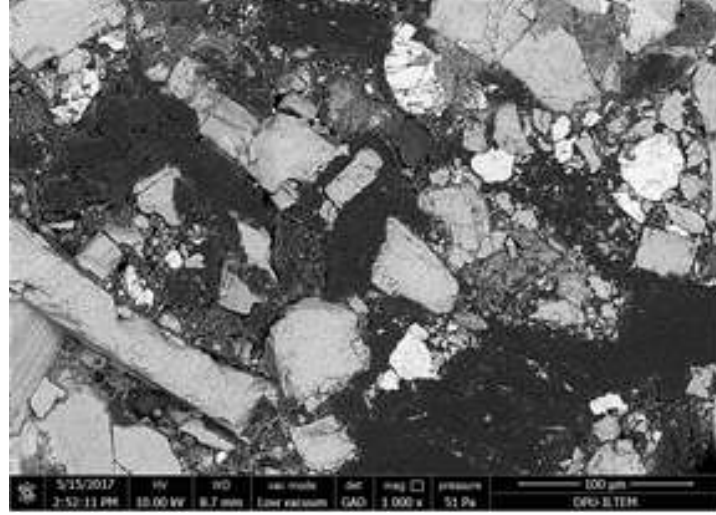
Şekil 5. Kompozisyonların elastik modülü grafikleri  
Figure 5. Elastic modulus graphs of compositions

#### Taramalı Elektron Mikroskopu (SEM) ile Karakterizasyon Sonuçları (Results of Characterization by Scanning Electron Microscopy-SEM)

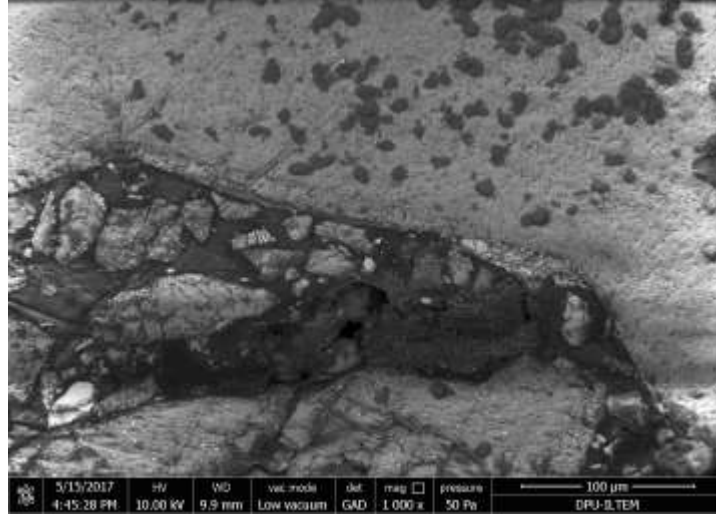
Laboratuvar ortamında üretilen RS1, RS2 ve RS3 numunelerinin taramalı elektron mikroskopu (SEM) görüntüleri Şekil 6'da verilmiştir. Görüntülerde reçine ve grafit ile üretilen RS1 referans numunesinin, minimum gözeneğe sahip olduğu, iri ve ince MgO taneleri ve pul grafit tanelerinin reçine ile birlikte yoğun bir malzeme oluşturduğu görülmektedir. Açık gri ile görülen taneler MgO tanelerini, koyu gri ile gözlenen taneler ise pul grafit tanelerini göstermektedir. Açık renkli bölgeler ise MgO içerisinden gelen kalsiyum silikat esaslı fazlardır.

RS2 numunesinde kullanılan sıvı atığın, reçine kadar bağlayıcı bir özelliğe sahip olmadığı görüntüde bulunan gözeneklerden ve dağılımdan da görülmektedir. Kullanılan sıvı atığın malzeme üzerinde ıslatma etkisi olduğu manyezit üzerinde bıraktığı kirliliklerde görülmektedir. Fakat bağlayıcılık olarak istenilen etkiyi göstermemektedir.

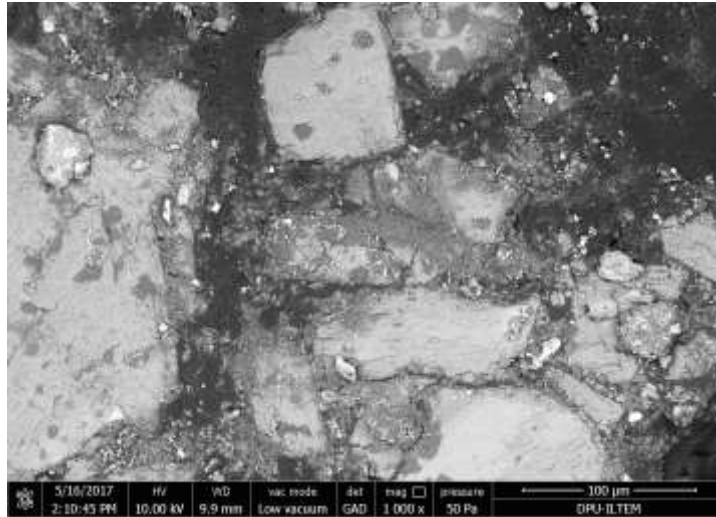
RS3 numunesinde sıvı atık ile reçinenin birlikte kullanımı, sadece sıvı atık kullanılan RS2 numunesine göre daha yoğun ve daha gözeneksiz bir yapı oluşturmuştur. Görüntülerden de anlaşılacağı üzere reçinenin kullanıldığı RS1 ve RS3 numuneleri, sıvı atığın kullanıldığı RS2 numunesinden daha yoğundur ve grafit taneler ile MgO taneleri arasında RS2 numunesine göre daha iyi bağlanma gözlenmektedir.



(a)



(b)



(c)

Şekil 6. SEM ile elde edilen geri yansıyan elektron görüntüleri a) RS1, b) RS2 ve c) RS3

Figure 6. The back scattered electron images obtained by SEM a) RS1, b)RS2, c)RS3 Obtained by SEM

## GENEL SONUÇLAR (CONCLUSIONS)

Kompozisyonların yoğunluk değerleri, açık gözenek miktarı azaldıkça artmaktadır. Tüm kompozisyonlar için yoğunluk değeri arttıkça ve % açık gözenek değeri azaldıkça SBM ve eğme mukavemeti değerlerinin de arttığı ve dolayısı ile gözenegin mekanik özellikler üzerine olumsuz etki ettiği gözlenmiştir. En yüksek yoğunluk, SBM, eğme mukavemeti, elastik modülü değerlerine grafit ve reçine ile elde edilen RS1 numunesinde ulaşılmıştır.

Pirolitik sıvı girdisi arttıkça üretilen kompozisyonların yoğunluk, SBM, eğme mukavemeti, elastik modülü değerleri azalmaya başlamıştır. RS2 kompozisyonu en düşük yoğunluk ve en düşük mekanik özelliklere (SBM, eğme mukavemeti ve elastik modülü) sahiptir.

Genel olarak sıvı atık girdisi olan RS2 ve RS3 malzemelerde daha yüksek oranda  $Al_2O_3$  ve  $SO_3$ 'e rastlanmıştır. Bu malzemelerin mekanik özellikleri RS1 malzemesinden daha kötüdür. S miktarının refrakter malzemelerde yüksek olmasının mekanik özelliklere olumsuz etki ettiği sonucuna ulaşılmıştır.

## TEŞEKKÜR

Bu çalışma Tübitak 115M371 numaralı proje tarafından desteklenmiştir. Verdiği teknik çalışma desteği için Nesibe Sevede Ülvan'a teşekkür ederiz.

## KAYNAKLAR (REFERENCES)

- Ahmad, S., Ahmad, M.I., 2013, "Desulfurization of Oils; Produced from Pyrolysis of Scrap Tires", *NUST Journal of Engineering Sciences*, Vol. 6 (1), pp. 27-32.
- Aydın, H., İlkılıç, C., 2012, "Optimization of Fuel Production from Waste Vehicle Tires by Pyrolysis and Resembling to Diesel Fuel by Various Desulfurization Methods", *Fuel*, Vol. 102, pp. 605-612.
- British Standard *Testing of Engineering Ceramics*, 1989, BS 7134 Section 1.2.
- Gönüllü, M.T., 2004, "Atık Lastiklerin Yönetimi", *Katı Atık Geri Dönüşüm Teknolojileri Semineri*, İSO, İstanbul.
- Isayev, A., 2005, *Recycling of Rubber*, Science and Technology of Rubber, Editörler: Mark, J.E., Erman, B., Eirich, F.R., Elsevier, Akron, United States, 663-701.
- Köksal, N.S., "Magnezya Esaslı Refrakter Malzemelerde Mekanik özelliklerin YSA ile Belirlenmesi", 5. *Uluslararası İleri Teknolojiler Sempozyumu (IATS'09)*, Karabük, 13-15 Mayıs 2009.
- Leung, D.Y.C., Wang, C.L., 1998, "Kinetic Study of Scrap Tyre Pyrolysis and Combustion", *Journal of Analytical and Applied Pyrolysis*, Vol. 45, pp. 153-69.
- Özgen, S., "Metalurji Sanayinde Grafit Oksit Refrakter Kompozitler", *TMMOB Metalurji Mühendisleri Odası, 5. Metalurji Kongresi*, Ankara, pp. 898-903, 21-25 Kasım 1988.
- Timuçin, M., Sesver, A., Sarioğlu N., 2014, "Elektrik Ark Ocağı Çelik Cürufalarında Faklı Oranlarda MgO Doygunluğunda Mg-C Tuğlanın Çözünürlük Davranışı", *Afyon Kocatepe Üniversitesi Fen ve Mühendislik Bilimleri Dergisi*, Cilt 14, Özel Sayı 1, pp. 517-521.
- Unapumnuk, K., Keener, T.C., Lu, M., Liang, F., 2008, "Investigation into the Removal of Sulfur from Tire Derived Fuel by Pyrolysis", *Fuel*, Vol. 87, pp. 951-956.
- Yazla, C., 1984, "Grafitli Refrakter Malzemelerin Özellikleri", *Metalurji Dergisi*, Vol. 32, pp. 8-11.
- Wampler, T.P., 2007, *Applied Pyrolysis Handbook*, 2. basım, CRC Press, Boca Raton, U.S.A.